Fabrication and characterization of ZnO-based microcavities working in the strong coupling regime : polariton laser

Feng Li

To cite this version:

Feng Li. Fabrication and characterization of ZnO-based microcavities working in the strong coupling regime : polariton laser. Other [cond-mat.other]. Université Nice Sophia Antipolis, 2013. English. NNT : 2013NICE4105 . tel-00944656

HAL Id: tel-00944656
https://theses.hal.science/tel-00944656v1

Submitted on 10 Feb 2014

UNIVERSITE DE NICE-SOPHIA ANTIPOLIS - UFR Sciences
Ecole Doctorale de Sciences Fondamentales et Appliquées

THESE

pour obtenir le titre de
Docteur en Sciences
de l'UNIVERSITE de Nice-Sophia Antipolis

Discipline : Physique

présentée et soutenue par
Feng LI

Fabrication and Characterization of ZnO-based Microcavities Working in the Strong Coupling Regime: Polariton Laser

Thèse dirigée par Jean-Yves DUBOZ
et co-dirigée par Jesus ZUNIGA-PEREZ
soutenue le 29. 11. 2013

Jury :

Alberto BRAMATI	Professeur, Université Paris VI	Rapporteur
Maurice SKOLNICK	Professeur, University of Sheffield	Rapporteur
Aristide LEMAITRE	Chargé de Recherche, CNRS	Examinateur
Maxime RICHARD	Chargé de Recherche, CNRS	Examinateur
Jesus ZUNIGA-PEREZ	Chargé de Recherche, CNRS	Co-directeur de thèse
Jean-Yves DUBOZ	Directeur de Recherche, CNRS	Directeur de thèse

Contents

Introduction

Light-matter interaction has been an intense research field for many decades. In 1946 Purcell proposed the idea that the spontaneous emission of a given emitter could be altered by its environment [1], which was experimentally demonstrated in the 1980s by the observation of either an enhancement [2] or an inhibition [3] of the spontaneous emission rates of single atoms placed inside microwave cavities. These investigations were performed in a system in which the cavity life time is sufficiently short so that the emitted photons escape from the cavity before being re-absorbed by the emitter. On the other hand, if the optical confinement is strong enough, photons in the cavity might be re-absorbed before they escape from the cavity, re-emitted back again into the cavity, in a back and forth energy exchange between the emitter and the cavity. In this case, the coupling between light and matter gives rise to new eigenstates, built upon the bare emitter and bare cavity modes, and drives the system into the so-called **strong coupling regime**. This regime was experimentally demonstrated in atomic physics during the 1980s [4] and 1990s [5,6].

In parallel to the development of atomic cavities, semiconductor optical cavities appeared in the 1960s thanks to the incipient field of optoelectronics, which included devices such as laser diodes [7,8]. Subsequently, and with the aim of enhancing light-matter coupling in solid-state systems, large quality factor and small mode volume cavities were intensively studied, especially since the early 1990s [9]. In a semiconductor, the first excited state is termed exciton and refers to a quasi-particle formed by an electron-hole pair bounded together via Coulomb interaction. Hopfield proposed that a photon inside a semiconductor can efficiently couple to excitons with the same wavevector and form new coupled photon-exciton states named exciton-polaritons [10]. In this picture, energy is conserved since it is reversibly converted from photons to excitons and vice versa. Exciton-polaritons are quasi-particles, partially light partially matter, that exhibit weighted properties of their two components. It should be noted that, as far as excitons behave as bosons (i.e. below the Mott density), polaritons will do so, given that photons are bosons too. The lack of an energy minimum in the dispersion curve of bulk exciton-polaritons makes the achievement of thermal equilibrium unviable; in this situation, bulk exciton-polaritons tend to accumulate at the so-called “bottleneck” region [11]. With the aim of effectively introducing an energy minimum and render polariton thermalization possible, cavity photons can be used instead. Cavity polaritons (i.e. exciton-polaritons in which the photon mode is not a free-space mode but a cavity one) were first observed in a GaAs quantum well microcavity by Weisbuch *et al* in 1992 [12], as evidenced by the anti-crossing of the lower polariton branch (LPB) and the upper polariton branch (UPB). This seminal article opened the way for polaritonics as a field in itself. During the following years, strong coupling regime was observed also on other semiconductor systems, including ZnCd(Mg)Se(S) [13] , CdTe [14] , organics [15], GaN [16] and ZnO [17].

The idea of Bose-Einstein condensation (BEC) was proposed by Einstein in 1925, by developing an early work of Bose, and it implies that an unlimited number of bosons can accumulate in the lowest energy state of a given system [18]. The experimental realization of

Bose-Einstein condensation was first demonstrated with ultra-cold atoms in 1995 by Cornell, Wieman and Ketterle [19,20]. In parallel, efforts were also made to demonstrate BEC of excitons in solid state systems [21-23]. The temperature at which BEC was achieved in these systems was in the nanoKelvin range, for atoms, and below 1K for excitons. Since the critical temperature for BEC is inversely proportional to the mass of the condensing particles, it might be argued that much higher condensation temperatures (indeed, from cryogenic up to room temperature) should be reachable in a system consisting of cavity polartions, as their effective mass can be orders of magnitudes smaller than that of excitons. In 1996, Imamoglu *et al* proposed that coherent light emission should be observed from a strongly-coupled cavity in which polaritons occupied massively the cavity ground-state. In this paper, it was suggested that such massive occupancy might be obtained through bosonic stimulated scattering [24]. If achieved, such a device should be given the name "**polariton laser**". The first unambiguous experimental report of polariton lasing was published by Le Si Dang *et al* in 1998 [25], followed by the first demonstration of **cavity polariton BEC** by Kasprzak *et al* in 2006 [26]. Both were achieved in CdTe-based microcavities at ~5K. These achievements, together with many others, have strongly encouraged the studies on polariton condensate during the past 10 years [27,28]. A more detailed review regarding polariton condensation can be found in the main text of this thesis.

The exciton binding energies in bulk GaAs and CdTe are 4 and 10meV, respectively, and might increase up to 25meV in CdTe-based quantum wells [11]. These values render excitons in these materials only suitable for observing nonlinearities at low temperature [29]. For this reason, since the early 2000s much attention has been paid to wide bandgap materials such as organic semiconductors, GaN and ZnO, which should render room temperature polaritonic devices feasible. Indeed, the first room temperature polariton lasers were demonstrated using GaN-based bulk and quantum well microcavities in 2007 and 2008, respectively [30,31]. Two years later, in 2010, room temperature polariton lasing was also observed in an organic-based microcavity [32].

ZnO is a II-VI semiconductor emitting in the UV range (bandgap ~3.36eV at room temperature), and is believed to be one of the most adapted materials for room temperature polariton lasing [33]. Its exciton binding energy reaches 60meV in bulk material, i.e. much larger than $k_B T$ at room temperature. Its large exciton oscillator strengths, typically four to ten times larger than in GaN, can lead to large Rabi splittings, while its high Mott density should enable to keep the bosonic behavior of exciton-polaritons even under high particle densities. However, the novelty of the material, compared to all other semiconductors named in the introduction, lead to a number of technological difficulties that have hindered the fabrication of high quality ZnO microcavities up to very lately. Indeed, before this thesis started there had not been any report of ZnO polariton lasing, even though strong coupling had been demonstrated at both low [17] and room [34-38] temperatures. Nevertheless, great progress in ZnO polaritonics has been made during the past three years. ZnO polariton laser was first demonstrated at 120K by a CNRS consortium [39] in 2011, in collaboration with EPFL, followed by a detailed investigation of LO-phonon assisted relaxation [40] in 2012. The year 2012 saw a burst of publications on ZnO polariton lasers, including the report by

Franke *et al* [41] above 200K, and the claim of room temperature polariton lasing by Lu and Lai *et al* [42,43]. In addition, the studies by Xie *et al* [44], in 2012, and Trichet *et al* [45], in 2013, have both indicated that polariton condensation could be achieved in ZnO microwires.

Objectives

The initial objective of this thesis was to fabricate and demonstrate a ZnO polariton laser working at room temperature. In order to achieve this goal, several fabrication strategies were developed in parallel. First of all the growth of high quality ZnO on nitride DBRs has been further optimized, with the aim of improving the existing approach for semi-hybrid (i.e. dielectric-based top DBR and nitride-based bottom DBR) ZnO microcavities, in which polariton lasing was achieved at low temperature in 2011. Moreover, new approaches enabling the fabrication of fully-hybrid (i.e. two dielectric-based DBRs) ZnO microcavities that display much larger cavity quality factors than those obtained before in any kind of ZnO cavity have been introduced.

The successfully-fabricated microcavities have enabled a step-by-step progress in the study of ZnO polaritons: from the initial demonstration of polariton lasing from low to room temperature, it has been possible to derive a complete phase diagram of polariton condensation for ZnO microcavities, similar as those for GaN [46,47]; the cross-correlation of experimental results and numerical simulations of the relaxation mechanisms in ZnO, has enabled to underline the importance of phonon-assisted processes in ZnO cavities, and their utility for room-temperature operation. Finally, new cavity configurations could be studied, opening the door to further spectroscopic studies and highlighting the originality of the ZnO system.

Outline

The first part of this manuscript presents the building blocks necessary to fabricate a ZnO-based microcavity operating in the strong-coupling regime and displaying polariton condensation. It contains three chapters:

Chapter 1 presents the physical properties of ZnO and describes its excitons. The fundamental concepts related to excitons, including binding energy, transition selection rules, oscillator strength and Mott density, are presented, highlighting ZnO specificities.

Chapter 2 introduces the basic principles of planar microcavities. The transfer matrix method for simulating light propagation in multi-layer systems is described in detail. Then, the working-principles of distributed Bragg reflectors (DBR) as well as of Fabry-Perot resonators consisting of a dielectric layer sandwiched between two DBRs are presented.

Chapter 3 gives a thorough description of exciton-polaritons and a historical review of this research field. First, the concept of exciton-polariton and strong coupling is introduced; then, the basic principles of polariton condensation are discussed; finally, an overview of major results on wide bandgap microcavities, in particular in ZnO microcavities, is presented.

The second part of this manuscript presents the major experimental results obtained from a fully-hybrid ZnO microcavity. It contains two chapters:

Chapter 4 describes the fabrication, morphological and linear optical properties of a fully-hybrid microcavity. The studied cavity, fabricated with a completely new strategy developed at CNRS-CRHEA, works in the strong coupling regime and exhibits a record *Q*-factor, the largest Rabi splitting as well as the widest accessible range of exciton-photon detuning among ZnO (and GaN) planar microcavities.

Chapter 5 discusses the properties of polariton condensation as observed in the fully-hybrid microcavity. Room temperature polariton lasing is demonstrated and the typical lasing features investigated. A complete condensation phase diagram is obtained for ZnO microcavities, which agrees well with numerical simulations and highlights the important role of photon-assisted polariton relaxation in ZnO. Then, the richness of the cavity is illustrated: polariton condensation is achieved from highly excitonic-like to highly photonic-like polaritons, and from low to room temperature. Mode competition, similar to that observable in ZnO microwires, is demonstrated in the thicker regions of the cavity, allowing an abrupt change of the exciton/photon fraction of the polariton condensate by just varying the excitation power.

The third part of this manuscript presents the major results obtained on semi-hybrid ZnO microcavities. It contains one chapter:

Chapter 6 presents the fabrication, morphological and optical properties of two semi-hybrid microcavities. The fabrication, which constitutes the largest portion of the chapter, covers the epitaxial growth of high quality $Al_{0.2}Ga_{0.8}N/AlN$ DBRs on patterned silicon substrates, and the epitaxial growth of high quality bulk ZnO layer on such DBRs, both being performed by molecular beam epitaxy. The spectroscopic studies reveal a negligible inhomogeneous photonic broadening, a high *Q*-factor and room temperature polariton lasing.

Finally, after a conclusion chapter where an outlook on the future possibilities of ZnO polaritonics is presented, an appendix section that lists several other fabrication approaches that were not successful has been included. These experiments comprise: (1) deposition of polycrystalline ZnO/ZnMgO quantum wells on dielectric DBRs; (2) epitaxial growth of bulk ZnO layer on $Al_{0.2}Ga_{0.8}N/Al_{0.85}In_{0.15}N$ DBRs; (3) fabrication of fully-hybrid microcavities containing homo-epitaxial ZnO/ZnMgO quantum wells.

Introduction

L'interaction entre lumière et matière est un domaine de recherche en pleine expansion depuis de nombreuses décennies. En 1946, Purcell a proposé l'idée que l'émission spontanée d'un émetteur pouvait être altérée par son environnement [1], ce qui a été démontré expérimentalement dans les années 1980 par l'observation d'un renforcement [2] ou d'une réduction [3] du taux d'émission spontanée des atomes placés à l'intérieur des cavités micro-ondes. Ces recherches ont été effectuées dans un système dans lequel le temps de vie de la cavité est suffisamment court pour que les photons émis s'échappent de la cavité avant d'être réabsorbés par l'émetteur. A l'inverse, si le confinement optique est suffisamment fort, les photons dans la cavité peuvent être réabsorbés avant qu'ils ne s'échappent de la cavité, ré-émis à nouveau dans la cavité, réabsorbés et ainsi de suite, menant à un échange d'énergie réversible entre l'émetteur et la cavité. Dans ce cas, le couplage lumière- matière donne naissance à de nouveaux états propres, construits à partir des modes nus de l'émetteur et la cavité, et le système est dit dans le **régime de couplage fort**. Ce régime a été démontré expérimentalement en physique atomique dans les années 1980 [4] et 1990 [5,6].

Parallèlement au développement des cavités atomiques, les cavités optiques à base de semiconducteurs sont apparues dans les années 1960 grâce à l'essor de l'optoélectronique et de ses dispositifs, tels que des diodes laser [7,8]. Dans un semiconducteur, le premier état excité reçoit le nom d'exciton, une quasi-particule formée par un paire électron-trou liée par l'interaction de Coulomb. Hopfield a démontré qu'un photon dans un semiconducteur se couple efficacement aux excitons de même vecteur d'onde, donnant lieu à de nouveaux états propres appelés polaritons excitoniques [10]. Dans cette situation, l'énergie est conservée car elle passe de façon réversible des excitons aux photons, et vice versa. Les polaritons excitoniques sont des quasi-particules, partiellement matière, partiellement lumière. Les photons sont des bosons. Les excitons sont, quant à eux, des bosons composites qui peuvent perdre leur caractère bosonique aux fortes densités (dites de Mott) quand les interactions entre électrons ou entre trous deviennent comparables à l'interaction au sein de la paire électron-trou. Par conséquent, les polaritons pourront eux aussi perdre leur caractère bosonique aux fortes densités. Dans le but d'améliorer le couplage entre lumière et matière dans ces systèmes semiconducteurs, des cavités avec de grands facteurs de qualité et de petits volumes modaux ont été intensément étudiées, surtout depuis le début des années 1990 [9]. Le régime de couplage fort a été mis en évidence dans une microcavité à base de puits quantiques de GaAs par Weisbuch *et al* en 1992 [12] : l'anti-croisement de la branche basse de polaritons (LPB) et la branche haute de polaritons (UPB) a été observé. Cet article fondateur a ouvert la voie au développement *de la polaritonique* en tant qu'un domaine en soi. Pendant les années suivantes, le régime de couplage fort a été observé également dans d'autres systèmes semiconducteurs, y compris dans du ZnCd(Mg)Se(S) [13], dans du CdTe [14], dans des organiques [15], dans du GaN [16] et, finalement, dans du ZnO [17].

.

L'idée de condensation de Bose-Einstein (BEC) a été proposée par Einstein en 1925, en développant un travail de jeunesse de Bose : elle implique l'accumulation d'un nombre illimité de bosons dans l'état de plus basse énergie d'un système donné [18]. La condensation de Bose-Einstein a été démontré pour la première fois avec des atomes ultra-froids en 1995 par Cornell, Wieman et Ketterle [19,20]. Parallèlement, des efforts ont été investis pour démontrer la BEC des excitons dans des systèmes semiconducteurs [21-23]. La température critique à laquelle la transition de phase BEC est obtenue était de l'ordre du nanokelvin, pour les atomes, et en-dessous 1K pour les excitons. Comme la température critique pour la BEC est inversement proportionnelle à la masse effective des particules qui condensent, des températures critiques beaucoup plus élevées (en effet, de cryogénique à température ambiante) pourraient être espérées dans un système constitué à base de polaritons de cavité, étant donné que comme leurs masses effectives peuvent être inférieures quelques ordres de grandeur à celle des excitons. Un autre intérêt des cavités est d'introduire un minimum d'énergie dans la courbe de dispersion des polaritons excitoniques et rendre possible la thermalisation des polaritons. Par contraste, les structures libres homogènes à 3D ne présentent pas de minimum d'énergie, les polaritons excitoniques ont tendance à s'accumuler dans la région dite de "bottleneck" [11], ce qui rend l'obtention de l'équilibre thermique très difficile. En 1996, Imamoglu *et al* ont proposé que l'émission de lumière cohérente devrait être possible à partir d'une cavité en couplage fort dans laquelle les polaritons occupent tous le même état (dans l'occurrence, l'état fondamental de la cavité). Dans cet article, il était suggéré que l'occupation massive de l'état de base pourrait être facilitée par diffusion bosonique stimulée [24]. Si un tel dispositif était fabriqué, il recevrait le nom de «**laser à polaritons**», étant donné qu'il émettrait de la lumière cohérente et que le mécanisme de gain serait dû aux polaritons. Le premier rapport expérimental d'un laser à polaritons sans ambiguïté a été publié par Le Si Dang *et al* en 1998 [25], suivi par la première démonstration de la **BEC des polaritons de cavité** par Kasprzak *et al*, en 2006 [26]. Tous les deux ont été réalisés dans des microcavités à base de CdTe et à ~5K. Ces réalisations, ainsi que beaucoup d'autres, ont fortement encouragé les études sur les condensats de polaritons pendant les 10 années suivantes [27,28]. Une revue plus détaillée concernant l'histoire de la condensation de polaritons peut être trouvée dans le texte principal de cette thèse.

Les énergies de liaison des excitons dans GaAs et CdTe massifs sont 4 et 10 meV, respectivement, et pourraient augmenter jusqu'à 25meV dans les puits quantiques à base de CdTe [11]. Ces valeurs cantonnent l'observation des non-linéarités liées aux excitons dans ces matériaux aux basses températures [29]. Pour cette raison, depuis le début des années 2000 beaucoup d'attention a été accordée aux matériaux semiconducteurs à large bande interdite tels que les organiques, le GaN et le ZnO, qui devaient rendre possible la fabrication des dispositifs polaritoniques fonctionnant à température ambiante. Et, de fait, les premiers lasers à polaritons à température ambiante ont été démontrés dans des microcavités à base de GaN massif d'abord et à base de puits quantiques ensuite, en 2007 et 2008 respectivement [30,31]. Deux ans plus tard, en 2010, le laser à polaritons à température ambiante a également été observé dans une microcavité à base d'un semiconducteur organique [32].

Le ZnO est un semiconducteur II-VI émettant dans la gamme UV (bande interdite ~3.36eV à température ambiante), et est considéré comme l'un des matériaux les plus adaptés pour les lasers à polaritons à température ambiante [33]. Son énergie de liaison d'exciton atteint

60meV dans du matériau massif c'est à dire beaucoup plus grande que k_BT à température ambiante. Ses grandes forces d'oscillateur, généralement quatre à dix fois plus grandes que dans du GaN, peuvent conduire à un éclatement de Rabi important, tandis que sa forte densité de Mott devrait permettre de garder le comportement bosonique des excitons même à des densités de particules élevées. Cependant, les études technologiques autour de ce matériau restent limitées, si nous le comparons au GaN par exemple, et un certain nombre de difficultés techniques restaient à surmonter avant de pouvoir fabriquer des microcavités à base de ZnO. Avant le début de cette thèse, il n'y avait pas eu de rapport de laser à polaritons à base de ZnO, même si le couplage fort avait été déjà démontré à basse température [17] et même à température ambiante [34-38]. Néanmoins, de grands progrès dans le domaine de la polaritonique à base de ZnO ont été réalisés au cours des trois dernières années. Un laser à polaritons en ZnO a été démontrée pour la première fois à 120K par un consortium CNRS [39] en 2011, en collaboration avec l'EPFL, suivi par une étude sur la relaxation de polaritons assistée par émission de phonons optiques [40] en 2012. L'année 2012 a vu une explosion des publications sur les lasers à polaritons à base de ZnO, y compris le rapport de Franke *et al* [41] autour de 200K, et la publication controversée du laser à polaritons à température ambiante par Lu et Lai *et al* [42,43]. En outre, les études par Xie *et al* [44], en 2012, et Trichet *et al* [45], en 2013, ont indiqué que la condensation de polaritons pourrait être atteint dans des microfils de ZnO .

Objectifs

L'objectif initial de cette thèse était d’obtenir un laser à polaritons à base de ZnO travaillant à température ambiante. Pour atteindre cet objectif, plusieurs stratégies de fabrication ont été développées en parallèle. Tout d’abord, la croissance de ZnO de haute qualité cristalline sur des miroirs de Bragg (en anglais, Distributed Bragg Reflectors, DBRs) à base de nitrures a été optimisée, avec l'objectif d'améliorer l'approche actuelle pour les microcavités semi-hybrides (c’est-à-dire, avec un DBR supérieur à base de diélectriques et un DBR inférieur à base de nitrures) ; c’est avec une telle approche que le premier laser à polaritons en ZnO a été réalisé à basse température en 2011. En outre, de nouvelles approches ont été développées permettant la fabrication de microcavités entièrement hybrides en ZnO (c’est-à-dire, avec deux DBRs diélectriques), qui ont permis, in fine, d’atteindre des facteurs de qualité de cavité beaucoup plus élevés que ceux obtenus auparavant dans n'importe quel type de cavité en ZnO.

Les microcavités fabriquées ont permis une progrès étape par étape dans l'étude des polaritons à base de ZnO: avec la démonstration initiale d’un laser à polaritons, depuis les basses températures jusqu’à température ambiante, il a été possible d'obtenir un diagramme de phases complet de la condensation de polaritons dans des microcavités en ZnO pour la première fois ; ce diagramme de phases ressemble à ceux des cavités en GaN [46,47]; la comparaison des résultats expérimentaux et des simulations numériques, qui prenaient en compte tous les mécanismes de relaxation polaritonique dans dZnO, a permis de souligner l'importance des processus assistés par phonons dans les cavités de ZnO, et a mis en évidence leur utilité pour le fonctionnement du dispositif à température ambiante. Enfin, de nouvelles configurations de cavité ont pu être étudiées (par exemple, des cavités « très épaisses »), ouvrant la porte à de nombreuses études spectroscopiques et soulignant l'originalité du système ZnO.

Plan

La première partie de ce manuscrit présente les fondamentaux nécessaires pour fabriquer une microcavité à base de ZnO dans le régime de couplage fort et permettant la condensation de polaritons. Elle contient trois chapitres:

Le chapitre 1 présente les propriétés physiques de ZnO et de ses excitons. Les concepts fondamentaux à propos d’excitons, y compris l'énergie de liaison, les règles de sélection des transitions optiques, la force de l'oscillateur et la densité de Mott, sont présentés, soulignant les spécificités de ZnO.

Le chapitre 2 présente les principes fondamentaux des microcavités planaires. La méthode de matrice de transfert pour simuler la propagation de la lumière dans des systèmes multi-couches est décrite en détail. Ensuite, les principes de fonctionnement des DBRs ainsi que des résonateurs Fabry-Perot, constitués d'une couche diélectrique placée entre deux DBRs, sont présentés.

Le chapitre 3 donne une description détaillée des polaritons de cavité et présente une revue historique de ce domaine de recherche. Tout d'abord, les concepts de polariton de cavité et couplage fort sont introduits, puis les principes fondamentaux de condensation de polaritons sont discutés ; enfin, un aperçu des principaux résultats dans les microcavités à semiconducteurs à large bande interdite, en particulier dans des microcavités à base de ZnO, est présenté.

La deuxième partie de ce manuscrit présente les résultats expérimentaux les plus importants obtenus dans une microcavité entièrement hybride à base de ZnO. Elle contient deux chapitres:

Le chapitre 4 décrit la fabrication, les propriétés morphologiques et les propriétés optiques linéaires d'une microcavité entièrement hybride. La cavité étudiée, qui a été fabriquée avec une stratégie complètement nouvelle élaborée au CNRS-CRHEA, travaille dans le régime de couplage fort et présente un facteur de qualité record pour les cavités ZnO (tout type confondu), l’éclatement de Rabi le plus grand parmi toutes les cavités ZnO planaires, ainsi que la gamme de désaccord exciton-photon accessible la plus large parmi toutes les microcavités à base de de ZnO (et de GaN).

Le chapitre 5 décrit les propriétés de condensation de polaritons telles qu’observées dans la microcavité entièrement hybride. D’abord, un laser à polaritons à température ambiante a été démontré et ses figures de mérite ont été étudiées. Le diagramme de phases de la condensation de polaritons ayant été obtenu pour la première fois, des simulations numériques ont été nécessaires pour appréhender le rôle des différents mécanismes de relaxation, soulignant l’importance de la relaxation de polaritons assistée par phonons dans ZnO. Ensuite, la richesse de la cavité est illustrée: des condensats de polaritons ont été obtenus allant des très excitoniques jusqu’aux très photoniques. Dans les parties plus épaisses de la cavité, typiquement pour des épaisseurs au-delà de 5λ, une compétition de modes laser (c’est-à-dire, des modes susceptibles de permettre la condensation de polaritons), est démontrée, ce qui a permis de valider le diagramme de phases déterminé au préalable et nous a donné la possibilité de changer, de façon brutale mais contrôlée, le poids exciton/photon des condensats de polaritons simplement en variant la puissance d’excitation.

La troisième partie de ce manuscrit présente les résultats principaux obtenus sur les microcavités semihybrides. Elle contient un chapitre :

Le chapitre 6 présente la fabrication, les propriétés morphologiques et optiques de deux microcavités semihybrides. La fabrication, qui constitue la plus grande partie de la section, couvre la croissance épitaxiale des DBRs à base d'$Al_{0.2}Ga_{0.8}N/AlN$ sur des substrats de silicium patternés, et la croissance épitaxiale de la couche de ZnO massive sur ces DBRs, les deux étant réalisées par épitaxie par jets moléculaires. Les études spectroscopiques révèlent un élargissement inhomogène photonique négligeable, un facteur de qualité *Q* élevé et des lasers à polaritons à température ambiante.

Enfin, après un chapitre de conclusions, où des idées sur les possibilités futures de la polaritonique à base de ZnO sont présentées, une section d’annexes qui contient plusieurs autres approches de fabrication, qui n'ont pas donné des résultats suffisamment intéressants pour entrer dans le texte principal, a été incluse. Ces expériences comprennent: (1) le dépôt des puits quantiques polycristallins ZnO/ZnMgO sur des DBRs diélectriques, (2) la croissance épitaxiale de la couche active de ZnO sur des DBRs $Al_{0.2}Ga_{0.8}N/A_{l0.85}In_{0.15}N$, et finalement (3) la fabrication de microcavités entièrement hybrides contenant des puits quantiques homo-épitaxiés à base de ZnO/ZnMgO.

I. Building Blocks

Chapter 1 ZnO and excitons in ZnO

Zinc Oxide (ZnO) is a very promising material for applications in visible-UV optoelectronics, electronics, especially as a transparent conducting oxide (TCO) and micro/nano-scale devices. Recently, the idea that ZnO can serve as active material for constructing a room temperature polariton laser, due to its excellent excitonic properties, was theoretically proposed [33,48] and experimentally studied [39,41,44]. Therefore, before we start to discuss ZnO-based microcavities and polariton lasers, it is essential to introduce its material properties, in particular the optical ones.

In this chapter, we will describe the crystalline and the electronic-band structures of ZnO, and we will focus then on ZnO excitons. We will also give a general view on the actual luminescence of ZnO excitons influenced by a non-perfect and unintentionally doped crystal structure.

1.1 Crystalline structure

ZnO is a II-VI semiconductor consisting of atoms of Zinc and Oxygen, with electronic configurations

$$^{64}_{30}Zn: (1s)^2(2s)^2(2p)^6(3s)^2(3p)^6(3d)^{10}(4s)^2 \tag{1.1}$$
$$^{16}_{8}O: (1s)^2(2s)^2(2p)^4 \tag{1.2}$$

This electronic configuration gives rise to a sp^3 hybridization, which results in four equivalent electronic orbitals for each atom. In this case, the compound semiconductor usually exhibits either a zincblende or a wurtzite structure, depending on the electronegativity of the constituent elements. For ZnO, at ambient temperature and pressure, the wurtzite structure exhibits the smallest energy and is therefore the thermodynamically stable phase [49,50]. All the ZnO considered in this thesis will be crystallized in the wurtzite structure.

1.1.1 Crystallographic directions and planes

The wurtzite crystalline structure is illustrated in Figure 1.1**a**. It consists of two hexagonal sub lattices that are shifted along the [0 0 0 1] direction (the *c*-axis) with respect to each other by 3/8 (in the ideal wurzite structure) of the *c* parameter labeled in Figure 1.1**a**. For ZnO at ambient conditions, the lattice parameters are a=0.325 nm and c=0.52 nm [50].

As illustrated in Figure 1.1**a**, the *c*-plane, in which the atoms of each element form a hexagonal lattice, is perpendicular to the *c*-axis. Figure 1.1**b** shows the lattice projected on the *c*-plane, where a coordinate system with three axes, *t*, *u* and *v*, can be established [51]. It is worth to mention that since we are actually in two dimensions, only two of the three values (*t*, *u*, *v*) are independent, with $v \equiv -(t+u)$. With the coordinates (*t*, *u*, *v*, *c*), we can define crystallographic planes (resp. directions) by the intersections (resp. projections) with the crystallographic axes, as illustrated in Figure 1.1. For example, the *c*-plane is noted as $(0\ 0\ 0\ 1)$, as it only intersects the *c*-axis. Two frequently studied planes, parallel to the *c*-axis, are the *m*-plane $(1\ \bar{1}\ 0\ 0)$ and the *a*-plane $(1\ 1\ \bar{2}\ 0)$, as illustrated in both Figure 1.1**a** and **b**.

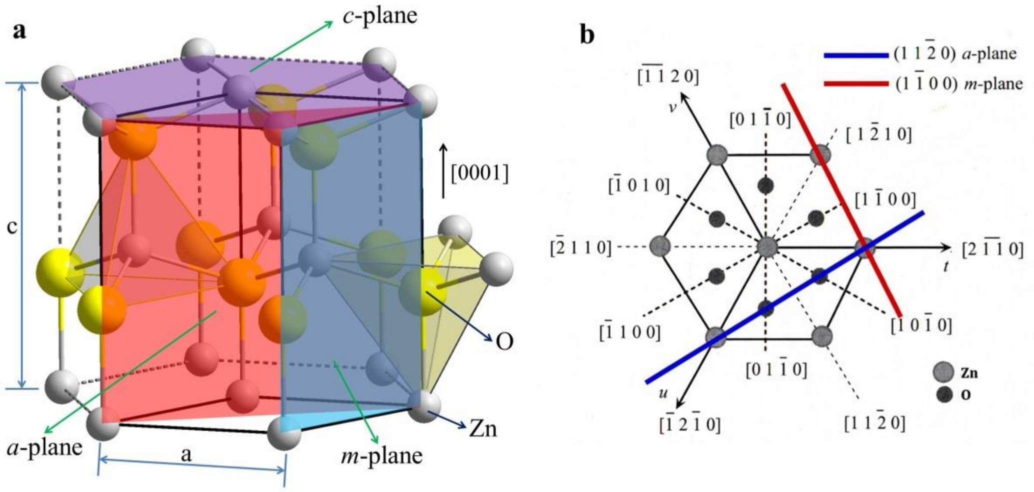

Figure 1.1 : Illustration of the wurtzite lattice in ZnO. a. Three dimensional representation with crystallographic planes identified; b. Atomic structure projected on the *c*-plane, with crystallographic directions and planes identified (from reference [51]).

1.1.2 Polarity

One unique property of the wurtzite structure is its crystal polarity. Indeed, the electronegativity difference between the Zn and O atoms, combined with a lower structure symmetry compared to cubic structures, gives rise to the fact that in ZnO the centers of positive and negative charges do not overlap exactly on each other. This leads to a self-built electrostatic dipole along the *c*-axis even without any applied external field. Those dipoles are summed up all over the crystal and form a macroscopic spontaneous electrostatic polarization. On the contrary, along the directions perpendicular to the *c*-axis, the positive and negative charge distributions are completely symmetric and, therefore, these directions exhibit no spontaneous electrostatic polarization, i.e. the polarization vector is parallel to the *c*-axis [52]. In this sense, the *c*-axis is called a polar axis and the *c*-plane a polar surface, while the *m*-plane and *a*-plane are nonpolar surfaces. There are also semipolar orientations, such as $(1\ 1\ \bar{2}\ 2)$, which form an angle between 0° and 90° with respect to the *c*-axis and for which the value of the spontaneous polarization is just weighted by the corresponding projection onto the considered plane (i.e. $\cos\theta$, θ being the angle with respect to the *c*-axis).

Due to the polarity-induced asymmetry along the *c*-axis, the directions $[0\ 0\ 0\ 1]$ and $[0\ 0\ 0\ \bar{1}]$ have different properties. By convention, the $[0\ 0\ 0\ 1]$ direction is defined as being parallel to the Zn-O bond parallel to the *c*-axis and going from a Zn to an O atom. With this convention, the electrostatic spontaneous polarization in ZnO is negative. Furthermore, in the literature the

[0 0 0 1] direction is referred to as zinc-polar, while the $[0\ 0\ 0\ \bar{1}]$ direction is referred to as oxygen polar. Accordingly, the $(0\ 0\ 0\ 1)$ c-plane is called the Zn-face, while the $(0\ 0\ 0\ \bar{1})$ c-plane is called the O-face.

The polarity plays a very important role in both the fabrication and the characterization of ZnO-based microcavities, since Zn-polar, O-polar, m-nonpolar and a-nonpolar ZnO layers have very different growth conditions as well as etching properties. Moreover, polar and nonpolar ZnO layers show different optical properties (e.g. polarization), especially when quantum wells are considered.

1.2 Band structure

ZnO is a direct-bandgap semiconductor. The bandgap energy of bulk ZnO at room temperature is ~3.36eV (~369 nm), making it interesting for optoelectronic devices working in the near-UV wavelength range. Its electronic band structure is determined by the combination of the crystal field, associated to the spontaneous electrostatic polarization, and the spin-orbit interaction [53].

In ZnO, the conduction band has an s-like character, associated with an orbital momentum $L = 0$, twice degenerated due to the electron spin. Because of the zero orbital momentum it is not affected by the spin-orbit interaction. Moreover, due to the isotropic character of the s-like wave function, it is not split by the crystal field, though its energy is slightly modified. On the other hand, the valence band consists of three degenerate p-like states each of which has a non-zero orbital momentum $L = 1$, with different z-components $L_z = 0, \pm 1$, respectively. The crystal field breaks the degeneracy, leaving the $L_z = \pm 1$ as two degenerate states at a higher energy and the $L_z = 0$ state at a lower energy. The spin-orbit interaction further breaks the degeneracy of the $L_z = \pm 1$ states, which have non-zero orbital momentum along the z-direction. The total momentum along the z-direction is expressed as $J_z = L_z + S_z$, where $S_z = \pm 1/2$ is the electron spin. Consequently, the $L_z = \pm 1$ states break into two energy levels: $J_z = \pm 3/2$ and $J_z = \pm 1/2$. In the particular case of ZnO, the $J_z = \pm 1/2$ states lie at a higher energy than the $J_z = \pm 3/2$ states, due to a negative spin-orbit interaction induced by the strong p-d coupling in the valence band [54]. This is the opposite situation compared to other wurtzite semiconductors such as GaN. The ZnO band structure is sketched in Figure 1.2. The three different valence bands are called A, B and C bands, from lower to higher energies for holes.

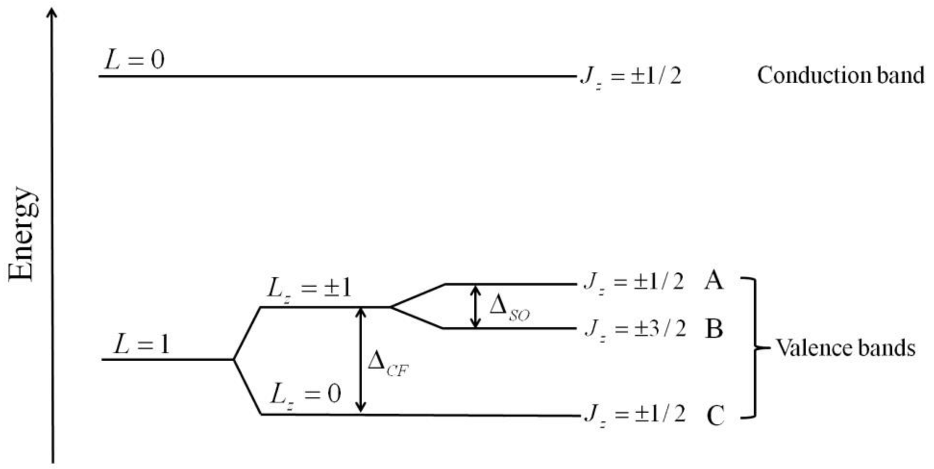

Figure 1.2: Illustration of the ZnO band structure. Δ_{CF} and Δ_{SO} correspond to the energy splittings induced by the crystal field and spin-orbit interaction, respectively [54].

1.3 Free excitons in ZnO

In a semiconductor, an electron in the conduction band and a hole in the valence band can be bounded together via Coulomb interaction to form a new type of quasi-particle: an exciton. Indeed, if ZnO is considered as an ideal material for room-temperature polaritonic devices it is because of its exceptional excitonic properties compared to more mature materials such as GaAs. In this section the basic concepts related to excitons will be introduced, and the unique properties of ZnO excitons will be highlighted.

1.3.1 Binding energy and Bohr radius

Composed of a positively charged particle (the hole) and a negatively charged particle (the electron), the exciton is structurally similar to a hydrogen atom and its wavefunction satisfies the hydrogen-like Schrödinger equation, with an effective binding energy given by:

$$E_b^n = \frac{R^*}{n^2} \qquad 1.3$$

where n is the principle quantum number, as in the hydrogen model, and R^* is the effective Rydberg energy, which is given by:

$$R^* = \frac{\mu e^4}{2\hbar^2 (4\pi\varepsilon_0\varepsilon)^2} \qquad 1.4$$

with $\mu = [(m_e^*)^{-1} + (m_h^*)^{-1}]^{-1}$, the reduced mass of the electron-hole system (m_e^* and m_h^* are the electron and hole effective masses, respectively), e the electron charge, ε the relative permittivity of the material, and $\hbar$ the reduced Planck constant.

The exciton binding energy characterizes its stability. In particular, for a given temperature if the thermal energy ($k_B T$) is larger than the exciton binding energy, most excitons will dissociate into free electrons and holes. In ZnO, the exciton binding energy (~60 meV [49]) being much larger than $k_B T$ at room temperature (~25 meV), thermal exciton dissociation is highly improbable. This is why ZnO is currently considered one of the best materials for devices exploiting excitons at room-temperature.

Similarly as in the hydrogen atom case, the effective Bohr radius of the exciton is defined by

$$a_B^* = \frac{\hbar}{\sqrt{2\mu R^*}} = \frac{\hbar^2 4\pi\varepsilon_0\varepsilon}{\mu e^2} \qquad 1.5$$

The exciton Bohr radius is also an important parameter as it determines the typical exciton-exciton distance (i.e. the exciton density) at which the fermionic character of the excitons begins to manifest itself. ZnO exciton has a Bohr radius of ~1.8 nm [50,55] .

1.3.2 Exciton energy

Unlike an isolated hydrogen atom located in vacuum, excitons are generated inside a crystal, whose effect should be considered in order to define the total energy of the exciton. First of all, the two components of the exciton, i.e, the electron and the hole, have their own potential energies due to the semiconductor band structure. Moreover, the exciton has a kinetic energy that corresponds to the movement of its center-of-mass. The Hamiltonian of the exciton H_X can be written as a sum of two commutating items [11]:

$$H_X = H_{mc} + H_{hl} \qquad 1.6$$

where H_{mc} is the Hamiltonian of the exciton center-of-mass and H_{hl} is the hydrogen-like Hamiltonian.

H_{mc} is determined by the semiconductor band structure and the kinetic energy of the exciton center-of-mass. Its eigenstates are plane wave-like, and its eigenenergies are given by

$$E_{mc}(k) = E_g + \frac{\hbar^2 k^2}{2M} \qquad 1.7$$

where $M = m_e^* + m_h^*$ is the exciton effective mass, k is the wavevector of the exciton, and E_g is the semiconductor bandgap energy which equals to the sum of the electron and hole energies at $k = 0$.

The eigenenergy of the hydrogen-like Hamiltonian H_{hl} is expressed by the exciton binding energy with a negative sign:

$$E_{hl}^{n} = -E_{b}^{n} = -\frac{R^{*}}{n^{2}} \qquad 1.8$$

The total energy of a single exciton inside a bulk crystal is therefore given by:

$$E_{X}^{n}(k) = E_{mc}(k) + E_{hl}^{n} = E_{g} + \frac{\hbar^{2}k^{2}}{2M} - \frac{R^{*}}{n^{2}} \qquad 1.9$$

Composed of an electron and a hole, the exciton can radiatively recombine and emit a photon and can also be, reciprocally, created by absorbing a photon. In photoluminescence, the dominant optical transition takes place usually near $k = 0$ and from the $n = 1$ state; in this case, the transition energy is

$$E_{X} \approx E_{g} - E_{b} \qquad 1.10$$

where

$$E_{b} = R^{*} = \frac{\mu e^{4}}{2\hbar^{2}(4\pi\varepsilon_{0}\varepsilon)^{2}} \qquad 1.11$$

In the case of ZnO, E_X = ~3.3eV at room temperature and increases up to ~3.37eV at low temperature, mainly due to the temperature dependence of the bandgap energy $E_g(T)$, which can be fitted by Varshni's law [50] $E = E(T=0) - \frac{\alpha T^{2}}{T+\beta}$, with parameters α=1.4×10^{-3}eV/K and β=1273.5K (See Chapter 4 for temperature-dependent measurements).

1.3.3 Selection rules for optical transitions

Even if we have said that excitons can couple to light and recombine into photons, its radiative recombination is only possible under certain conditions. Depending on whether these conditions, referred to as "selection rules", are satisfied or not, excitons are classified into "bright excitons" and "dark excitons" respectively. Only "bright excitons" satisfy the selection rules and, therefore, can interact with light [56].

The first selection rule comes from the symmetry of the exciton wavefunction. The dipole-transition probability of a bare exciton (coupled to a continuum of states) reads [11]

$$\left|H_X^D\right|^2 = \left|\left\langle X \left|H_X^D\right|0\right\rangle\right|^2 = NB\left|\varphi_{nlm}(0)\right|^2 \left|\left\langle \varphi_c^e \left|H_e^D\right| \varphi_v^e \right\rangle\right|^2 \qquad 1.12$$

where $H_X^D = \langle X|H_X^D|0\rangle$ is the dipolar matrix element, with $|X\rangle$ and $|0\rangle$ corresponding to the exciton state (initial state of the optical transition) and the recombined ground state (final state of the optical transition), and $\widehat{H}^D_{X/e}$ the dipole interaction Hamiltonian for the exciton (*X*) or the electron-hole (*e*). $\left|\varphi^e_{c/v}\right\rangle$ corresponds to the wavefunction of an electron in the conduction(*c*)/valence(*v*) band. *N* is the number of unit cells in the crystal and *B* is the volume of the unit cell.

$\varphi_{nlm}(0)$ is the value of the exciton's envelope function at the origin ($\vec{r} = 0$) of the radial coordinate, with hydrogen-like quantum numbers n, l and m. From Equation 1.12, $\varphi_{nlm}(0)$ has to be non-zero for the dipole-transition to be allowed. That is to say, only s-like ($l = 0$) excitons, which have an envelope function with non-zero value at $\vec{r} = 0$, can recombine via dipole interaction to emit photons, whilst $l \neq 0$ states are dipole-forbidden. The exciton ground state has an s-like wavefunction and satisfies this selection rule.

In addition, there is a second selection rule besides $l = 0$, which is related to the spin of the exciton. As the electron has a spin projection of $\pm 1/2$ and the holes have either $\pm 3/2$ or $\pm 1/2$, the total spin projection of an exciton is therefore either $J = \pm 2, \pm 1$ or 0. Since the photon has a spin of ± 1, the $J = \pm 2, 0$ excitons cannot directly couple to light unless a spin-flip process is involved in the recombination, whilst the $J = \pm 1$ excitons can directly couple to light.

Although the selection rules introduced above apply to all real crystals, in ZnO the conditions get complicated due to its anisotropy and multiple valence bands. A detailed analysis on the group symmetry of the ZnO excitons can be found in [49] and [54]. In ZnO there are twelve different kinds of excitons among which five are bright. Those bright excitons, and due to degeneracy, result actually in three different optical transition energies, as summarized in Table 1.1. In strain-free bulk ZnO, A and B excitons interact mainly with light polarized perpendicular to the *c*-axis, whilst C excitons mainly interact with light parallel to the *c*-axis [57]. The three exciton transitions can be very clearly identified through polarization-dependent reflectivity measurements on an *m*-nonpolar bulk ZnO, where the collected light contains both $E \perp C$ and $E \parallel C$ components. At room temperature, the photoluminescence of bulk ZnO is mainly dominated by A and B excitons (their ratio being given by the corresponding Boltzmann occupation factor), as well as by their phonon replicas (see below).

Exciton transition	Wavefunction group symmetry	Energy at 300K (meV)	Energy at 0K (meV)	Polarization
A	Γ_5 (×2)	3309	3375.5	mainly $E \perp C$
B	Γ_5 (×2)	3315	3381.5	mainly $E \perp C$
C	Γ_1	3355	3420	mainly $E \parallel C$

Table 1.1 : Summary of the properties of A, B and C excitons. "(×2)" refers to the degeneracy level.

1.3.4 Oscillator strength

The oscillator strength is a magnitude characterizing the strength of an optical transition and it is a key parameter to achieve the strong exciton-photon coupling. In order to understand the concept of oscillator strength, the semi-classical theory of light-matter interaction within the linear regime will be introduced.

In this theory, a macroscopic dielectric function $\varepsilon(\omega)$ is introduced to describe the polarization field generated inside the crystal by an external electromagnetic field. In a system consisting of excitons (the dielectric function treatment can be extended to other polarization fields, as plasmons, for example), each single exciton can be described as a charged oscillator that can be driven by a force exerted by an external electrical field. If the classical oscillator has a charge e, a resonance frequency ω_0 and is driven by a polarized electrical field $\vec{E}_0 e^{-i\omega t}$, its movement can be described by

$$m\ddot{\vec{x}} + m\gamma\dot{\vec{x}} + m\omega_0^2\vec{x} = e\vec{E}_0 e^{-i\omega t} \qquad 1.13$$

where $\vec{x}$ is the position, m is the mass and γ is the damping rate of the oscillator. The Fourier transform of Equation 1.13 describes the oscillator's response to a continuous spectrum of external field frequencies

$$\vec{x}(\omega) = \frac{e\vec{E}_0 / m}{\omega_0^2 - \omega^2 + i\gamma\omega} \qquad 1.14$$

The dipole moment of the oscillator is

$$\vec{p} = e\vec{x} = \frac{e^2 / m}{\omega_0^2 - \omega^2 + i\gamma\omega}\vec{E}_0 \qquad 1.15$$

Now we consider the response of a system consisting of N oscillators per unit volume under the action of an electric field. The total polarization reads $\vec{P} = N\vec{p}$. By definition, the electric displacement $\vec{D}$ is expressed as

$$\vec{D} = \varepsilon_0\vec{E} + P = \varepsilon_0(1 + \frac{Ne^2}{\varepsilon_0 m}\frac{1}{\omega_0^2 - \omega^2 + i\gamma\omega})\vec{E} \qquad 1.16$$

$\vec{E}_0$ in Equation 1.15 is replaced by $\vec{E}$ which represents the electric field in Equation 1.16. Comparing Equation 1.16 with $\vec{D} = \varepsilon_0\varepsilon\vec{E}$, we get

$$\varepsilon = 1 + \frac{f}{\omega_0^2 - \omega^2 + i\gamma\omega} \qquad 1.17$$

$$f = \frac{Ne^2}{\varepsilon_0 m} \qquad 1.18$$

From Equation 1.17, the parameter f, which has a dimension of $(\text{time})^{-2}$, quantifies how strong the oscillators respond to the external electromagnetic field, and is therefore called the oscillator strength.

The expressions above have been derived from a model of classical charged oscillators. However, unlike a classical oscillator, the exciton is a quantum particle whose optical response needs to be described rigorously within a quantum mechanical formalism. In this case, the oscillator strength in Equation 1.18 should be replaced by a term containing the matrix element of the exciton dipole transition, which finally leads to

$$f = \frac{2N\omega_X}{\varepsilon_0 \hbar} \left| H_X^D \right|^2 \qquad 1.19$$

where ω_X is the exciton resonance frequency, which is equivalent to ω_0 in the classical oscillator model. The term $\left| H_X^D \right|^2$ is the matrix element of the exciton dipole transition, as defined in Equation 1.12. Since in quantum mechanics it is usually more convenient to deal with energy than frequency, the factor $\hbar$ has been added into the deduction process of the oscillator strength and therefore f has a dimension of $(\text{energy})^2$.

Moreover, to account for all the non-excitonic oscillators that respond to the extrernal electric filed but which are spectrally far from the excitonic resonances, ε_0 in Equation 1.16 needs to be replaced by $\varepsilon_0\varepsilon_b$ (b for background). Finally, the dielectric function can be expressed as:

$$\varepsilon = \varepsilon_b \left[1 + \frac{f}{(\hbar\omega_0)^2 - (\hbar\omega)^2 + i(\hbar\gamma)(\hbar\omega)} \right] \qquad 1.20$$

or

$$\varepsilon = \varepsilon_b + \frac{f'}{(\hbar\omega_0)^2 - (\hbar\omega)^2 + i(\hbar\gamma)(\hbar\omega)}$$

1.21

in which $f' = f\varepsilon_b$. It should be noted that when discussing the exciton oscillator strength in the context of strong-coupling, a number of slightly different definitions are used (compare for instance [51,58,59]). All these definitions, including also those on general textbooks [49,60], are essentially equivalent and differ just in some constant (which eventually changes the dimensions of the oscillator strength). For consistency, in this thesis manuscript the oscillator strength definition with dimension of (energy) ^{2} will be always used, and it will be always clearly indicated whether it is f or f' what is being used.

In semiconductors, the oscillator strength is often determined by measuring the longitudinal-transverse splitting, ω_{LT} (see reference [61] for measurements on ZnO), since the oscillator strength for a given exciton transition is given by: $f = 2\hbar\omega_{LT}\hbar\omega_0$. This provides an experimental method to determine the oscillator strength for many materials [62]. Unfortunately, in ZnO it is not accurate to quantify the exciton oscillator strength by $\hbar\omega_{LT}$ because the A and B exciton transisions are too close [61]. Instead, fs autocorrelation measurements, as those previously used in GaN [63], can be employed to extract the oscillator strength of each individual excitonic transition. In ZnO, these amount to $f'_A =$ ~0.155 eV^2 and $f'_B =$ ~0.25 eV^2, which is the largest among conventional inorganic materials, making ZnO an ideal candidate for devices working in the strong coupling regime [64].

1.3.5 Mott density

Even if composed of two fermions (the electron and the hole), the exciton spin is an integer and, therefore, it can behave as a boson (composite boson) provided the density of excitons is kept below a certain level. Indeed, when the density of excitons is so large that the average distance between two adjacent excitons is getting close to the exciton Bohr radius, the Coulomb interaction between the electron and the hole becomes screened by the adjacent carriers. Under these conditions, the exciton description is no longer valid and the fermionic character of the exciton constituents begins to manifest itself. The critical density at which this phase transition takes place is called the Mott density, N_{Mott}. Below N_{Mott}, the gas of electron and holes can be described in terms of an exciton gas, whereas above N_{Mott} they behave as an electron-hole plasma. While the exact Mott density in ZnO is still under debate and numerous values (obtained by indirect methods) can be found in the literature, a consensus is found for N_{Mott}^{ZnO} ~(0.3-20)×10^{18}cm^{-3}, which is around 1/10 of the value $1/a_B^{*\,3}$ [65].

This large Mott density allows to inject a large numbers of particles into the system while simultaneously keeping the bosonic character of excitons, which is essential for achieving room temperature polariton lasing/polariton condensation.

1.4 Bound-excitons: Low temperature photoluminescence

As temperature is reduced from room to cryogenic temperatures, the thermal energy decreases and excitons might get bounded to impurity atoms, but also to point defects or extended structural defects. Since the localization energies are typically smaller than 15-20 meV, these excitons get delocalized at room-temperature so that free exciton emission takes over (see Figure 4.7). Since numerous impurities incorporate into ZnO, at low temperature the photoluminescence of ZnO becomes complicated as shown in Figure 1.3 for a bulk ZnO at 4.2K [55], due to the appearance of numerous bound exciton emissions. The chemical nature of the involved impurities[1] has been identified by coupling doping and magneto optic experiments [66], and a comprehensive review is given in reference [55].

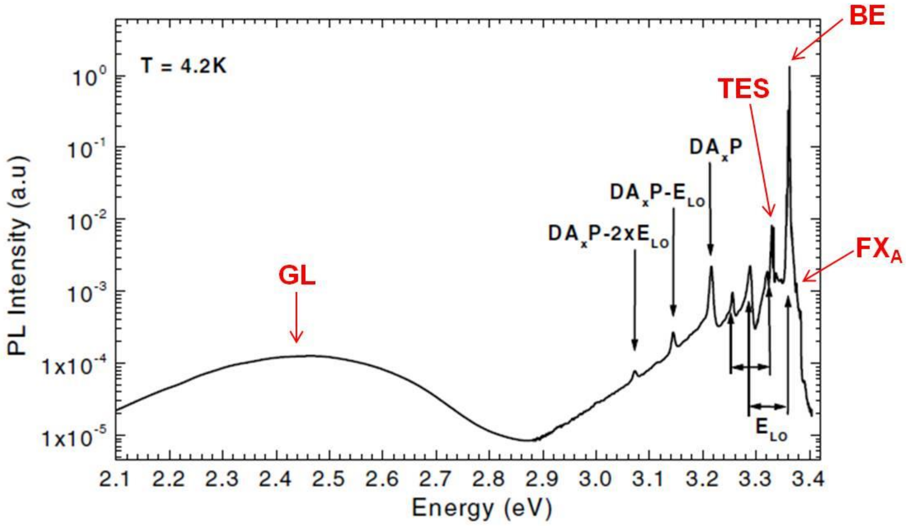

Figure 1.3 : Low temperature photoluminescence of a bulk ZnO extracted from reference [55]. Bound excitons (BE), free exciton (FX_A), donor-acceptor pairs (DA_xP), and deep level (such as the Green Band, GL) transitions can be identified, as well as their associated phonon replicas. The labels in red are added to the original figure for the purpose of better presentation in this thesis.

Together with the bound-exciton emissions, whose energies lie close to the band gap, some defects or impurities (e.g. Cu, V_O) might introduce energy levels within the bandgap and therefore serve as deep level recombination centers, compared to the shallow nature of the donor or acceptor levels discussed above. Typically, ZnO exhibits a deep level emission, the so-called green luminescence (GL) band [50], centered at ~2.5 eV. The intensity ratio between the near-band edge and the green emissions is sometimes employed as a measure of the ZnO quality, and might be affected but the growth and processing (etching, annealing, etc.) conditions.

1.4.1 Phonons

There are 12 phonon modes in the wurtzite ZnO structure, including one longitudinal-acoustic (LA), two transverse-acoustic (TA), three longitudinal-optical (LO), and six transverse-optical (TO) branches. The dispersion of various phonons in ZnO can be found in Figure 1.4 [67].

In particular, it should be noted that there is a LO-phonon band with anenergy of E_{LO}=72 meV, which might interact strongly with excitons. Indeed, a quasi-particle formed by an exciton coupled to an LO phonon, the so-called polaron, was observed since the very first studies on ZnO[57].

---

[1] Though not shown in Figure 1.3, with the high-resolution spectrum in the excitonic range, the bound exciton peak (BE) is resolved as several sub-peaks corresponding to different donors and/or acceptors in ZnO, and the free A-exciton peak becomes more distinguishable.

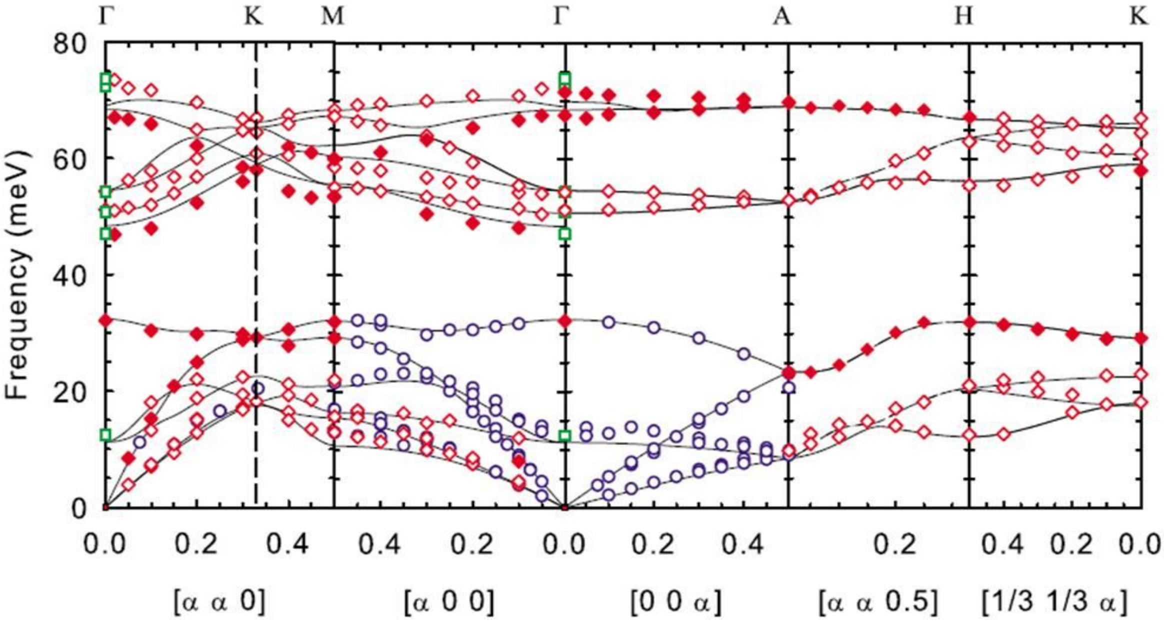

Figure 1.4: Extracted from Reference [67]. Phonon-dispersion relations of ZnO along the main symmetry directions.

1.5 Conclusion

In this chapter the basic properties of bulk ZnO material have been introduced. The major concepts related to excitons, including binding energy, transition selection rules, oscillator strength and Mott density, have been presented. All those concepts are important for further understanding the physics related to exciton-polaritons and polariton condensates.

Chapter 2 Optical Microcavities

In the last chapter we have discussed the optical transitions associated to exciton recombination within a semiconductor. In a thin layer, when a photon is emitted by an exciton it usually escapes from the material before it can be reabsorbed and re-emitted again by a second exciton. Optical microcavities have been developed with the aim of confining photons, thereby increasing their lifetime inside the material, and favor their interaction with the resonances of the active material.

In this chapter we will first present the general properties of a Fabry-Perot cavity, and then we will focus on a special case: planar microcavities with distributed Bragg reflectors (DBRs).

2.1 Fabry-Perot cavities

The Fabry-Perot (FP) architecture was introduced by the French physicists Charles Fabry and Alfred Perot as an interferometer. As shown in Figure 2.1, the structure consists of two strictly parallel planar mirrors separated by a certain medium. If the mirrors reflectivities are large enough, the interference fringes that build up as light goes through (or when it is being reflected) are very sharp and can be employed in high-resolution spectral analysis, as initially conceived by Charles Fabry and Alfred Perot. Nowadays, with the advent of lasers and light-emitting diodes, the FP cavity is mostly used as a passive optical structure enabling to tune the emission properties of the emitters embedded therein.

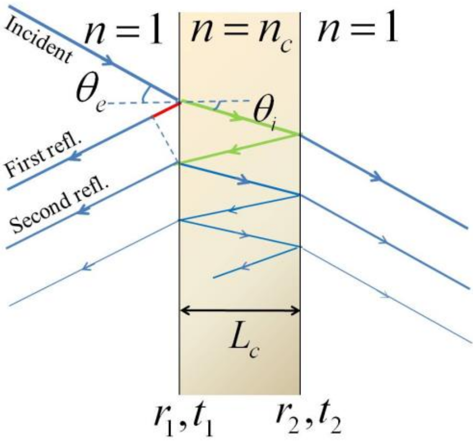

Figure 2.1: Schematic picture of the Fabry-Perot structure

2.1.1 General description

Figure 2.1 shows the structure of a Fabry-Perot cavity. The cavity medium, which is surrounded by air in this example, has a refractive index n_c and a thickness of L_c, which is the cavity length. The left (resp. right) mirror has reflectivity and transmission coefficients of r_1 and t_1 (resp. r_2 and t_2). The incident light forms an angle θ_e with respect to the normal to the interface, while the transmitted light forms an angle θ_i whose value is determined by Snell-

Descartes law of refraction. The optical path difference δ between the first and the second reflected beams is just given by the difference between the green and red paths depicted in Figure 2.1:

$$\delta = \frac{2n_c L_c}{\cos\theta_i} - \frac{2n_c L_c}{\cos\theta_i}\sin\theta_i \sin\theta_e = 2n_c L_c \cos\theta_i \qquad 2.1$$

The total reflected (A_r) and transmitted (A_T) amplitudes are given by

$$A_r = \sum_n A_n^r = A_i\left(-r_1 + t_1^2 r_2 e^{ik_0\delta}\frac{1}{1-r_1r_2e^{ik_0\delta}}\right) \qquad 2.2$$

$$A_t = \sum_n A_n^t = A_i e^{ik_0\frac{n_c L_c}{\cos\theta_i}} t_1 t_2 \frac{1}{1-r_1r_2e^{ik_0\delta}} \qquad 2.3$$

where $A_i$is the incident wave amplitude, and A_n^r (resp. A_n^t) represents the amplitude of the nth reflected (resp. transmitted) light wave. $k_0 = 2\pi/\lambda_0$ is the wavevector of the incident light in vacuum. The total transmission T_C and reflectivity R_C in intensity by the cavity read:

$$T_C = |t_C|^2 = \left|\frac{A_t}{A_i}\right|^2 = \frac{(t_1t_2)^2}{1+(r_1r_2)^2 - 2r_1r_2\cos(k_0\delta)} \qquad 2.4$$

$$R_C = |r_C|^2 = \left|\frac{A_r}{A_i}\right|^2 = \frac{1+(r_1r_2)^2 - (t_1t_2)^2 - 2r_1r_2\cos(k_0\delta)}{1+(r_1r_2)^2 - 2r_1r_2\cos(k_0\delta)} \qquad 2.5$$

with t_C and r_C the transmission and reflection coefficients in amplitude. As herein the considered media are absorption-less, the total reflected and transmitted intensities satisfy

$$R_C + T_C = 1 \qquad 2.6$$

The calculated reflectivity and transmission spectra (in intensity) of a Fabry-Perot cavity are shown in Figure 2.2. The reflectivity minima (also the transmission maxima) correspond to the optical resonant modes confined inside the cavity, which are characterized by the resonant condition:

$$k_0\delta = 2q\pi \qquad 2.7$$

in which q is an integer.

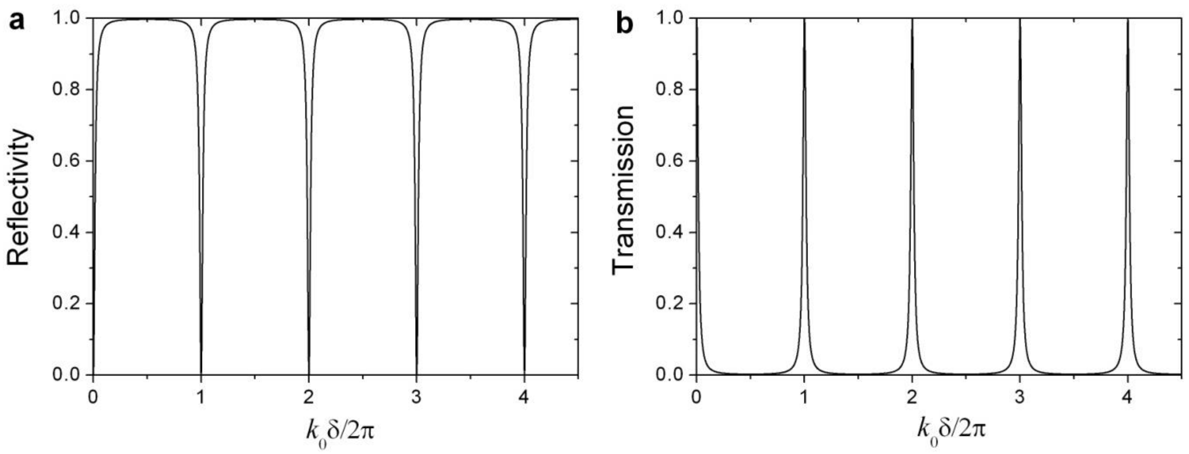

Figure 2.2: Reflected (**a**) and transmitted (**b**) intensity of a Fabry-Perot cavity with $r_1 = r_2$ =0.95

2.1.2 Angular dispersion

As Equation 2.7 contains the parameter δ, which is a function of the angle (see Equation 2.1), the resonant condition is therefore angular-dependent. Substituting Equation 2.1 into Equation 2.7 we get (with $\sin\theta_e = n_c \sin\theta_i$):

$$2L_c\sqrt{(n_c k_0)^2 - (k_0 \sin\theta_e)^2} = 2q\pi \qquad 2.8$$

First we define the term $k_c = n_c k_0$ as the wavevector inside the cavity. Then, based on the geometry of the light path we define $k_\parallel = k_0 \sin\theta_e = k_c \sin\theta_i$ as the in-plane wavevector that is parallel to the cavity surfaces (mirrors). One can easily see that $k_\parallel$ is always conserved when light crosses any interface. With the definitions above, Equation 2.8 can be re-written as:

$$k_{c,q} = \sqrt{k_{||}^2 + \left(\frac{q\pi}{L_c}\right)^2} \qquad 2.9$$

As k_c can be written as $k_c = \sqrt{k_\parallel^2 + k_\perp^2}$ with $k_\perp$ the wavevector component perpendicular to the cavity surfaces, we get the expression of $k_\perp$ by comparing with Equation 2.9:

$$k_{\perp,q} = \frac{q\pi}{L_c} \qquad 2.10$$

Equation 2.10 shows that the optical wave is confined and, therefore, quantized only in the direction perpendicular to the cavity mirrors, while it is free in the direction parallel to the cavity mirrors. The quantum number q is called the order of the cavity mode and it counts, for a given mode, the number of half-wavelengths the electric field oscillates during a single trip between the two cavity mirrors. If the length of a cavity is an integer multiple q of $\lambda/2$ ($\lambda_0/2n_C$), then the resonance will be obtained for normal incidence ($k_{\|}$= 0), and this cavity will be referred to as a $q\lambda/2$ cavity.

Thus, for a given cavity thickness q becomes a fixed parameter[1] and the only variable in Equation 2.9 is $k_{\|}$. Noticing that the photon energy is given by $E = \hbar c k_0 = (\hbar c/n_c)k_c$, with c the light velocity in vacuum, the cavity photon dispersion (i.e. its energy as a function of the wavevector) can be obtained taking into account Equation 2.9 and can be written as

$$E(k_{||}) = \frac{\hbar c}{n_c}\frac{q\pi}{L_c}\sqrt{1+\left(\frac{L_c k_{||}}{q\pi}\right)^2} \qquad 2.11$$

Close to normal incidence (θ_e, θ_i ~0) we have $k_{\|} \ll k_{\perp}$ and, therefore, $L_c k_{\|}/(q\pi) \ll 1$ (Equation 2.10). Equation 2.11 can be then approximated as

$$E(k_{||}) = \frac{\hbar c}{n_c}\frac{q\pi}{L_c}\left(1+\frac{1}{2}\left(\frac{L_c k_{||}}{q\pi}\right)^2\right) = E_0 + \frac{\hbar^2 k_{||}^2}{2m_{ph}^*} \qquad 2.12$$

with

$$E_0 = \frac{q\pi\hbar c}{n_c L_c} \qquad 2.13$$

$$m_{ph}^* = \frac{q\pi\hbar n_c}{c L_c} \qquad 2.14$$

where m_{ph}^* is the so-called cavity photon effective mass and E_0 is the cavity photon energy at normal incidence ($k_{\|} = 0$). Equation 2.12 describes the cavity photon as a non-zero-mass particle and, by analogy with semiconductor physics, it is said to have been obtained within the effective mass approximation. The cavity photon dispersion is plotted in Figure 2.3**a** with (Equation 2.12) and without (Equation 2.11) the effective mass approximation. We can see that only at very large in-plane wavevectors, corresponding to angles larger than 60°-70°, a significant energy difference is obtained between the exact calculation and the effective mass approximation (larger than ~20meV) .

---

[1] For thick cavities, several modes with different qs can fulfill the resonance condition of the cavity. In this case q is a fixed parameter when we focus on one specific mode.

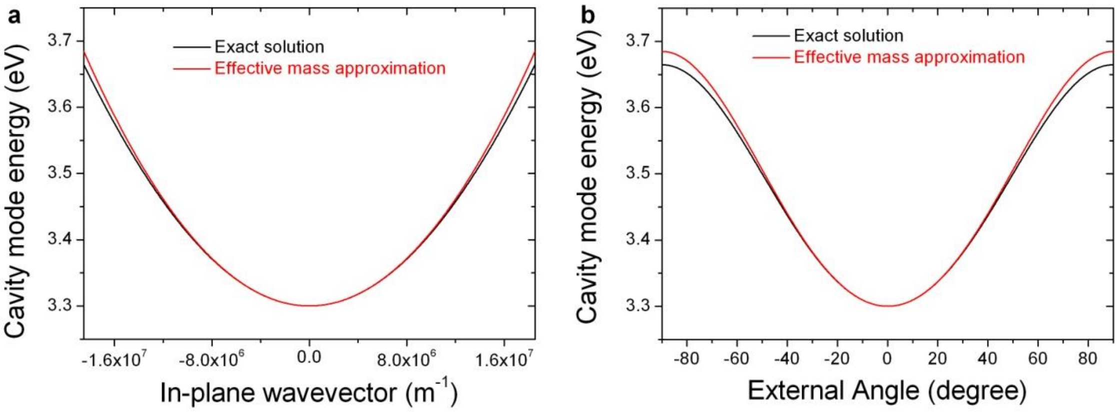

Figure 2.3: Photon dispersion in a Fabry-Perot microcavity as a function of in-plane wavevector (**a**) and external angle (**b**), with both the exact (black line) and the effective mass approximation (red line) solutions. The ranges of horizontal axes in **a** and **b** are equivalent. The cavity is a λ-cavity with E_0=3.3eV and n_c=2.3.

Since the magnitude that is experimentally accessible is the external angle, rather than the in-plane wavevector, the cavity mode dispersion is usually plotted as a function of the external angle. The wavevector can be converted to the external angle through the relation $k_\parallel = k_0 \sin\theta_e$. By substituting this expression into Equations 2.11 and 2.12, we get the exact and approximated angular dispersions, E vs. θ_e, as plotted in Figure 2.3**b**. One might also notice that the exact angular dispersion (E vs θ_e) can be deduced directly from Equation 2.1 and 2.7, without introducing the in-plane wavevector.

2.1.3 Quality factor

In a microcavity, since the mirrors reflectivity is not 1 the intensity of the confined cavity mode decays with time by photon escaping through the mirrors. These losses are characterized by a dimensionless parameter, the cavity quality factor Q, which is defined as the ratio between the energy stored inside the cavity and the energy dissipated per optical cycle, multiplied by 2π:

$$Q = \left| \omega_c \frac{U}{dU/dt} \right| \tag{2.15}$$

where ω_c is the angular frequency of the cavity mode, U is the electromagnetic energy stored inside the cavity and dU/dt is the energy loss rate. It yields

$$U(t) = U_0 e^{-\omega_c t/Q} = U_0 e^{-t/\tau} \tag{2.16}$$

where U_0 is the initial energy injected into the cavity. $\tau = Q/\omega_c$ is the lifetime of the cavity mode, which gives the average time that each photon has been confined inside the microcavity before it goes out through the mirrors. Considering the relationship between the electromagnetic energy and the electric field amplitude $U(t) \propto |E(t)|^2$, the electric field can be expressed as

$$E(t) = E_0 e^{-\omega_c t/2Q} e^{-i\omega_c t} \tag{2.17}$$

where E_0 is the initial amplitude corresponding to U_0.The Fourier transform of Equation 2.17 gives the field and energy distribution in the frequency domain:

$$U(\omega) \propto |E(\omega)|^2 \propto \frac{1}{(\omega - \omega_c)^2 + (\omega_c / 2Q)^2} \tag{2.18}$$

This is a Lorentz-like distribution with a full-width-half-maximum (FWHM) $\Delta\omega = \omega_c/Q$, which yields

$$Q = \frac{\omega_c}{\Delta\omega} = \frac{E_c}{\Delta E} \approx \frac{\lambda_c}{\Delta\lambda} \tag{2.19}$$

where E and λ represent the cavity photon energy and wavelength, respectively. The approximation "≈" is valid when $\lambda_c \gg \Delta\lambda$. Equation 2.19 is commonly used to determine experimentally the Q, since it is enough to measure the energy and linewidth of the cavity mode. The photon lifetime of the cavity mode can be expressed by

$$\tau = \frac{Q}{\omega_c} = \frac{1}{\Delta\omega} \tag{2.20}$$

The Q-factor has two complementary physical interpretations, depending on the actual application of the Fabry-Perot structure: (1) when working as a cavity to confine light, which is the main interest in this thesis, the Q-factor represents the lifetime of the confined photon mode; (2) when working as an interferometer, the Q-factor represents the spectral resolution and is related to the interferometer finesse. These two physical meanings are *linked* to each other through a Fourier transform, which establishes a correspondence between the time and the frequency/energy domains.

As already stated, the Q is governed by the cavity losses; these can be due to some mirror transmission, or light-absorption inside the microcavity, or light-scattering due to imperfect interfaces, etc. For an ideal absorption-less Fabry-Perot cavity as shown in Figure 2.1, only the mirror losses contribute to reduce the value of Q or, equivalently, to increase the linewidth broadening of the cavity modes. Under these ideal conditions, the relationship between the mode spectral linewidth and the mirror properties can be derived from Equation 2.4. As an example, transmission spectra at normal incidence ($\theta_e = 0$) for different mirrors reflectivity coefficients are shown in Figure 2.4. The linewidth of the cavity mode is reduced sharply with increasing mirror reflectivity. Reflectivities, for both mirror, of 0.9 (black), 0.95 (red), 0.99

(green) and 0.999 (blue) result in Qs of 30, 61, 316 and 3125, respectively. This means that we need very highly reflective mirrors (r>0.99) to achieve a Q-factor compatible with room temperature polariton lasing (Q ~ 1000) [48]. Ordinary metallic mirrors cannot provide such high reflectivities and, therefore, more sophisticated structures are required, as will be introduced in the next section.

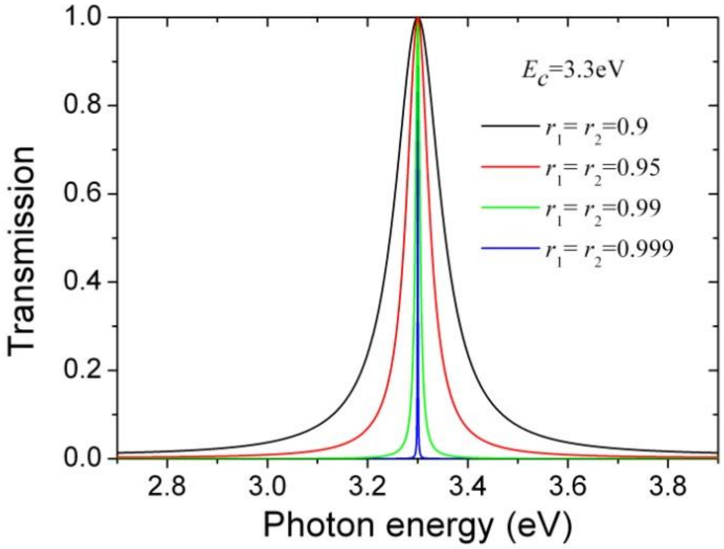

Figure 2.4: Calculated normal-incidence ($\theta_e = 0$) transmission spectra of a Fabry-Perot λ-cavity with four different mirror reflectivity coefficients. The cavity parameters are the same as in Figure 2.3.

2.2 Planar microcavities

The requirement of highly reflective mirrors leads irremediably to the use of distributed Bragg reflectors (DBRs). The planar microcavities that will be considered in this work will consist of an active medium, with a thickness in the order of the photon wavelength, embedded between two DBRs. In this section we will introduce the transfer-matrix method that enables to simulate the light propagation inside such multi-layer optical structures. Then, we will describe the main properties of DBRs and planar cavities based on the simulations results provided by this method.

2.2.1 Transfer matrix method

The transfer matrix method is well-adapted for simulating light propagation inside multilayer systems. We consider first the most simple system containing two different media with an infinite interface, as shown in Figure 2.5**a**, with refractive indices n_0 and n_1, respectively. The incident and transmitted light rays satisfy the Descartes-Snell law $n_0 \sin\theta_0 = n_1 \sin\theta_1$. The complex amplitude of the electric field at a position z can be written as $E(z) = E^+(z) + E^-(z)$, where $E^+(z)$ and $E^-(z)$ represent individually light waves traveling in the $+z$ and the $-z$ directions, respectively. We now define a two dimensional vector Φ built upon these complex amplitudes:

$$\Phi(z) = \begin{bmatrix} E^{+}(z) \\ E^{-}(z) \end{bmatrix} \qquad 2.21$$

based on which all the transfer matrix calculations will be performed.

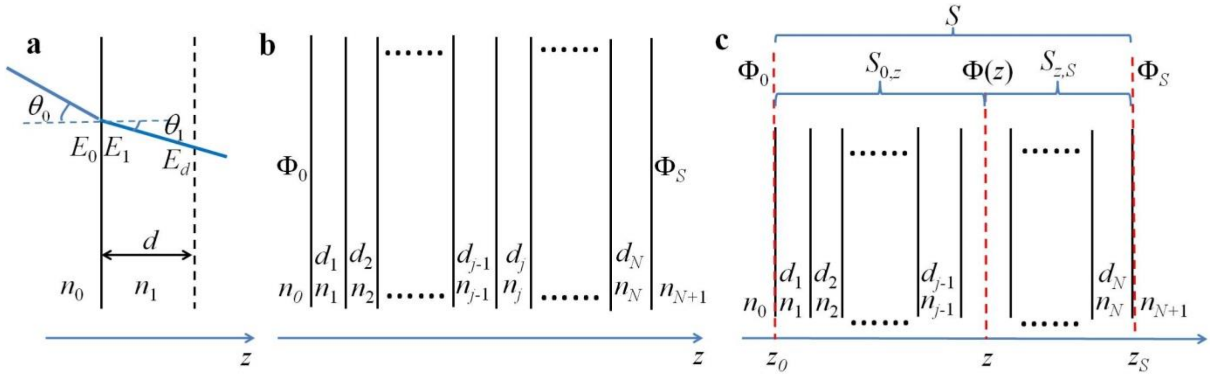

Figure 2.5: Illustration of a two-media system (**a**) and a multilayer system (**b**). The coordinate axis perpendicular to the interfaces is labeled as z-axis. **c** Schematics illustrating the method for calculating the electric field distribution inside the system in **b**.

Transfer matrix at the interface

We first consider the light incident from medium n_0 into medium n_1 ; at the interface between the two media (in this section we will refer to each medium by its refractive index) Fresnel's equations apply:

$$r_{0,1} = \begin{cases} \dfrac{n_0 \cos\theta_0 - n_1 \cos\theta_1}{n_0 \cos\theta_0 + n_1 \cos\theta_1} & (s - \text{polarization}) \\[2ex] \dfrac{n_0 \cos\theta_1 - n_1 \cos\theta_0}{n_1 \cos\theta_0 + n_0 \cos\theta_1} & (p - \text{polarization}) \end{cases} \qquad 2.22$$

$$t_{0,1} = \begin{cases} \dfrac{2n_0 \cos\theta_0}{n_0 \cos\theta_0 + n_1 \cos\theta_1} & (s - \text{polarization}) \\[2ex] \dfrac{2n_0 \cos\theta_0}{n_1 \cos\theta_0 + n_0 \cos\theta_1} & (p - \text{polarizition}) \end{cases} \qquad 2.23$$

where $r_{0,1}$ (resp. $t_{0,1}$) is the reflection (resp. transmission) coefficient at the interface. s- (resp. p-) polarization corresponds to a wave with its electric field oscillating perpendicular (resp. parallel) to the plane of incidence, which is defined by the incident ray and the normal to the interface. Obviously the two cases become identical at normal incidence ($\theta_0 = \theta_1 = 0$).

Similarly, if we consider the light incident from medium n_1 into medium n_0 at the same interface, we can get the corresponding reflectivity and the transmission coefficients, $r_{1,0}$ and $t_{1,0}$ from Fresnel's equations just by exchanging the subscripts "0" and "1" in Equations 2.22 and 2.23, through which we derive the relationship

$$r_{1,0} = -r_{0,1}, \quad t_{1,0} = (1 - r_{0,1}^2)/t_{0,1} \tag{2.24}$$

which is equivalent to

$$r_{1,0} r_{0,1} + t_{1,0} t_{0,1} = 1 \tag{2.25}$$

As shown in Figure 2.5**a**, we label E_0 and E_1 the electric field amplitude $E(z)$ just at the two sides of the interface. If we only consider the wave incident on the interface from the +z direction, (in which case $E_1^- = 0$), the reflectivity and transmission coefficients represent just the ratios between the electric field amplitudes at each side of the interface

$$r_{0,1} = E_0^- / E_0^+ \tag{2.26}$$

$$t_{0,1} = E_1^+ / E_0^+ \tag{2.27}$$

For the wave incident only from the –z direction ($E_0^+ = 0$), we have the similar expressions

$$r_{1,0} = E_1^+ / E_1^- \tag{2.28}$$

$$t_{1,0} = E_0^- / E_1^- \tag{2.29}$$

From the expressions of the reflection and transmission coefficients in Equation 2.26 to 2.29 and considering waves incident from both ±z directions, we can write the electric field in medium n_0 as a function of the electric field in medium n_1 thanks to an "interface transfer matrix", which reads:

$$\begin{bmatrix} E_0^+ \\ E_0^- \end{bmatrix} = \begin{bmatrix} 1/t_{0,1} & -r_{1,0}/t_{0,1} \\ r_{0,1}/t_{0,1} & t_{1,0} - (r_{0,1} r_{1,0})/t_{0,1} \end{bmatrix} \begin{bmatrix} E_1^+ \\ E_1^- \end{bmatrix} \tag{2.30}$$

By taking into account Equations 2.24, the matrix form in Equation 2.30 can be simplified to

$$\begin{bmatrix} E_0^+ \\ E_0^- \end{bmatrix} = \frac{1}{t_{0,1}} \begin{bmatrix} 1 & r_{0,1} \\ r_{0,1} & 1 \end{bmatrix} \begin{bmatrix} E_1^+ \\ E_1^- \end{bmatrix} \tag{2.31}$$

which can be written in the Φ-vector form (Equation 2.21):

$$\Phi_0 = I_{0,1} \Phi_1 \tag{2.32}$$

with $\Phi_0 = \begin{bmatrix} E_0^+ \\ E_0^- \end{bmatrix}$, $\quad \Phi_1 = \begin{bmatrix} E_1^+ \\ E_1^- \end{bmatrix}$ and

$$I_{0,1} = \frac{1}{t_{0,1}} \begin{bmatrix} 1 & r_{0,1} \\ r_{0,1} & 1 \end{bmatrix}. \qquad 2.33$$

$I_{0,1}$ is the transfer matrix at the interface from medium n_0 to medium n_1.

Transfer matrix for free propagation

Now we consider the light propagating freely in the medium n_1 within a distance d, as illustrated in Figure 2.5**a**. We label E_d the electric field amplitude after this propagation. We have

$$\begin{bmatrix} E_1^+ \\ E_1^- \end{bmatrix} = \begin{bmatrix} e^{-in_1 k_v d \cos\theta_1} & 0 \\ 0 & e^{in_1 k_v d \cos\theta_1} \end{bmatrix} \begin{bmatrix} E_d^+ \\ E_d^- \end{bmatrix} \qquad 2.34$$

where k_v is the vacuum wavevector. The equation can also be written in the Φ-vector form

$$\Phi_1 = L_{1,d} \Phi_d \qquad 2.35$$

where

$$L_{1,d} = \begin{bmatrix} e^{-in_1 k_v d \cos\theta_1} & 0 \\ 0 & e^{in_1 k_v d \cos\theta_1} \end{bmatrix} \qquad 2.36$$

is defined as the transfer matrix for free propagation of a distance d in material n_1. From Equations 2.32 and 2.35 we can get

$$\Phi_0 = I_{0,1} L_{1,d} \Phi_d = M_{0,1.d} \Phi_d \qquad 2.37$$

where $M_{0,1,d} = I_{0,1} L_{1,d}$ is the transfer matrix that describes the structure illustrated in Figure 2.5**a**: a light beam passes through an interface (between 0 and 1) and then travels freely within a certain distance (d). This structure is the basic element for constructing a multilayer system.

Transfer matrix of multilayer systems

As illustrated in Figure 2.5**b**, a multilayer system is constructed by stacking a number of individual units similar to that shown in Figure 2.5**a**. The whole system contains N layers each of which has a finite thickness d_j and a refractive index n_j ($j = 1,2 \dots n$). This N-layer structure is surrounded by a medium n_0 on the left, and a medium n_{N+1} on the right, both of which are semi-infinite. We define the left boundary of the system as the interface between material n_0 and n_1 at the n_0 side, and the right boundary as the interface between material n_N and n_{N+1} at the n_{N+1} side. The whole system is therefore described by

$$\Phi_0 = S\Phi_S \tag{2.38}$$

$$S = \left(\prod_{j=1}^{N} M_{j-1,j,d_j}\right) I_{N,N+1} = \left(\prod_{j=1}^{N} I_{j-1,j} L_{j,d_j}\right) I_{N,N+1} \tag{2.39}$$

where Φ_0 (resp. Φ_S) is the Φ-vector at the left (resp. right) boundary of the N-layer system, as labeled in Figure 2.5**b**. S is the overall transfer matrix of the system.

Reflectivity, transmission and absorption

Once the transfer matrix S has been constructed, it is straightforward to calculate the total reflectivity and transmission of the system. Consider a wave entering the system from the left boundary and leaving the system through the right boundary. Equation 2.38 reads explicitly:

$$\begin{bmatrix} E_0^+ \\ E_0^- \end{bmatrix} = \begin{bmatrix} S_{11} & S_{12} \\ S_{21} & S_{22} \end{bmatrix} \begin{bmatrix} E_S^+ \\ 0 \end{bmatrix} \tag{2.40}$$

where S_{11} , S_{12}, S_{21} and S_{22} are the four matrix elements of S. E_S^-=0 because there is no back-travelling light after the right boundary, as we have considered a semi-infinite medium n_{N+1}. The total reflected r_s and transmitted t_s amplitudes are therefore

$$r_s = \frac{E_0^-}{E_0^+} = \frac{S_{21}}{S_{11}} \tag{2.41}$$

$$t_s = \frac{E_S^+}{E_0^+} = \frac{1}{S_{11}} \tag{2.42}$$

As r_s and t_s contain both the real and the imaginary parts of the amplitude ratios, they actually characterize both the amplitude and the phase response to the system. If we focus only on the light intensity, its reflectivity R and transmission T can be calculated as

$$R = r_s r_s^* = |r_s|^2 = \left|\frac{S_{21}}{S_{11}}\right|^2 \qquad 2.43$$

$$T = t_s t_s^* = |t_s|^2 = \left|\frac{1}{S_{11}}\right|^2 \qquad 2.44$$

In a system with light absorption, we can also calculate the total intensity absorption by

$$A=1-R-T \qquad 2.45$$

Electric field distribution

By convention, the complex amplitude of the incident light beam is set to 1, namely E_0^+=1. Then we have

$$\Phi_0 = \begin{bmatrix} 1 \\ r_s \end{bmatrix}, \quad \Phi_S = \begin{bmatrix} t_s \\ 0 \end{bmatrix} \qquad 2.46$$

with r_s and t_s being obtained from the whole system's transfer matrix S. In order to get further insight into the response of optical microcavities, it is interesting to obtain the Φ-vector at any arbitrary position z inside the system. To do so, either the transfer matrix from the left boundary z_0 to the position z ($S_{0.z}$ in Figure 2.5**c**) needs to be calculated or the transfer matrix from the position z to the right boundary z_S ($S_{z.S}$ in Figure 2.5**c**). Thus, Φ(z) can be calculated either through

$$\Phi_0 = S_{0,z}\Phi(z) \qquad 2.47$$

or through

$$\Phi(z) = S_{z,S}\Phi_S \qquad 2.48$$

Once Φ(z) has been determined, the electric field amplitude at any point within the structure can be reconstructed as $E(z) = E^+(z) + E^-(z)$, and the light intensity can be computed as $I(z) = E(z)E^*(z) = |E(z)|^2$.

2.2.2 Distributed Bragg Reflectors (DBRs)

A DBR is a periodic system constructed by repeatedly stacking identical bi-layers each of which consist of two quarter-wavelength layers with different refractive indices (noted as n_a and n_b). The structure can also be illustrated by Figure 2.5**b**, just by making $n_j = n_a$ when j is odd and $n_j = n_b$ when j is even, and fixing the thickness of each layer to $d_j = \bar{\lambda}/4n_j$. If the above-described conditions are fulfilled, the light interference inside the structure results in a very large reflectivity around $\bar{\lambda}$, which is the target mirror wavelength in vacuum ($\bar{\lambda} = hc/\bar{E}$). Thus, contrary to metals, the DBRs reflectivity can be easily tuned by modifying the geometric parameters of the structure.

As a multi-layer system, the DBR structure can be simulated easily using the transfer matrix method described above in which, depending on the wave polarization (s- or p-polarized), different formulas (Equations 2.22 and 2.23) should be used. In this chapter we perform simulations assuming an s-polarized electromagnetic wave.

The simulated optical field distribution inside DBR structures is shown in Figure 2.6. The layer thicknesses are set to be quarter-wavelength for $\bar{E} = 3.300$eV, which is the ZnO exciton energy at room temperature. In order to understand the effect of the refractive index contrast in the DBRs properties, two different sets of (n_a, n_b) have been employed: (1) n_a=2.2, n_b=1.5, which are close to the refractive indices of the HfO_2/SiO_2 couple used in our experiments[1]; (2) n_a=2.0, n_b=1.7, which exhibit a reduced refractive index contrast compared to HfO_2/SiO_2, while maintaining the same mean refractive index value. Figure 2.6**a** and **b** show the electric field intensity distribution when light with a photon energy $E = \bar{E}$ is incident from the left. In both **a** and **b**, most of the light intensity is found close to the incident surface but displaying a certain penetration into the mirror, typical of interference-based reflectors, and which will be discussed later. At the layer interfaces, the electric field exhibits either nodes or anti-nodes. That is to say, at the photon energy of $\bar{E}$ the light propagates ¼ of the wavelength in each quarter-wavelength layer, indicating no additional phase shift induced by the interfaces. By comparing **a** and **b,** we can already state that the penetration length increases with decreasing refractive index contrast.

---

[1] The exact refractive indices of HfO_2/SiO_2 deviate slightly from 2.2/1.5 and need to be measured for each deposition. In this chapter we use the value 2.2/1.5 for the sake of illustration. The exact values will be used in later chapters when simulating experimental results.

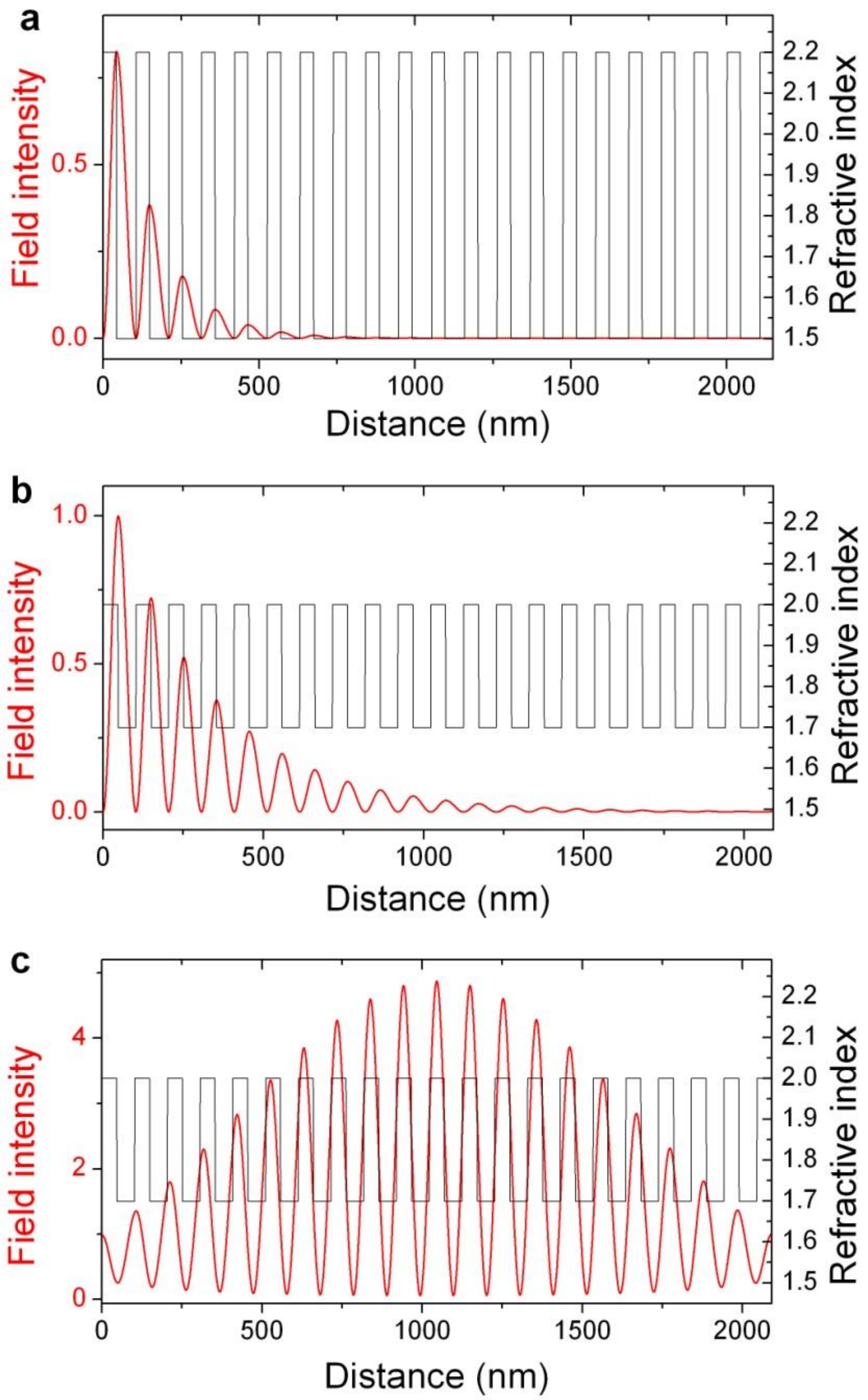

Figure 2.6: Electric field distribution simulated by the transfer matrix method in a 20.5 pair-DBR, and whose layer thicknesses are adapted for a maximum reflectivity at $\bar{E}$=3.300eV. **a** and **b**, Electric field distribution for a photon energy $E = \bar{E}$, but for DBR with different refractive indices: n_a=2.2, n_b=1.5 for **a**; n_a=2.0, n_b=1.7 for **b**. **c**, Electric field distribution for the same structure as in **b**, but calculated at a photon energy E=3.080eV, corresponding to the first Bragg mode. The light is incident from the left side and has an intensity of 1.

The calculated reflectivity spectra of DBRs with different refractive index contrast and different pairs are shown in Figure 2.7**a** and **b**, respectively. Each spectrum exhibits a relatively flat, high-reflectivity range of photon energies centered around $\bar{E}$. This energy range is called the stopband and its spectral FWHM the stopband width. Indeed, the reflectivity reaches more than 0.999 in both Figure 2.7**a** (red) and **b** (green). Figure 2.7**a** shows that both the reflectivity value and the stopband width increases with the refractive index contrast. Figure 2.7**b** shows that for a given refractive index contrast, the reflectivity value increases with the number of pairs, while the stopband width decreases with the number of pairs[1]. Therefore, in order to simultaneously achieve high reflectivity, large stopbands and small penetration lengths, we need bi-layers with the largest refractive contrast possible.

The minima of the reflectivity spectra (see Figure 2.7), called the Bragg modes, correspond to light confined inside the DBR structure, as shown in Figure 2.6**c**, where the field intensity distribution corresponding to the reflectivity minimum at E=3.080eV of the red curve in Figure 2.7**b** has been plotted. The intensity field profile shows that the Bragg mode is distributed along the entire DBR structure, with a slight intensity enhancement (compared to the intensity enhancement of a cavity mode, to be discussed later).

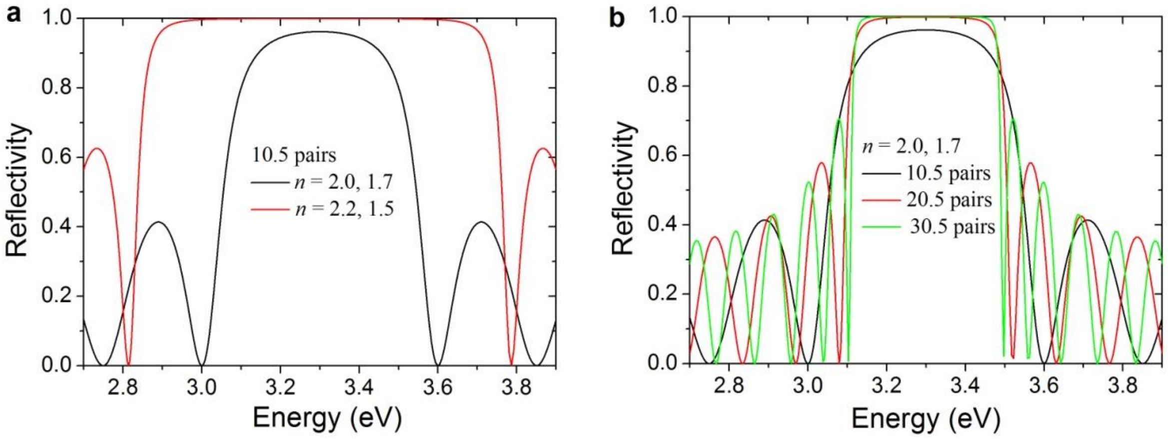

Figure 2.7: Calculated DBR reflectivity using the transfer matrix method. The layers thicknesses are set to be quarter-wavelength of $\bar{E} = 3.300$eV. **a** 10.5-pair DBR with bi-layer refractive indices $n = 2.0,\ 1.7$ (black) and $n = 2.2,\ 1.5$ (red). **b** DBRs with bilayer refractive indices $n = 2.0,\ 1.7$ and containing 10.5 (black), 20.5 (red) and 30.5 (green) pairs.

Within the stop band, high reflectivity (more than 0.999) is achieved provided the number of pairs is sufficiently high, making the DBR a perfect mirror for realizing high-Q microcavities. Functioning as a mirror, the DBR not only maximizes the reflected intensity but also changes the phase of the incident light. The phase shift induced by the DBR can be analyzed through the complex amplitude reflectivity r_s, which is calculated by the transfer matrix method.

Figure 2.8 shows the spectrally-resolved phase shift for a 10.5-pair DBR with n_a=2.2, n_b=1.5 fabricated for a central energy $\bar{E}$=3.300 eV. The phase shift is zero at $\bar{E}$ and varies almost linearly around $\bar{E}$.

---

[1] This is true when the stopband width is defined as the FWHM. However, the high-reflectivity range (e.g. >99% of the maximum reflectivity), which is the useful stopbband width in a microcavity, may not decrease with increasing number of pairs.

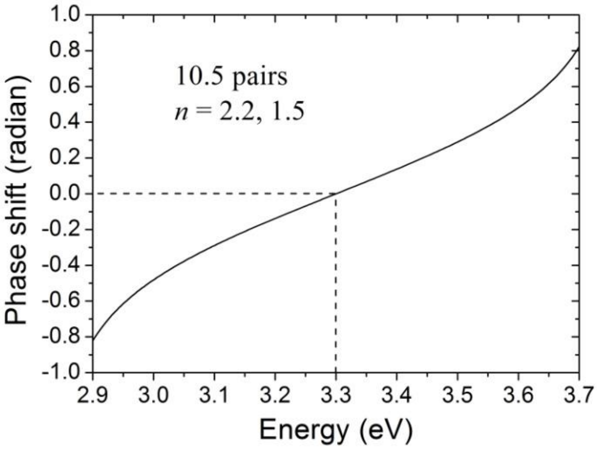

Figure 2.8: Calculated phase shift of a 10.5-pair DBR with n=2.2, 1.5.

Close to the central DBR energy, the phase dispersion can be approximated by

$$\phi(E) = 2n_0(k - \bar{k})L_{DBR} = \frac{2n_0 L_{DBR}}{\hbar c}(E - \bar{E}) \tag{2.49}$$

where n_0 is the refractive index of the surrounding material at the incident side. L_{DBR} is called the effective length of the DBR: if we replace the DBR structure by an ideal mirror at a distance L_{DBR} behind the incident surface, it will introduce exactly the same phase shift as the DBR does. In this sense, the light's behavior in a DBR is equivalent to a free propagation by a distance L_{DBR} before getting reflected by an ideal mirror. Therefore, L_{DBR} is approximately the penetration depth of the incident light into the DBR [28], although the effective length and the penetration depth are not exactly identical. If the number of pairs is sufficiently high and the DBR can be approximated by an infinite number of pairs structure, the effective length is given by [68]

$$L_{DBR} = \frac{\bar{\lambda}}{4n_0}\frac{n_{l0}}{n_{h0}}\frac{n_h}{n_h - n_l} \tag{2.50}$$

where n_h (resp. n_l) is the maximum (resp. minimum) between n_a and n_b; n_{h0} (resp. n_{l0}) is the maximum (resp. minimum) between n_0 and the refractive index of the first DBR layer. The detailed deduction of this equation involves the transfer matrix method [28], from which we already see that the effective length increases with decreasing ($n_h - n_l$), as evidenced by Figure 2.6**a** and **b**.

2.2.3 Planar microcavities with DBRs

A planar microcavity is constructed by placing a dielectric medium between two mirrors with the aim of confining and enhancing the electric field inside this medium. If DBRS are used, instead of the most common metallic mirrors, large Q-factors can be achieved thanks to the high reflectivity that they can provid. Figure 2.9 shows the calculated field distribution in a ZnO λ-cavity (n_c=2.3, λ corresponds to photon energy of 3.300eV) with an 8-pair HfO_2/SiO_2 DBR ($n_{a,b}$ = 2.2, 1.5, $\bar{E}$=3.300eV) on both sides. The optical field is mainly confined inside the ZnO active region and decays exponentially into the DBRs. Furthermore, the confined optical mode is ~500 times more intense than the incident light (set to 1 in the calculation). These two properties (field confinement and intensity enhancement) will be crucial for achieving the strong-coupling regime in planar microcavities, as described in the next chapter. Since even for the cavity mode some of its intensity is found out of the dielectric medium constituting the cavity, it is interesting to introduce a magnitude that quantifies the spreading of the electric field out of the dielectric medium. Such magnitude is the effective length of the microcavity, which is defined by

$$L_{eff} = L_c + L_{DBR1} + L_{DBR2} \qquad 2.51$$

where L_{DBR1} and L_{DBR2} represent the penetration depth into each of the two DBRs (note that, as we have already said, the effective length of a DBR is close to but does not match the penetration depth) .

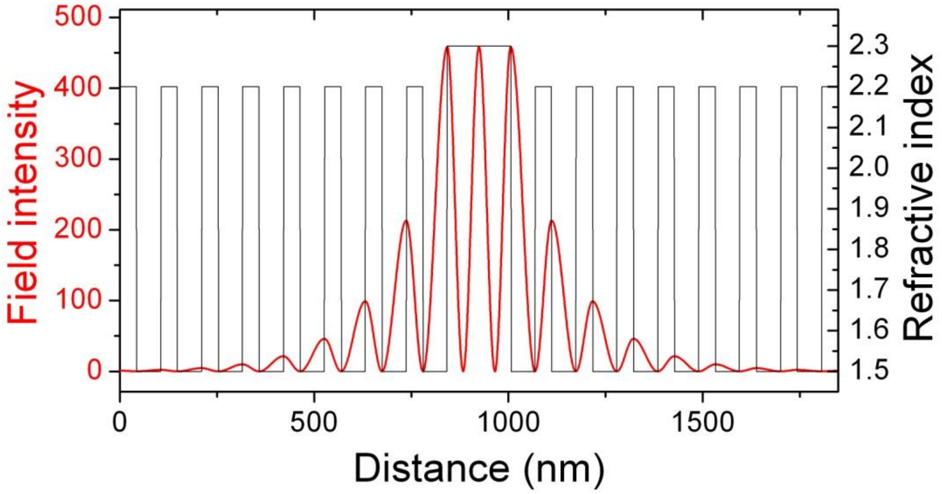

Figure 2.9: Calculated electric field distribution in a ZnO bulk (n_c=2.3) λ-cavity surrounded by an 8 pair-HfO_2/SiO_2 DBR (n = 2.2, 1.5) at each side with $\bar{E}$=3.300eV. The incident light has a photon energy of $\bar{E}$ and an intensity of 1.

The calculated reflectivity for such a cavity structure is shown in Figure 2.10. Similarly as in an ideal Fabry-Perot cavity, a reflectivity minimum appears at the center of the DBR stop band (3.3eV), which corresponds to the cavity photon mode. Bragg modes are also clearly identified. From the detail shown in Figure 2.10**b** it can be seen that only 8 pairs of HfO2/SiO_2 at each side of the ZnO cavity yield a theoretical Q of more than 3000, highlighting the advantage of using HfO2/SiO_2 dielectric DBRs (to be compared with 18 pairs of AlAs/AlGaAs or 20 pairs of AlN/AlGaN to obtain the same Q).

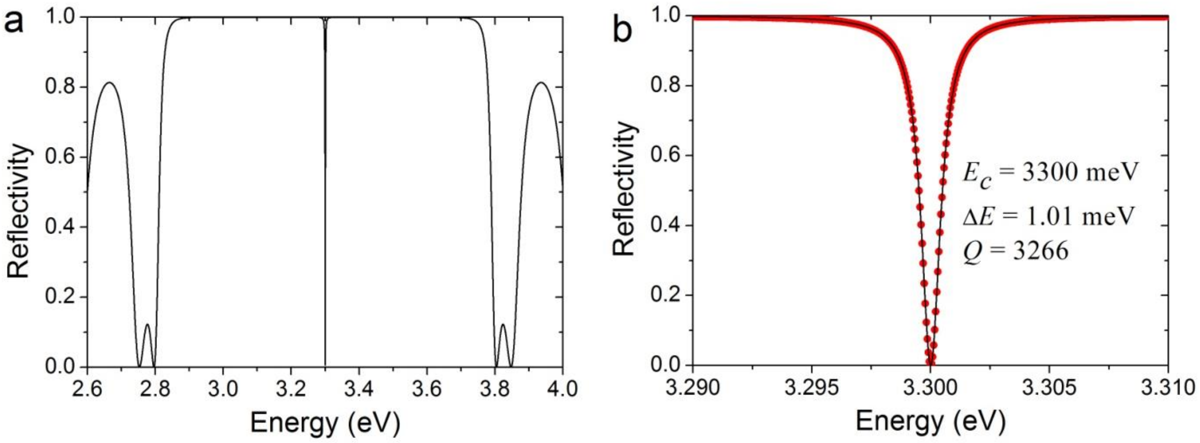

Figure 2.10 **a**. Calculated reflectivity spectrum for the same microcavity as in Figure 2.9. **b**. Enlarged view of **a** at the energy range around 3.300eV, with the calculated data points shown as red circles.

Indeed, the calculated Q as a function of the number of DBR pairs, for refractive indices corresponding to HfO_2/SiO_2, is shown as the black line in Figure 2.11. If the cavity is symmetric, i.e. with the same DBR structure at each side, the Q increases exponentially with the number of DBR pairs. The same cavity structure with reduced DBR refractive index contrast is also calculated for comparison, shown as the red line in Figure 2.11, from which we can see that this reduction of the refractive index contrast results in a Q drop of 1 to 2 orders of magnitude, depending on the number of pairs in each DBR.

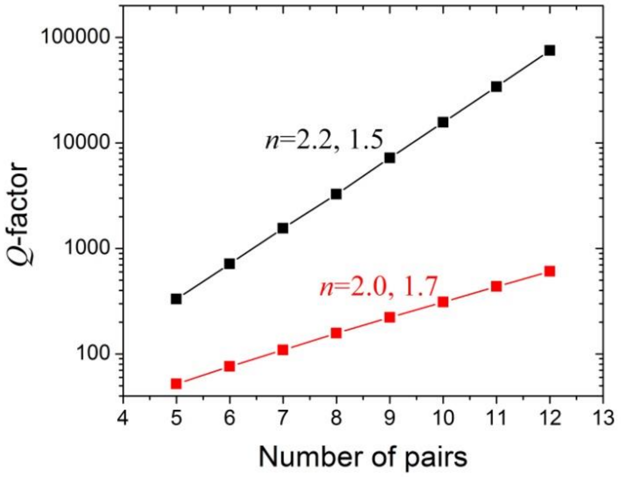

Figure 2.11: Calculated Q as a function of the number of DBR pairs at each side of the cavity. DBR refractive indices used for calculation are n =2.2, 1.5 (black) and n =2.0, 1.7 (red).

The calculated reflectivity spectra for different incident angles are shown in Figure 2.12**a**. When going to higher incident angle, both the cavity mode and the Bragg modes shift to higher energies. Specifically, the dispersion of the cavity mode is extracted from Figure 2.12**a** and plotted in Figure 2.12**b**, which shows that the dispersion curve is similar to the ideal Fabry-Perot cavity (Figure 2.3**b**), but with a slightly different curvature. This is due to the phase shift induced by the DBRs for the non-normal incident cases: L_c and n_c in Equation 2.14 need to be replaced by more complicated terms that results in a decrease of the cavity photon effective mass.

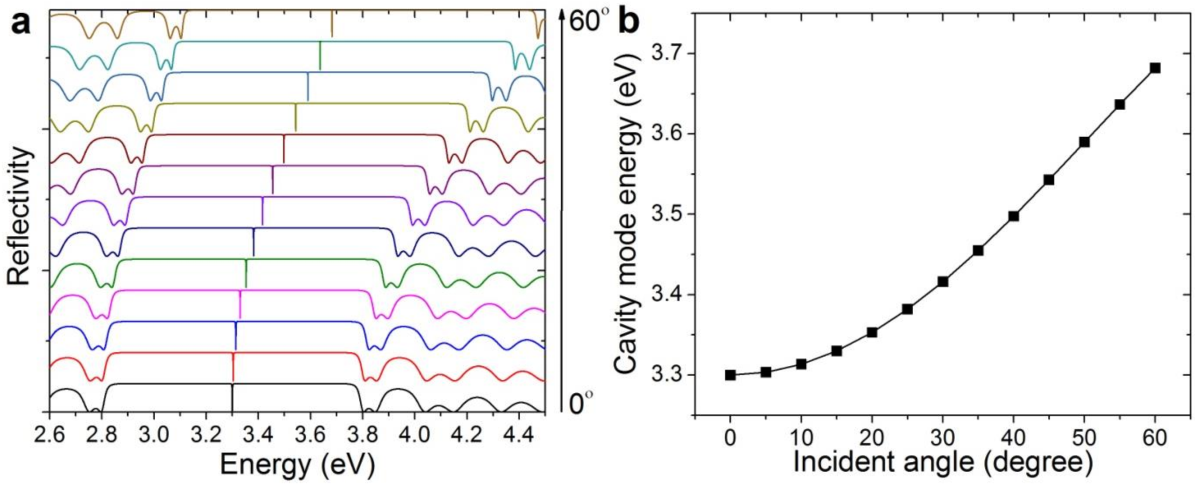

Figure 2.12: **a**. Calculated reflectivity spectra for s-polarized light with different incident angles (0° to 60°) for the same cavity structure as in Figure 2.10. Each spectrum is shifted upwards for clarity. **b**. Cavity mode energy as a function of incident angle. The incident light is s-polarized.

It is worth to mention that for the angular-dependent transfer matrix simulations we have supposed s-polarized light. The angular dispersion of the p-polarized light is qualitatively the same but not quantitatively: the effective length of the DBR increases with angle for p-polarization, whereas it decreases for s-polarization. Furthermore, the reflectivity value of the DBR increases with angle for s-polarization whereas it decreases with angle for p-polarization [69]. Due to the slightly different angular-evolution between the s- and p-polarized light, a TM-TE splitting of the cavity mode can be observed at large angles [69]. Detailed analysis regarding the polarization dependence of the angular dispersion and the effective length can be found in Reference [69].

2.3 Conclusion

In this chapter, the basic concepts and principles of planar microcavities have been introduced. The powerful simulation tool for light propagation in microcavities, namely the transfer matrix method, is described in detail and applied for understanding the properties of DBR structures, which are the key element for achieving high-*Q* microcavities. Most important, the structure formed by placing a dielectric medium in between two DBRs enhances the electric field intensity for some well-defined wavelengths, and confines the electric field within the dielectric medium.

Chapter 3 Exciton-polaritons

Polaritons are the quasi-particles arising from the coupling between electromagnetic waves and electric dipole excitations. In semiconductors, bulk polaritons are generated when an exciton and a photon couple together, becoming thereby the eigenstate of the system. These bulk polaritons are annihilated only at the surface of the crystal (or, eventually, at crystal defects), where a photon might escape into free space. In semiconductor microcavities, polaritons are formed by coupling an exciton with a cavity photon, whose dispersion properties are different from those of a photon in free space, as discussed in the previous chapter. These exciton-cavity photon polaritons (which will be referred to, from now on, as polaritons or cavity polaritons) exhibit partially light-like and partially matter-like properties. These polaritons behave as bosons and as such might condense into a macroscopically populated state, through a Bose-Einstein phase transition and emit coherent light, process which is termed polariton lasing.

In this chapter, some of the physics related to cavity-polaritons will be discussed. Section 3.1 will give a detailed description of cavity-polaritons, from both a classical and a quantum point of view. Section 3.2 will introduce the physics of cavity-polariton condensates, while Section 3.3 will describe cavity-polaritons in wide bandgap microcavities, and will provide the state-of-the-art in ZnO-based microcavities.

3.1 Cavity polaritons

In chapter 1 we have discussed the properties of “bright” excitons. In a semiconductor microcavity when a “bright” exciton interacts with a photon, their respective physical properties are modified by each other and the new term “cavity-polariton” is used to describe the coupled state. If the interaction between the exciton and the cavity photon is weak enough, the coupling can be treated as a perturbation and the eigenstates of the exciton-cavity photon polariton system can still be approximately described by bare excitons and bare photons; this situation is termed “weak-coupling regime”. On the contrary, if the interaction is so strong that bare excitons and bare cavity photons are no longer valid for describing the eigenstates of the the system, a new quasi-particle needs to be introduced, whose properties are partially matter-like partially light-like. This situation is described as being “the strong-coupling regime”. While strictly speaking we have in both situations exciton-cavity photon coupled states, the description of the system is made in terms of cavity polaritons only in the strong coupling regime, while the concept of exciton and photon are still used to describe the weak coupling regime.

3.1.1 Classical description of exciton-cavity photon coupling

A general interpretation based on classical electrodynamics

The classical description treats photons as a classical electromagnetic field and excitons as an ensemble of dipole oscillators, whose effect is taking into account through the dielectric function of the material. The classical model for excitons has already been introduced in Section 1.3.4, with the associated dielectric function given in Equation 1.20. Noting $E_X = \hbar\omega_0$, $E = \hbar\omega$ and $\gamma_X = \hbar\gamma$, Equation 1.20 is re-written as

$$\varepsilon(E) = \varepsilon_b \left[1 + \frac{f}{{E_X}^2 - E^2 + i\gamma_X E} \right] \tag{3.1}$$

where E_X and γ_X represent the energy and the homogeneous linewidth of the exciton emission, respectively. The dielectric function of a material and its refractive index are closely related since

$$\tilde{n}(E) = n(E) + i\kappa(E) = \sqrt{\varepsilon(E)} \tag{3.2}$$

$$n(E) = \Re\left(\sqrt{\varepsilon(E)}\right) \tag{3.3}$$

$$\kappa(E) = \Im\left(\sqrt{\varepsilon(E)}\right) \tag{3.4}$$

in which $n(E)$ is the real part of the complex refractive index, and is usually termed *refractive index*, and $\kappa(E)$ is the imaginary part of the complex refractive index, and is usually termed *extinction index* of the material. Similarly, the background refractive index is defined as $n_b = \sqrt{\varepsilon_b}$, which corresponds to the refractive index of the material without exciton contribution.

The classical description of cavity photons has already been introduced in Section 2.1. At normal incidence, the energy of the cavity mode as a function of the material refractive index is given by Equation 2.13, which can be re-written in the following way

$$n(E) = \frac{q\pi\hbar c}{L_c}\frac{1}{E} = \frac{n_{c0}E_{c0}}{E} \tag{3.5}$$

This equation gives the value of the refractive index required for having the cavity mode at E, with a fixed cavity length L_c determined by the parameters n_{c0} and E_{c0} [59]. Since Equation 3.3 gives the actual refractive index of the cavity material as induced by the excitons, the energy of the cavity-polaritons in the microcavity is thereby determined by simultaneously satisfying Equations 3.3 and 3.5. These two curves have been plotted in the upper panels of Figure 3.1: the straight inclined line corresponds to equation 3.5, while the other three curves (one horizontal and two Lorentz-like) correspond to equation 3.3 calculated with different exciton parameters, which have been chosen for comparison purposes. The cold cavity (i.e.

without excitons and, therefore, without any coupling involved) is designed to exhibit its resonance for the exciton energy (with $E_{c0} = E_X$ =3.3eV and $n_{c0} = n_b$=2.3).

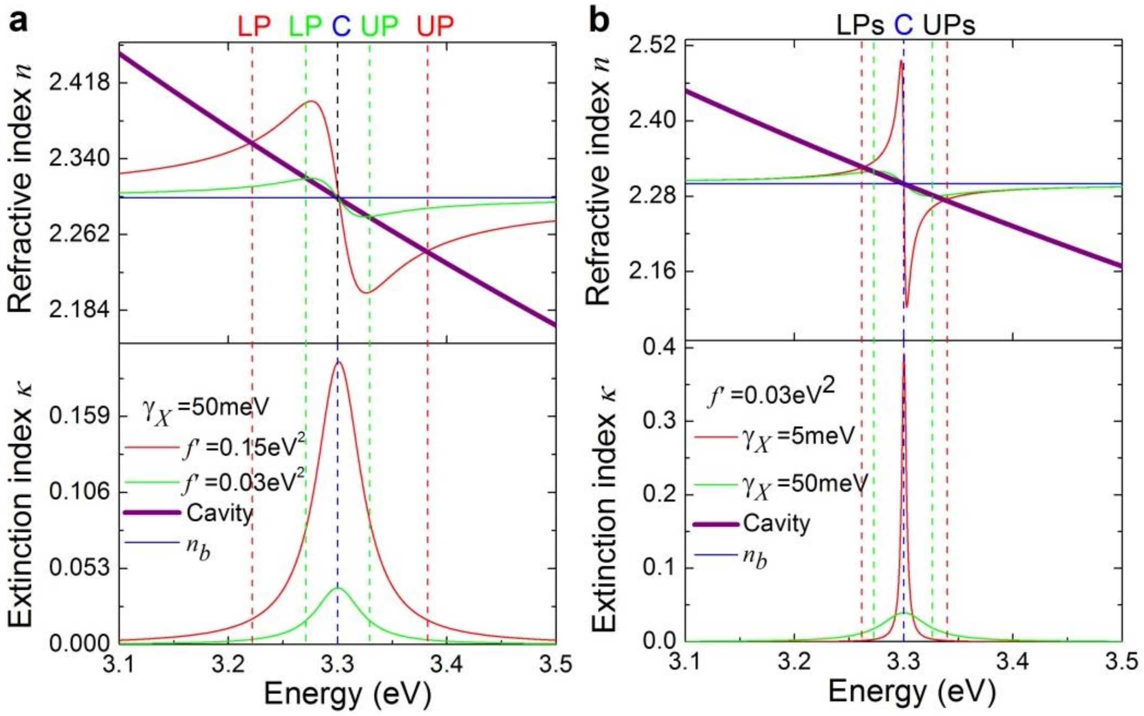

Figure 3.1: Classical description of exciton-cavity photon coupling. The thick purple lines correspond to the cavity mode dispersion defined by Equation 3.5 with $E_{c0} = E_X$=3.300eV and $n_{c0} = n_b$=2.3. The horizontal blue lines represent the background refractive index n_b=2.3. The calculated refractive and extinction indices are shown in the upper and the lower panels (read or green solid curves), respectively. The resulting upper and lower polariton modes (UP and LP) correspond to the intersections between the refractive index curve and the cavity mode dispersion. **a**. Dependence of Rabi splitting on the oscillator strength: f'=0.15eV^2 for the red curve and f'=0.03eV^2 for the green curve, with γ_X=50meV for both cases. **b**. Dependence of Rabi splitting on the exciton linewidth: γ_X=5meV for the red curve and γ_X=50meV for the green curve, with f'=0.03eV^2 for both cases.

For the first curve corresponding to equation 3.3 we suppose there is no exciton resonance, namely f=0, and therefore the material has dispersion-less background refractive index $n_b = \sqrt{\varepsilon_b}$ (horizontal blue lines). Its intersection with the cavity mode dispersion defined by Equation 3.5 (thick purple lines) determines the optical mode of the bare cavity, which is found at 3.3eV and is labeled “C” in the figure. If the material has excitons therein, its refractive index $n(E)$ and its extinction coefficient $\kappa(E)$ are strongly modified, as shown by the red/green curves in the upper and lower panels, respectively. The new modes resulting from the cavity photon-exciton interaction, namely the cavity-polaritons, are determined by the intersection of the $n(E)$ curve and the cavity mode dispersion. For each $n(E)$ curve, the central intersection point at 3.3eV is located at the extinction maximum and it represents a mode that is strongly absorbed [70]. The other two intersection points, which can be experimentally accessed by reflectivity measurements, are called lower polariton (LP) and upper polariton (UP) modes. They are separated in the spectrum by a certain amount of energy called the Rabi splitting, noted as $\hbar\Omega$ (with Ω being called the Rabi frequency). An observable Rabi splitting is the signature of the strong coupling between the exciton and the cavity photon. In the off-resonance case, the thick purple line shifts upwards or downwards, depending on the actual cavity thickness, leading to a correspondent shift of both the lower and upper polariton modes. These shifts will be further illustrated through the transfer matrix method later in this section.

The influence of the oscillator strength and the exciton linewidth on the Rabi splitting is illustrated in Figure 3.1**a** and **b**, respectively. It is obvious from Figure 3.1**a** that by increasing the oscillator strength larger Rabi splittings can be achieved and, thereby, enhance the exciton-cavity photon coupling. When reducing the oscillator strength, the $n(E)$ curve gets more and more flattened and approaches the n_b line, which will finally result in the loss of the strong coupling regime and will bring the system into the weak coupling regime with no Rabi splitting being further observable. On the other hand, as shown in Figure 3.1**b** the broadening of the exciton linewidth leads to a decrease of the Rabi splitting and, finally, to the transition into the weak coupling regime.

Simulations with the transfer matrix method

In the previous discussion only the exciton linewidth has been accounted for, while the effect of the cavity photon linewidth has not been considered. Indeed, the cavity photon linewidth can be viewed as the “thickness” of the cavity mode dispersion line (thick purple) in Figure 3.1, which will lead to an additional broadening of the polariton modes. If the spectral linewidths of the lower and upper polaritons are wider than their splitting, partially determined by the exciton oscillator strength, the two polariton modes might merge together with no Rabi splitting being resolved. This effect can be better illustrated using the transfer matrix method, which simulates the real cavity structure with all factors (cavity photon linewidth, exciton linewidth and oscillator strength) taken into consideration. To introduce the excitons into the transfer matrix simulations, we just need to replace the cavity refractive index n_c, which was set constant in Chapter 2, by the complex refractive index $\tilde{n}(E)$ defined in Equation 3.2.

The calculated reflectivity, transmission and absorption spectra using the transfer matrix method are shown in Figure 3.2. Different parameters related to the cavity structure and the exciton properties are chosen for comparison purposes, as detailed in the figure caption. One can notice that the splitting between the UP and LP has the smallest value in the absorption, and the largest value in the transmission. In this sense, the strong coupling regime is guaranteed by the observation of a Rabi splitting in the absorption spectrum [71], whereas the observation of the Rabi splitting in reflectivity (or transmission) does not necessarily mean so. Therefore, Figure 3.2**a** and **b** corresponds to the strong coupling regime, while Figure 3.2**d** corresponds to the weak coupling regime, since neither in absorption nor in reflectivity a Rabi splitting is observed. Interestingly, in Figure 3.2**c** a Rabi splitting is observed in reflectivity but not in absorption. This kind of situation belongs to the intermediate coupling regime, which will be discussed later in more detail. Indeed, increasing the cavity photon linewdith leads to a reduction of the Rabi splitting or even the loss of the strong coupling regime, as illustrated by the absorption spectra in Figure 3.2**b** and **c** (in which the photon linewidth is varied by changing the number of DBR pairs).

For this thesis it is important to note that if the cavity linewidth and the exciton linewidth are sufficiently small compared to the Rabi splitting (e.g. these ratios amount to γ_X/Ω_{Rabi} =50meV/86.1meV=0.58 and $\gamma_{Ph}/\Omega_{Rabi}$ =10.6meV/86.1meV=0.12, respectively in Figure 3.2**a**), the splittings in reflectivity and absorption are almost identical. Therefore, in high-Q microcavities with narrow exciton linewidths the strong coupling regime can be demonstrated by measuring the reflectivity, which is from an experimental point of view easier to measure than absorption; furthermore, in some of our cavities the substrate is not transparent, which impedes absorption measurements. An alternative method to demonstrate the strong coupling regime is to measure the photoluminescence, as it represents the absorption spectrum multiplied by a Boltzmann occupation factor [72]. However, its interpretation is sometimes not straightforward as it can be influenced by carrier localization, e.g. in quantum well based microcavities, and by the absence of significant UPB polaritons, especially in large Rabi splitting microcavities (typically ZnO-based microcavities) where the Rabi splitting is much larger than the thermal energy. Furthermore, in microcavities where the Rabi splitting is much larger than the exciton binding energy, such as in wide bandgap materials as GaN and especially ZnO, the UPB can be pushed above the band-to-band absorption edge [73]. In this case, the UPB might not be even observed in reflectivity, thereby imposing a correlation between experimental spectra and transfer-matrix simulations necessary to guarantee the type of regime in which the cavity operates.

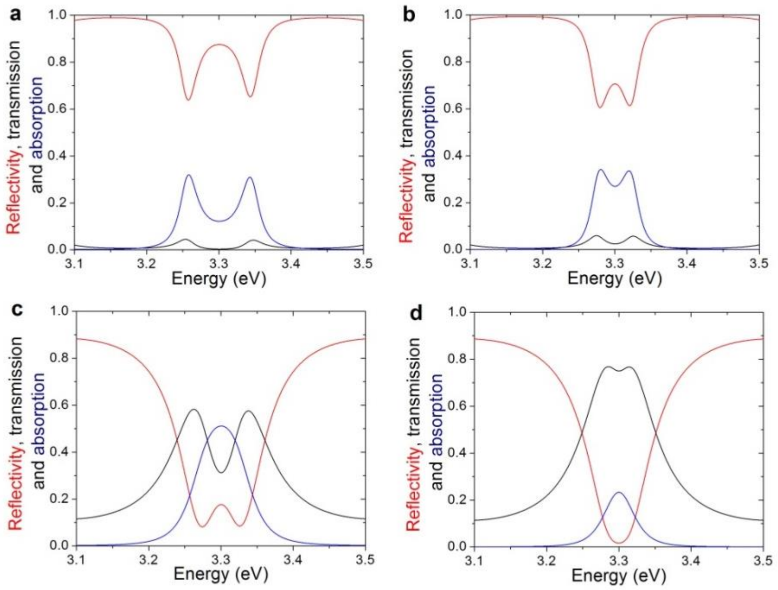

Figure 3.2: Calculated reflectivity (red), transmission (black) and absorption (blue) spectra using the transfer matrix method. The cavity length is set to be at resonance for the exciton energy. The DBRs materials have refractive indices n=2.0, 1.7 and $\bar{E}$=3.3eV. Different parameters regarding the exciton properties and the cavity structures are applied: **a**. f'=0.15eV^2, γ_X=50meV and 10 pairs of DBR at each side. **b**. f'=0.05eV^2, γ_X=50meV and 10 pairs of DBR at each side. **c**. f'=0.05eV^2, γ_X=50meV and 4 pairs of DBR at each side. **d**. f'=0.01eV^2, γ_X=50meV and 4 pairs of DBR at each side. The calculated cold cavity Q and photon linewidths are: in **a** and **b** Q=311 and γ_{Ph}=10.6meV; in **c** and **d** Q=34 and γ_{Ph}=96.7meV.

In a microcavity we define the exciton-photon detuning as $\delta = E_c - E_X$, where E_c is the bare cavity photon energy (i.e. the energy of the cavity mode in a cavity with the same background refractive index but without exciton resonances). The calculated absorption spectra for two different cavities, one in the strong-coupling regime and the other in the weak one, are plotted in Figure 3.3 as a function of detuning; the bare cavity mode is tuned from 3.2eV to 3.4eV, resulting in a detuning from -100meV to 100meV (the exciton energy is taken as 3.3eV). For the microcavity illustrated in Figure 3.3**a** the polariton dispersion as a function of the detuning is plotted in Figure 3.3**c**, where the upper and lower polariton modes form what are called the upper polariton branch (UPB) and the lower polariton branch (LPB). Unlike the bare exciton and the bare cavity modes, which cross each other at zero detuning, the UPB and LPB exhibit an anti-crossing. This anti-crossing is considered as the experimental evidence for the achievement of the strong coupling regime. The minimum energy separation between the UPB and LPB is found at $\delta = 0$ and corresponds to the Rabi splitting. On the contrary, for the weak coupling case illustrated in Figure 3.3**b**, which has been obtained by simultaneously reducing the exciton oscillator strength and the photon lifetime, the cavity mode dispersion in the presence of excitons is approximately the same as that of the bare cavity mode, plotted as a dashed line in Figure 3.3**c**. No anti-crossing feature is observed. In this case, the cavity mode can be continuously tuned across the exciton transition, the only effect being the absorption enhancement at the crossing point [74]. In this case it is not necessary to introduce the concept of exciton-polariton to describe the system behavior.

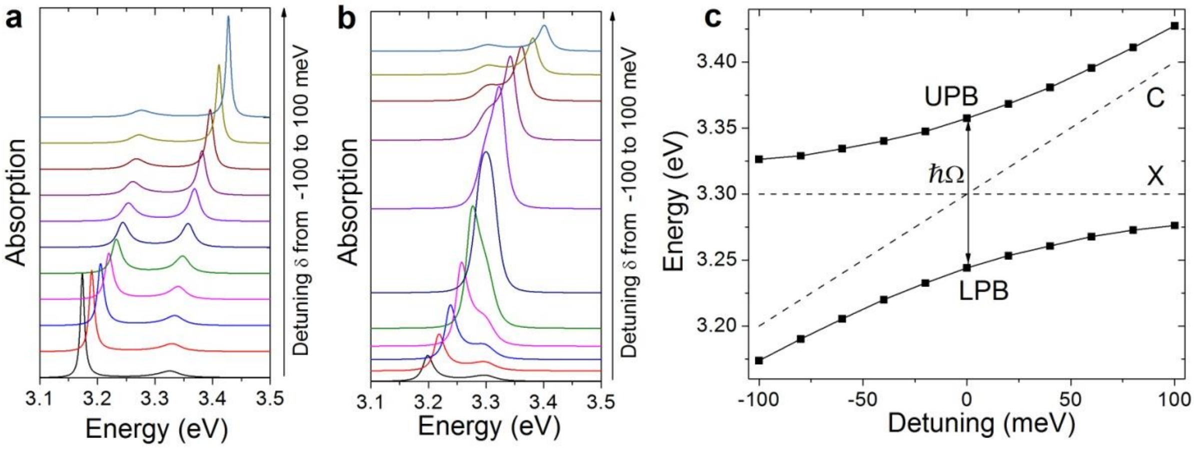

Figure 3.3: Strong coupling versus weak coupling regime simulated by the transfer matrix method. The exciton energy is fixed at E_X=3.3eV, while the cavity mode energy varies from 3.2eV to 3.4eV, corresponding to a detuning range from -100 to 100meV in both **a** and **b**. The plotted spectra are vertically shifted with increasing detuning for clarity. **a** and **b** correspond to the strong coupling and the weak coupling regimes respectively, and are achieved by using different cavity and exciton parameters. In **a,** f'=0.15eV^2, γ_X=50meV and 10 pairs of DBR (n=2.2, 1.5) at each side; in **b,** f'=0.01eV^2, γ_X=50meV and 4 pairs of DBR (n=2.2, 1.5) at each side. **c.** Solid lines (with square symbols) represent the UPB and LPB energies extracted from **a,** as a function of detuning. Dashed lines represent the bare cavity (C) and the bare exciton (X) modes.

It is worth to notice that analytic expressions for the polariton dispersion and the Rabi splitting can be obtained from the transfer matrix treatment of the system provided some approximations are made (see details in Reference [28]). The final expressions are basically the same as those derived from the coupled-oscillator model, which will be introduced in the next section. In this thesis, the transfer matrix method has been mainly used to design a cavity structure with some pre-defined optical properties, while a coupled-oscillator model has been used to determine the detuing and the excitonic/photonic fraction by comparison with the experimental data.

3.1.2 Quantum description of exciton-photon coupling

The quantum description treats the excitons and the photons as quantized fields, the strong coupling regime being thereby well reproduced by a coupled-quantum oscillator model.

Quantization of exciton and photon fields

In order to treat the optical field as a quantum particle, second quantization is applied, which allows to identify one particle with one excitation of the field [28]. First of all, a set of orthonormal states $\{|\phi_i\rangle\}$ is chosen as the basis of the system, which correspond to the different eigenmodes of the field excitation. Considering a system containing n_i excitations in the ith mode $|\phi_i\rangle$, the state of the whole system is written as

$$|\Psi\rangle = |n_1, n_2, ..., n_i, ...\rangle \tag{3.6}$$

Each excitation is viewed as a quantum particle with an energy $\hbar\omega_i$, in which ω_i is the oscillator frequency of the ith state. Therefore, the total energy in the ith state is given by $(n_i + \frac{1}{2})\hbar\omega_i$, with $\hbar\omega_i/2$ the energy of vacuum. $a_i^\dagger$ and a_i are defined as the creation and annihilation operators respectively and their effect consists in adding ($a_i^\dagger$) or removing (a_i) one excitation in the ith mode, namely

$$a_i^\dagger |n_1, n_2, ..., n_i, ...\rangle = \sqrt{n_i + 1}\,|n_1, n_2, ..., n_i + 1, ...\rangle \tag{3.7}$$

$$a_i |n_1, n_2, ..., n_i, ...\rangle = \sqrt{n_i}\,|n_1, n_2, ..., n_i - 1, ...\rangle \tag{3.8}$$

The operator $a_i^\dagger a_i$ is called the number operator and yields the number of particles in the ith mode without changing the state of the system:

$$a_i^\dagger a_i |n_1, n_2, ..., n_i, ...\rangle = n_i |n_1, n_2, ..., n_i, ...\rangle \tag{3.9}$$

which shows that $|n_1, n_2, ..., n_i, ...\rangle$ is an eigenstate of $a_i^\dagger a_i$ with the eigenvalue n_i. The operator $a_j^\dagger a_i$ represents a physical process in which one particle in the ith state is annihilated, giving rise to anther particle in the jth state. A more detailed description of second quantization can be found in References [75] and [28].

Exciton-photon coupling

In this section the exciton-photon coupling will be described in terms of a quantum "coupled-oscillator", in which we will make the low particle density approximation; this allows neglecting the exciton-exciton interaction. Let us consider the excitons and the photons with a given wavevector k, whose states are noted as $|X_k\rangle$ and $|Ph_k\rangle$, respectively, and with $a_k^\dagger$ (resp. a_k) and $b_k^\dagger$ (resp. b_k) defined as the creation (resp. annihilation) operators for the photon and the exciton modes, respectively. Using $|X_k\rangle$ and $|Ph_k\rangle$ as the base of the system, the non-interacting Hamiltonian which excludes the exciton-photon coupling reads:

$$H_k^0 = E_X(k) b_k^\dagger b_k + E_{ph}(k) a_k^\dagger a_k \tag{3.10}$$

in which $E_X(k)$ and $E_{ph}(k)$ are the exciton and the photon energies at wavevector k, respectively. The eigenstates of H_k^0 can be written as $\left|n_k^X, n_k^{ph}\right\rangle$ where n_k^X and n_k^{ph} are the numbers of excitons and photons at wavevector k in the system. These states are named bare states, as they describe uncoupled particles with independent physical properties. The interaction between the exciton and the photon involves optical transitions with an interaction Hamiltonian given by

$$H_k^{\text{int}} = g(b_k^\dagger a_k + a_k^\dagger b_k) \tag{3.11}$$

where $b_k^\dagger a_k$ (resp. $a_k^\dagger b_k$) represents the absorption (resp. emission) of a photon and the creation (resp. annihilation) of an exciton. This process is directly related to the optical transition strength, for which the coupling factor g is given by

$$g = \frac{1}{2}\sqrt{f}\int d\vec{r}\, u_{ph}(\vec{r}) u_X(\vec{r}) \tag{3.12}$$

where f is the exciton oscillator strength and $\int d\vec{r}\, u_{ph}(\vec{r}) u_X(\vec{r})$ is the overlap between the electromagnetic field $u_{ph}(\vec{r})$ and the exciton wave function $u_X(\vec{r})$. Specifically, if the electromagnetic field is confined in a planar microcavity, and we assume that excitons only exist in the active region, the overlap is just determined by the penetration depth of the optical field into the DBRs, namely

$$g = \frac{1}{2}\sqrt{\frac{fL_c}{L_{eff}}} \quad \grave{} \tag{3.13}$$

The total Hamiltonian of the exciton-photon coupled system, valid for particles with wavevector k, reads

$$H_k = H_k^0 + H_k^{\text{int}} = E_X(k) b_k^\dagger b_k + E_{ph}(k) a_k^\dagger a_k + g b_k^\dagger a_k + g a_k^\dagger b_k \qquad 3.14$$

The matrix form of H_k , in the $\left| n_k^X , n_k^{ph} \right\rangle$ basis, is expressed as

$$\begin{pmatrix} E_X(k) & g \\ g & E_{ph}(k) \end{pmatrix} \qquad 3.15$$

which can be diagonalized to obtain the eigenenergies of the system

$$E_{LP}(k) = \frac{E_X(k) + E_{ph}(k)}{2} - \frac{\sqrt{\left(E_X(k) - E_{ph}(k)\right)^2 + 4g^2}}{2} \qquad 3.16$$

$$E_{UP}(k) = \frac{E_X(k) + E_{ph}(k)}{2} + \frac{\sqrt{\left(E_X(k) - E_{ph}(k)\right)^2 + 4g^2}}{2} \qquad 3.17$$

and the corresponding normalized eigenvectors

$$\begin{pmatrix} C_X(k) \\ C_{ph}(k) \end{pmatrix} \text{ and } \begin{pmatrix} C_{ph}(k) \\ -C_X(k) \end{pmatrix} \qquad 3.18$$

in which

$$C_X(k) = \frac{1}{\sqrt{1 + \left(\frac{E_{LP}(k) - E_X(k)}{g} \right)^2}} \qquad 3.19$$

$$C_{ph}(k) = -\frac{1}{\sqrt{1 + \left(\frac{g}{E_{LP}(k) - E_X(k)} \right)^2}} \qquad 3.20$$

$E_{LP}(k)$ and $E_{UP}(k)$ are the energies of the lower and upper polariton branches, corresponding to the new eigenenergies of the coupled system. $C_X(k)$ and $C_{ph}(k)$ are the so-called Hopfield coefficients [10] and satisfy $|C_X(k)|^2 + \left|C_{ph}(k)\right|^2 = 1$. The Hamiltonian of the coupled system can be therefore re-expressed in a diagonalized form in terms of the dressed states

$$H_k = E_{LP}(k) p_k^\dagger p_k + E_{UP}(k) q_k^\dagger q_k \qquad 3.21$$

in which $p_k^\dagger$ (resp. p_k) and $q_k^\dagger$ (resp. q_k) are the creation (resp. annihilation) operators for the lower and upper polaritons with wavevector k, respectively. Their expressions in terms of the bare exciton and photon operators read

$$p_k^\dagger = C_X(k)b_k^\dagger + C_{ph}(k)a_k^\dagger \qquad 3.22$$

$$q_k^\dagger = C_{ph}(k)b_k^\dagger - C_X(k)a_k^\dagger \qquad 3.23$$

The eigenstates of H_k can be expressed as $||n_k^{LP}, n_k^{UP}\rangle\rangle$, where n_k^{LP} and n_k^{UP} are the number of lower and upper polaritons in the system with wavevector k, respectively. These new eigenstates are called dressed states, as they result from the exciton-photon coupling, compared to the bare states $|n_k^X, n_k^{ph}\rangle$. Though optical transition processes involve a_k and b_k, rather than p_k and q_k, they can still represent photon emission out of the cavity given that in the dressed-state picture, only transitions from $||n_k^{LP}, n_k^{UP}\rangle\rangle$ to $||n_k^{LP}-1, n_k^{UP}\rangle\rangle$ or $||n_k^{LP}, n_k^{UP}-1\rangle\rangle$ are allowed, which give rise to emission energies either at $E_{LP}(k)$ or $E_{UP}(k)$ in the radiation spectra [28], respectively.

From 3.18, the $||LP_k\rangle\rangle = ||1{,}0\rangle\rangle$ and the $||UP_k\rangle\rangle = ||0{,}1\rangle\rangle$ states can be expressed in the bare exciton/photon states base

$$||LP_k\rangle\rangle = C_X(k)|X_k\rangle + C_{ph}(k)|Ph_k\rangle \qquad 3.24$$

$$||UP_k\rangle\rangle = C_{ph}(k)|X_k\rangle - C_X(k)|Ph_k\rangle \qquad 3.25$$

$|C_X(k)|^2$ and $|C_{ph}(k)|^2$ are therefore the exciton (resp. photon) and photon (resp. exciton) fractions of the lower (resp. upper) polaritons, respectively. Figure 3.4**a** shows the calculated eigenenergies of the upper and lower polariton branches (Equations 3.16 and 3.17) as a function of detuning $\delta = E_{ph} - E_X$, exhibiting an anti-crossing arising due to the coupling. The Rabi splitting, that corresponds to the splitting at $\delta = 0$, equals to $2g$. The exciton and photon fractions of the lower polariton branch are shown in Figure 3.4**b**. As the polariton branch approaches (resp. moves away from) the exciton dispersion, the exciton (resp. photon) fraction increases. Therefore, the polariton exhibits more exciton-like or photon-like physical properties depending on the exact detuning and the branch it populates. This is of major importance for *polaritonics*, in general, and for ZnO in particular as will be shown in later chapters.

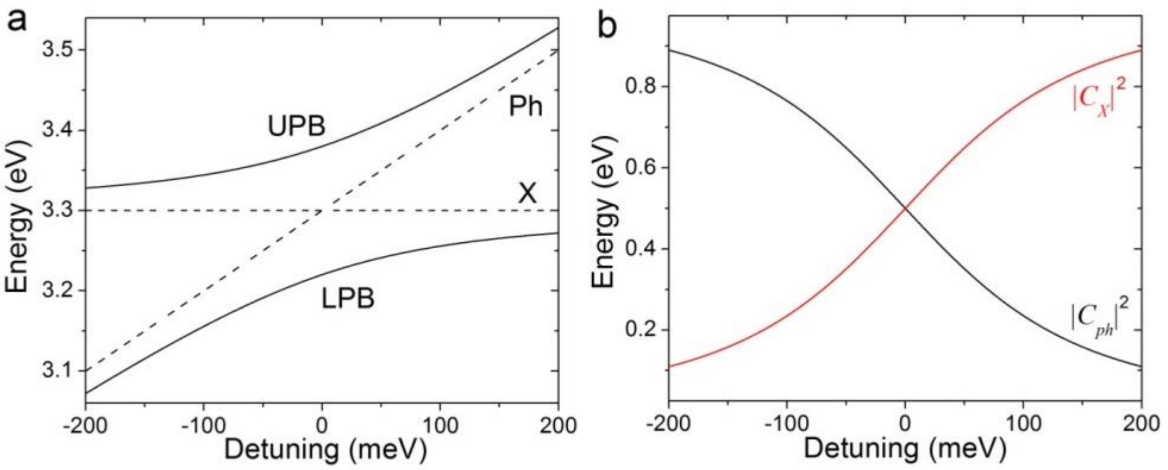

Figure 3.4: **a**. Upper and lower polariton branches as a function of detuning for $k_{\parallel}$=0. The bare cavity and exciton modes are shown as dashed lines. **b**. The exciton (red) and the photon (black) fraction of the lower polariton branch at $k_{\parallel}$=0 as a function of detuning. Parameters used: E_X=3.300eV, g=80meV.

Cavity polaritons

In a microcavity, cavity polaritons are formed through the coupling between the excitons in the active material and the cavity photons. Unlike bulk polaritons, which have a free three dimensional k, cavity polaritons are free particles only in two-dimensions, given that their vertical wavevector $k_{\perp}$ is fixed by the cavity confinement. As already discussed in Section 2.1.2, the cavity photon energy varies with the in-plane wavevector $k_{\parallel}$ whilst the exciton, which has a much larger effective mass than the cavity photons, exhibits a constant energy value throughout the same $k_{\parallel}$ range (this is only true within a $k_{\parallel}$ range sufficiently close to $k_{\parallel}$=0, which is usually the range for studying exciton-photon coupling). Therefore, for a given cavity structure, the exciton-photon detuning changes with $k_{\parallel}$. Thus, to prevent any misunderstanding the detuning of the cavity (also noted as δ) is defined as the exciton-photon detuning $E_{ph} - E_X$ at $k_{\parallel}$=0. The calculated LPB and UPB angular dispersions in microcavities with a Rabi splitting of 160meV and δ= -200, 0 and 200 meV are shown in Figure 3.5**a**, **b** and **c**, respectively. The anti-crossing feature can be only observed in the negative and zero detuning cases, as they include the on-resonance ($E_X = E_C$) case. At around $k_{\parallel}$=0, the LPB becomes more exciton-like with increasing detuning, while the UPB becomes more photon-like. The curvature of the polariton branches decrease as they approach the exciton energy, indicating an increase of the associated polariton effective mass. This kind of angular dispersion can be experimentally measured through angular-resolved reflectivity, photoluminescence or transmission measurements. In this work, where the substrates are opaque[1], only reflectivity and photoluminescence will be employed.

---

[1] For our full-hybrid mirocavities (will will be presented in Chapter 4 and 5) the substrate itself is not opaque, but since we use a metal to glue the structure to the substrate, the transmission is close to zero.

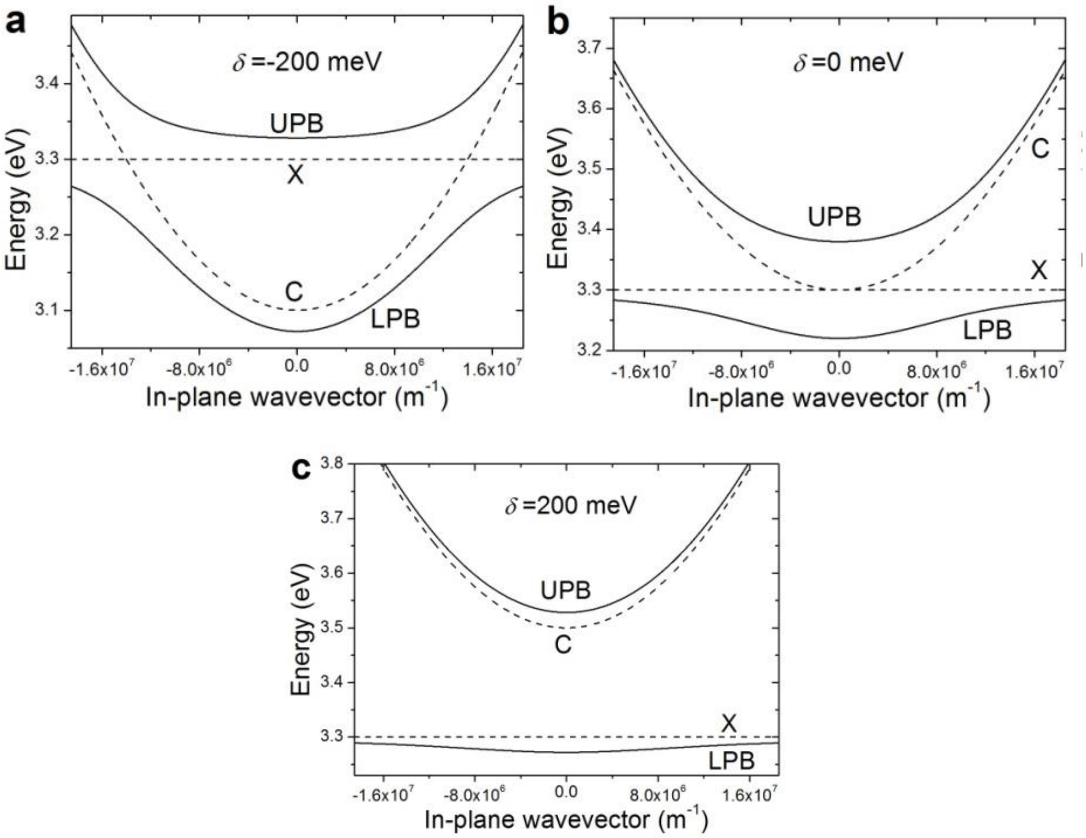

Figure 3.5: Angular dispersions of the lower and upper polariton branches in microcavities exhibiting negative (**a**), zero (**b**) and positive (**c**) detunings with the exciton. The bare cavity and exciton dispersions, labeled as C and X respectively, are shown as dashed lines. Parameters used: λ-cavity with n_c=2.3, E_X=3.300eV and g=80meV.

Mode broadening within the coupled oscillator model: effect on the coupling regime

As already discussed in Section 3.1.1, the exciton and photon broadenings can strongly affect the Rabi splitting as well as the coupling regime. Indeed, we can introduce the broadening into the coupled oscillator model in a semi-classical way, by including an imaginary term in the exciton and photon eigenenergies [76]. The matrix form of the Hamiltonian for the coupled system then reads

$$\begin{pmatrix} E_X(k) - i\gamma_X & g \\ g & E_{ph}(k) - i\gamma_{ph} \end{pmatrix} \tag*{3.26}$$

in which γ_X is the exciton homogeneous linewidth, mainly determined by the interaction with phonons or defects in the crystal, and γ_{ph} is the photon spectral linewidth, determined by the light losses within the cavity (mirror losses, interface scattering, etc.). Thus, in microcavities $\gamma_{ph} = \gamma_c \propto 1/Q$. It should be noted that the broadening due to the interaction between excitons and cavity photons (e.g. the exciton radiative lifetime) is already taken into account in g and, therefore, should not be added to the linewidth broadening introduced now. The eigenenergies of the coupled system are obtained by diagonalizing the Hamiltonian, which yields

$$E_{UP,LP}(k) = \frac{E_X(k) + E_{ph}(k)}{2} - i\frac{\gamma_X + \gamma_{ph}}{2} \pm \frac{\sqrt{\left(E_X(k) - E_{ph}(k) - i(\gamma_X - \gamma_{ph})\right)^2 + 4g^2}}{2} \quad 3.27$$

Specifically, at zero detuning (where $E_X = E_{ph} = E$), we get

$$E_{LP} = E - \frac{\sqrt{4g^2 - (\gamma_X - \gamma_{ph})^2}}{2} - i\frac{\gamma_X + \gamma_{ph}}{2} \quad 3.28$$

$$E_{UP} = E + \frac{\sqrt{4g^2 - (\gamma_X - \gamma_{ph})^2}}{2} - i\frac{\gamma_X + \gamma_{ph}}{2} \quad 3.29$$

Therefore, the Rabi splitting reads

$$\hbar\Omega = \sqrt{4g^2 - (\gamma_X - \gamma_{ph})^2} \quad 3.30$$

The strong coupling regime is only achieved when $4g^2 > (\gamma_X - \gamma_{ph})^2$, which yields a real value of the Rabi splitting. In the weak coupling regime, for which $4g^2 < (\gamma_X - \gamma_{ph})^2$, $\hbar\Omega$ becomes imaginary and does not result in any measureable energy splitting; in this case, the coupling modifies the *polariton* linewidth. As g is directly related to the exciton oscillator strength f, the coupling regime is essentially determined by the interplay between the exciton oscillator strength and the photon/exciton linewidths.

In particular, since for a given bulk microcavity at a certain temperature f and γ_X are fixed and determined by the quality of the active material and the exact temperature, the coupling regime is mainly governed by the cavity Q-factor, which dictates the cavity photon lifetime. The effect of Q in the polariton eigenenergies according to Equations 3.28 and 3.29 is illustrated in Figure 3.6. The imaginary and real parts of E_{LP} and E_{UP}, corresponding to the polariton broadening and energies, are shown in Figure 3.6**a** and **b**, respectively. In the weak coupling regime, there is no energy splitting and, thus, the system can still be described in terms of bare excitons and photons. However, their respective linewidths are modified by the coupling with the other particle, as illustrated in Figure 3.6**a**. The exciton linewidth increases with the cavity Q-factor, exhibiting an enhanced spontaneous emission rate that can be explained by the Purcell effect [1]. Similarly, due to the exciton-photon coupling the cavity photon lifetime can be increased larger than what would be merely expected from the increase of the Q. This effect has been exploited to achieve photon thermalization, although the discussion of the coupling regime in this experiment is still an open question [77]. In the strong coupling regime, the eigenenergy splits into two values and the concept of polaritons is necessary to describe the system. Within this simple model, the upper and lower polariton linewidths equal to the average value of the uncoupled exciton and photon linewidths and, thus, decrease with increasing *Q*-factor.

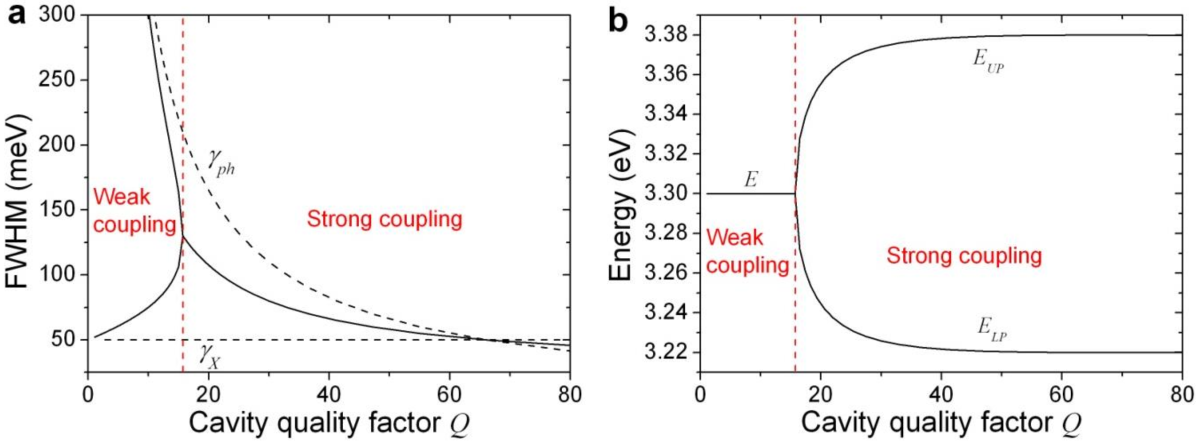

Figure 3.6: Calculated FWHM (solid lines in **a**) and energy (solid lines in **b**) of the polaritons as a function of cavity *Q*-factor, according to Equations 3.28 and 3.29. In **a**, the FWHM of the uncoupled excitons and photons are also plotted as black dashed lines. Parameters used: E=3.300eV, g=80meV, γ_X=50meV.

While the above-described approach to introduce the broadening of the excitons and cavity photons describes well some of the observed features, such as the transition from the weak to the strong-coupling regime as a function of *Q*, it underestimates the *Q* necessary to observe the strong-coupling regime; for the parameters used in Figure 3.6 the necessary *Q* ~16. Indeed, the Rabi splitting derived from Equation 3.30 does not guarantee the observation of an energy splitting in the absorption spectrum. In this context, Savona *et al* calculated the expression for the splitting to be observed in absorption, which imposes stronger conditions on the ratio between the coupling factor and the exciton/photon broadenings [78]

$$\hbar\Omega_{abs} = 2\sqrt{g^2 - \frac{\gamma_X^2 + \gamma_{ph}^2}{2}} \qquad 3.31$$

This expression yields a minimum cavity Q factor ~33 for achieving the strong coupling regime with the same parameters used in Figure 3.6. It is worth to mention here that in order to achieve polariton lasing it is necessary to obtain a *Q*-factor much larger than that just necessary to achieve the strong coupling, as will be discussed later. The diagram of the different coupling regimes is illustrated in Figure 3.7. The system is in strong coupling when $2g^2 > \gamma_X^2 + \gamma_{ph}^2$ and in weak coupling when $4g^2 < (\gamma_X - \gamma_{ph})^2$, with the area in between corresponding to the intermediate coupling regime [79], where a Rabi splitting can be derived from the coupled-oscillator model but cannot be observed in the absorption spectrum.

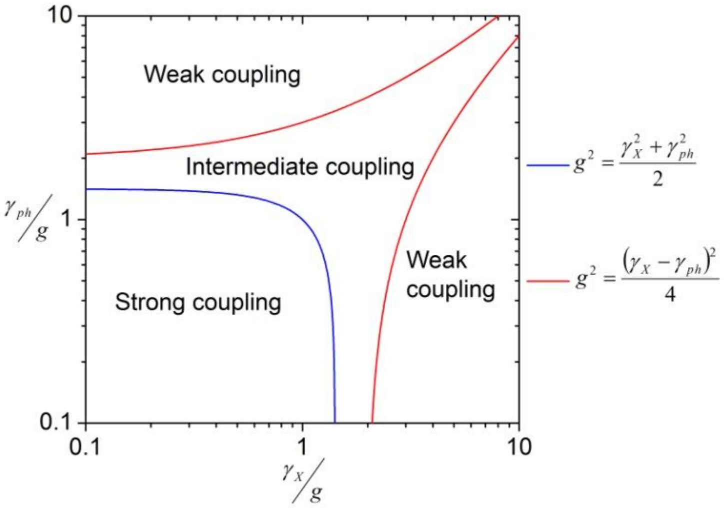

Figure 3.7: Diagram of the conditions necessary for having different coupling regimes.

Mode broadening within the coupled oscillator model: cavity Q determination

It should be noted that the broadening of the polariton modes depends on the exact detuning, given that it results from the contribution of the exciton/photon linewidths weighted by the relative excitonic/photonic fractions: the polariton linewidth approaches the exciton (resp. cavity photon) one when the excitonic (resp. photonic) fraction increases. Thus, as long as there is exciton-photon coupling, it is not possible to measure directly the cold cavity *Q* (e.g. from reflectivity spectra), given that the linewidth broadening or narrowing due to the coupling needs to be considered. As presented in Figure 3.8, the LPB linewidth is getting broadened when approaching the exciton mode in the case of a high *Q* cavity (Figure 3.8**a**), whilst it is getting narrowed in the case of a low *Q* cavity (Figure 3.8**b**), where the “high *Q*” or “low *Q*” definition is mainly determined by comparing with the exciton linewidth. Therefore, when determining the cold cavity *Q* in a strongly-coupled microcavity, all the above effects need to be considerd: the exciton and photon linewidths, the coupling strength, the exact detuning, etc.

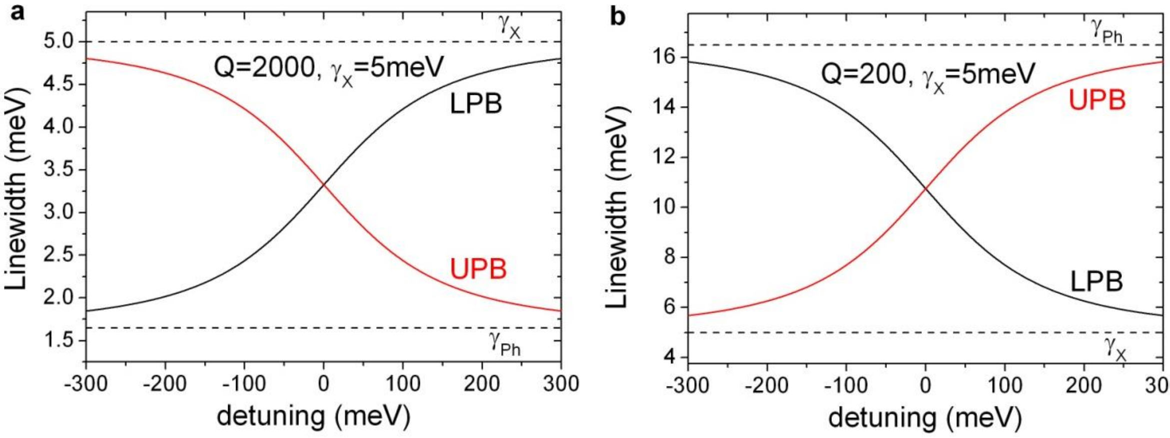

Figure 3.8: Calculated LPB and UPB linewidths as a function of detuning. g=80meV. The exciton linewidth is set to be γ_X =5meV, while the cavity photon linewidth varies. In **a**, *Q*=2000 (γ_{Ph}=1.65meV) and in **b**, *Q*=200 (γ_{Ph}=16.5meV).

Coupling with multiple exciton or multiple photon modes

The coupled oscillator model can be extended to systems with multiple exciton transitions. When n excitons couple simultaneously with the same cavity mode, the matrix form of the system's Hamiltonian can be written as

$$\begin{pmatrix} E_{X_1} - i\gamma_{X_1} & 0 & \cdots & 0 & g_1 \\ 0 & E_{X_2} - i\gamma_{X_2} & \ddots & \vdots & g_2 \\ \vdots & \ddots & \ddots & 0 & \vdots \\ 0 & \cdots & 0 & E_{Xn} - i\gamma_{Xn} & g_n \\ g_1 & g_2 & \cdots & g_n & E_{Ph} - i\gamma_{Ph} \end{pmatrix} \tag{3.32}$$

The polariton energies, their lifetimes, and the associated Hopfield coefficients can be obtained from the eigenvalues and eigenvectors of expression 3.32. This Hamiltonian is suitable for describing ZnO cavities, where three different exciton resonances, named A, B and C excitons (see Chapter 1), exist.

For the case of multiple cavity photons, each cavity mode only couples with excitons that have the same spatial wavefunction [80], and the same wavevector, and therefore can be considered independently of each other, i.e, each cavity mode will have its own independent matrix 3.32.

3.2 Polariton condensate

As illustrated in Figure 3.5, the cavity polariton dispersion has an absolute energy minimum at $k_{\|}$=0 for the LPB, which is the ground state of the system. It is therefore possible for a large number of exciton-polaritons, which are bosons, to accumulate at this energy level. Thus, at a given temperature if the particle density is sufficiently high the system might undergo a phase transition, close in many aspects to a Bose-Einstein condensation, and macroscopically occupy the ground state. The coherent light emission arising from the condensed polaritons is termed polariton lasing.

3.2.1 Bose-Einstein condensation: a brief introduction

The idea of Bose-Einstein condensation was first proposed by Einstein in 1925, by developing an early work of Bose, and suggested that an unlimited number of bosons can accumulate in the lowest energy state of a given system [18]. Consider N non-interacting bosons in a volume R^d (R is the system size and d is the system dimension) at a temperature T. Their energy distribution is described by the Bose-Einstein distribution function:

$$f_B(\vec{k},T,\mu)=\frac{1}{\exp\left(\frac{E(\vec{k})-\mu}{k_BT}\right)-1} \qquad 3.33$$

in which $\vec{k}$ is the d-dimensional wavevector, k_B is the Boltzmann constant and μ is the chemical potential. The lowest energy of the system is defined as zero, and we must have $\mu \leq 0$ to keep $f_B(\vec{k},T,\mu)$ always non-negative. The total particle number can be expressed as

$$N(T,\mu)=\sum_{\vec{k}} f_B(\vec{k},T,\mu)=\frac{1}{\exp\left(-\frac{\mu}{k_BT}\right)-1}+\sum_{\vec{k},\vec{k}\neq 0} f_B(\vec{k},T,\mu) \qquad 3.34$$

in which the ground state (at E=0 and $\vec{k}$=0) is explicitly separated from the others. The particle density can be derived by integrating over the reciprocal space:

$$n(T,\mu)=\lim_{R\to\infty}\frac{N(T,\mu)}{R^d}=n_0(T,\mu)+\frac{1}{(2\pi)^d}\int_0^\infty f_B(\vec{k},T,\mu)d\vec{k} \qquad 3.35$$

where

$$n_0(T,\mu)=\lim_{R\to\infty}\frac{1}{R^d}\frac{1}{\exp\left(-\frac{\mu}{k_BT}\right)-1} \qquad 3.36$$

is the ground state density, which vanishes if μ is non-zero. The chemical potential μ increases with particle density n as seen from Equations 3.33, 3.34 and 3.35. Therefore the maximum particle density that the system can accommodate, with the assumption that n_0=0, is given by

$$n_{crit}(T)=\lim_{\mu\to 0}\frac{1}{(2\pi)^d}\int_0^\infty f_B(\vec{k},T,\mu)d\vec{k} \qquad 3.37$$

n_{crit} is called the critical density. The integral converges for $d > 2$ but diverges for $d \leq 2$, which is to say, in two- or less dimensional systems the system can accommodate up to infinite particles within the standard Bose-Einstein picture of non-interacting bosons. However, in three (or more) dimensional systems, the chemical potential reaches zero when $n = n_{crit}$. If the particle density is continuously increased above this critical density, all the extra particles condense into the ground state, whose density becomes non-zero when $\mu = 0$ (Equation 3.36), namely,

$$n_0(T)=n(T)-n_{crit}(T) \qquad 3.38$$

This is the standard (i.e. ideal bosons in 3D) Bose-Einstein condensation (BEC), a phase transition characterized by a massive occupation of a single quantum state, where all the condensed bosons share exactly the same wavefunction and are thereby coherent. The critical density n_{crit} increases with temperature T. If the total density is fixed, BEC can be achieved by decreasing the temperature below a critical value T_{crit}. Both n_{crit} and T_{crit} increase with the particle mass m, which is implicitly included in the $E(\vec{k})$ term of Equation 3.33.

The experimental realization of Bose-Einstein condensation was first achieved with ultra-cold atoms (T_{crit} in nanoKelvin range) in 1995 by Cornell, Wieman and Ketterle [19,20], who shared the Noble Prize in physics in 2001. Due to their much lighter mass, excitons in semiconductors were also proposed as good candidates for BEC [81,82]. In this case, in order to condensate the radiative lifetime of excitons should be much longer than their thermalization time and, therefore, dark excitons seem the most suitable candidates. However, in bulk materials non-resonantly excited dark excitons are often trapped by local structural disorder, preventing them to behave like free bosons. Moreover, the detection of the condensed phase is difficult since, by definition, light emission is not allowed from dark excitons. To overcome these difficulties, indirect excitons in coupled quantum wells have been intensively studied, with the advantage that the spatially-separated electrons and holes lead to very long exciton radiative lifetimes. Indeed, exciton BEC was first reported by Butov *et al* [21,22] and Snoke *et al* [23] in such systems during the early 2000s, with a critical temperature below 1K.

In principle, “bright” excitons might also be good candidates for BEC, despite their shorter lifetime. However, the difficulty lies in the fact that their coupling with light gives rise to bulk exciton-polaritons, whose lower energy branch becomes photon-like when the wavevector k approaches zero. In this case, the ground state of the bulk polariton dispersion, namely the k=0 photon state, does not exist. Therefore, strictly speaking the BEC of bulk polaritons is forbidden. This problem is solved in the system of cavity polaritons, whose LPB dispersion has a well-defined energy minimum at $k_{\parallel}$=0 that may serve for polariton condensation. As we have already shown in previous sections, long polariton lifetimes can be achieved by fabricating microcavities with large Q-factors. Moreover, since cavity polaritons can have an effective mass four to five orders of magnitude smaller than the exciton (depending on the actual exciton/photon fraction), the corresponding critical temperature is achievable with standard cryogenic techniques and might even rise up to room temperature. Before ending this section it should be noted that, strictly speaking, cavity polaritons cannot go through a BEC phase transition as they are two dimensional particles. However, in two dimensional systems weakly-interacting particles can go undergo a phase transition from a normal towards a superfluid phase, which is named as Kosterlitz-Thouless (K-T) phase transition [83,84], and can be regarded approximately as a local BEC given that the superfluid is a collective bosonic phase-coherent state.

3.2.2 Historical introduction of polariton condensation

In 1992, Weisbuch and coworkers experimentally observed the strong exciton-photon coupling in a GaAs-based microcavity [12], which inaugurated the field of cavity polaritons. In 1996, Imamoglu *et al* proposed that coherent light emission should be observed from cavity polaritons, which could have relaxed to the final state through bosonic stimulated scattering [24]. This type of coherent light source has been named since then polariton laser which, contrary to conventional lasers, does not require electronic population inversion. The first unambiguous experimental report of polariton lasing was published by Le Si Dang *et al* in 1998 [25]. In the meantime, the idea of using a resonant probe beam to trigger the stimulated scattering process was proposed by Tassone in 1999 [85], and the final state stimulation through polariton-polariton scattering was experimentally observed by Savvidis *et al* in 2000 [86]. The first experimental demonstration of polariton BEC was conducted by Kasprzak *et al* in a CdTe microcavity at 5K in 2006 [26]. In this work, the main experimental features of a polariton BEC were established, including massive occupation of the ground state, thermalization of the polariton distribution, as well as spatial coherence. Subsequently, polariton BEC was also demonstrated in a GaAs-based microcavity with an artificially-generated real space trap, which enhanced polariton relaxation [87]. Different trapping approaches have been also applied in lower dimensional cavity structures (wires and pillars), where polariton condensation has been also achieved [88,89].

Following the demonstrations of polariton BEC, the experimental and theoretical studies on the physics of polariton condensates have multiplied during the recent years and have yielded numerous exciting achievements: these include polariton condensates superfluidity [90,91], quantized vortices [92,93], solitons [94,95], magnetic monopoles [96], and multistability [97,98], just to cite some of them. The manipulation of polariton condensates has been performed by spatially modifying the cavity structures [88,99,100], as well as by using different pumping schemes [99,101].

Whereas for the moment practical applications of polariton condensates or lasers seem far away, numerous advances in this sense have been made, including electrically pumped polariton diodes[102-104], polariton circuits [105,106], Terahertz emission schemes [107] and, lately, electrically-injected polariton lasers [108,109].

3.2.3 Dynamics of polariton condensation

Unlike ideal bosons with infinite lifetimes, cavity polaritons have finite lifetimes and, thus, need to be continuously fed by an external pumping. This situation makes polariton condensation differ dramatically from an ideal BEC. Initially, the pumping creates hot electron-hole pairs (if the pumping is not resonant, as will be the case all along the current manuscript) that relax very fast (in the fs range), mainly by interaction with optical phonons, to exciton states at large wavevectors. As sketched in Figure 3.9, these excitons go subsequently through a thermalization process, which corresponds to the relaxation along the

LPB from large to small wavevectors. For the situation depicted in Figure 3.9, which corresponds to a given detuning, the bottom of the LPB constitutes a natural polariton trap, in reciprocal space. For the LPB, and close to $k_{\|}=0$, the polaritons become more photon-like with sharply reduced effective mass and density of states. Polaritons around the trap region usually exhibit short lifetimes due to their photon composition, while the excitons initially created at the large-$k_{\|}$ region, far from the light cone, have long lifetimes (~hundreds of ps), given that their radiative decay is largely reduced. At “low” polariton densities and when the excess exciton kinetic energy, with respect to the minimum of the LPB, is less than the optical photon energy, polaritons thermalize towards the lattice temperature mainly through polariton-acoustic photon interaction, which is a rather slow process; it requires ~10ps to relax less than 1meV of energy [28]. As a result, large number of excitons accumulate at the edge of the polariton trap in reciprocal space, unable to relax further to $k_{\|}=0$ because their lifetimes become shorter than the required relaxation time, as illustrated in Figure 3.9. This is named the bottleneck effect [110], which also exists in bulk polariton systems.

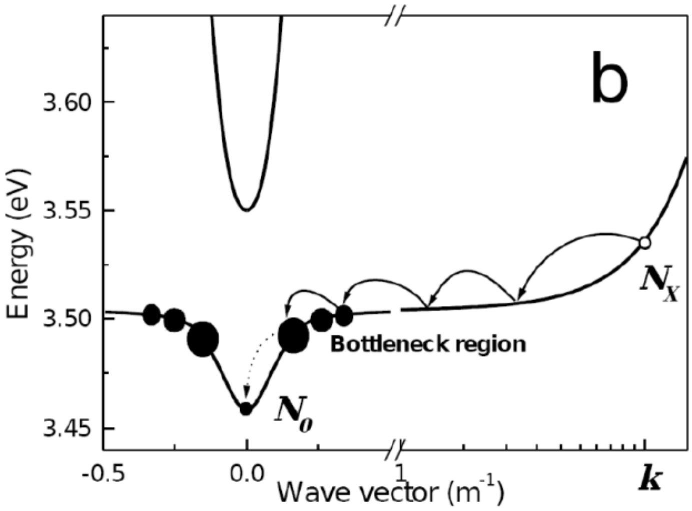

Figure 3.9: Extracted from Reference [28]. Sketch of the polariton relaxation along the LPB.

To overcome this bottleneck effect, one direct way is to increase the polariton lifetime, which usually involves complicated techniques for ultra-high-Q cavity fabrication. Alternatively, fast thermalization mechanisms such as polariton-optical phonon interaction [40] and polariton-free carrier interaction [111] are helpful to overcome the bottleneck effect, although they are only applicable in specific materials/situations or cavity structures. Most important, polariton relaxation might be also assisted by polariton-polariton scattering, whose intensity depends on the polariton density: in this case, two polaritons go through elastic scattering, with one polariton scattered towards $k_{\|}=0$ and the other into larger-$k_{\|}$ states, respecting energy and momentum conservation. Though this process does not reduce the overall temperature of the polariton gas, it can be very efficient and indeed allows, in some cases, to overcome the bottleneck effect.

The above discussion illustrates well the fact that in many cases, the polariton system is out-of-equilibrium and despite this fact it can still undergo a phase transition by massively occupying the ground state. Thus, in a microcavity system the phase transition can be driven either by the thermodynamics of the system, by the relaxation kinetics or by a tradeoff between both aspects. If we note τ_{pol} as the LPB lifetime, and τ_{rel} as the time needed for polaritons to relax from the excitonic reservoir at large wavevectors to the bottom of the LPB, after being created by the external pumping, three different relaxation regimes can be distinguished [47,112]:

Regime I: $\tau_{rel} \ll \tau_{pol}$. The polariton distribution reaches a quasi-thermal equilibrium and can be described by a certain temperature, i.e. by a Boltzmann distribution, which is not necessarily the lattice temperature. In this case polariton BEC can be achieved and its threshold is mainly given by the thermodynamics of the transition (similar to the ideal case).

Regime II: $\tau_{rel} \gg \tau_{pol}$. The polariton distribution is out of equilibrium and cannot be described by a temperature. In this case, polariton condensation can be achieved by increasing the particle density, which enhances polariton-polariton interaction and, thus, reduces τ_{rel}. The condensate threshold is not given by the thermodynamical criterion but mainly by the polariton relaxation kinetics. The non-equilibrium features of the initial system make this type of phase transition hardly comparable to a BEC[1].

Regime III: An intermediate regime between I and II, where both thermodynamics and kinetics play a role in the condensation threshold, can be distinguished.

The relaxation dynamics of polaritons can be simulated using the semi-classical Boltzmann rate equations, which for bosons read [110]:

$$\frac{dn_{k_\parallel}}{dt} = P_{k_\parallel} - \Gamma_{k_\parallel} n_{k_\parallel} - n_{k_\parallel} \sum_{k'_\parallel} W_{k_\parallel - k'_\parallel} (n_{k'_\parallel} + 1) + (n_{k_\parallel} + 1) \sum_{k'_\parallel} W_{k'_\parallel - k_\parallel} n_{k'_\parallel} \qquad 3.39$$

in which $n_{k_\parallel}$ is the number of polaritons in the state with in-plane wavevector $k_\parallel$. $P_{k_\parallel}$ and $\Gamma_{k_\parallel}$ are the pumping (polaritons created in $k_\parallel$ state by pumping) and decay (radiative and non-radiative) rates. $W_{k_\parallel - k'_\parallel}$ is the total scattering rate from $k_\parallel$ state to $k'_\parallel$ state through polariton-phonon, polariton-polariton, and polariton-free carrier interactions. It is important to note that since polaritons are bosons, the scattering into a given state is proportional to the number of particles in the given state plus one, which is often termed as “bosonic final state stimulation”. This term enhances polariton relaxation, with respect to fermionic particles, and contributes to overcome the bottleneck effect.

---

[1] In some special situations it is possible to reach a thermalized condensed phase from a non-thermalized uncondensed phase by increasing the particle density. See figure 5 of Ref [112].

3.2.4 Polariton lasing versus photon lasing

The term “polariton lasing” is usually used to describe the coherent light emission from the polariton condensate, irrespective of the condensate nature (in-equilibrium or out-of-equilibrium [112]). Thus, a microcavity displaying polariton condensation can be called a polariton laser; whether it is referred to as a “polariton condensate” or “a polariton laser” depends just in the context of the discussion. Many similarities exist between polariton lasing and conventional photon lasing, including nonlinear intensity increase above threshold, spectral linewidth reduction due to the build-up of temporal coherence, onset of spatial coherence, etc. Nevertheless, polariton lasing has its own features which can be used to distinguish it from conventional photon lasing experimentally. The wavefunction of the polariton condensate $\psi(\vec{r})$ can be obtained from the generalized Gross-Pitaevsii equation [99,113,114]:

$$\left\{-\frac{\hbar^2}{2m}\nabla^2+V_{ext}(\vec{r})+V_{res}(\vec{r})+g|\psi(\vec{r})|^2\right\}\psi(\vec{r})=\mu\psi(\vec{r}) \qquad 3.40$$

in which m is the polariton effective mass, μ is the chemical potential, and g is the polariton-polariton interaction constant (not to be confused with the coupling factor introduced in 3.1.2). $V_{ext}(\vec{r})$ is the external potential induced by the cavity structure, including cavity/exciton disorder. $V_{res}(\vec{r}) = g_{res}n_{res}(\vec{r})$ is the repulsive potential due to the uncondensed excitons in the exciton reservoir, with g_{res} the interaction constant and $n_{res}(\vec{r})$ the exciton reservoir density distribution. The two terms $V_{res}(\vec{r})$ and $g|\psi(\vec{r})|^2$ give rise to a blueshift of the condensate energy with respect to the LPB minimum below threshold. Moreover, polaritons also gain kinetic energy from the repulsive interaction and travel away from the pumping area, which modifies the angular and spatial emission features with respect to an ideal BEC of non-interacting bosons.

One difference between polariton and photon lasing lies in the angular emission pattern. Due to repulsive interactions, the polariton condensate is blueshifted in energy above the LPB minimum, covering a certain angular range and exhibiting a non-disperssive angular pattern, as shown in Figure 3.10**a** [115]. In the particular case where a small pumping spot is used as external pumping source, condensed polaritons can be ejected from the pumping region and gain some momentum k_{c0}, as shown in Figure 3.10**b** [115]. Indeed, due to this effect polaritons propagate away from the pumping area, as experimentally studied by Wertz *et al* [88] or Tanese *et al* [116]. On the contrary, conventional photon lasing occurs at the bottom of the bare cavity mode, and the emissions is concentrated around $k_{\parallel}$=0, following the cavity angular dispersion. Besides, photons have no repulsive interaction and are only emitted from the pumping area. This has allowed to nicely differentiate both type of emissions within the same microcavity [99].

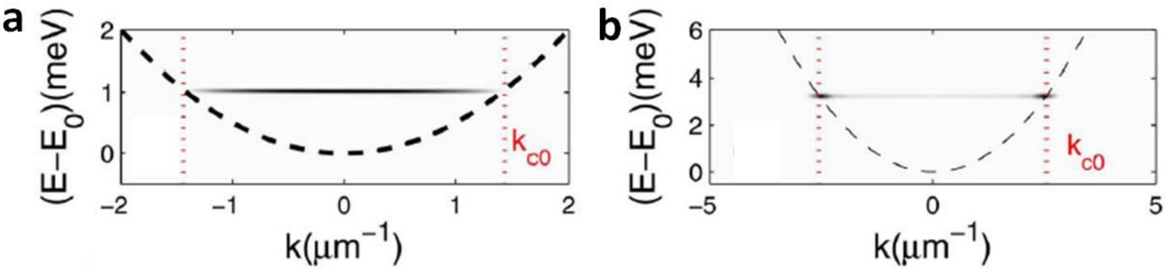

Figure 3.10: Extracted from Ref [115]. Numerical simulation of the angular-resolved emission spectra of a polariton condensate as obtained by solving the Gross-Pitaevsii equation. The polariton condensate emission intensity is presented in grey scale. The dashed black line shows the LPB dispersion and the red dotted line shows the free polariton wavevector k_{c0} at the condensate energy [115]. **a** and **b** correspond to the cases of large pumping spot (20μm) and small pumping spot (2μm), respectively.

The stability of excitons in the system is important for achieving polariton lasing. On one hand, if the temperature is high enough to promote thermal exciton dissociation (i.e. k_BT~E_b), excitons are no longer stable and the system can transit into the weak coupling regime, where only conventional photon lasing is feasible. On the other hand, if the particle density corresponding to the polariton lasing threshold exceeds the exciton Mott density, excitons will go through a phase transition transforming them into an electron-hole plasma before condensation occurs and, thus, polariton lasing will be no longer achievable [89]. This last effect leads sometimes to ambiguity in the experimental demonstration of polariton lasing, especially in the negative detuning case where the bare cavity mode is close to the LPB, as illustrated in Figure 3.5**a**. When the polariton energy blueshift, which is supposed to be induced by the repulsive interactions in the case of polarion lasing, is similar to the energy difference between the bare cavity mode and the LPB at $k_\parallel$=0, it is difficult to judge whether the lasing origin is of polaritonic nature or not. In this sense, a blue shift smaller than the bare cavity-LPB energy difference needs to be observed in order to unambiguously demonstrate polariton lasing. In some cavity structures, a double threshold behavior can be observed, with the first and second thresholds corresponding to polariton and photon lasing, respectively [89,117]. However, for the moment this behavior has been only observed in GaAs-based microcavities, whose photon lasing threshold is higher than (or at least comparable with) the exciton Mott density [117-119]. For wide-bandgap materials, with very high Mott densities, this phenomenology has not been yet observed; in some cases the lack of observation comes from the fact that the DBR damaging threshold is achieved before photon lasing occurs.

3.3 Wide bandgap polariton lasers

If industrial applications of polariton-based devices are to be developed, they will probably require room temperature operation. This condition requires that the excitons of the active region have to be stable at room temperature requiring, in turn, that the exciton binding energy is larger than roughly k_BT (25.6meV at room temperature). Furthermore, since the polariton trap in reciprocal space should be also larger than k_BT [47], otherwise polaritons might thermally escape from the trap, efficient relaxation will be necessary in order to relax such large amount of energy. Since we have already seen that polariton-polariton scattering might be an effective relaxation mechanism, especially at large particle densities, the larger the Mott density of the active material the better, since larger densities will be possible without dissociating the excitons. These two conditions point towards wide bandgap semiconductors as the best candidates. Though the fabrication of high-*Q* microcavities based on these materials is extremely challenging, remarkable achievements that have overcome the technological difficulties have been reported in the last fifteen years. In this section, an overview of various wide bandgap polariton lasers will be given, paying special attention to ZnO, for which the state-of-the-art will be presented.

3.3.1 Organics

Organic semiconductors have Frenkel-type excitons [28,120], which exhibit extremely large binding energies (~1eV) comparable to the exciton transition energy, guaranteeing the high stability of excitons at room temperature even under large particle densities. Indeed, the first report of strong exciton-photon coupling in an organic microcavity by D. Lidzey *et al*, in 1998, was already at room temperature [15]. However it was not until 2010 that the first organic polariton lasing was demonstrated by S. Kena-Cohen *et al* in an organic single-crystal microcavity, also at room temperature [32]. The main challenge for fabricating organic microcavities is to find materials that can be grown in the form of single crystal [121] and that exhibit a sufficiently large damage-threshold, since many of the organic materials do not survive under high pumping power. Nowadays, studies are still on-going to develop new adapted organic materials as well as to combine the benefits of organic and inorganic materials within one and the same polariton device [122-124].

3.3.2 GaN

GaN (Gallium Nitride) and its alloys (AlGaN, InGaN, etc) are the second most exploited semiconductor in terms of business revenues, just after silicon. Their widespread use is mainly driven by optoelectronic devices such as LEDs [125,126] (the largest market for GaN), laser diodes [127] and VCSELs [128,129]. The GaN exciton binding energy is 26meV for bulk material and ~50meV for quantum wells, which exceed the room temperature thermal agitation. Besides, due to their industrial implementation, fabrication techniques of GaN based devices have got more mature than other wide bandgap semiconductors. Intensive studies on GaN-based microcavities were carried out for achieving room temperature polariton lasing. These works were started by a collaboration among several CNRS (Centre National de la Recherche Scientifique) groups (CRHEA and LASMEA), which lead in 2003 to the first observation of the strong coupling regime in a GaN microcavity at 5K, by Antoine-Vincent *et al.*[16]. The cavity was made of a bulk GaN active region capped by a top dielectric DBR, while the bottom-part reflectivity was provided by the silicon substrate. Still with a simple cavity structure, the same groups succeeded in observing the strong-coupling regime at room-temperature in 2005 in a GaN-based microcavity [130]. Subsequently, the optical properties of the cavities were improved by growing a bottom AlGaN/AlN DBR, under the GaN active layer, enabling them to study the coupling of two exciton levels with a single cavity mode [131] as well as the influence of various top mirrors on the strong coupling regime [132]. In all these references the strong coupling regime was demonstrated by reflectivity measurements. Shortly after, Stokker-Cheregi *et al* studied in the same kind of cavities polariton relaxation along the LPB and showed the presence of a strong bottleneck effect, which could be nevertheless overcome by increasing the temperature/polariton density [133]. However, no polariton lasing could be achieved. In parallel, room temperature strong coupling in GaN-based bulk microcavities was also reported by Alyamani *et al* in 2007 [134].

Compared to these first cavities, the achievement of room temperature polariton lasing required further improvement of the cavity *Q*-factor and a reduction of the exciton inhomogeneous broadening, mainly limited by the strain gradient within the thickness of the active region. The most successful works to overcome these difficulties were performed by N. Grandjean’s group, at Ecole Polytechnique Fédérale de Lausanne (EPFL, Switzerland) and their collaborators. They developed the MOCVD (metal-organic chemical vapor deposition) growth of crack-free AlInN/AlGaN DBRs on GaN templates, which greatly improved the bottom mirror reflectivity [135]. The cavities were composed of such a bottom DBR, a GaN bulk or multiple quantum well (MQW) layer as the active region, and a top dielectric DBR, demonstrating a local Q-factor as large as ~2800 [136]. One of the sole drawbacks present in these first-generation microcavities was the presence of a large inhomogeneous photonic broadening [136]. Around 2006, the strong coupling regime was achieved and intensively studied at room temperature on both the bulk and the MQW GaN microcavities [137-139]. The first room temperature polariton laser was demonstrated soon after on the bulk GaN microcavity by Christopoulos *et al*, in 2007 [31]. In 2008 they studied the polarization properties of the polariton laser previously achieved and observed a spontaneous polarization build-up process, which was interpreted in terms of a spontaneous symmetry breaking occurring during polariton condensation[140]. In the same year, room temperature polariton lasing was also demonstrated on a GaN microcavity with MQWs [30]. A thorough characterization of the condensation characteristics (polariton lasing threshold versus detuning and temperature) was conducted in the next years, enabling the same group to derive for the first time a complete phase diagram for GaN-based polariton lasers [47]. The experimental observations were well reproduced by numerical simulations carried out in the group of G. Malpuech [141,142]. Recently, an alternative active region based on nonpolar GaN, for which thick QWs could be used due to the absence of Quantum Confined Stark effect, was investigated: the inherent anisotropy of this orientation, in terms of both refractive indices and exciton polarization, render the behavior of polariton branches [143] and lasing emission [144] much richer.

3.3.3 ZnO: state-of-the-art

In 2002 M. Zamfirescu *et al* proposed ZnO as one of the *most adapted* materials for room temperature polariton lasing, thanks to its exciton stability and large oscillator strength [33]. Six years later R. Johne *et al* [48] carried out more sophisticated numerical simulations for ZnO microcavities, taking into account polariton relaxation dynamics, and established the guidelines to achieve room-temperature polariton lasing, mainly related to the cavity-Q factor. Indeed, the advantages of ZnO as the active material for room temperature polariton lasing were obvious, as illustrated in Table 3.1. The large exciton binding energy (much larger than $k_B T$ at room temperature) and the large Mott density guarantee the stability of excitons at room temperature and under large particle densities, respectively. Furthermore, the large oscillator strength leads to large Rabi splittings, as discussed in 3.1, and therefore ensures the achievement of the strong coupling regime at room temperature even for relatively low cavity-Q microcavities. Detailed comparative studies among different materials, including ZnO, can be found in the article of Faure *et al* [73].

Material	Binding energy in bulk (quantum wells)	Oscillator strength f	Mott density in bulk (quantum wells)
GaAs	4.8 (~ 14) meV [11,145]	~250 meV^2 [12]	3-12×10^{16} cm^{-3} (~4×10^{10} cm^{-2}) [146]
CdTe	10 (~25) meV [11,14]	~1000 meV^2 [14]	0.5-2×10^{18} cm^{-3} (~1×10^{12} cm^{-2}) [147]
GaN	26 (~50) meV [148,149]	~3000 meV^2 [139]	2-3×10^{18} cm^{-3} (~2×10^{12} cm^{-2}) [146]
ZnO	60 meV [49]	~40000 meV^2 [64]	0.5-20×10^{18} cm^{-3} [49]

Table 3.1: Parameters of excitons for different semiconductor materials.

If we consider that the top DBR problem is solved by using dielectric materials, which is a rather optimistic assumption given the difficulty of their fabrication, the major difficulty for achieving high quality planar ZnO microcavities lies in the lack of suitable materials for the bottom DBR. The reason is that we need simultaneously:

1. A bottom crystalline DBR displaying a small lattice mismatch with respect to ZnO.
2. A bottom DBR consisting of bi-layers with large refractive index contrast.

Unfortunately, these two conditions are difficult to be satisfied simultaneously. Therefore, the existing fabrication methods usually sacrifice one condition or the other. In this sense, the aim of this thesis is to find methods that solve these two requirements in one and the same cavity. In the following, we will review the approaches developed by the different groups working on ZnO microcavities (planar or not) whose schematic structures are sketched in Figure 3.11.

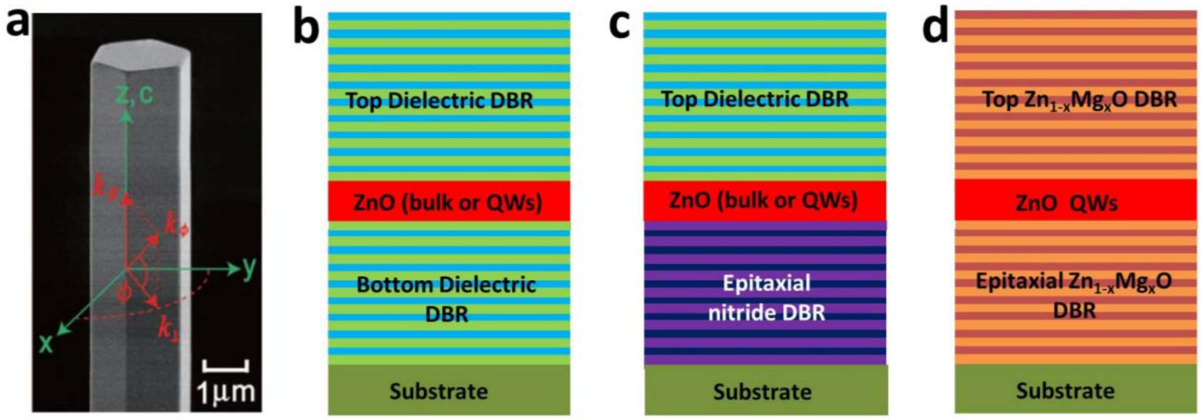

Figure 3.11: Sketches of various ZnO microcavity structures: **a**. microwires (figure extracted from reference [44]), **b**. fully-hybrid microcavities, **c**. semi-hybrid (hetero-epitaxial) microcavities, and **d**. monolithic microcavities.

Microwires

As the fabrication technology of high-Q planar ZnO microcavities is highly demanding, much easier approaches have been introduced; these are mainly based on the exploitation of ZnO microstructures that tend to form, naturally, hexagonal resonators elongated along the ZnO *c*-direction. ZnO microwires have hexagonal cross-sections, as illustrated in Figure 3.11**a**, that present confined photonic Whispering-Gallery Modes (WGMs) in which light circulates mainly close to the periphery of the hexagonal cross-section. Eventually, Fabry-Perot modes can be also sustained between two opposite facets within the hexagon [150]. The most complete studies on this kind of cavities have been carried out by M. Grundmann's group (Germany) and, especially, by a collaboration between Z. Chen's group in Fudan University (China) and M. Richard's group at Institut Néel (France).

(a) *Before this thesis started.*
In 2008, Z. Chen's group fabricated tapered ZnO microwires by a vapor-phase transport method, under atmospheric pressure, on which the anti-crossing feature that confirmed the strong-coupling regime was observed by moving along the diameter gradient, given that the WGMs energy is inversely proportional to the resonator diameter [38].

(b) *During this thesis.*
In 2011 the Chinese-French collaboration performed angle-resolved measurements along the microwire directions perpendicular and parallel to the elongation axis ($k_{\perp}$ and $k_{\parallel}$ in Figure 3.11**a**), and demonstrated the quasi-1D character of WGM-based polaritons [151]. In this work they observed, for the first time, an ultra-large vacuum Rabi splitting in ZnO microcavities (>200meV), which leads to a strong quenching of the phonon-induced polariton broadening at room-temperature, even for excitonic fraction approaching 50%, and enables to retain narrow polariton states even at such high temperatures. More recently, Z. Chen's group demonstrated polariton parametric scattering at room temperature in a ZnO microwire [44], while M. Richard's group measured the spatial coherence of large-excitonic fraction condensates [45].

Despite all their advantages such as the easiness of fabrication and the high-crystal quality, ZnO microwires have significant disadvantages too. In particular, the free spectral range and the cavity-Q factor are not independent, as both depend strongly on the diameter of the microwire. In order to increase the free-spectral range of the bare WGMs, and therefore increase the energy separation between consecutive LPBs, one needs to decrease the wire diameter; in turn, this reduces the cavity *Q*-factor dramatically due to increasing diffraction losses [152]. Moreover, it is difficult to do shape engineering in a microwire to modify the potential for polaritons, although very recently the use of patterned substrates was shown to provide such potential modulation [153]. For these reasons, although planar microcavities are more challenging from the fabrication point of view, they also provide more degrees of freedom.

Fully-hybrid microcavities

The structure of a fully-hybrid microcavity is illustrated by Figure 3.11**b**. The ZnO active region is surrounded by two dielectric DBRs, which are usually constituted by amorphous or polycrystalline materials. Since dielectric DBRs have high reflectivities (the bi-layer refractive index contrast can attain in some cases up to ~30-35%), these microcavities have the potential for exhibiting large *Q*-factors without the need of many DBR pairs, compared to other material systems. However, if the ZnO is deposited directly onto the bottom dielectric DBR, the final active layer is usually polycrystalline, exhibiting relatively low material quality.

(a) *Before this thesis started.*
The fully-hybrid approach based on the deposition of ZnO directly into dielectric materials, by pulsed laser deposition, has been largely exploited at the University of Leipzig by M. Grundmann's group. Since their first observation of the strong-coupling regime in 2008, with a measured vacuum Rabi splitting of 78meV on a ZnO cavity with ZrO_2/MgO DBRs [154], they have developed a number of dielectric materials for the DBRs, achieving the strong-coupling regime up to 410K in 2009 by using YSZ (yttria stabilized zirconia) and Al_2O_3 bilayers [35]. In parallel, they used those DBR structures to fabricate one-dimensional ZnO resonators on which the strong coupling regime was also achieved [155].

(b) *During this thesis.*
Their study on the polarization properties of this last cavity revealed a large (~6 meV) TE-TM splitting and a strong polarization dependence on the polariton scattering rates, which affects polariton relaxation along the LPB [156]. Finally, in 2012 they achieved polariton lasing [41], as shown in Figure 3.12**a**. The investigated cavity consists of a bulk ZnO $\lambda/2$ active layer sandwiched between two 10.5-pair YSZ/Al_2O_3 DBRs. The polycrystalline ZnO active layer exhibits preferentially *c*-plane orientation, with grains of about 100nm in diameter. The surface roughness (root mean square) is ~1.9nm for the ZnO and ~1nm for the DBRs, which leads to a cavity *Q*-factor of ~1000, with a vacuum Rabi splitting of ~80meV. Polariton lasing was observed up to 240K at negative detunings, while at positive detunings an electron-hole plasma emission was detected. Furthermore, they characterized the polariton lasing threshold as a function of temperature and δ, as shown in Figure 3.12**b**; while their results in the threshold values show a large scattering, they seem to indicate that the polariton lasing threshold increases with temperature and with detuning, similar to GaN [47] and contrary to previous theoretical calculations [48].

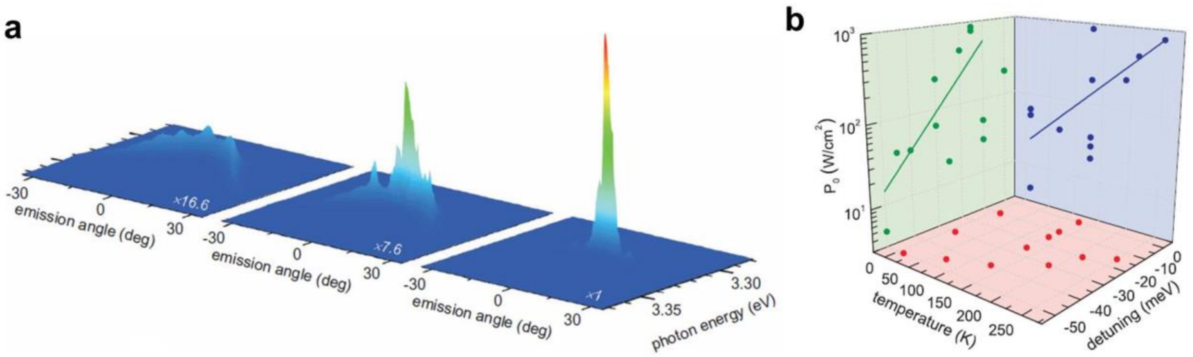

Figure 3.12: Extracted from Reference [41]. **a**. From the left to the right: Fourier images in a linear color scale below ($P = 0.4P_0$), slightly above ($P = 1.1P_0$) and clearly ($P = 1.25P_0$) above threshold (P_0) for T = 130K and a detuning of −40meV. **b**. Threshold power density for polariton condensation as a function of temperature and detuning.

Semi-hybrid (hetero-epitaxial) microcavities

The semi-hybrid approach wants to be a compromise between good ZnO material quality and good cavity properties, as illustrated in Figure 3.11**c**. The ZnO active layer is grown on top of a nitride bottom DBR by an epitaxial growth technique and capped by a dielectric top DBR. On one hand, the nitride layers have lattice parameters close to those of ZnO, which allows the growth of a single crystalline active region. On the other hand, although for an equal number of pairs the nitride DBR is much less reflective than the dielectric DBR (bi-layer refractive index contrast of ~10-13% compared to ~25-35%), in principle the epitaxial techniques allow for growing a large number of pairs, which can eventually compensate this disadvantage. Moreover, for the top DBR one can still take the advantage of using a dielectric one.

(a) *Before this thesis started.*

The first report on the strong coupling in planar ZnO microcavities was published by R. Shimada *et al*, at University of Viginia (United States) in 2008 [37]. The cavity was a semi-hybrid one consisting of an AlGaN/GaN bottom DBR grown by MOCVD on a sapphire substrate, a ZnO active layer grown by MBE (molecular beam epitaxy) and a top SiN/SiO_2 DBR deposited by non-epitaxial means. The authors claimed a cavity Q-factor of 100 and an estimated Rabi splitting of 50meV at room temperature. However, a detailed look on the spectra reveals that actually the claimed upper polariton branch seems to be dispersionless (although the energy position they extract from their fit is dispersive) and the claimed lower polariton branch seemed to follow the cavity photon dispersion up to 30° [51]. A more convincing claim, although some of the reported results are rather enigmatic (e.g. the population and visibility of the UPB data in Figure 4c of reference [34]), was made in 2009 by J. R. Chen *et al.* (at the National Chiao Tung University in Taiwan, Republic of China), who reported the achievement of room temperature strong-coupling in a semi-hybrid ZnO microcavity [34] by angle-resolved PL measurements in which the dispersion of the polariton branches can be easily distinguished.

The CNRS groups, with whom this thesis has been performed, made a number of contributions to the development of semi-hybrid ZnO microcavities before this thesis started. The teamwork involves a collaboration between four CNRS laboratories: CRHEA (Centre de Recherche sur l'Hétéro-Epitaxie et ses Application), Institut Pascal, L2C (Laboratoire Charles Coulomb) and LPN (Laboratoire de Photonique et de Nanostructures). In 2009 they demonstrated the strong coupling regime on a semi-hybrid ZnO microcavity grown by MBE on a nitride AlN/AlGaN bottom DBR, grown itself by MBE on silicon, and completed by a top metal mirror [17]; the stong-coupling regime was achieved despite the low *Q*-factor (less than 50). In this report, they performed reflectivity measurements and observed the ZnO bulklike behavior even in the strong coupling regime, due to the large excitonic absorption in ZnO, and showed that for ZnO cavities thicker than ~λ/2 the UPB cannot be observed due to a strong absorption. In the same year, they used top dielectric DBRs and improved the cavity *Q*-factor to ~100 [36], which enabled them to observe the strong coupling regime between excitons and the cavity mode, as well as between excitons and the first Bragg mode, both at room temperature. This coupling with Bragg modes had been previously observed in CdTe-based microcavities [157] and needs to be carefully considered in microcavities where the Rabi splitting is comparable to the DBRs stopband widths. The reason is that polaritons can eventually relax towards the Bragg-associated LPBs, which display much shorter lifetimes, and prevent condensation at the bottom of the cavity-mode associated LPB [36].

(b) *During this thesis.*
The CNRS groups continued to improve the quality of the semi-hybrid ZnO microcavities, by increasing the number of the AlN/AlGaN pairs and by ameliorating the crystalline quality of the ZnO, with the aim of achieving polariton lasing. In May 2011, they reported laser emission with excitonic gain from low to room temperature, but the system switched from the strong to the weak coupling regime at the lasing threshold [158]. These results were very promising for demonstrating ZnO polariton lasers. Indeed, shortly after in October 2011 they reported, in collaboration with the group of N. Grandjean at EPFL, polariton lasing in a semi-hybrid ZnO microcavity up to 120K, which was the first demonstration of a ZnO polariton laser [39]. The microcavity consisted of a 5λ/4 bulk ZnO active layer embedded between a bottom 13-pair AlGaN/AlN DBR and a top 12 pair SiO_2/Si_xN_y DBR, exhibiting a *Q*-factor of ~500 and a vacuum Rabi splitting of ~130meV. Polariton lasing in that cavity was demonstrated by a massive occupation of the LPB $k_{\|}=0$ state, i.e. a non-linear increase of the emission intensity, and by the spectral linewidth narrowing, as shown in Figure 3.13. The 3 meV-blueshift at threshold, much smaller than the energy separation between the LPB and the cavity mode (57meV), evidences that lasing occurred in the strong coupling regime. However, neither below nor above threshold the polariton gas was in thermal equilibrium, as shown by Figure 3.13**d**. They continued to optimize the cavity fabrication with HfO_2/SiO_2 top DBRs which resulted in a local *Q*-factor of 650 [40]. That same year, the CNRS consortium studied the role of LO-phonons in polariton relaxation within a ZnO cavity, and observed that the polariton lasing threshold was reduced when the energy separation between the exciton reservoir and the LPB minimum was in resonance with the LO-phonon energy [40]. More recent results of the CNRS groups will be discussed later, as they were achieved within this thesis.

It is also worth to mention that with heteroepitaxial ZnO it is also possible to fabricate a fully-hybrid ZnO microcavity by etching away the substrate and placing a dielectric DBR on each side of the epitaxial ZnO [159]. This approach has guided some of the work of this thesis.

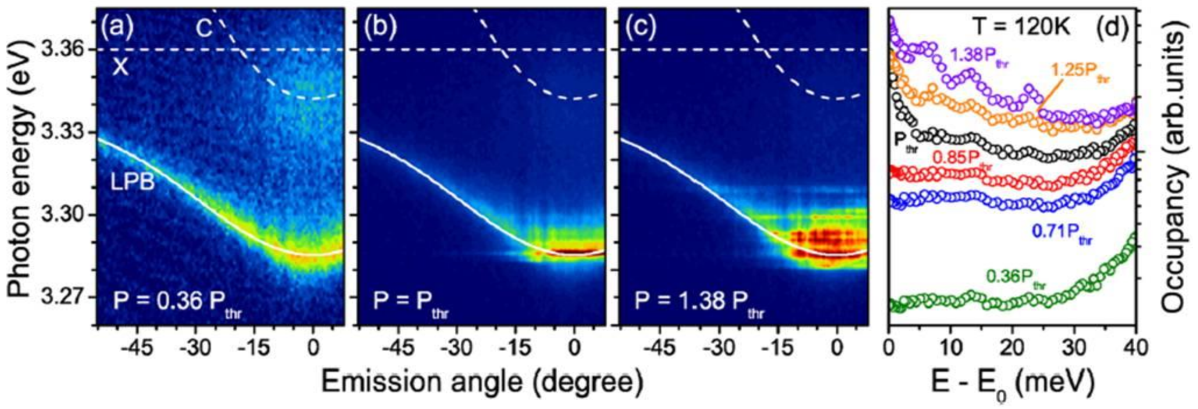

Figure 3.13: Extracted from Reference [39]. Demonstration of polariton lasing at 120K in a semi-hybrid ZnO microcavity. (a)-(c) Fourier space PL images of the microcavity as a function of excitation power. The solid white lines (resp. the dashed white lines) represent the simulated LPB dispersion (resp. bare cavity and bare exciton dispersions). (d) Occupancy of the LPB as a function of emission energy.

During the same period, the group from National Chiao Tung University continued their work on semi-hybrid ZnO microcavities on GaN-on-sapphire templates, and conducted a more detailed study of the strong coupling regime features [160]. In 2012, they claimed the achievement of polariton lasing at room temperature on a semi-hybrid ZnO cavity exhibiting a *Q* factor of 200 [43]. Typical lasing features, such as a nonlinear increase of output intensity Vs input intensity and spectral linewidth narrowing, were observed. They also showed the angular dispersions below and above threshold, as reproduced in Figure 3.14. While the cavity seems to display a lasing emission, it is difficult to conclude the coupling-regime in which this emission takes place. The reason is that, due to the large negative δ value (-119meV) compared to the calculated Rabi splitting (98meV for the location where “polariton” lasing occurs, and 48meV for the location where “conventional” lasing occurs), the LPB is very photonic-like and, therefore, the blueshift below threshold brings the bottom of the LPB very close to the bare cavity mode. Thus, conventional photon lasing cannot be absolutely excluded. Besides, the experimental *Q*-factor of 200, determined with a spot of 3µm, seems too low to enable efficient polariton relaxation down to the bottom of the LPB, especially when compared with numerical simulations carried out on ZnO-based cavities [48]. In August 2012 they reported again ZnO polariton lasing at room temperature [42] at a slightly smaller (in absolute value) negative δ, but still in the order of the vacuum Rabi splitting. Once again, lasing occurs close to the bare cavity mode and no lasing is presented at more positive δ, where the demonstration of polariton lasing would be more conclusive. Finally, in 2013 they published a review paper with systematical studies on different detunings as well as the polariton relaxation features [161]. This series of measurements seem to confirm that they are actually in the strong-coupling regime and that polariton lasing occurs; however, only highly negative detunings allow them to observe polariton lasing.

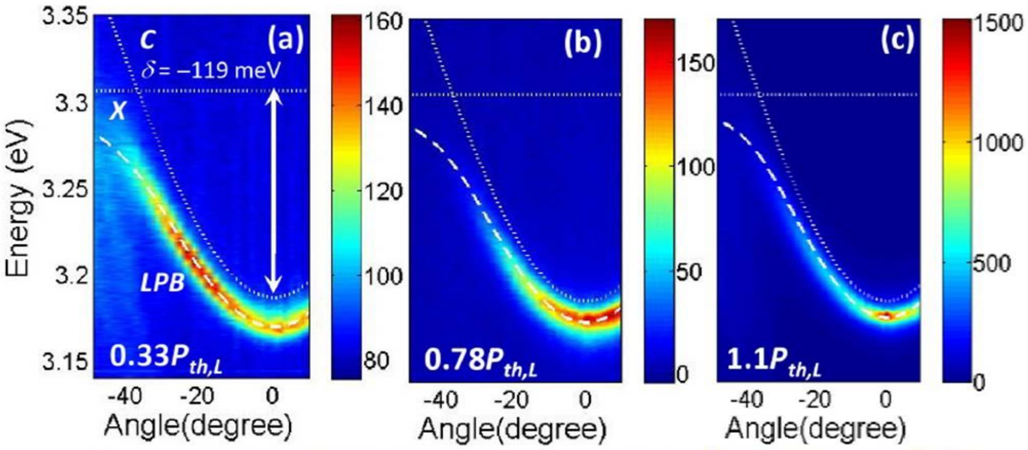

Figure 3.14: Extracted from Reference [43]. Fourier space PL images as a function of excitation power. The dashed white line (resp. the dotted white lines) represents the simulated LPB dispersion (resp. cavity and exciton dispersions).

Monolithic microcavities *(during this thesis)*

Monolithic microcavities involve "homoepitaxial" growth of a ZnO bulk or a ZnO/ZnMgO MQW active region on $Zn_{1-x}Mg_xO/Zn_{1-y}Mg_yO$ DBRs. Strictly speaking the cavities discussed hereafter are not homoepitaxial, since the substrate was sapphire. This approach allows to have single crystalline ZnO quantum wells as the active region but shows a major difficulty, namely the low reflectivity of $Zn_{1-x}Mg_xO/Zn_{1-y}Mg_yO$ DBRs due to a reduced bi-layer refractive index contrast (~5-8%). F. Henneberger's group, at Humboldt University of Berlin (Germany), has made the biggest advances on such microcavities. In January 2011 they reported on the realization of a vertical cavity surface emitting laser (VCSEL) based on a monolithic ZnO microcavity, which exhibited a *Q*-factor of 450 and lasing in the weak coupling regime [162]. In November 2011, they reported on for the first time the achievement of strong coupling in a monolithic MQW microcavity up to 150K [163], although to date they have not reported polariton lasing, even at low temperature, in any of their cavities.

Table 3.2 gives a summary on the properties of different planar ZnO microcavities discussed above.

Cavity type	ZnO active layer	Embedding high-quality QWs quantum wells	DBR bi-layer refractive index contrast / reflectivity	Overall stop band width
Fully-hybrid[1]	Polycrystalline or amorphous	Extremely difficult	~30-35% / high	Large
Semi-hybrid	Single crystalline by heteroepitaxy	Difficult	Bottom:~10-13% / moderate; Top:~30-35% / high	Small
Monolithic	Single crystalline by homoepitaxy	Relatively easy	~5-8% / low	Small

Table 3.2: Comparison of properties of different planar ZnO microcavities.

---

[1] In the state-of-the-art "fully-hybrid" refers to the cavity fabricated through direct deposition of ZnO onto dielectric materials. Our cavity which will be presented in Chapters 4 and 5 is also fully-hybrid but fabricated in a completely different way.

3.4 Conclusion

This chapter gives a detailed description of exciton-polaritons and a historical review of this research field: (1) The concept of exciton-polaritons and strong coupling was introduced by considering both classical and quantum models; (2) the basic principles of polariton condensates were discussed, together with a brief historical review; (3) the major results on wide bandgap microcavities, with a special focus on ZnO cavities, was presented, clearly differentiating the achievements that were obtained before this PhD work and during its realization.

II. Fully-hybrid ZnO microcavities

Chapter 4 Fabrication and linear optical properties of fully-hybrid ZnO microcavities

Fully hybrid microcavities, i.e. with two dielectric DBRs, seem in principle the best candidates to obtain a microcavity with optimum photonic properties thanks to the DBRs large absolute reflectivities, small field penetration depths and large stopbands. To fabricate such a cavity, the most straightforward approach consists in depositing a ZnO film, or ZnO/ZnMgO quantum wells, directly onto the dielectric materials as tempted by other groups, the best results being obtained by the team of Prof. Dr. M. Grundmann and Dr. R. Schmidt-Gründ in Universität Leipzig. In collaboration with this last team and LPN, we explored this approach by depositing the ZnO-based materials at CRHEA-CNRS by molecular beam epitaxy (MBE). Unfortunately, the crystalline quality of the material we deposited, textured along the *c*-axis but with large twist values, was always limited, compared to single-crystalline ZnO, and we decided not to pursue this approach. Experimental results on this approach can be found in Appendix A.

Our results together with those of other groups indicate that incorporating a high-quality ZnO active region in between two dielectric DBRs is very challenging. Indeed, before this thesis started there had been no successful attempts combining single-crystalline ZnO and two dielectric DBRs. In this thesis we have succeeded in developing a completely new fabrication approach that merges the merits of the best possible ZnO bulk material with high-quality dielectric DBRs, developed at LPN (CNRS) by the team of Sophie Bouchoule. The final cavities exhibit record cavity Q-factors and large vacuum Rabi splittings. In this chapter, the fabrication process and the linear optical properties of such microcavities will be described.

4.1 Cavity fabrication

As already discussed in 3.3.3, the key point for having single-crystalline ZnO active region is to avoid its growth/deposition on polycrystalline or amorphous materials. Our approach consists in circumventing this problem by introducing a commercially-available ZnO substrate in between dielectric materials without the requirement of ZnO growth/deposition.

4.1.1 General process flow

The fabrication process consists of four basic steps, schematically depicted in Figure 4.1**a** to **d**:

(a) A 6.5-pair HfO_2/SiO_2 dielectric DBR is deposited by ion-beam-assisted (Ar, O_2) electron-beam vacuum evaporation on the single-crystalline ZnO substrate, which is 500µm thick.

(b) The DBR is completed by the evaporation of a ~ 200-nm thick Al layer to achieve a nominal mirror reflectivity of ~ 99.8 % at the Bragg wavelength (λ ~ 380 nm), and to allow for subsequent substrate transfer. The whole structure is then turned upside-down and transferred onto a host substrate (pyrex glass) using anodic bonding between Al and pyrex.

(c) The ZnO substrate is thinned down to a thickness of several tens to hundreds nanometers, by a combined etching and polishing process.

(d) A 10-pair HfO_2/SiO_2 DBR is deposited on top of the processed ZnO substrate, the cavity being completed.

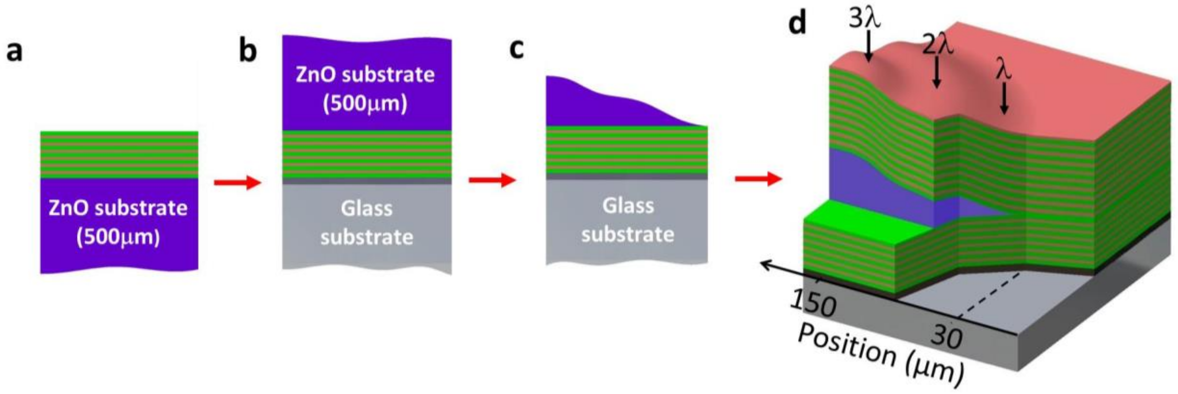

Figure 4.1: Schematics of the fabrication of the fully hybrid ZnO microcavity. **a-d** correspond to the fabrication steps explained in the main text.

4.1.2 Thinning of the ZnO substrate

The main difficulty of the general process as described above consists in thinning the 500µm thick substrate degrading neither its optical properties nor its surface flatness, and keeping a "*reasonable*" thickness gradient that limits the photonic inhomogeneous broadening. Indeed, it is the sole step in this cavity fabrication that had never been exploited before by any other research group, given that the previous fully-hybrid cavities with single-crystalline active regions were based on an heteroepitaxial structure that exploited the presence of an etch-stopping layer for the removal of the substrate [159,164]. The successful process requires the combination of chemical etching and polishing. In order to understand why this was the only process, among all those that we tempted, that worked correctly we will first describe the most common methods for thinning a substrate, and we will then discuss the advantages and disadvantages of each of them. This discussion will illustrate the logical path that brought us to the successful process.

One of the most commonly used methods to thin a layer is wet chemical etching. Compared to most semiconductors, in particular GaN, ZnO can be etched by almost any acid solution: in what follows, we will focus on the results we obtained with H_2SO_4:H_2O_2 as the etchant. The first difficulty in controlling the chemical etching of ZnO arises from its anisotropic and polar crystal structure. Indeed, ZnO substrates with different crystallographic orientations or polarities react very differently with the etchant:

(1) The Zn-face is not etched at room temperature; at higher temperatures it can be etched but resulting in very serious surface damage. Therefore, the Zn-face was excluded for chemical etching.

(2) The O-face ZnO substrate is very easy to etch, with an etching rate of ~8µm/min at room temperature and for an acid solution H_2SO_4:H_2O_2:H_2O = 1:1:6[1]. Interestingly, during etching the surface becomes initially rough, being covered with hexagonal pyramids (morphology similar to that in Figure 4.2**b**), and recovers a relative smoothness once ~100µm are etched away. These values might depend on the exact carrier concentration of the substrate.

(3) The *m*-nonpolar ZnO substrate can be etched at room temperature, exhibiting an etching rate of ~4µm/min for an acid concentration H_2SO_4:H_2O_2:H_2O = 1:1:6.

Based on the above tests, we decided to process the O-face and *m*-plane rather than the Zn-face. A common problem to all the wet etching performed is the huge thickness inhomogeneity, regardless of the crystal orientation/polarity or the initial surface roughness. Usually, after 1 or 2 hours of etching, the whole ZnO sample exhibits a curved surface, with its thickness varying typically from 0 to ~50µm, within a 2×2 mm^2 area (meaning a thickness gradient of ~25nm/µm). This thickness gradient would result in an extremely large inhomogeneous photonic broadening, compared to the expected Rabi splitting, effectively preventing any optical study on the cavity. Therefore, the desired thinning quality cannot be achieved solely by wet chemical etching.

Mechanical grinding and polishing is another way to reduce the sample thickness, as widely used for the preparation of transmission electron microscopy (TEM) semiconductor samples. However, standard grinding steps employed in TEM are not well fitted for our purpose because: (1) It is difficult to know precisely the remaining ZnO thickness during the grinding, especially when the final layer should be no thicker than 1µm. Therefore an effective way to avoid over-grinding and under-grinding is necessary. (2) As the DBR/ZnO structure is “loosely” bonded to a glass substrate, it tends to break and peel off under strong external forces, especially when getting thin (<20µm). Therefore, grinding with a standard hard disk cannot be applied to our sample below a certain “critical” thickness. (3) The mechanical grinding/polishing creates an “optical dead layer” at the ZnO surface, which does not emit light. In older to solve this last problem, the eventual grinding step would need to be terminated by some chemical etching/cleaning.

From the previous considerations, based on numerous tests, we finally decided to combine grinding, polishing and chemical etching in a certain order as to exploit their relative advantages. The final procedure, as applied on an O-face ZnO sample, is described as follows:

(1) Hard grinding. Starting from the structure of Figure 4.1**b**, the ZnO substrate is mechanically grinded with a hard polishing disk (with polishing grinds going from 30µm to 3µm in size) down to a thickness of ~20-30µm. Usually, this thickness can be easily reached by standard grinding steps, with small risk to break or over-grind the sample.

---

[1] H_2SO_4 has a 96% concentration while H_2O_2 has 30%, which are standard values for commercially available products.

(2) Wet chemical etching. After step (1), we have a ~20-30µm thick ZnO layer on top of a HfO2/SiO_2 DBR bonded onto a glass substrate. This structure is immersed into the etchant H_2SO_4:H_2O_2:H_2O = 1:1:6, which etches only ZnO and does not affect the underlying HfO_2/SiO_2 DBR. Frequently, due to the combined effect of an inhomogeneous etching and an initial thickness gradient, induced by the mechanical grinding step, on one area of the sample the ZnO layer is completely removed and the underlying DBR exposed, while on the other parts the ZnO layer still covers the surface, as shown in Figure 4.2**a** . The exposed DBR, not affected by the etchant, has an extremely smooth surface, at optical wavelengths, while the ZnO layer presents a very rough surface covered with hexagonal pillars and pyramids, as shown in Figure 4.2**b**. This difference in surface roughness can be clearly identified by naked eye during the etching, providing a practical way to confirm the ZnO zero-thickness level and thereby to avoid over- or under-etching of the sample. Usually, the remaining ZnO layer has a thickness variation from 0 to ~8µm in a 3×3mm^2 region (2.6nm/µm), which needs to be further reduced.

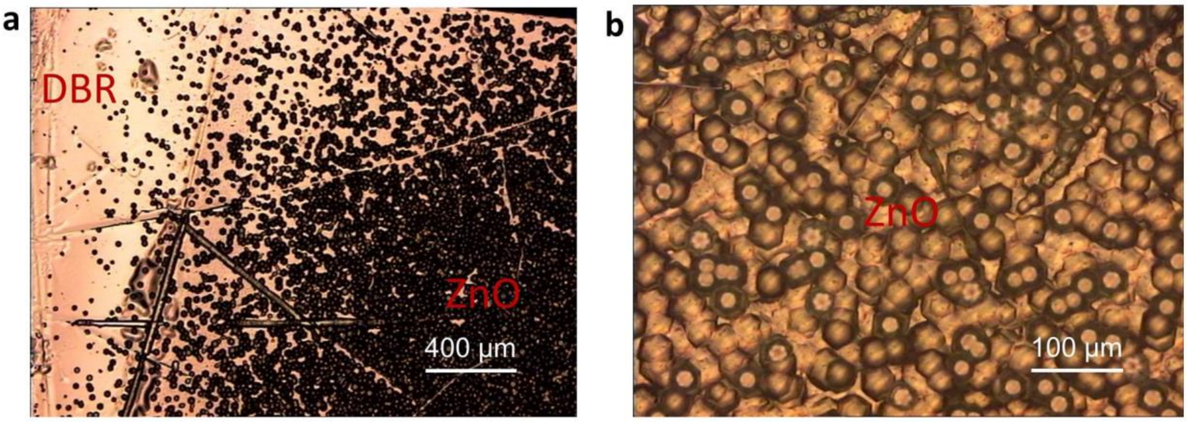

Figure 4.2: Optical microscope images of the sample surface after wet chemical etching. The ZnO is etched from the O-face. **a**. Lower magnification view showing the areas of the exposed DBR and the remaining ZnO. **b**. Higher magnification view on the area of the remaining ZnO.

(3) Hard polishing. The sample shown in Figure 4.2 goes through another grinding/polishing process using hard disks with smaller polishing grinds (typically 3 µm to 1µm). The aim of this step is to further reduce the ZnO thickness, the thickness gradient, and the surface roughness. The hexagonal pillars and pyramids are continuously grinded during the polishing and finally vanish, resulting in a recovery of the smooth surface as before the chemical etching. The hard polishing must be then stopped to avoid over-grinding and peeling-off of the ZnO layer, which is already thinned down to 0~3µm at the end of this step.

(4) Soft polishing. The purpose of this step is to further decrease the ZnO thickness while simultaneously reducing the thickness gradient. The polishing diamonds have a diameter of 0.25µm, which further reduces the ZnO surface roughness to ~1.5nm, as shown in Figure 4.3**b**. This process is usually applied in TEM for smoothing the surface, rather than removing materials, and reduces the layer thickness extremely slowly (it may take weeks to remove a few microns of ZnO). Despite its slowness, its advantages are obvious. First of all, such a slow speed makes it almost impossible to

over-polish the sample. Furthermore, when the remaining ZnO layer thickness is in the order of optical wavelengths, color fringes due to interference can be observed under optical microscope, as shown in Figure 4.3**a**. This allows to estimate the thickness gradient, which can be further reduced if necessary by soft polishing. The total area of the remaining ZnO on the sample may seriously shrink, leaving some areas with nothing but the glass substrate (e.g. dark regions in Figure 4.3**a**).

(5) Chemical-mechanical polishing. The thinning process needs to be terminated by a chemical process that effectively removes the "optical dead layer" induced by the last polishing step, and simultaneously reduces the surface roughness. For this purpose, we use colloidal silica (also referred as "SYTON" by its trademark) to further polish the sample. The silica particles are ~20nm in diameter and lead to a smooth polished surface. Moreover, the diluted colloidal silica is slightly base-like and reacts with ZnO, enabling a combined chemical-mechanical process. The final surface is presented in Figure 4.3**c**. Although the optical microscopy image (Figure 4.3**a**) looks the same as the surface obtained after Step (4), atomic force microscopy (AFM) images (Figure 4.3**b** and **c**) demonstrate undoubtedly an improved surface smoothness by the final polishing.

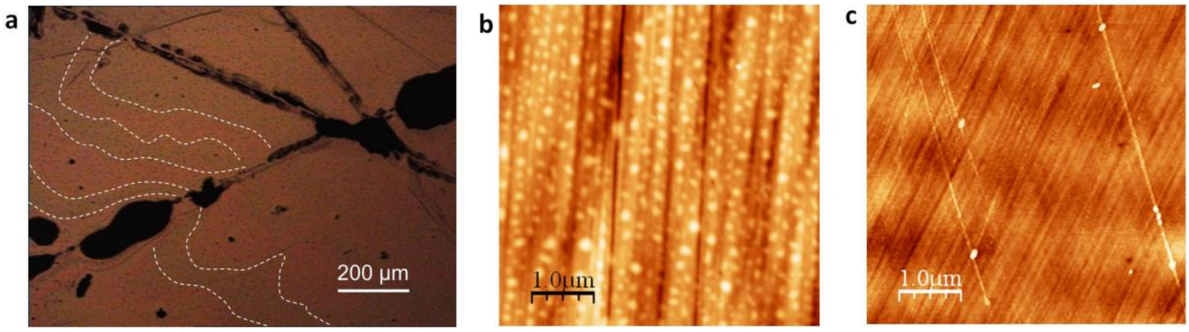

Figure 4.3: **a**. Optical microscopy image of the ZnO surface after the final polishing. White dashed lines are drawn parallel to the color fringes for enhancing visibility. **b**. Atomic force microscopy (AFM) image of ZnO surface after Step (4), exhibiting a room-mean-square (RMS) roughness ~1.5nm. **c**. AFM image of the ZnO surface corresponding to **a**, exhibiting RMS roughness ~5Å.

4.2 Optical spectroscopy: Fourier imaging and excitation sources

In order to characterize the optical properties of the microcavity, we need to monitor the angular dispersion of the sample emission, which is well achieved by a Fourier imaging technique [58] . The basic principle of Fourier imaging is illustrated in Figure 4.4**a**. All the light beams emitted from the sample ("real space") with at an angle θ are focused onto one point located at a distance $f\tan\theta$ from the center O' in the lens' focal plane; this means that each point in the lens' focal plane corresponds to a specific emission angle on the sample. Therefore, the lens/objective in the microscope set-up enables to Fourier transform the real space (x,y), into the momentum space (k_x,k_y), thereby enabling to study the emission angular distribution. Our experimental setup, adapted for both real space and Fourier imaging, is illustrated in Figure 4.4**b**. It should be noted that other configurations are also possible [165]. In this setup, Lens 1 is called the Fourier plane lens, which can be removed and inserted freely from/into the optical path. When Lens 1 is removed from the system, the objective images the sample to infinity, which is again imaged by Lens 2 at the entrance of the spectrometer, making the setup a real-space imaging system. When Lens 1 is inserted into the system, it images the focal plane of the objective, namely the momentum space of the sample emission, to infinity, which is then imaged by Lens 2 at the entrance of the spectrometer. In this case the setup becomes a Fourier imaging system. The image is subsequently dispersed by a spectrometer and detected by a two-dimensional CCD array. The spectrometer resolves the wavelength along the x-direction, leaving the y-direction unaffected. Therefore the CCD detects the wavelength λ in the x-dimension and the spatial coordinate in the y-dimension, displaying (λ, y) in the case of real-space imaging, and (λ, k_y) in the case of Fourier-space imaging. (λ, k_y) is equivalent to (E, θ) , which is the cavity or polariton angular dispersion that we need to acquire.

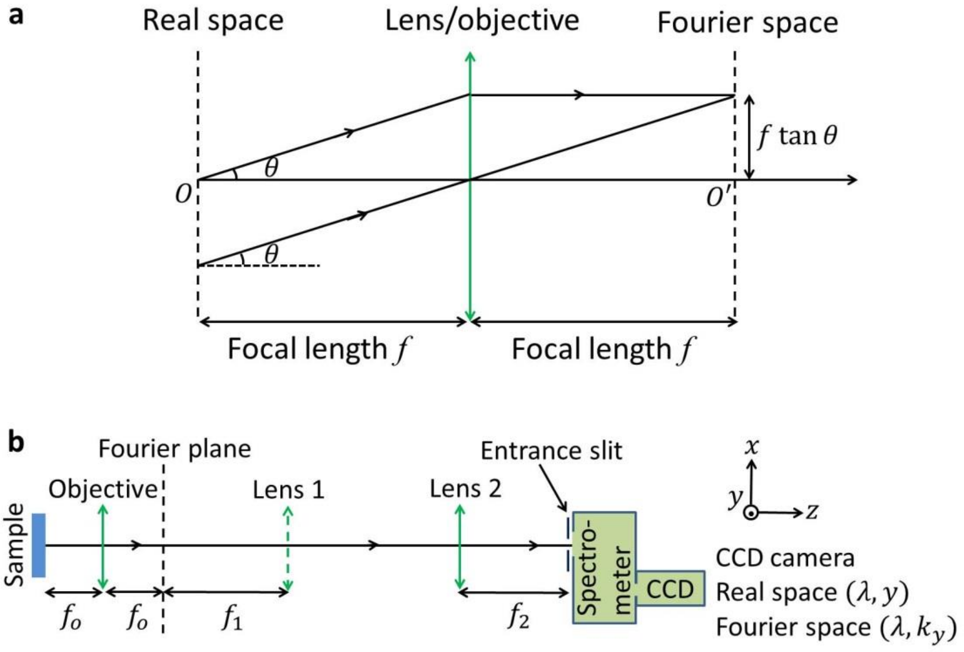

Figure 4.4: Illustration of the Fourier imaging technique. **a**. Basic principles of Fourier imaging. **b**. Experimental setup used for Fourier imaging. Lens 1 is a removable lens for exchange between real and Fourier spaces. f_o, f_1 and f_2 refer to the focal lengths of the Objective, Lens 1 and Lens 2 respectively. The axes of x, y and z referred to in the main text are labeled.

Most often the microcavities described in this thesis were characterized within a micro-photoluminescence (µPL) setup. The imaging and detecting parts of the µPL setup are the same as the system introduced above, where the microscope objective has a numerical aperture of 0.4. For the excitation we have used two different schemes. At Institut Pascal, the sample is excited using 130fs laser pulses (central wavelength of 266 nm and repetition rate of 76 MHz), obtained by tripling the frequency of a mode-locked Ti:Al_2O_3 laser. At Laboratoire Charles Coulomb (L2C), the sample is under quasi-continuous excitation with a 266 nm Nd:YAG laser (repetition rate 4kHz and pulse duration 400ps). In both cases, the excitation spot can be focused to a size of ~2µm by the microscope objective.

The real-space and Fourier imaging measurements that will be described in the next sections and in the next chapter were carried out in collaboration with L. Orosz and F. Reveret, in the team of Prof. Joel Leymarie (Institut Pascal), and with O. Kammoun, R. Hahe, C. Brimont and T. Guillet, in the team of T. Guillet (Laboratoire Charles Coulomb), during several stays financed by the EU under the CLERMONT4 project (Coordinator: Prof. Alexey Kavokin).

4.3 Morphological and optical properties

In this section we will show the characterization of the HfO_2/SiO_2 DBR, the single-crystalline ZnO substrate, and the fabricated microcavity.

4.3.1 HfO_2/SiO_2 DBR

The deposition technique of dielectric HfO_2/SiO_2 DBRs has been developed in CNRS-LPN by the team of S. Bouchoule during the last years, enabling very abrupt interfaces between the two materials (Figure 4.5**a**). Furthermore, *in-situ* measurement of the layers' refractive indices can be performed during the deposition process, guaranteeing the correct thickness of each layer. As a consequence, a reference HfO_2/SiO_2 DBR deposited on Si exhibits a surface roughness of ~5Å, a high reflectivity, and a stop band width of ~700meV (FWHM: full-width-half-maximum), as shown in Figure 4.5**b** and **c**.

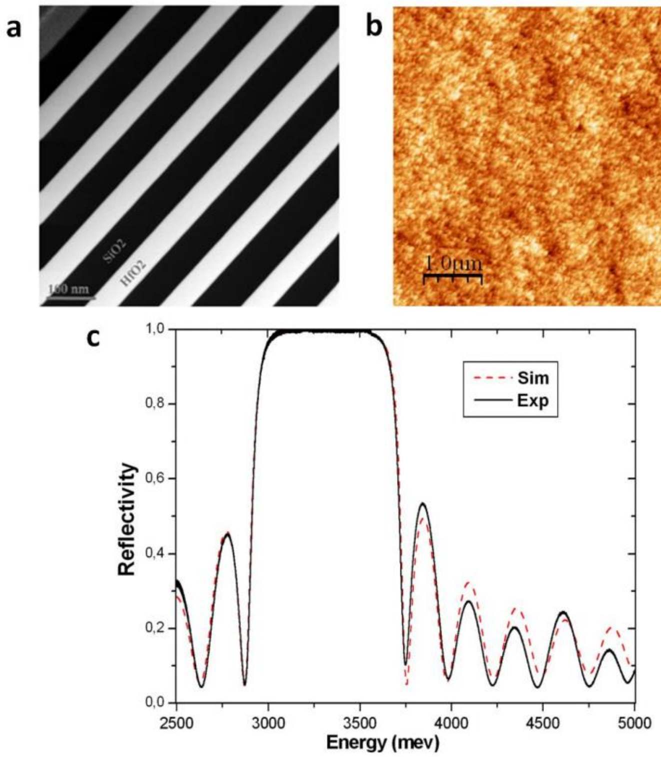

Figure 4.5: Properties of the HfO_2/SiO_2 DBR. **a**. Scanning transmission electron microscopy image of the DBR cross-section. **b**. 5×5µm^2 AFM image of the DBR surface, showing RMS roughness of ~7Å. **c**. Reflectivity measurement of the DBR (black solid) with the corresponding transfer-matrix simulations (red dashed), showing a stop band width of ~700meV.

4.3.2 ZnO substrate

Commercially-available ZnO substrates are purchased by CNRS-CRHEA from CRYSTEC [166] for studying the homoepitaxial growth of ZnO-based heterostructures. As they are also used as the active material in our microcavities, it is important to confirm its good morphological and optical properties.

The surface, as inspected by atomic force microscopy, displays atomic terraces ~250nm wide (although the exact terrace width depends on the actual miscut of the substrate), and exhibits a RMS roughness of 1.3Å, in a 5×5µm^2 area, as shown in Figure 4.6.

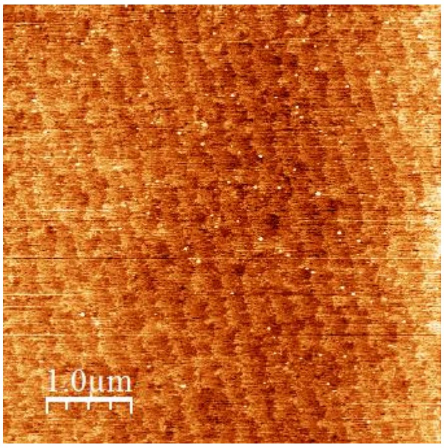

Figure 4.6: 5×5µm^2 AFM image of the Zn-ZnO substrate surface, showing a surface roughness (RMS) of 1.3Å.

The optical properties of the as-received substrate were investigated by temperature-dependent photoluminescence. The measurements are shown in Figure 4.7. While numerous PL features can be observed at low temperature (Figure 4.7**a**), most of them vanish at higher temperature (~150K) suggesting donor- and/or acceptor-bound excitons. We can identify the origin of most of these emission features by comparing with previous studies (Figure 1.3) [55]; their origin is labeled in Figure 4.7**a** and **b**: free exciton (FX), donor-bound excitons (D^0X), first and second LO-phonon replicas of free excitons (FX-LO and FX-2LO, respectively), donor-bound exciton phonon replicas (D^0X-LO), two-electron-satellite transitions (TES), and donor-acceptor-pair (DAP) transitions, which have been introduced in 1.4. At low temperature (10K), three donor-bound excitons can be identified. When increasing the temperature, bound excitons get ionized due to thermal activation and free excitons dominate the emission spectra. The free-exciton energy redshifts, due to the thermal-induced shrinking of the bandgap, and ends up at about ~3.3eV at room temperature, as shown in Figure 4.7**c**. The temperature-dependent free-exciton energy can be fitted with Varshni's law using $\alpha=1.4\times10^{-3}$eV/K and $\beta=1273.5$K. The integrated emission intensity experiences a decay with increasing temperature (Figure 4.7**d**) due to enhanced non-radiative recombination. The bound-exciton linewidth at low temperature is below 1meV, indicating excellent material quality. The free-exciton linewidth, initially below 3meV at low temperature, increases with rising temperature due to interaction with phonons, reaching an FWHM of ~50meV (Figure

4.7**e**) at 300K, in good agreement with the studies from Klingshirn *et al* (Figure 4.7**f**) [65]. It should be noted that the FWHM is obtained by fitting the free exciton and its phonon replicas (mainly FX-LO) into separate peaks, which which are well resolved only at low and intermediate temperatures.

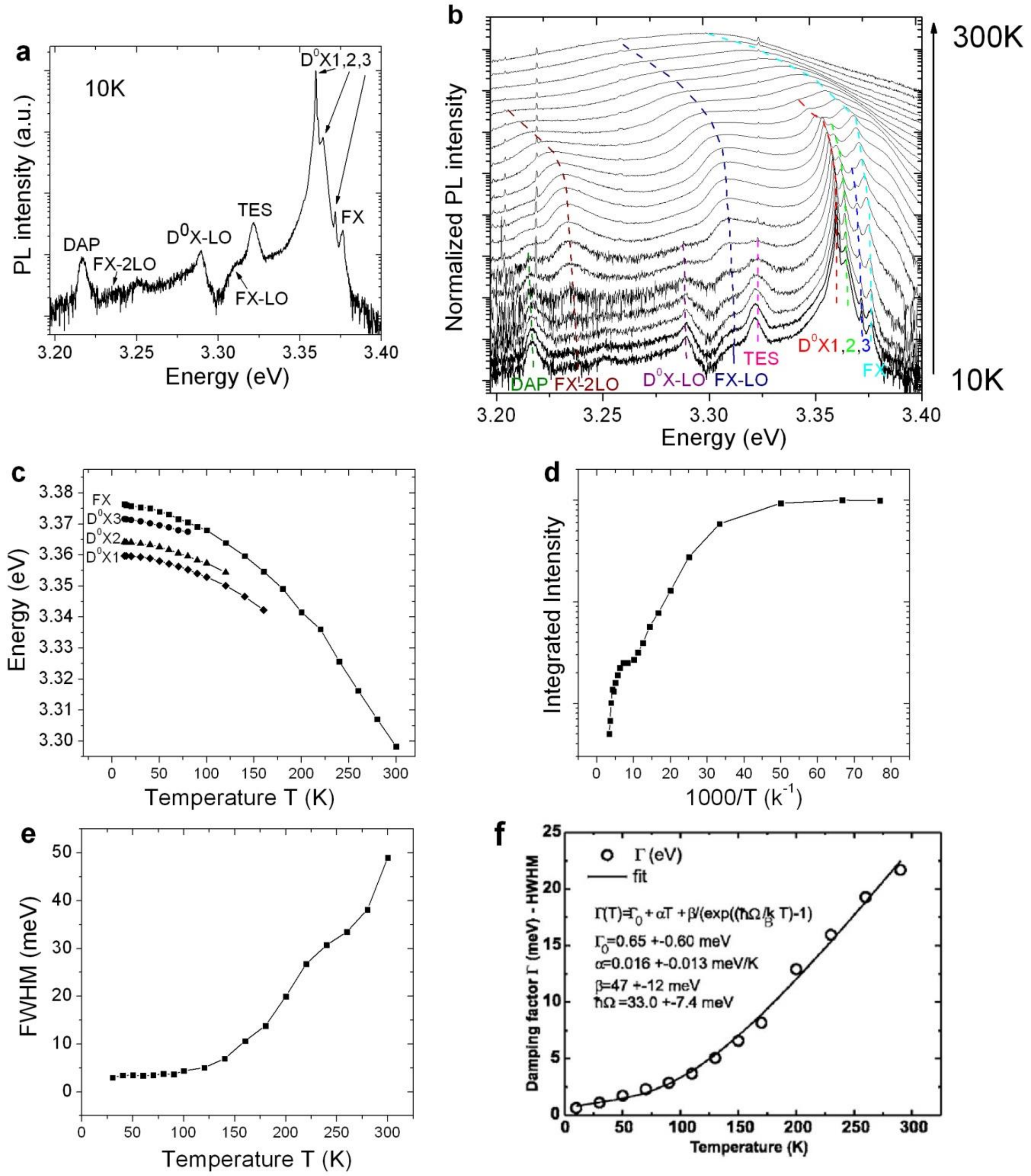

Figure 4.7: Optical properties of a Zn-face ZnO substrate. **a**. Photoluminescence at 10K with typical emission features labeled. **b**. Temperature dependent spectra from 10K to 300K. From bottom to top: 10K, 15K, 20K to 100K -with 10K intervals-, 120K to 300K -with 20K intervals-. Typical emission features are connected by dashed lines with different colors. See the main text for their identification **c**. Energy vs. temperature of the A-free exciton (FX) and the three donor-bound excitons (D^0X1 to 3). **d**. Integrated intensity of the near-bandgap region as a function of 1000/temperature. **e**. Spectral linewidth (FWHM) of the free-exciton emission as a function of temperature. **f**. Extracted from Reference [65]: spectral linewidth (HWHM) of the free-exciton emission as a function of temperature. Note that the linewidth is expressed in full-width-half-maximum in **e** but half-width-half-maximum in **f**.

4.3.3 The fabricated cavity

The completed microcavity exhibits typically a surface roughness of ~1nm, as shown in Figure 4.8.

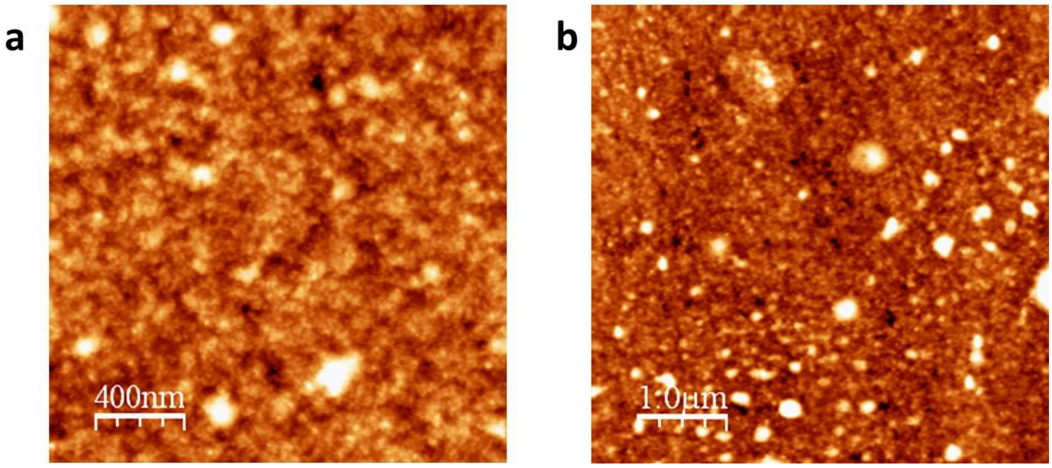

Figure 4.8: AFM images of the completed microcavity. **a**. 2×2µm^2 image displaying a roughness of 0.89nm. **b**. 5×5µm^2 image displaying a RMS roughness of 1.26nm.

According to our design, the fabricated microcavity should benefit from the good photonic properties of the fully-hybrid structure, as well as the good excitonic qualities inherited from the ZnO substrate. Moreover, the naturally formed thickness gradient should allow to access a large range of exciton-photon detunings. The next paragraphs will illustrate all these three points.

Cavity-thickness gradient

During the fabrication process, the ZnO active layer is inhomogeneously polished/etched and a thickness gradient is naturally formed. While most epitaxial microcavities are forced to display a thickness gradient, typically by stopping the rotation of the sample during MBE or MOVPE growth, the resulting thickness gradient is in the order of several nanometers across the whole 2” wafer. The thickness gradient observed in our microcavity shows two main differences compared to “conventional epitaxial” microcavities: first, the thickness gradient is not symmetric with respect to any reference direction (e.g. in MBE, the thickness gradient direction is determined by the geometry of the Knudsen cells with respect to the sample), and second, the absolute thickness gradient can attain locally much larger values (ten or even hundred times larger).

While a large and inhomogeneous thickness gradient, illustrated in Figure 4.9 for a certain in-plane direction on the sample, leads to undesired effects, such as photonic inhomogeneous broadening, it can also provide interesting properties and configurations:

1. It allows to study within one single sample a complete set of detunings, going from extremely negative to extremely positive (e.g. for the polariton condensation phase

diagram it was possible to have detunings from about -200meV to about 400meV, i.e. from $-\Omega_{Rabi}$ to about $+2\Omega_{Rabi}$).

2. It allows to study cavities displaying exactly the same mirrors but different active regions, e.g. λ-cavity vs. 3λ-cavity. In particular, it allows to study single-mode cavities but also multimode cavities where the relative position of the modes can be finely tuned.
3. Numerous polariton landscapes can be explored: these might be used to strongly accelerate a polariton condensate, such as in the region around x=25μm in Figure 4.9, where the LPB shift is in the order of 7.5meV/μm, or rather trap it, as in the natural real-space trap formed around x=175μm in the same figure.

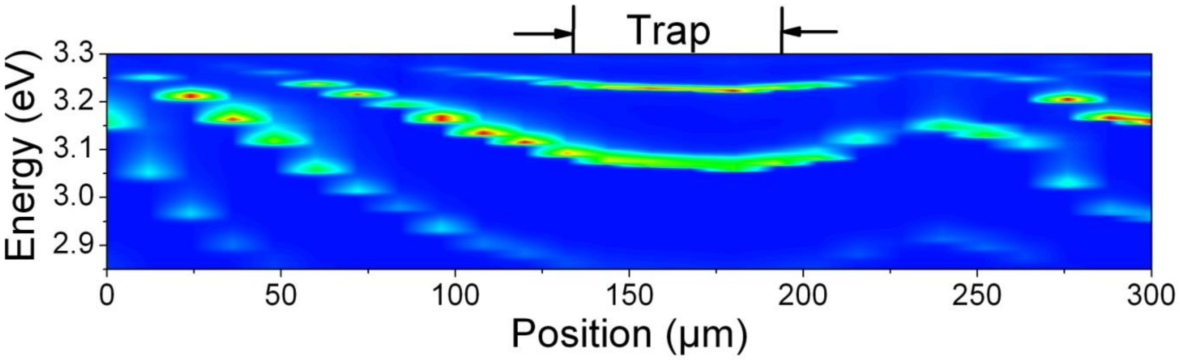

Figure 4.9: Energy vs. position mapping along a certain in-plane direction. The measurements are performed with fs excitation and by measuring a series of spots (12μm interval) along the thickness gradient.

While some examples of what can be done with such a rich *palette* will be given in the current work, many others (e.g. polariton condensate propagation) are still under investigation.

The *Q*-factor

The simulated reflectivity and the associated electric field distribution, at the cavity wavelength, for an empty[1] λ-cavity with the same DBRs as deposited in the fully-hybrid cavity, are shown in Figure 4.10. The cavity is designed to be in resonance at $\bar{E}$=3.3eV, as the models used in Chapter 2. The refractive index of HfO_2 and SiO_2 are taken from the experimentally measured values at Institut Pascal by spectroscopic ellipsometry. The calculation yields a *Q*-factor of ~8500, while the cavity mode energy is shifted by 0.9meV compared to the designed value (3.3eV), due to the phase shift induced by the Al layer, which was not considered in chapter 2 and that we now take into account to simulate the real cavity structure.

---

[1] empty means that we assume a constant refractive index without excitons for the active region

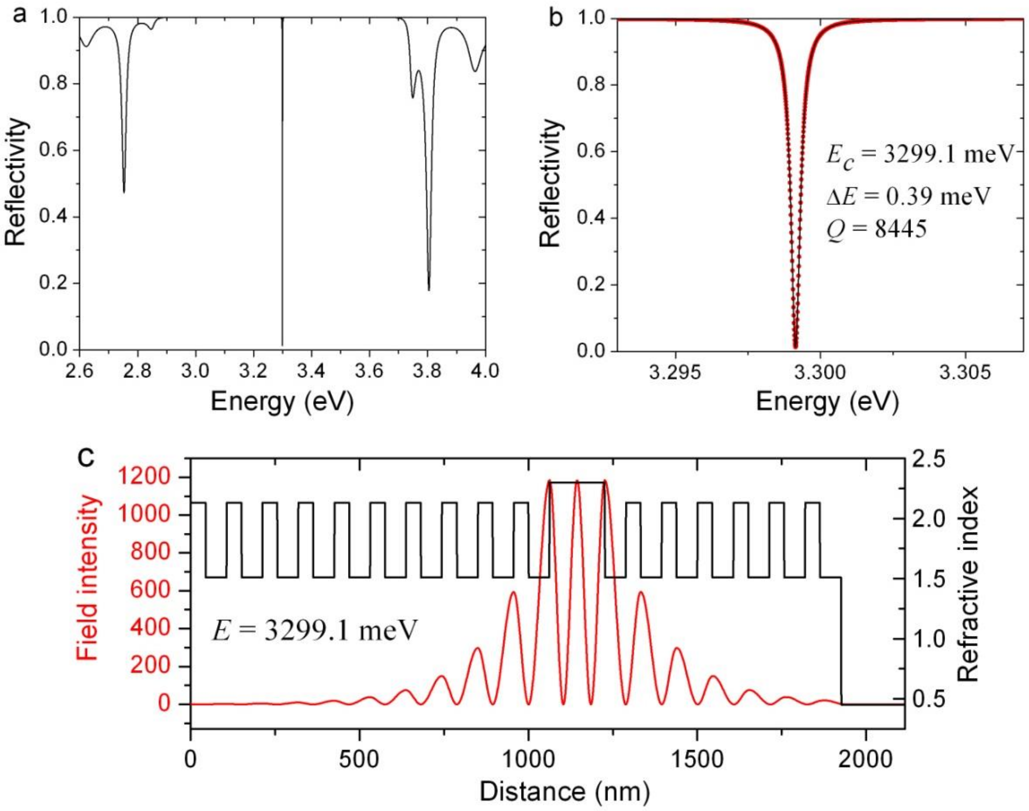

Figure 4.10: Transfer matrix simulation of a λ-cavity as fabricated using the etching technique: **a**. calculated reflectivity, **b**. a detailed look of the cavity mode, allowing to calculate the Q-factor, and **c**. calculated optical field distribution of the cavity mode. Light is incident from the left side, at zero angle, and has an intensity of 1.

An experimentally measured μPL spectrum at room temperature is shown in Figure 4.11**a**, with the corresponding Fourier image. At this spot the cavity-exciton detuning is -20meV. Since the Rabi splitting in this cavity varies typically from 180meV to 260meV, depending on the exact location (as will be discussed later), this detuning can be considered close to zero and, therefore, corresponds to a photonic (excitonic) content of ~50%. The measured FWHM is 1.2meV. If the photonic content were 100%, this would mean a *Q*-factor of ~2600. However, due to the strong exciton-photon coupling this linewidth has a double contribution, one being determined by the exciton homogenous broadening and the second one being purely of photonic origin, as discussed in Chapter 3. Although the ZnO exciton linewidth at room temperature is about ~50meV, under certain circumstances its contribution to the polariton linewidth might be much smaller. Trichet *et al* [151] studied experimentally and theoretically this feature and concluded that when the exciton-photon coupling is much stronger than the exciton-phonon coupling (i.e. if Ω_{Rabi}>E_{LO} and the detuning is such that Ex-E_{LPB}>E_{LO}), the phonon-induced broadening contributing to the LPB linewidth is much smaller than if these conditions are not fulfilled. In their article, the authors estimated an exciton-induced broadening at room temperature of ~1meV theoretically, and 2-3meV experimentally, for a 47% excitonic fraction polariton (a situation very close to ours in terms of δ), which needs to be considered for obtaining the intrinsic *Q* of the cavity from the measurement shown in Figure 4.11**a**. Thus, since the exact contribution of the exciton-induced broadening is not quantitatively clear, we have plotted in Figure 4.11**b** the calculated LPB linewidth, at zero detuning, as a function of the cold cavity Q for a series of exciton-induced broadenings (from 0.5 to 3meV). The experimental LPB linewidth in Figure 4.11**a** is plotted as the thick horizontal line, whose cross-points with the other lines indicate the confident range of Q-factors actually displayed by our cavity. By assuming an exciton-induced broadening of 1-2meV, we estimate a Q-factor between 2300 and 8200.

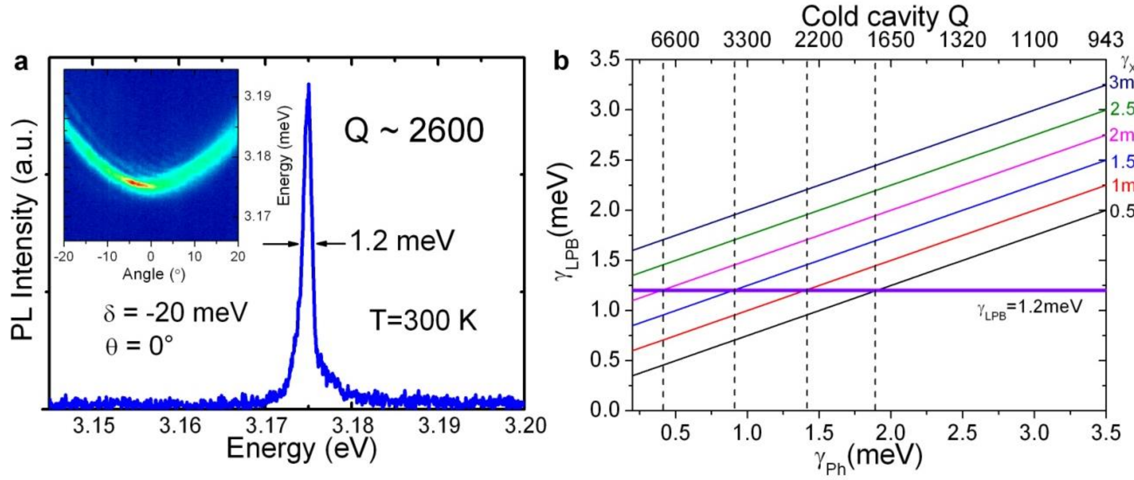

Figure 4.11: **a**. μPL spectrum measured at an angle of 0° and T = 300 K below the polariton lasing threshold. The inset shows the corresponding Fourier space image. **b**. Calculated LPB linewidth γ_{LPB} at zero detuning as a function of the cold cavity Q (cavity photon linewidth γ_{Ph}) with different exciton-induced broadenings γ_X ranging from 0.5 to 3meV. The thick horizontal line represents γ_{LPB}=1.2meV as measured in **a**.

Equally important is the fact that the observed angular dispersion may actually consist of several overlapping adjacent polariton modes, caused by the fabrication-induced thickness gradient and that cannot be resolved individually. Thus, even if the micro-PL measurements were performed with an excitation spot size of 2 μm, an inhomogeneous peak broadening of photonic origin might still be present and, therefore, should be considered in the analysis of the “intrinsic” Q. Such adjacent LPB modes can be figured out from the Fourier space image in Figure 4.11**a**, although they cannot be used to extract a reliable measurement of the modes linewidth. The situation changes drastically as soon as we cross the polariton lasing threshold (which will be discussed in the next chapter). Indeed, at 5K and just slightly above the lasing threshold, when the fraction of polaritons in the condensed state is sufficiently low to still allow observation of the dispersion of the uncondensed polaritons, a reliable linewidth measurement of such adjacent LPBs can be done (see Figure 4.12**a** and **b**). While the condensed polaritons, at 3.309eV, are dispersionless, the uncondensed polaritons are still distributed along a dispersive curve. This series of discrete uncondensed polariton modes, which display equivalent dispersions but at slightly different energies, can be easily distinguished in Figure 4.12**a**. From their linewidths, we estimate an intrinsic cavity Q in the order of 3000-4000, as labeled in Figure 4.12**b**; again, an excitonic contribution masks the intrinsic Q of the cavity. Compared to the situation illustrated in Figure 4.11**a**, it is difficult to assess whether the excitonic contribution is larger or smaller, since in this case two effects might counteract each other: on the one hand the detuning is more positive, thereby increasing the excitonic contribution, while on the other hand the temperature and, the associated phonon broadening, is smaller. Nevertheless if we consider an exciton-induced broadening of ~1meV at 5K [64], a similar analysis as in Figure 4.11**b** still reveals an *Q*-factor range of several thousands.

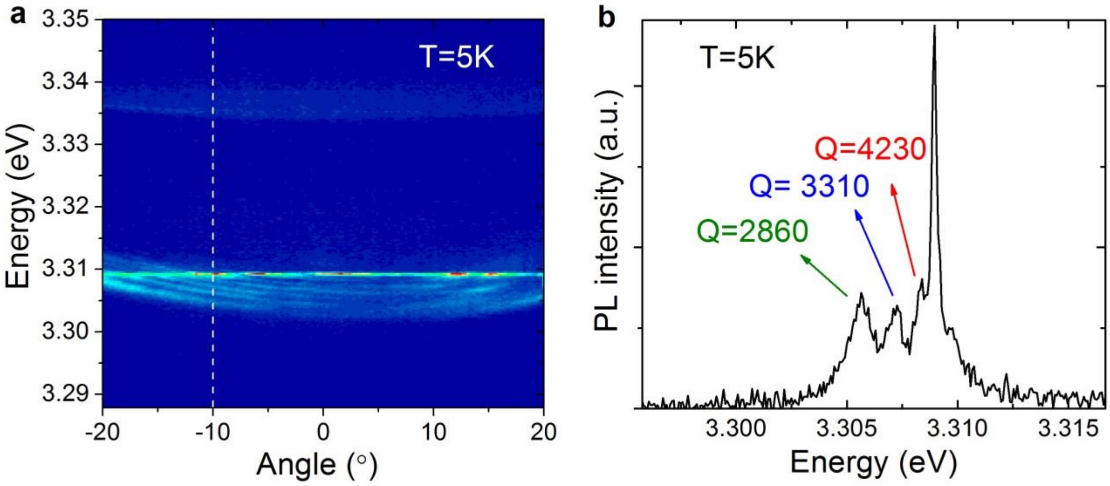

Figure 4.12: **a.** Fourier space image of the polariton emission just above the lasing threshold at 5K, with both condensed and uncondensed polariton dispersions observable. **b**. Spectrum extracted from **a**, at an angle of -10° (while dashed line), and Qs associated to each mode.

4.4 Demonstration of the strong coupling regime

Due to the very large exciton oscillator strengths in ZnO, microcavities based on this material family should be able to exhibit extremely large vacuum Rabi splittings (exceeding 200meV). This was already evidenced in the ZnO-microwire literature [151], where an almost perfect (i.e. 100%) overlap between the electric field and the excitons, mandatory for realizing large Rabi splittings, was obtained. This large overlap was guaranteed by the use of whispering gallery modes, for which the tunneling of the electromagnetic field into air is negligible. In our microcavity, the good overlap is provided by the large refractive index difference between the two dielectric materials used in the DBRs.

Unfortunately, from the characterization point of view such large Rabi splittings lead to a number of difficulties in demonstrating the strong-coupling regime both in photoluminescence and in reflectivity: in the first case the UPB is not thermally populated, not even at room temperature ($\Omega_{Rabi}/2>>k_BT$), while in the second case the UPB is strongly absorbed due to a resonance energy far above the ZnO band gap [17,73]. Thus, since only the lower polariton branch can be detected, it is neither possible to observe the anti-crossing between the polariton branches, which is the footprint of the strong-coupling regime, nor to measure directly the Rabi splitting.

Thus, further experimental features appearing due to the strong-coupling regime need to be assessed to determine whether the microcavity operates, or not, in this regime. The experimental evidences are:

(1) *The evolution of the LPB energy with ZnO thickness*. First, as can be seen in Figure 4.13, the LPBs never cross, not even approach, the exciton dispersion (white solid line), while in principle they might if the cavity operated in the weak-coupling regime. Second, and most important, the curvature of the LPB is strongly distorted from the bare cavity mode, as simulated taking into account the ZnO refractive index and removing the excitonic contribution, when approaching the exciton energy. This is a clear effect related to the strong exciton-photon coupling. This last feature was previously used to demonstrate the strong coupling in ZnO microwire cavities [38].

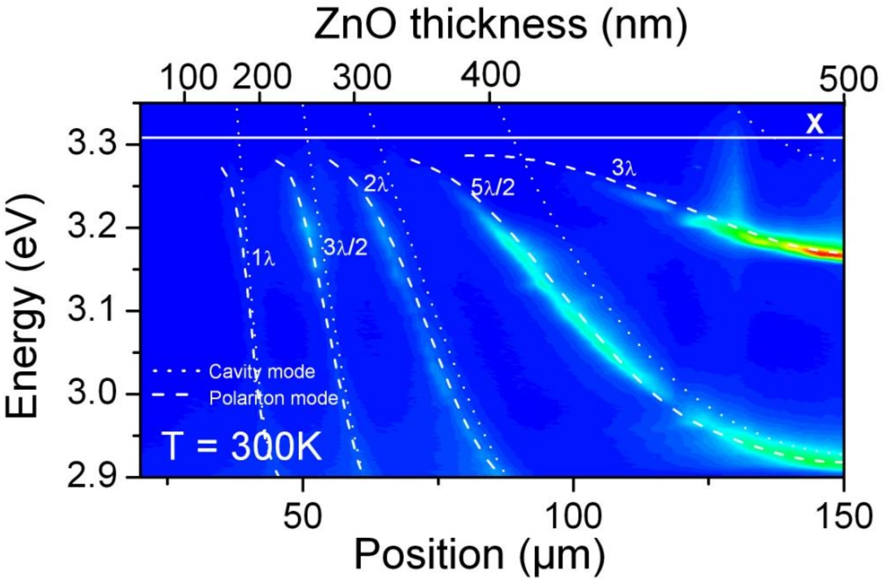

Figure 4.13: Spectra vs. position on a region with ZnO thickness gradient. The measurement is performed with quasi-continuous excitation and by moving continuously along the thickness gradient. Five LPBs are observed when the cavity thickness changes from λ to 3λ, where λ is the wavelength corresponding to the excitonic resonance (shown in solid line). The dashed (resp. dotted) lines show the calculated dispersion of the LPB (resp. bare cavity modes).

(2) *The angular dispersion of the LPB at different exciton-photon detunings*. By tilting the sample, the angle-resolved emission can be followed up to about 47° (we recall that the NA of the microscope objective employed is 0.4). The dispersions thus measured are shown in Figure 4.14, with **a**, **b**, **c** and **d** corresponding to exciton-photon detunings of about +155meV, +130meV, +70meV and -80meV, respectively (if we assume that the microcavity operates in the strong-coupling regime). The curvature of the LPB modes, i.e. $\frac{d^2E}{dk_{\parallel}^2}$, is greatly reduced when approaching the exciton energy, indicating a dramatic increase of the polariton effective mass due to the increasing exciton content.

(3) *The linewidth of the LPB at different exciton-photon detunings*. If we assume that the Q-factor does not vary "*much*" from point to point, then the strong linewidth increase as the LPB approaches the exciton resonance can be considered as a further proof of the strong-coupling regime, since this broadening could then be understood as an increasing contribution of the excitonic broadening (at room temperature) to the LPB linewidth.

(4) <u>*Phenomenology above the lasing/condensation threshold*</u>. The phenomenology observed above the nonlinear emission threshold, which will be described in the next chapter, can be consistently and "*easily*" explained if the strong-coupling regime is assumed.

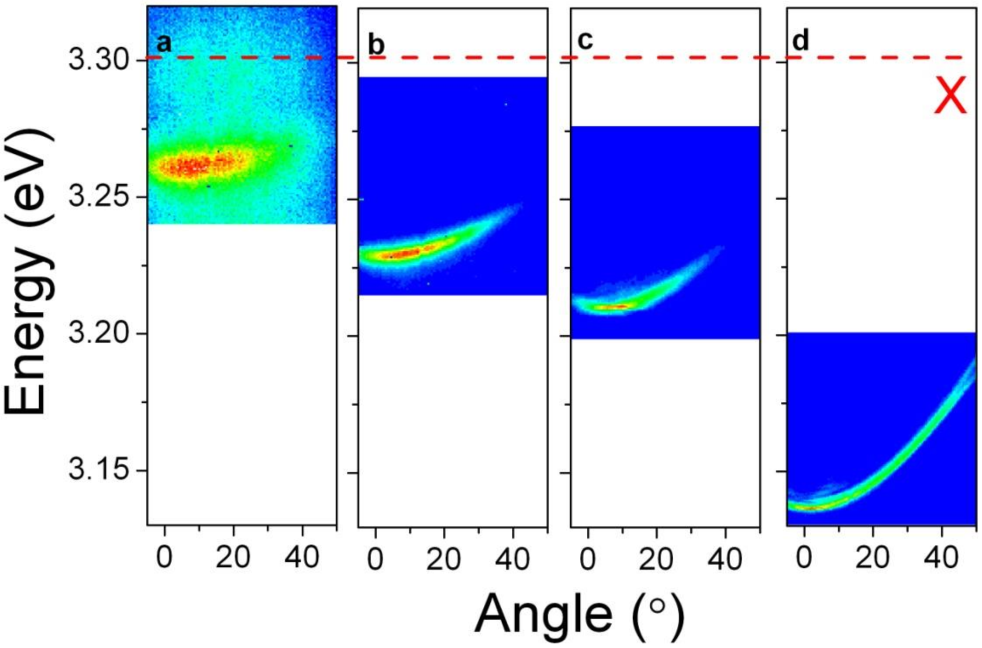

Figure 4.14: Fourier images measured at room temperature showing angular dispersions up to 50° for detunings of +155meV (**a**), +130meV(**b**), +70meV(**c**) and -80meV(**d**). The LPB linewidths measured at zero angle are 14.7meV (**a**), 7.3meV (**b**), 3.0meV(**c**) and 1.6meV (**d**).

Rabi splitting determination

In order to determine the value of the Rabi splitting as a function of the ZnO active layer thickness, a combination of transfer-matrix simulation and a coupled-oscillator model was used to simulate the "dispersions"[1] measured experimentally, such as in Figure 4.13. These calculations were carried out at Institut Pascal by L. Orosz. For the simulations we considered as known inputs the ZnO material parameters (namely its refractive index and exciton oscillator strengths), which were determined by ellipsometry, continuous-wave and autocorrelation measurements in bulk ZnO substrates [64].

The thickness for each position is obtained by finding the ZnO thickness that best fits the position of all the LPBs present within the energy range explored and whose positions are given by transfer matrix simulation. Once the thickness has been determined, the Rabi splitting is calculated by artificially removing in the simulations the band-to-band ZnO absorption, and by calculating the minimum energy difference between the measured LPB and the calculated UPB[2].

---

[1] Strictly speaking energy vs. position are not dispersion curves.

[2] For a given thickness the Rabi splitting is calculated for the mode which is in resonance with the exciton.

The as-calculated Rabi splitting as a function of ZnO thickness is shown in Figure 4.15. It varies from 180meV to 260meV with increasing thickness, which can be understood by taking into account the fact that the thicker the active layer, the larger the L_c/L_{eff} ratio (see Equation 3.13 and Section 3.1.2) and, therefore, the larger the Rabi splitting. These huge Rabi splitting values are comparable to those of organic semiconductors [15,32] and indicate, similarly to the microwire case [38,151], an extremely large spatial exciton-photon overlap.

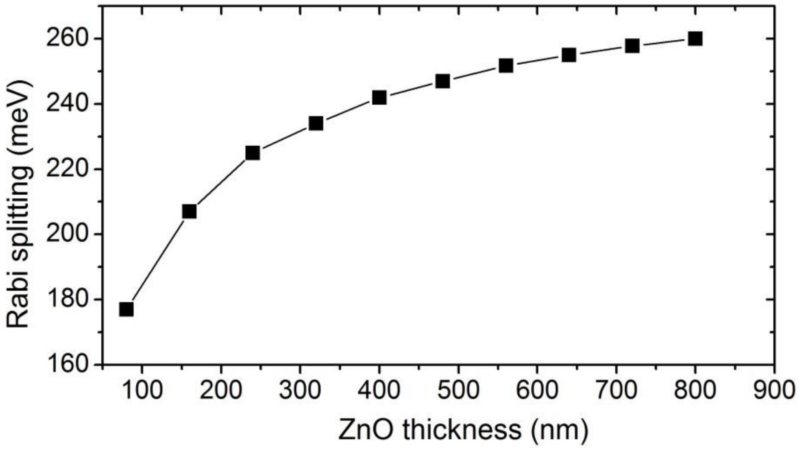

Figure 4.15: Estimated Rabi splitting versus ZnO thickness. The square symbols correspond to the actually calculated points, while the connecting line is a guide for the eyes.

4.5 Conclusion

In this chapter we discussed the fabrication as well as the morphological and linear optical properties of a completely new type of fully-hybrid ZnO microcavities, which combine the good material quality of ZnO substrates and the advantages of double dielectric UV-DBRs. The cavity operates in the strong coupling regime, displays a record Q-factor of several thousands and large Rabi splitting, comparable to those found in organic microcavities. Moreover, the large thickness gradient allows to access a large range of cavity thicknesses and, therefore, a large range of detunings.

Chapter 5 Polariton condensation in fully-hybrid ZnO microcavities

The fully-hybrid microcavity described in Chapter 4 is further studied by micro-photoluminescence to explore the possibility of achieving polariton condensation. On this cavity we demonstrate unambiguously room temperature polariton lasing, and determine the complete polariton condensation phase diagram for a ZnO microcavity for the first time. Furthermore, due to the large range of exciton/photon detunings that we have access to in this cavity, the exciton/photon fractions have been tuned from almost pure exciton-like to almost pure photon-like, enabling to dramatically modify the behavior and properties of the created polariton condensates.

5.1 Room temperature polariton lasing

The initial goal of this PhD thesis, i.e. to fabricate a ZnO polariton laser working at room temperature, has been achieved on this fully-hybrid ZnO microcavity.

Figure 5.1 shows angle-integrated (**a**) and angle-resolved (**b**, **c** and **d**) µ-PL spectra taken under quasi-continuous excitation, with various excitation powers, at an arbitrary position within the sample. At this position, the lower polariton branch (LPB) is located at about 3.184eV. Its angular dispersion can be fitted, as given by the dashed black lines in **b**, **c** and **d**, considering a Rabi splitting of about Ω_{Rabi}~230meV and a slightly negative detuning of (δ=-8meV). This implies that the bare cavity mode associated to this LPB is out of scale in Figure 5.1 **a**. Since the absolute δ value is small compared to the Rabi splitting ($|\delta|/\Omega_{Rabi}<5\%$), the studied LPB displays an almost 50% matter-50% light character. At low pumping power (Figure 5.1**b**) the LPB dispersion is well observed, with polaritons accumulating at ~15-20°. This means that the LPB lifetime is too short to enable polaritons to reach the energy minimum, at the bottom of the LPB, and results in a system out of thermal equilibrium.

If the pumping power is increased further, at 0.8 P_{Thr}, a certain number of polaritons start to accumulate at 0° at a dispersionless energy-level, blueshifted with respect to the LPB dispersion. Above threshold, a single sharp peak dominates the emission spectrum (thick blue line of Figure 5.1**a**) whose angular dispersion is completely flat. At a certain pumping power, the laser becomes multimode, as exemplified in the inset of Figure 5.1**a**. It is noteworthy that above threshold, the polariton condensate is mainly observed at wavevectors close to zero (and spanning a range from -10° and +10°, in Figure 5.1**d**), despite the small excitation spot employed. Indeed, experimental results by Richard *et al* [167], in a CdTe-based microcavity, by Franke *et al*, in a ZnO-based cavity [41], and by Wert *et al* [88], in a GaAs-based cavity, as well as theoretical studies by Wouters *et al* [115], showed that under "small" excitation conditions polaritons concentrate, in momentum space, at finite ±k wavevectors with $k\neq0$: this can be due either to emission from localized states in disordered structures (in the first and, most probably, the second experimental cases) or due to quasi-ballistic expansion of the polariton condensate (in the last experimental case). However, this feature is not observed in our room temperature measurements, where most polaritons concentrate around k=0 (though some appear at finite k, around ~20°). Several reasons can be invoked: primarily, the heavy polaritons used in the current study (~50% exciton fraction compared to ~23.5% in Reference [41]) exciton fraction), which leads to a reduced particle acceleration, and also the efficient energy relaxation at room-temperature by interaction with phonons. As a result, the repulsive potential induced by the exciton reservoir mainly broadens the k-space distribution of the condensate around k=0.

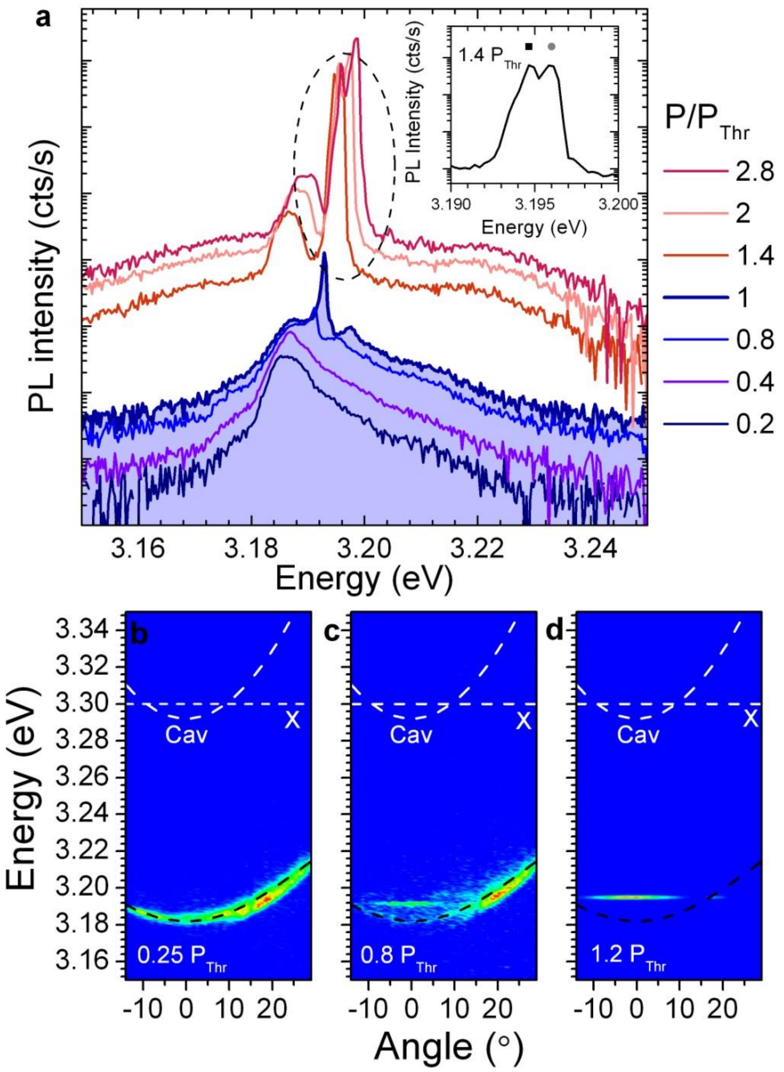

Figure 5.1 : Emission features of a fully-hybrid ZnO room-temperature polariton laser. **a**. Power dependent series of angle integrated µPL spectra measured at 300 K under quasi-continuous excitation. The excitation power relative to the threshold power is indicated for each spectrum, where P_{Thr} = 0.6 nJ/pulse is the polariton lasing threshold. Inset: a detailed view of the spectrum at $1.4P_{Thr}$ circled by the dashed line in **a**. The first (resp. second) lasing mode is labelled by black square (resp. grey circle). **b**, **c** and **d**: Fourier space images (in linear scale) of the microcavity emission measured at 300 K and at the same point as in **a**, under excitation power densities of $0.25P_{Thr}$ (**b**), $0.8P_{Thr}$ (**c**), and $1.2P_{Thr}$ (**d**). Dashed lines correspond to the simulated LPB (black), bare cavity (white, Cav) and exciton (white, X) dispersion curves. At this point the cavity optical thickness is 3λ, the Rabi splitting is 230meV and the detuning of the shown LPB is -8meV (see Figure 4.13 in Chapter 4).

The characteristics of the room temperature polariton lasing, extracted from Figure 5.1**a**, are presented in Figure 5.2. For the current position, the transition is accompanied by a nonlinear increase of the output power (Figure 5.2**a**) by a factor 620 for a 28% increase in the excitation power, and a reduction of the emission linewidth (Figure 5.2**b**) well below the bare cavity mode linewidth, a clear signature of the onset of temporal coherence. Indeed, the linewidth reduction as a function of pumping power allows to better define the polariton lasing threshold, as seen in Figure 5.2**a**, **b** and **c**. As discussed in 3.2.4, an extremely important aspect to ensure that the cavity still operates in the strong-coupling regime above the nonlinear threshold, *i.e.* with no transition into the weak-coupling one, is that the blueshift (Δ_{blue}) below threshold should be small compared to the actual Ω_{Rabi} and, especially, compared to the energy difference between the bare cavity mode and the LPB (107meV for the current position). In Figure 5.2**c** these ratios amount to $\Delta_{blue}/\Omega_{Rabi}$ ~6 meV/230 meV~3 % (at most 5 % for any of the studied detuning) and $\Delta_{blue}/(E_{Cav}-E_{LPB})$ ~ 6 %. These numbers ensure that lasing is occurring in the strong-coupling regime.

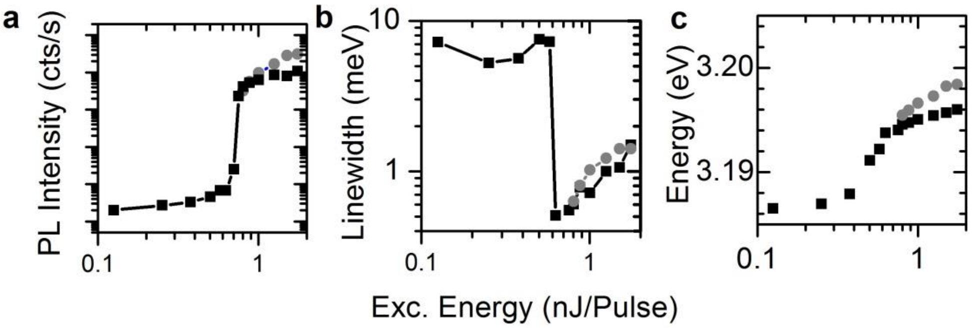

Figure 5.2: Room temperature polariton lasing characteristics extracted from Figure 5.1**a**: **a**. Integrated intensity, **b**. linewidth and **c**. energy of the LPB/first lasing mode (square) and second lasing mode (circle), as a function of the excitation power. Above threshold, the square and circle symbols correspond to the two lasing modes appearing in the inset of Figure 5.1**a**.

A comparison of the $\Delta_{blue}/(E_{Cav}-E_{LPB})$ ratios reported in the recent GaN and ZnO litterature is established in Figure 5.3. Besides this thesis, the only other ZnO microcavity that has been claimed to display room temperature polariton lasing, by Lai *et al* [42,43], reports a $\Delta_{blue}/(E_{Cav}-E_{LPB})$ ~ 37.5% which is ~6 times larger. The room temperature ZnO polariton laser reported in this chapter displays the smallest $\Delta_{blue}/(E_{Cav}-E_{LPB})$ ratio, comparable to the values reported by EPFL on GaN-based microcavities.

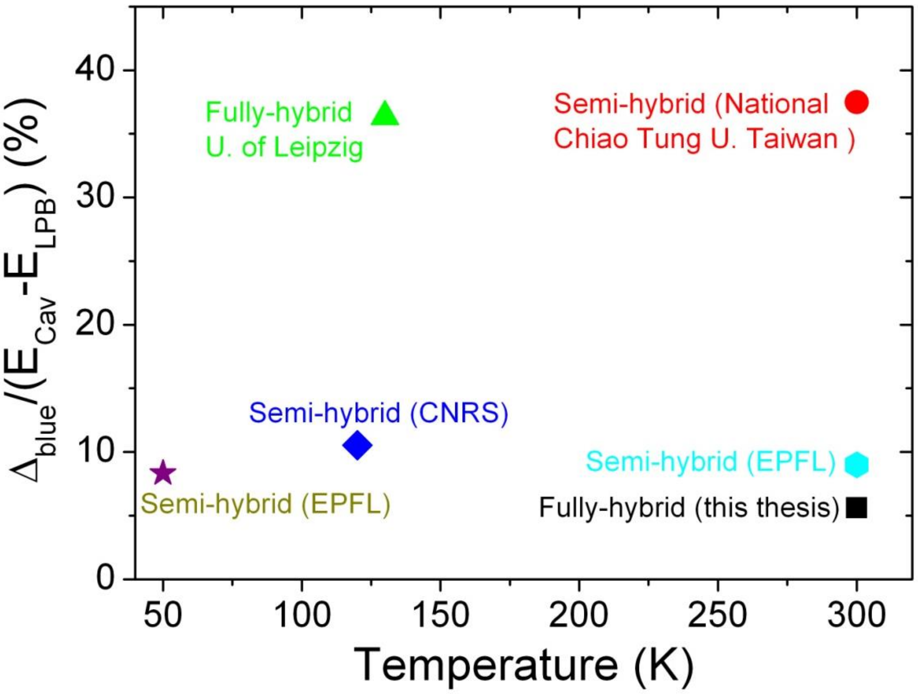

Figure 5.3: The ratio of Δ_{blue} $/(E_{Cav} - E_{LPB})$ extracted from the reports of different groups on their ZnO or GaN microcavities, plotted as a function of temperature. Black square: this thesis, fully-hybrid ZnO microcavity; blue diamond: CNRS, semi-hybrid ZnO microcavity [39]; green triangle: University of Leipzig, fully-hybrid ZnO microcavity [41]; red circle: National Chiao Tung University Taiwan, semi-hybrid ZnO microcavity [42]; hexagon: EPFL, semi-hybrid GaN microcavity [30]; star: EPFL, semi-hybrid GaN microcavity at low temperature [168].

5.2 Condensation phase diagram

Establishing a polariton condensation phase diagram consists in determining the polariton condensation threshold as a function of temperature (T) and cavity photon-exciton detuning (δ): $P_{\text{Thr}} = f(T, \delta)$. In order to experimentally obtain a complete phase diagram, the cavity must exhibit polariton condensation from low to room temperature (or above) and provide, simultaneously, access to a very large range of detunings. Since our cavity is the first ZnO microcavity that satisfies both these two conditions, we were able to achieve for the first time a complete condensation phase diagram for ZnO polaritons.

5.2.1 Qualitative description of condensation phase diagram

As discussed in 3.2.3, polariton condensation is governed by both thermodynamics (i.e. energy distribution of the system states) and relaxation kinetics (i.e. polariton lifetime), according to which the system can be classified into different condensation regimes: see references [112] and [47]. Generally speaking, the condensation threshold is determined by a tradeoff between the LPB polariton lifetime (τ_{pol}), the LPB polariton relaxation time (τ_{rel}) and the critical density for condensation (n_{crit}), which all depend on both the detuning and the temperature.

In order to apprehend the effect of each parameter, we will first fix the temperature and consider the evolution as a function of detuning, as illustrated in Figure 5.4**a**. Following the conclusions in 3.2.3, we can qualitatively relate the condensation regimes to different detunings:

(1) When going from very negative towards more positive detunings the exciton fraction of LPB polaritons increases, resulting in longer τ_{pol}[1], stronger polariton-polariton interaction and larger polariton effective mass. Therefore, τ_{pol} increases and τ_{rel} decreases due to enhanced polariton-polariton interaction and reduced depth of the polariton trap. When $\tau_{rel} \ll \tau_{pol}$, the system is in regime I of Figure 5.4**a** (also of 3.2.3), where the relaxation is kinetically easy and allows efficient thermalization of the polaritons. Unfortunately, the larger the polariton effective mass the larger the critical condensation density since the polariton density of states increases [47]. Regime I is also called the thermodynamic regime because in it, and below threshold, polaritons have enough time ("lifetime") to be either in thermal equilibrium with the lattice or in quasi-thermal equilibrium (i.e. the polariton gas is in self-equilibrium and a T_{pol} can be defined, even if in general T_{pol} does not need to be equal to $T_{lattice}$) and the condensation density is given by the thermodynamics of the problem.

(2) When going from very positive towards more negative detunings the photon fraction of LPB polaritons increases, resulting in shorter τ_{pol}, weaker polartion-polariton interaction and smaller polariton effective mass. Therefore, τ_{pol} decreases and τ_{rel} increases due to reduced polariton-polariton interaction and increased depth of the polariton trap. When $\tau_{rel} \gg \tau_{pol}$ the system is in regime II of Figure 5.4**a** (also of 3.2.3), where the relaxation is kinetically difficult and the polaritons hardly thermalize towards the LPB bottom. Fortunately, the smaller the LPB polariton effective mass the smaller the critical density for condensation. Regime II is also called the kinetic regime because in it, and below the condensation threshold, polaritons are usually out of thermal equilibrium, and polariton condensation is mainly governed by the relaxation kinetics.

---

[1] Exciton lifetimes in ZnO (30-100ps) are much longer compared to the photon lifetimes that we have obtained in this cavity. In general it is not mandatory that the "matter" lifetime is larger than the photon lifetime.

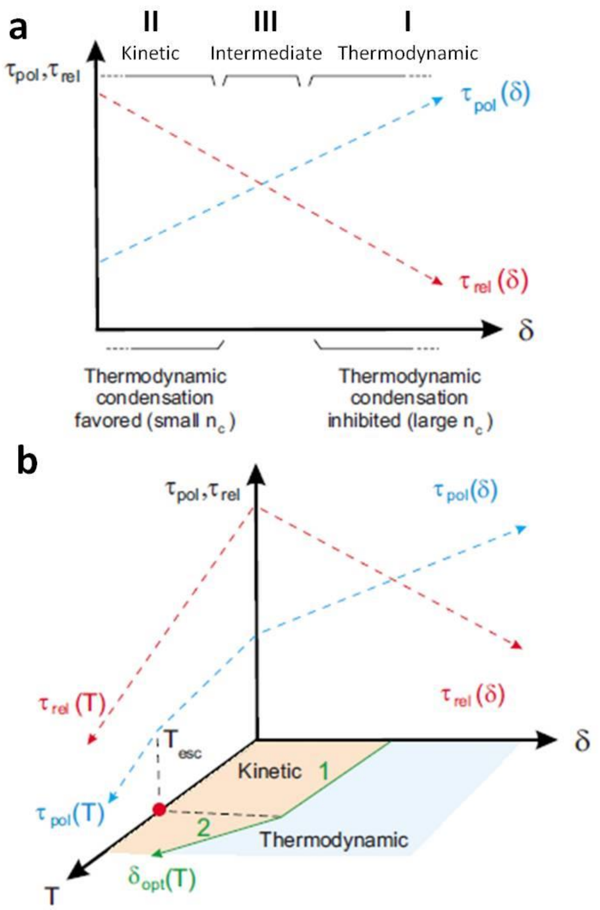

Figure 5.4: Extracted from Reference [47] but slightly modified to fit the text of this manuscript. **a**. Schematic description of the dependence of the LPB polariton lifetime and the LPB polariton relaxation lifetime under nonresonant excitation at a given temperature as a function of detuning. It qualitatively shows the regions where either the kinetics (region II) or the thermodynamics (region I) determine polariton condensation, as well as an intermediate region where both mechanisms need to be taken into account (region III). **b**. Refined qualitative diagram showing the evolution of the characteristic polariton times controlling condensation, as a function of either δ or T. This 3D diagram allows to define the curve $\delta_{opt}(T)$ that separates regions where condensation is dominated by kinetics or by thermodynamics [47].

In order to compare more easily the characteristics of the two condensation regimes they have been summarized Table 5.1.

Regime	**Thermodynamic regime**	**Kinetic regime**
Conditions	$\tau_{rel} \ll \tau_{pol}$	$\tau_{rel} \gg \tau_{pol}$
Favored detuning	Positive	Negative
Relaxation kinetics	Fast relaxation, *kinetically easy* for condensation	Slow relaxation, *kinetically difficult* for condensation
Critical density BEC theory	High critical density	Low critical density
Thermalization below threshold	Thermal equilibrium	Out of thermal equilibrium
Condensation threshold determined by	Thermodynamics	Kinetics

Table 5.1: Characteristics of each condensation regime.

It should be noted that in Table 5.1 "favored detuning" indicates the trend in terms of the detuning, but it is not an absolute assertion: for example, positive detunings ($\delta > 0$) do not guarantee the achievement of the thermodynamic regime, but means that by going towards more positive detunings it is more likely to reach the thermodynamic regime. The definition of the regimes is essentially given by the relative ratio between τ_{rel} and τ_{pol}. From this qualitative discussion it turns out that there must be a detuning δ_{opt} that "optimizes" simultaneously the critical density, which is the limiting factor in the thermodynamic regime, and the relaxation time, which is the limiting factor in the kinetic regime. For this "tradeoff" regime (III in Figure 5.4**a**), the condensation threshold is determined by both kinetics and thermodynamics. Thus, when going from negative to positive detuning, the condensation threshold first decreases, reaching its minimum at δ_{opt}, and then rises. This P_{Thr} vs. δ curve constructs a phase diagram: below this curve the polaritons are in the uncondensed phase while above this curve they are in the condensed phase.

Now, the δ can be set constant and T can be varied, as illustrated in Figure 5.4**b**, and its influence on the different parameters controlling polariton condensation can be analyzed. If we consider, as a first approximation, exciton-polaritons as an ideal gas of non-interacting bosons its critical condensation density would be a continuously-increasing function of temperature (from a naive point of view we could expect a $T^{3/2}$ dependence) and, thus, an overall increase of the condensation threshold with temperature could be expected.

If we now consider its effects on the characteristic times of the system, we can first notice that τ_{rel} is reduced at all detunings with increasing temperature due to enhanced polariton-phonon interactions, resulting in a shift of the intermediate regime towards more negative detunings (as illustrated by Figure 5.4**b**); this is equivalent to a decrease in δ_{opt}. Additionally, when the polariton trap depth is comparable to the kinetic energy associated with a given lattice temperature, thermal escape of polaritons from the bottom of the LPB to higher $k_{\parallel}$ states is expected [46], making more positive detunings less favored. This effect, though only important at sufficiently high temperatures (above T_{esc} in Figure 5.4**b**), pushes δ_{opt} to more negative values. Finally, temperature can also affect τ_{pol} given that a temperature raise is usually accompanied by a decrease of the exciton nonradiative lifetime. However, since the free-exciton nonradiative lifetime at room-temperature, which varies from about 30ps in homoepitaxial films to almost 100ps in bulk ZnO substrates, is much larger than the cavity photon lifetime, the direct effect of temperature on the polariton lifetime seems negligible (i.e. its lifetime is mainly governed by the cavity lifetime). Besides, the increase in the exciton homogenous broadening, induced by enhanced exciton-phonon interaction, will bring a decrease in the Rabi splitting, which might be important in the cases where thermal polariton escape is not negligible. This last effect would push δ_{opt} towards more negative values. The effects induced by the temperature rise and their influence on the condensation threshold and optimum detuning are summarized in Table 5.2. The general conclusions are: (1) when raising the temperature, P_{Thr} undergoes an overall increase, but not necessarily the same at all detunings, due to the variation of the optimum detuning with temperature. (2) δ_{opt} undergoes a decrease with increasing temperature.

Effect / Influenced property	Temperature increase			
	n_{crit} increase	τ_{rel} decrease	τ_{pol} unaffected (or slightly decreased)	Thermal escape
P_{Thr}	Increase	Decrease	unaffected (or slightly increased)	Increase
δ_{opt}	Decrease	Decrease	Unaffected (or slightly decreased)	Decrease

Table 5.2: Effects induced by increasing temperature, and their influence on the condensation threshold P_{Thr} and the optimum detuning δ_{opt}.

Irrespective of the material system, a quantitative understanding of the condensation phase diagram, i.e. $P_{\mathrm{Thr}} = f(T, \delta)$, involves solving the semi-classical Boltzmann rate equations for bosons, as introduced in 3.2.3, since only in the "pure" thermodynamic regime a good threshold approximation might be obtained from general boson-condensation considerations. From the experimental point of view, its measurement implies having access to a large range of detunings and temperatures. Furthermore, if it wants to be determined up to room temperature, this can only be possibly realized in wide bandgap semiconductors, which can keep the bosonic behavior of exciton-polaritons up to this temperature. Indeed, the first condensation phase diagram up to room temperature was obtained by Butté *et al* only in 2009 [46], and then by Levrat *et al* in 2010 [47] on MQW GaN polariton lasers. The phase diagram in reference [47] is shown in Figure 5.5. From 160K to 320K, the authors observed the threshold minimum corresponding to the optimum detuning, which increases with temperature as theoretically expected. At lower temperatures, namely from 4K to 120K, they are limited by the range of accessible detunings in their cavity and, therefore, they have only observed the decreasing trend of P_{Thr} with increasing detuning without yet being able to reach δ_{opt}. However, extrapolating the trends at higher temperatures one can expect a continuously-decreasing function $\delta_{opt}(T)$ within the whole temperature range, as indicated by the thick black line.

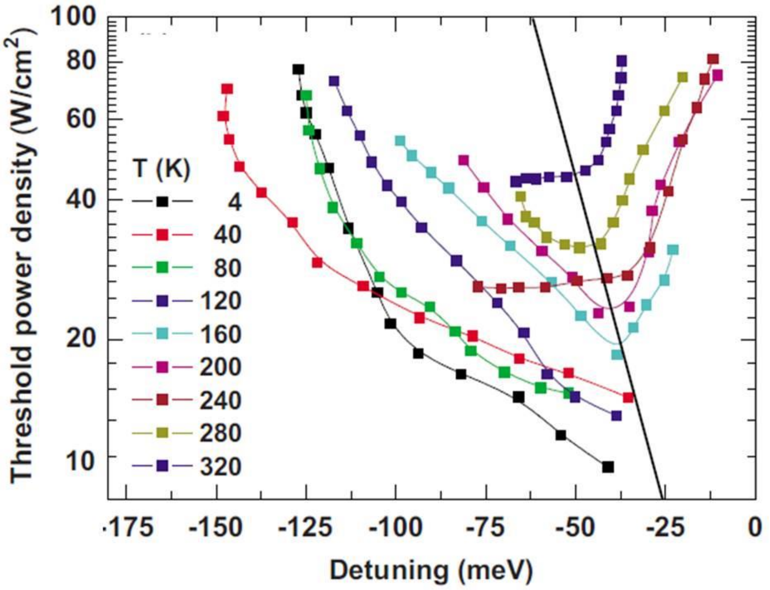

Figure 5.5: Copied from Reference [47] but slightly modified to fit the text of this thesis. Experimental threshold power density as a function of detuning at various temperatures [47].

5.2.2 The complete phase diagram of polariton condensation in a ZnO microcavity

Compared to the GaN microcavity shown in Figure 5.5 (or in reference [46]), the ZnO microcavity described in this chapter has one main advantage for deriving the condensation phase diagram: a very large range of accessible detunings for which condensation takes place, which is obviously the consequence of a large Q and a large Ω_{Rabi} all over the sample.

The measured and theoretically calculated condensation phase diagrams are shown in Figure 5.6. In order to facilitate the discussion, the phase diagram has been plotted as a function of two different magnitudes: detuning (Figure 5.6**a** and **c**), and energy offset between the exciton reservoir and the LPB minimum ($E_X - E_{LPB}$, Figure 5.6**b** and **d**). The experimental data were originally obtained in terms of energy offset, and converted into detuning with the help of the transfer matrix method described in 4.4, while the exciton/photon fractions for a specific detuning (or energy offset) were further derived from the coupled-oscillator model. It should be noted that the *translation* of energy offset into detuning introduces an additional uncertainty, which increases when going towards very positive detunings. This is because when approaching the exciton energy, the LPB becomes highly excitonic-like and its energy and dispersion vary very little compared to the further increase of the bare cavity mode energy. As a result, a very tiny uncertainty in the measured LPB could lead to a large uncertainty of the calculated bare cavity mode and, thus, the detuning. This situation becomes different when going to negative detunings, where the LPB becomes more photonic-like and its energy and dispersion depend more strongly on the bare cavity mode. Supposing a Rabi of 240meV, an uncertainty of LPB energy Δ_{LPB}=1meV (considering the typical measured LPB linewidth ~2meV) gives an uncertainty of detuning Δ_δ= 15meV at δ=+400meV but only Δ_δ= 2meV at δ=0. Moreover, since the excitonic-induced LPB broadening is more important at positive detunings (and the homogeneous excitonic broadening is larger than the photonic one), this leads, finally, to a larger measurement uncertainty of Δ_{LPB} at positive detunings.

The theoretical simulation was performed by D. Solnyshkov and G. Malpuech, at Institut Paascal, by numerically solving the semi-classical Boltzmann rate equations. The main parameters used in the simulation are the LO-phonon energy, E_{LO}=72meV, the exciton Bohr radius, a_B =18Å, the electron effective mass, m_e =0.24 m_0 , the hole effective mass, m_h=0.98m_0 (where m_0 is the free electron mass), a deformation potential D =15eV, an exciton non-radiative lifetime=50ps, which is taken to be independent of temperature, a cavity quality factor Q=4000 and an inhomogeneous broadening of 1meV.

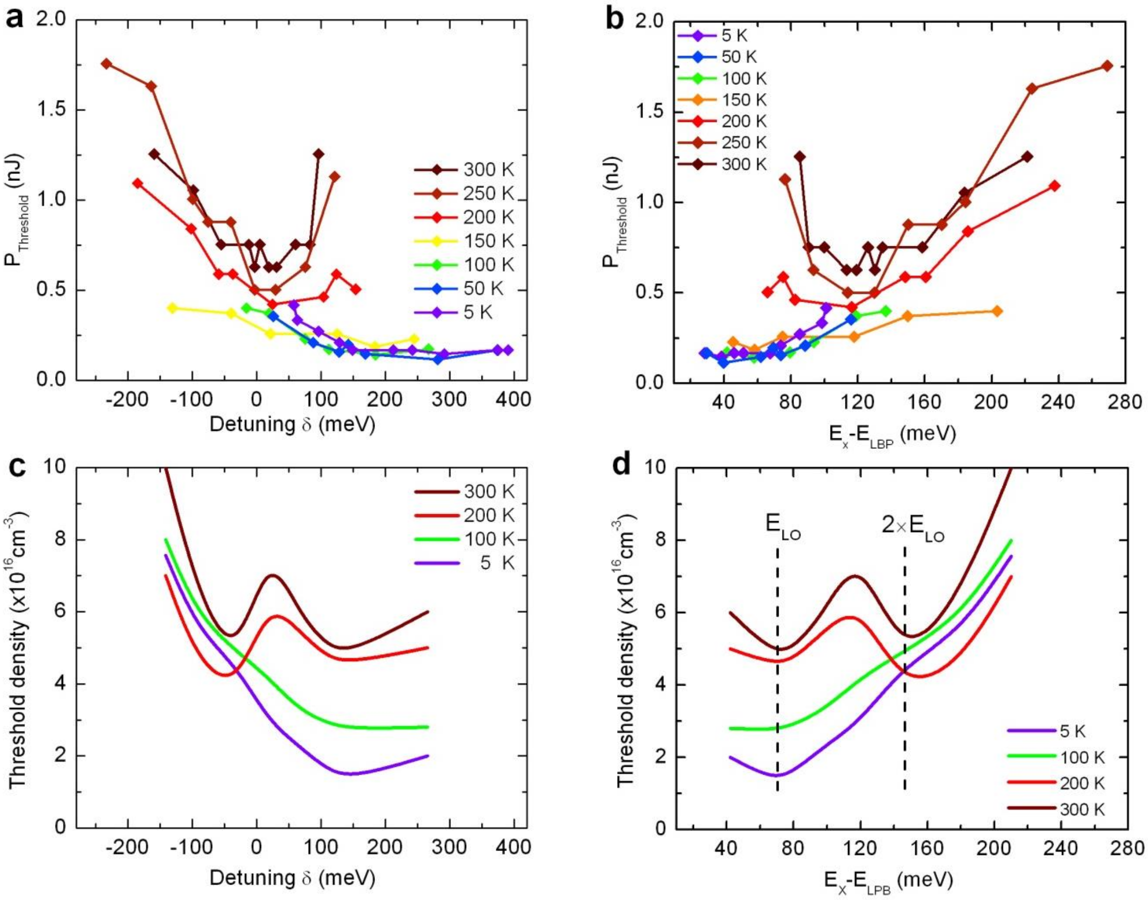

Figure 5.6: Measured (**a** and **b**) and simulated (**c** and **d**) polariton condensation phase diagram of the fully hybrid ZnO microcavity from low to room temperature. The condensation threshold power/density is plotted as a function of detuning δ in **a** and **c**, and as a function of energy offset between the exciton and the LPB minimum ($E_X - E_{LPB}$) in **b** and **d**. The measurement is performed under quasi-continuous excitation (repetition rate 4kHz and pulse duration 400ps) in a region where the cavity thickness amounts to ~2.5λ.

In good agreement with the previous qualitative description, the condensation threshold undergoes an overall increase with temperature, while $\delta_{opt}(T)$ shifts towards more negative values. However, in contrast with the observations in GaN based cavities, for most temperatures (5~250K), the optimal detuning of our ZnO based structure is positive, as theoretically expected [48], being slightly positive or zero at room temperature. This different behavior is due to the large Rabi splitting value: ~240meV for the current ZnO cavity compared to ~40meV for the bulk-GaN and ~56meV for the MQW-based one. This Rabi splitting induces a very deep energy minimum at the bottom of the LPB while keeping a large density of final states and, therefore, fast relaxation kinetics. The depth of the trap induced by the large Rabi splitting is especially advantageous at room temperature, where thermal escape of polaritons can play a deleterious role on the polariton lasing threshold, as evidenced already in GaN-based cavities [46]. In the current ZnO cavity, thermal escape might play a role in limiting condensation only at room temperature and for very positive detunings. Indeed, it should be noted that for this cavity, at δ=0meV, the polariton trap in momentum space is of the order of 115meV, much larger than the 25meV corresponding to the thermal energy at room temperature.

To further illustrate the distinction between Kinetics & Thermodynamics, the polariton distribution in momentum space below threshold has been plotted in Figure 5.7 for two detunings at either side of $\delta_{opt}(T)$ at room temperature. As discussed in section 5.2.1, when $\tau_{pol} < \tau_{rel}$ (i.e. in the kinetic regime) polaritons do not live long enough to attain the bottom of the LPB, and accumulate at a nonzero momentum (in this example at θ=20°). This situation can be exacerbated by decreasing the LPB polaritons lifetime by going towards even more negative detunings, as will be shown in Figure 5.11**b**. On the other hand, when $\tau_{pol} > \tau_{rel}$ (i.e. in the thermodynamic regime), which can be achieved by increasing the exciton fraction of the LPB polaritons, polaritons are able to relax more easily down to the minimum energy state, as evidenced by an accumulation of polaritons at the bottom of the LPB even below threshold.

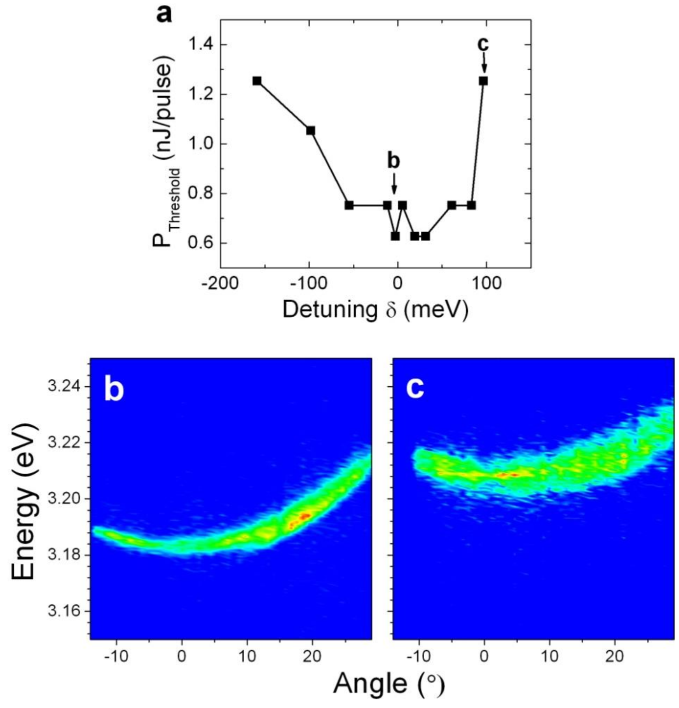

Figure 5.7: **a**. threshold power as a function of detuning at 300K. **b** and **c**, Fourier space images below threshold under quasi-continuous excitation corresponding to the detunings indicated by the arrows in **a**.

5.2.3 ZnO peculiarities: single and multiple LO-phonon assisted polariton relaxation

The most noticeable feature in the theoretically simulated phase diagrams, shown in Figure 5.6**b** and **d**, is the presence of two local threshold minima at room temperature that gently faint into only one at low temperatures. These two minima, whose experimental observation will be discussed in the following, are associated to a large enhancement of polariton relaxation by interaction with LO phonons. The first dip, at $E_X - E_{LPB}$ = ~72meV, is induced by efficient polariton scattering directly from the exciton reservoir to the LPB minimum via interaction with one LO-phonon, as was previously observed at low temperatures in a CdTe-cavities [112], and more recently in both a GaN [169] and a hybrid ZnO cavity [40]. Most interesting, above 200K there is a second minimum slightly deeper than the first one, at about $E_X - E_{LPB}$ =144meV, which corresponds to a relaxation process bringing polaritons directly from the excitonic reservoir to the bottom of the LPB by emission of two LO phonons.

In Figure 5.8**a** the offset $E_X - E_{LPB}$ for which the minimum threshold is measured (under quasi-continuous excitation), is plotted as a function of temperature. In accordance with the theoretical calculations, at room-temperature the minimum threshold is achieved when the bottom of the LPB is resonant with the excitonic reservoir mediating two LO phonons. Indeed, the minimum threshold seems to be obtained at slightly smaller energies, although this can be blurred by the large homogenous broadening of the excitonic reservoir at these temperatures, as illustrated by the error bars in Figure 5.8**a**. It should be noticed further that T in Figure 5.8**a** refers to the lattice temperature, which may differ from the electronic temperature (which is the temperature that should be strictly used, but that is difficult to determine in our experiments). The importance of phonon-assisted relaxation lies in the fact that the accessible polariton trap depth (at room-temperature) is larger than what would be exploitable only with relaxation mediated by polariton-polariton interaction; this, in combination with the large Rabi splitting, allows to use a trap sufficiently deep to prevent thermal polariton escape, in contrast with GaN [47]. As temperature is reduced, the optimum offset shifts to smaller values and becomes compatible with an emission of one LO phonon, the accordance between the expected energy resonance and the measured one being perfect at these intermediate temperatures. Finally, at even lower temperatures the optimum offset is no longer dominated by a phonon-assisted process, but is dictated by the kinetics of the system; thus, in this last case in order to reduce the relaxation time a more positive detuning (equivalent to a smaller offset), and thereby a higher excitonic content, is required. Still, a local minimum associated to LO-phonon assisted relaxation can be observed on the Threshold Vs Offset curve at low temperatures (see Figure 5.8**b**), similarly as in CdTe [112]and GaN [169].

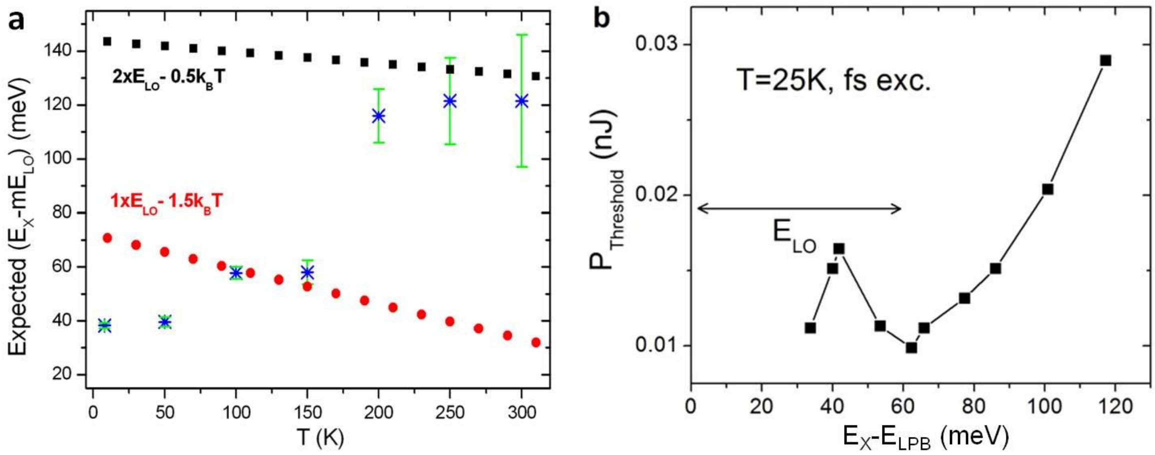

Figure 5.8: **a**. Blue stars represents the energy offset $(E_X - E_{LPB})$ corresponding to the optimum detuing (δ_{opt}) as a function of sample temperature. Black squares and red circles present 2×E_{LO}-0.5k_BT and 1×E_{LO}-1.5k_BT, respectively. **b**. Threshold power vs. $(E_X - E_{LPB})$ under femtosecond excitation at 25K.

To further confirm the origin of the dominating relaxation process in each of these temperature ranges, the dependence of the integrated output intensity on the excitation density (P), under quasi-continuous excitation, has been studied. The curves corresponding to the optimum offsets at 5K, 100K and 300K are shown in Figure 5.9**a**, **b** and **c**, respectively. At the lowest temperature, a quadratic dependence on the pumping power (P^2) is obtained, compatible with a two-particle process such as exciton-exciton scattering and consistent with the high excitonic fraction (~88%) of the LPB at this positive detuning (+291meV). On the other hand, at 100K and 300K the output intensity shows a linear (P^1) dependence on the pumping power, as expected for a process such as exciton-LO phonon scattering where only one exciton is involved.

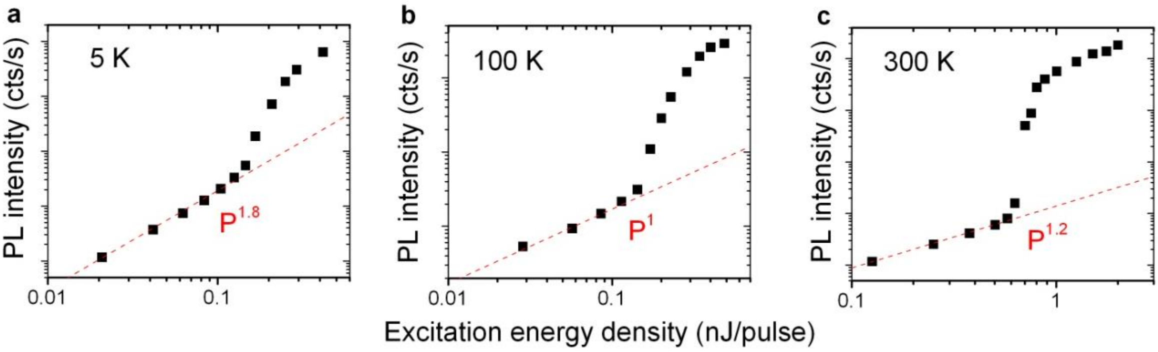

Figure 5.9: Integrated photoluminescence intensity as a function of excitation energy density under quasi-continuous excitation, corresponding to the optimum detuning at 5K(**a**), 100K(**b**) and 300K(**c**), respectively. The excitation dependence below threshold is fitted as a power function for each graph (red dashed lines).

5.2.4 From excitonic to photonic condensate

In the strong exciton-photon coupling community the most mature material in terms of microcavity fabrication is, by far, GaAs[1]. In this material, photonic contents of ~70% can be considered as "highly-photonic" [170,171]. For the current ZnO cavity, the accessible excitonic/photonic fraction range does not only allow to study "highly-photonic" but also "highly-excitonic" polariton condensates. In Table 5.3 the range of the studied exciton-photon detunings at which condensation has been achieved, and of the corresponding exciton-photon fractions are indicated. This table highlights the fact that by changing the detuning and the operating temperature it is possible to have access to polariton condensates with photonic and excitonic fractions larger than 70%. Particularly interesting and novel[2] is the possibility of achieving polariton condensates with very large excitonic fractions, $|X|^2>90\%$, as this should enable to achieve long-lifetime polariton condensates even with relatively small *Q*s. Furthermore, it can be seen that properties associated with the exciton fraction, such as the interaction constant, can be tuned by a factor ~6, whereas properties associated with the photonic fraction, such as polariton effective mass and lifetime, can be tuned by a factor ~20.

Temperature (K)	Detuning (meV)	Excitonic fraction	Photonic fraction
300	+91 to -152	68% to 24%	32% to 76%
250	+118 to -214	72% to 17%	28% to 83%
150	+273 to -132	87% to 26%	13% to 74%
5	+450 to +105	96% to 63%	4% to 37%

Table 5.3: Range of exciton-photon detunings in which polariton condensation has been achieved and the corresponding extreme excitonic/photonic fractions.

Within this large range of condensation conditions, polariton condensation is typically accompanied by a nonlinear rise of the output intensity, of 2 to 4 orders of magnitude, a line sharpening of one order of magnitude and a moderate blue shift of the LPB energy. The measured blueshifts vary from about 1 to about 10 meV, i.e. less than 4% of the actual Rabi splitting, with no clear trend being observed as a function of temperature or detuning. This scatter in blueshifts below threshold has been also found in other wide-bandgap microcavities studied in the last years, including ZnO [41] and GaN [168].

With the aim of illustrating the large varierty of condensation conditions, Figure 5.10 shows some representative spectra and polariton condensation characteristics (output intensity, linewidth and blueshift) as a function of excitation density for two "extreme" examples. As expected from the discussion in the previous section, exciton-like condensates show, below threshold, a quadratic dependence of their output intensity as a function of input intensity due

---

[1] In terms of number of studies, the CdTe-based system should be also considered.

[2] To our knowledge similar excitonic fractions have been only observed very recently by the team of M. Richard in ZnO microwires [45].

to the exciton-exciton scattering mechanism being the dominant one. For the highly-photonic condensate the dependence is close to $P^{1.5}$, highlighting the fact that at this detuning both LO-phonon scattering and exciton-exciton scattering play a role in the relaxation process. Indeed, the energy offset $(E_X - E_{LPB})$ of the photonic-like polariton is larger than 2xLO-phonon energy and, therefore, the sole LO-phonon assisted mechanism is not sufficient to bring excitons down to the LPB minimum; for this reason, and despite the polaritons small excitonic fraction, exciton-exciton scattering is still necessary.

These two examples illustrate the fact that while polariton condensation, irrespective of the detuning at which it occurs, displays some common features, e.g. linewidth narrowing (which is a consequence of the onset of temporal coherence), some other features commonly associated to condensation might differ strongly depending on the exact detuning. An example of this unequal behavior is given by the “nonlinear” rise of the output intensity above the condensation threshold: except for the very excitonic case of Figure 5.10**a**, where the nonlinear rise is less than one order of magnitude, in all the other points shown until now the increase is of several orders of magnitude. Indeed, for very large positive detunings, i.e. for LPB polaritons with very large excitonic fractions, the transition to a condensed phase seems to be almost thresholdless, from the “Output Intensity Vs Input Intensity” curve point of view. This might be explained by the fact that at this detuning range τ_{rel} becomes short compared to τ_{pol} and, therefore, polaritons can efficiently relax from the reservoir into the bottom of the LPB without being lost or without being accumulated at the bottleneck region. On the opposite case, for very photonic-like condensates, a large number of polaritons accumulate at the bottleneck region so that, as soon as stimulated scattering is efficient enough to overcome it, a large intensity increase (i.e. a large number of polaritons relax down to the bottom of the LPB) is detected. Examples illustrating this behavior are found in Figure 5.10**c** and **d**.

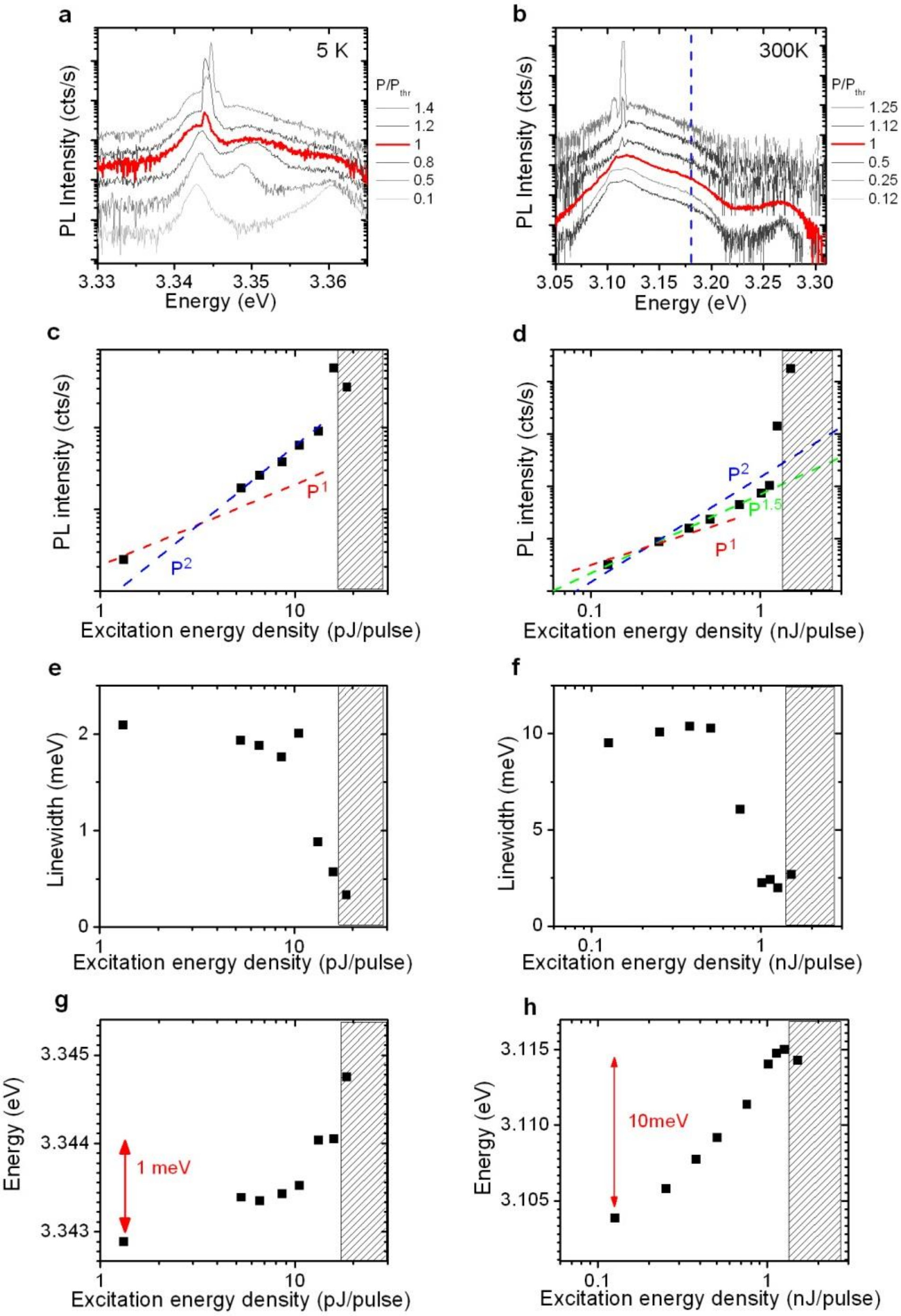

Figure 5.10: Polariton condensation features (Output intensity, linewidth and blueshift) as a function of excitation energy density for *large* positive and *large* negative detunings. **a**, **b**. Spectra at various excitation intensities, with red curves corresponding to the condensation threshold. **c**, **d.** integrated output intensity. **e**, **f.** full width at half maximum. **g**, **h.** energy of the main emission peak. **a**, **c**, **e**, **g**: 5K and δ= +390 meV (exciton fraction 92%); **b, d, f, h**: 300K and δ =-124meV (photon fraction 77%). Spectra at 5K were acquired under 130fs pulsed excitation (76MHz repetition rate) and at $k_{\|}$=0, while at 300K they were acquired under quasi-continuous 0.4 ns excitation (4kHz repetition rate) and are angle-integrated. The dashed areas in (**c-h**) indicate input intensities for which condensation at more than one energy level occurs: in these regions, the reported values for each of the magnitudes correspond to the state whose threshold is lower. The dashed line in **b** indicates the position of the bare cavity mode, as given by transfer matrix simulations of the fabricated structure. Power functions are plotted as dashed lines in **b** and **d** for discussing the excitation dependence below threshold.

To further highlight the importance of the excitonic/photonic fraction in the condensates properties, and emphasize the richness of the current cavity, the angle-resolved emission of two points at very different δ are shown in Figure 5.11. Below threshold, the exciton-like dispersion is spectrally-narrow, being very weakly affected by the photonic inhomogeneous broadening induced by the thickness gradient (Figure 5.11**a**). Obviously, the low temperature employed ensures that phonon-induced broadening is also negligible. On the other hand, the more-photonic like condensate exhibits below threshold a large inhomogeneous broadening (Figure 5.11**b** left panel). In this case, the position of the LPB below threshold ensures that the LPB is phonon-protected [151] and that its broadening is not governed by interaction with phonons. Furthermore, the photonic origin of the inhomogeneous broadening is further confirmed by the presence of several neighboring LPB modes associated to different cavity modes. The differences are also clear above threshold: the exciton-like condensate, which appears well above the LPB dispersion, is wide in k-space due to its interaction with the excitonic reservoir; on the contrary, above threshold the photonic condensate is much less affected by the exciton reservoir, which is localized within the 2 µm pumping laser spot, and, therefore, shows a narrower distribution in k-space.

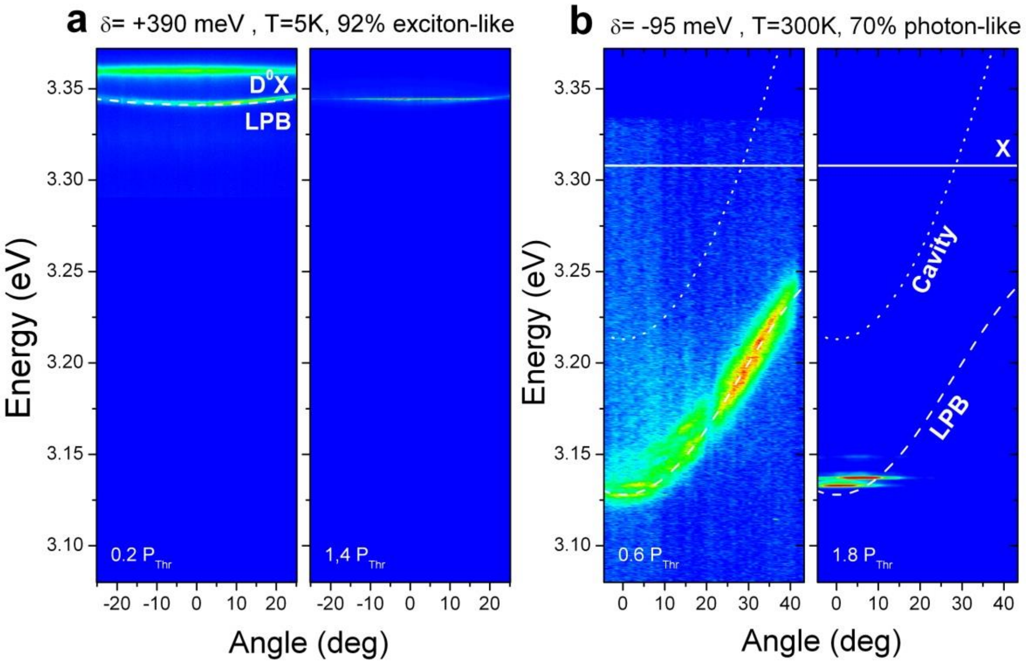

Figure 5.11: **a**. Fourier space images of the emission below (left) and above (right) the condensation threshold for an LPB with a 92 % exciton fraction, corresponding to a 2.5λ cavity mode. The data is taken under 130 fs pulsed excitation. Below threshold, the emission consists of the LPB and the non-dispersive donor-bound exciton transition (D^0X). **b** Same as **a**, but taken under quasi continuous excitation at 300 K and for a 3λ cavity mode. The photon fraction of the LPB is 70 %. The simulated LPB, cavity and exciton modes are plotted as dashed, dotted and solid lines respectively.

5.3 Studies on thicker regions

The condensation phase diagram described was obtained by measuring a region where the thickness of the ZnO active layer was sufficiently thin (from 2 to 3λ), so that only one LPB was present in the studied wavelength range, while possible co-existing LPBs were either out of the DBR stop-band or far enough from the studied LPB to have any noticeable influence. This allowed to study polariton condensation on one polariton mode independently of all the others. Nevertheless, in this fully-hybrid cavity a remarkable region can be achieved on the thicker parts (ZnO active layer thickness>3λ): under these circumstances, multiple LPBs lie close enough to each other so that their mutual influence on condensation can be studied. This situation reminds a lot what is observed in ZnO microwires cavities [38,44,151], where the number and spacing of cavity modes can be modified by varying the microwire diameter.

5.3.1 Mode switching: varying ZnO thickness

When the cavity thickness amounts to ~6-7λ, several coexisting photonic modes can couple independently to the exciton mode (See Section 3.1.2). The result is the appearance of closely-separated, compared to the Rabi splitting, LPBs. Typically, at a given excitation spot and for temperatures in the order of 70K two or three LPBs, associated to cavity modes displaying different detunings, can be observed within the studied energy range. This enables to experimentally test the measured phase diagram: the idea behind is that since for a given temperature several LPBs exist nearby, one of them, displaying the lowest threshold, will be “chosen” by polaritons to condense. In this manner we can sweep different detunings and explore the tradeoff between Kinetics and Thermodynamics for a given temperature.

A detailed investigation has been performed at 70K, as shown in Figure 5.12. The detunings of three consecutive LPBs, labeled by 1, 2 and 3, is shown in Figure 5.12**a** as a function of the ZnO active layer thickness. The LPB modes in which polariton condensation takes place are connected with a solid line. When the ZnO thickness changes from 852nm to 913nm (i.e. we move from left to righ in Figure 5.12**a**), all three LPBs go to less positive detunings and condensation is continuously observed from LPB2, as confirmed in Figure 5.12**b**, **c** and **d,** which contain k-space images (both below and above threshold) corresponding to the ZnO thicknesses of 852nm, 865nm and 903nm in Figure 5.12**a**. At these positions, even though LPB3 is thermodynamically favorable, the kinetics of this branch (LPB3) is not efficient enough to accumulate sufficient polaritons at its bottom. On the contrary, polaritons in LPB2 have a larger effective mass (i.e. larger excitonic fraction) and, therefore, a sufficiently small τ_{rel} to be able to accumulate at its bottom, while LPB1 is too much excitonic-like and has a much larger critical density for condensation. As a result, LPB2 turns to be the branch closest to the optimum detuning among the three LPBs, as sketched in the left panels of Figure 5.12**b** to **d**. This “mode competition” illustrates nicely the physical meaning behind the phase diagram. As thickness increases and the photonic fraction of LPB2 becomes larger, τ_{rel} (resp. τ_{pol}) for polaritons in this branch becomes larger (resp. smaller). At a thickness of 913nm, the LPB2 mode becomes too much photon-like and the condensate switches from LPB2 to LPB1, for which the excitonic fraction is larger and, therefore, τ_{rel} shorter. Consistently, condensation continuous to take place on LPB1 (exemplified in Figure 5.12**e**) until the next mode switching occurs, illustrating once again the tradeoff between Kinetics and Thermodynamics.

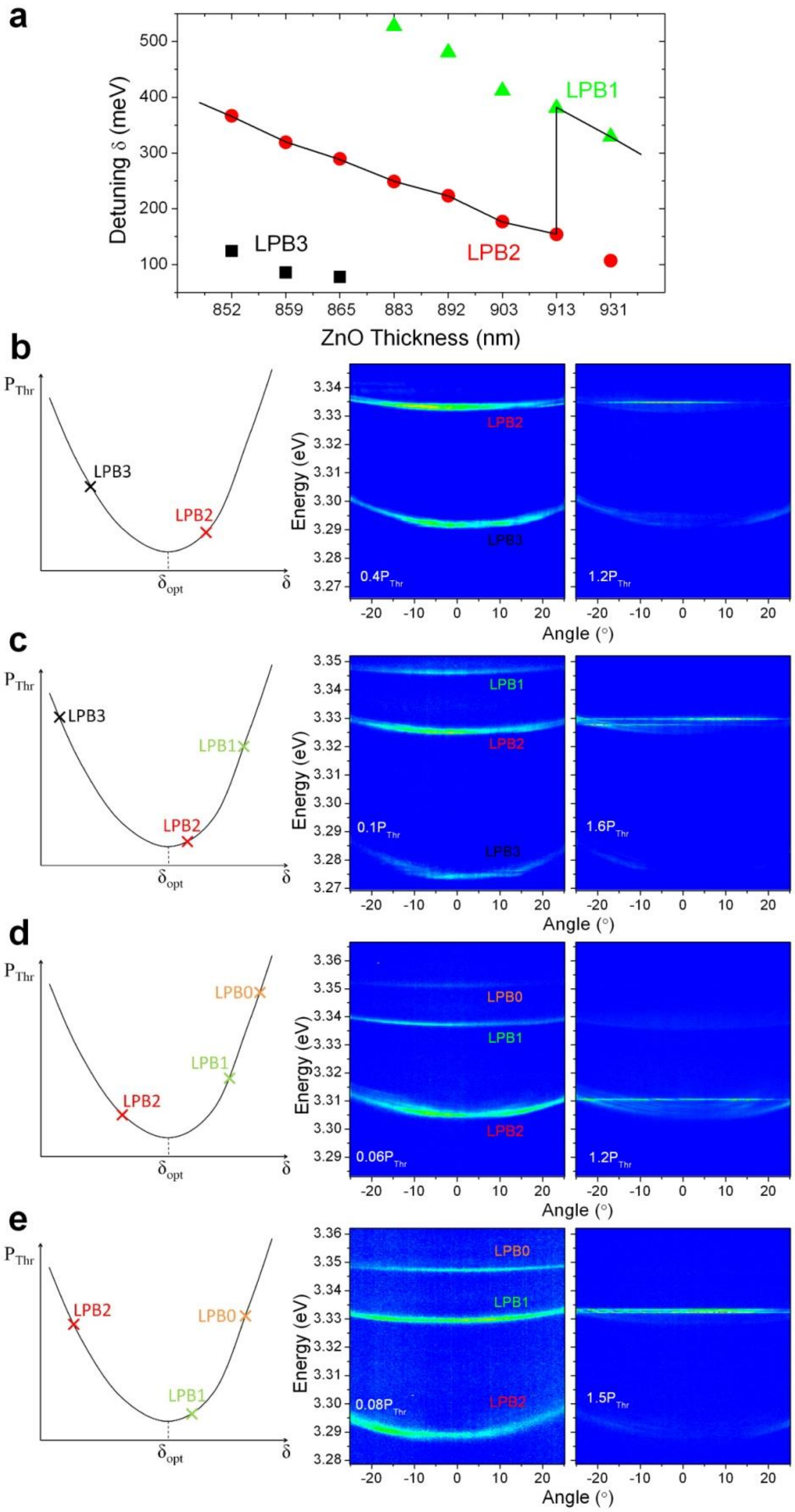

Figure 5.12: **a.** Detuning versus ZnO thickness for three LPBs. The solid line binds the modes on which polariton condensation occurs. The data are taken under 130 fs pulsed excitation at 70 K. **b**, **c**, **d** and **e.** Sketches of LPBs in the phase diagram (left panel) and Fourier images (right panel) corresponding to ZnO thicknesses of 852nm (**b**), 865nm (**c**), 903nm (**d**) and 931nm (**e**) in **a**. The Fourier images in each graph are taken both below (left) and above (right) threshold. LPB0 in **d** and **e** is out of scale in **a**.

5.3.2 Mode switching: varying pumping intensity

In 5.3.1 the physics of the phase diagram (i.e. τ_{rel} Vs τ_{pol}) has been tested by varying the detuning of every LPB branch, which simultaneously modifies τ_{rel} and τ_{pol}. In addition, a second approach has been found to modify only one of the characteristic times (τ_{rel}), while maintaining the other (τ_{pol}) constant. This can be done by varying the excitation power, which can modify τ_{rel} through the exciton-exciton scattering term, while staying at the same pumping spot, which ensures that the detuning (and τ_{pol}) of each branch remains constant (*albeit* some δ modification due to exciton oscillator strength saturation).

The experiment is shown in Figure 5.13, where a spot comparable to the ZnO thickness of 913nm in Figure 5.12**a** is studied. Three LPB branches, with photon fractions of 3% (LPB0), 7% (LPB1) and 27% (LPB2), are observed in Figure 5.13**a** below threshold. At threshold, condensation occurs first on the intermediate branch LPB1 (7 % photon), as shown in Figure 5.13**b**. Polariton relaxation towards the bottom of this branch is kinetically easier compared to LPB2 (i.e. τ_{rel} (1) < τ_{rel} (2)), which would be more thermodynamically favorable but kinetically more difficult. A further increase of the pumping intensity increases the polariton relaxation rate, via enhanced exciton-exciton scattering, and, therefore, reduces τ_{rel} for all LPBs. By doing this, the tradeoff between Kinetics and Thermodynamics is displaced towards the thermodynamically favorable states that display lower energy and shorter polariton lifetime. Indeed, this is demonstrated in Figure 5.13**c**, where an increase of just 20% of the pumping intensity (1.2P$_{\mathrm{Thr}}$) allows polaritons to relax down to the bottom of LPB2, which shows a 27% photonic fraction and is thermodynamically favorable.

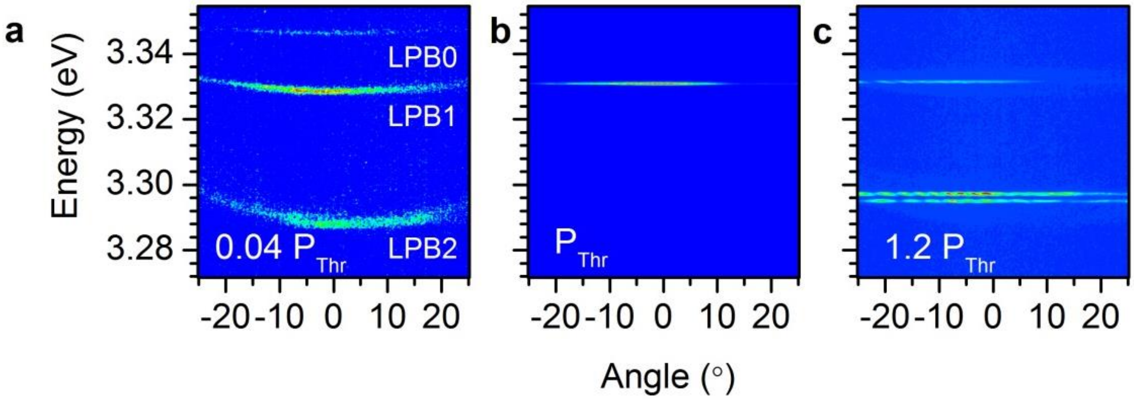

Figure 5.13: Fourier space images illustrating mode switching as a function of pumping intensity (situation similar to the point with a thickness of 913 nm in Figure 5.12**a**). **a**. Image below the condensation threshold. **b**. Image taken at the condensation threshold. Polariton condensation occurs on LPB1 (7 % Photon). **c**. At 1.2 P$_{\mathrm{Thr}}$, polariton condensation occurs preferentially in mode LPB2 (27 % photon). The data are taken under 130fs pulsed excitation at 70 K.

We have further investigated the mode-switching mechanism to confirm its consistency with our understanding of the condensation phase diagram and the experimental determination that we have carried out. First of all, an increase of pumping intensity always leads to a mode switching towards a more photonic-like mode, which is more thermodynamically favorable but kinetically more difficult, whilst the opposite process never occurs. This confirms the fact that the switching is governed by the enhancement of the polariton relaxation rate, which eventually determines the favored LPB for condensation via the ratio between τ_{pol} and τ_{rel}. Secondly, an appropriate energy separation between the two LPB branches is required in order to observe the mode switching. In Figure 5.13 the separation between LPB1 and LPB2 is ~40meV. If the separation is too small, the two LPBs share similar dynamics and condense simultaneously, within experimental precision, as observed in ZnO microwires [44]. Finally, if the separation is too large, the more photonic-like LPB would be so far away from the optimum detuning that condensation on that branch would require very high excitation intensity, eventually high enough to damage the sample.

5.3.3 Modification of polariton properties by mode switching

Interestingly, during the mode switching operating in Figure 5.13, the photonic fraction of the condensate increases by a factor 4 by passing from one branch (LPB1) to another (LPB2). This big change in photonic fraction should, in principle, strongly modify the properties of the created condensate. Such an effect is clearly visible via the k-space distribution of the condensed polaritons. The condensate occurring on the LPB1 shows a wide homogeneous peak in k-space, due to the interaction of the heavy exciton-like polaritons with the localized excitonic reservoir. On the other hand, the more photonic condensate of LPB2 shows a series of discrete well-defined sharp peaks up to large wave vectors values. The different condensate k-space distributions are induced by the different response of each condensate to both, the thickness gradient and the excitonic reservoir. It is important to note here that since the pumping spot is obviously the same for the two condensates, the "photonic" potential profile (i.e. the one given by the cavity and DBR thicknesses fluctuations) seen by the two condensates is strictly the same. The typical polariton potential profiles seen by the polaritons in LPB1 and LPB2 are depicted in Figure 5.14**a**, where the effect of unequal excitonic and photonic fractions is readily observed. It is composed of a Gaussian potential induced by the excitonic reservoir, which acts on the excitonic part of the polaritons, and a staircase potential induced by the thickness gradient, acting on the photonic part only. The height of a step corresponds to 1 monolayer variation of the cavity thickness. A simulation, based on the numerical solution of the modified Gross-Pitaevskii equation [172] using the above-mentioned potential, and carried out by D. Solnyshkov and G. Malpuech, from Institut Pascal, reproduces qualitatively the experimental data.

The model involves calculating the wavefunction of 2 dimensional polaritons, ψ, coupled with the equation for the effective two dimensional reservoir density n_R (found as the 3D density multiplied by the cavity thickness L). It includes polariton-polariton interactions, stimulated scattering from the reservoir to the condensate and energy relaxation processes [172]:

$$i\hbar\frac{\partial\psi}{\partial t} = -\frac{\hbar^2}{2m_{pol}}\Delta\psi + i\gamma n_R\psi - \frac{i\hbar}{2\tau_{pol}}\psi + \alpha(|\psi|^2 + n_R)\psi + U_{pol}\psi + i\Lambda_0\frac{n_R}{\max(n_R)}\frac{\hbar^2}{2m_{pol}}\Delta\psi \quad 5.1$$

$$\frac{\partial n_R}{\partial t} = D\Delta n_R - \frac{n_R}{\tau_R} - \gamma n_R |\psi|^2 \qquad 5.2$$

Here, m_{pol} is the polariton mass, γ is the rate of stimulated scattering, $\alpha \approx 10xE_b a_B^3 / L$ is the polariton-polariton interaction constant [173] mediated by the interaction between bulk excitons (x is the excitonic fraction), U_{pol} is the staircase potential with a step length of 2.5 µm, τ_{pol} is the polariton lifetime, Λ_0=0.01 is a dimensionless energy relaxation parameter, D is the exciton diffusion coefficient and τ_R is the reservoir lifetime. An exciton reservoir is created at t=0, together with a seed for polariton condensate at the top of this reservoir. In the case of more photonic polaritons (27% photon), the contribution of the staircase potential to the effective potential seen by polaritons is about 4 times higher than in the highly excitonic case (7% photon). This potential accelerates polaritons in one direction [174], as recently evidenced in another cavity system where the staircase potential was created by a spatially varying non-resonant pump and was acting on the excitonic part [175]. In our case, the condensate propagates along the main thickness gradient, away from the pumping area, and crosses the successive polariton modes associated with the discrete values of the 2 dimensional potential. This effect leads to the observation of a discrete series of wavevectors, corresponding to the steps of the staircase. On the contrary, in the highly excitonic case, this potential is washed out, and the only effect observed is the acceleration within the potential created by the excitonic reservoir. Since the exciton-like polaritons are heavy, the acceleration leads to a broadening of the maximum of emission in the reciprocal space, and not to the creation of two discrete wave vector states +-k, as theoretically described by Wouters *et al* [115] and observed in other ZnO cavities [41]. One can notice that similar effects were already observable in the k-space images in Figure 5.12, where one branch (LPB2 in Figure 5.12) continuously increases its photon fraction by moving along the thickness gradient. However, in this last case it might be argued that the "photonic" potential profile might change as the excitation spot moves along the thickness.

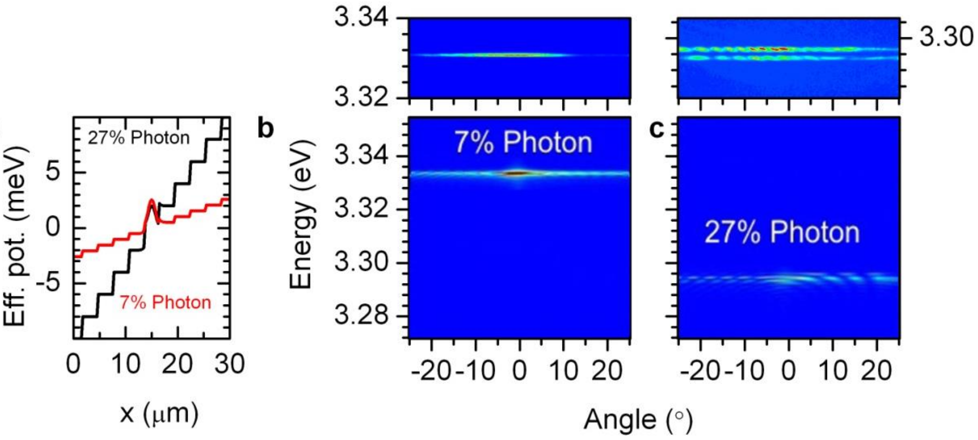

Figure 5.14: **a**. Effective potential seen by the polaritons on LPB1 and LPB2, respectively. **b** and **c**. Calculated emission of the polariton condensate created under the 2 µm pumping area and propagating in the potentials shown on **a**. The experimental results in Figure 5.13**b** and **c** are re-shown in the insets above **b** and **c** for comparison.

5.4 Laser heating during optical pumping

Before concluding this chapter it is important to address the eventual problem of sample heating due to the large excitation optical powers employed. The reason is that dielectric materials are very bad thermal conductors, compared to metals or even conventional semiconductors and, therefore, in the fully-hybrid microcavities the heating produced by the external pumping must be evacuated mostly by the active region. This bad thermal sinking might induce residual heating and raise the lattice temperature of our crystal. This effect should be, in principle, exacerbated when pumping the cavity with a femtosecond/picosecond source (in our case, pulse duration 0.13ps and 76MHz repetition rate), compared to ns excitation (0.4ns and 4kHz repetition rate), given that typically in semiconductors the timescale for thermal diffusion is in the order of ns to μs. This prompted us to use the ns excitation source for determining the complete phase diagram described in 5.2.

To address the “heating issue” of fs/ps sources, the lattice temperature was “measured” by determining the energy shift of the donor bound exciton transition as a function of excitation power. Measurements were carried out at a cryostat temperature of 75K and are shown in Figure 5.15. The measurements were taken at a sufficiently positive detuning so that lasing could not be observed before thermal effects became observable (See Figure 5.6**a** and **b**): this allows to increase the pumping power while still working below threshold. As illustrated in Figure 4.7**b**, the D^0X energy decreases with increasing temperature. By comparing this curve with Figure 5.15, the actual lattice temperature under a certain excitation power could be estimated. The importance of heat dissipation through the active layer is obvious from Figure 5.15, given that the onset of heating and its absolute value are smaller and larger, respectively, for thinner ZnO layers: for <3λ/2 cavity, effective sample heating starts at ~1pJ/pulse, while for a 2.5λ cavity it starts at ~10pJ/pulse. At high pumping powers, the actual temperature of the excited spot can be 50K~80K above the cryostat temperature, as illustrated in Figure 5.15. This effect probably contributes to the fact that polariton lasing could only be observed under fs/ps excitation up to about 200K, whereas it could be achieved up to 300K by ns excitation.

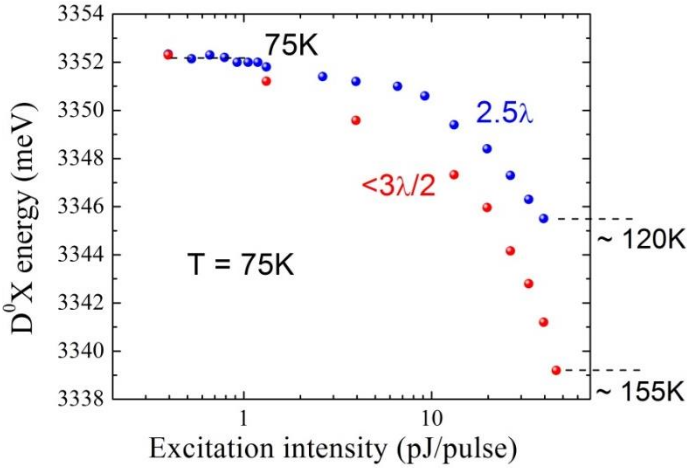

Figure 5.15: Donor bound exciton energy as a function of excitation intensity at 75K, measured on <3λ/2 (red) and 2.5λ (blue) regions. The energy redshift is taken as an internal temperature measurement for each excitation intensity.

5.5 Conclusion

In this chapter, polariton condensation was studied within a fully-hybrid ZnO microcaviy. We first demonstrated room temperature polariton lasing, and then studied the characteristics of the ZnO polariton condensate in a cavity displaying an extremely large Rabi splitting (~240meV). On the cavity thin regions (~2.5λ), we derived a complete condensation phase diagram that agrees well with a theoretical analysis of polariton relaxation in ZnO and highlights the important role of phonon-assisted relaxation in ZnO. Polariton condensation is achieved over an unprecedented range of experimental parameters: from 5K to 300K, and for excitonic fractions ranging from 17% to 96%. On the cavity thick regions (6-7λ) we demonstrated mode switching by varying either the active layer thickness or the excitation power. In both cases, the phase diagram could be experimentally tested and confirmed.

III. Semi-hybrid ZnO microcavities

Chapter 6 Fabrication and optical properties of semi-hybrid ZnO microcavities

In Chapters 4 and 5 we have developed a new strategy of cavity fabrication that has allowed us to perform studies on ZnO *polaritonics* that were hindered up to now due to a low Q. However, the fully-hybrid microcavities described in the previous chapters have some limitations: first of all, for some physical studies it is essential to have large areas with an homogeneous ZnO thickness, which was not achievable with the etching/polishing method employed in chapter 4; in particular, if polariton propagation and condensate interactions need to be controlled by predefining a given polariton potential profile, an initial flat polarion landscape is required. Moreover, and thinking in a long-term timescale, the growth of planar cavities in conventional substrates, such as sapphire and silicon, might enable the integration of polariton lasers with other functionalities. For these reasons we have developed, in parallel to the fully-hybrid approach previously discussed, a fabrication approach where we combine the epitaxial growth of a nitride-based DBR together with the epitaxial growth, thereon, of the active ZnO region (Figure 3.11**c**).

Thus, we will first introduce the cavity design and the fabrication equipment at CNRS-CRHEA (namely MBE). Then, the epitaxial growth of high-quality AlGaN/AlN DBRs and ZnO active region will be described in detail. The morphological and optical characterizations of the half and complete cavities will be shown, ending the chapter with the most recent results on nonlinear processes observed in such a cavity.

6.1 Cavity design and fabrication system

The general structure of a semi-hybrid ZnO microcavity has been shown in Figure 3.11**c**, where we have described the state-of-the-art. The challenges of such a cavity fabrication are mainly two: (1) The growth of high-reflectivity nitride DBRs and (2) the growth of high-quality ZnO active layers on the nitride DBRs. At CNRS-CRHEA these two technological aspects have been addressed in parallel during years by means of two independent MBE systems, devoted exclusively to the growth of nitrides and oxides, respectively.

6.1.1 Cavity design

The cavity structure is illustrated in Figure 6.1**a**. First, a 30-pair $Al_{0.2}Ga_{0.8}N$/AlN bottom DBR is grown on a Si (110), or Si(111), substrate by MBE, and subsequently a ZnO active layer of $7\lambda/4$ thickness is grown on the $Al_{0.2}Ga_{0.8}N$ layer (the topmost layer of the bottom DBR), also by MBE. It should be noted that the growth on silicon substrates imposes some constraints in the bottom DBR that finally determine the actual cavity design. Finally, the cavity is completed with the deposition of an 11-pair HfO_2/SiO_2 DBR by ion-beam-assisted (Ar, O_2) electron-beam vacuum evaporation. The cavity mode is designed to be at 3.25eV, i.e. about 50meV below the ZnO exciton energy at room temperature (3.3eV).

The thickness of the ZnO active region is not an integer value of half the wavelength, but rather has an extra quarter-wavelength thickness (i.e. $7\lambda/4=3\lambda/2+\lambda/4$). This is necessary because of the asymmetric refractive index distribution between the upper and lower DBRs: for the top DBR the layer in contact with the ZnO is SiO_2, which has the lower refractive index of the bilayer (n_{SiO2}=1.50, n_{HfO2}=2.13), while for the bottom DBR it is the layer with higher refractive index ($Al_{0.2}Ga_{0.8}N$) that is in contact with ZnO (n_{AlGaN}=2.456, n_{AlN}=2.15 [176]). This refractive index distribution induces a π-phase shift during one complete photon roundtrip in the cavity, which needs to be compensated for by an additional quarter-wavelength layer between the two DBR mirrors.

The cavity design is also constrained by the "epitaxial growth": on one hand, the growth of high-quality nitrides on silicon requires necessarily the deposition of an initial AlN directly on top of the substrate, which imposes thereby the actual bilayer ordering of the bottom DBR; on the other hand, the lattice mismatch between ZnO and AlGaN, irrespective of the Al composition, is smaller than with AlN, reinforcing the use of AlGaN as final bottom DBR layer. Finally, as it will be discussed later in this chapter, the ending of the bottom DBR by an AlGaN rather than AlN contributes, together with the substrate patterning, to the achievement of crack-free DBRs, which would not be possible if the DBR was finished by an AlN layer. Indeed, this last condition is the strongest of all three described. For the topmost DBR, the stacking is imposed by the fact that in order to guarantee a higher reflectivity, the material in contact with air must be that with larger refractive index (namely HfO_2).

The transfer matrix simulations of the reflectivity spectrum, prior to the introduction of ZnO excitons (i.e. without strong-coupling), and of the optical field distribution at the energy of the cavity mode are shown in Figure 6.1**b-e.** Ideally, a *Q*-factor of 38100 is expected (Figure 6.1**d**). The simulated stopband width is limited to ~340meV by the bottom DBR, whose Bragg modes are faintly observed within the larger stopband of the top HfO2/SiO2 DBR, as displayed in Figure 6.1**c**. Furthermore, the optical field penetrates more into the bottom DRB than into the top DBR, due to the smaller refractive index contrast of $Al_{0.2}Ga_{0.8}N$/AlN compared to HfO2/SiO2.

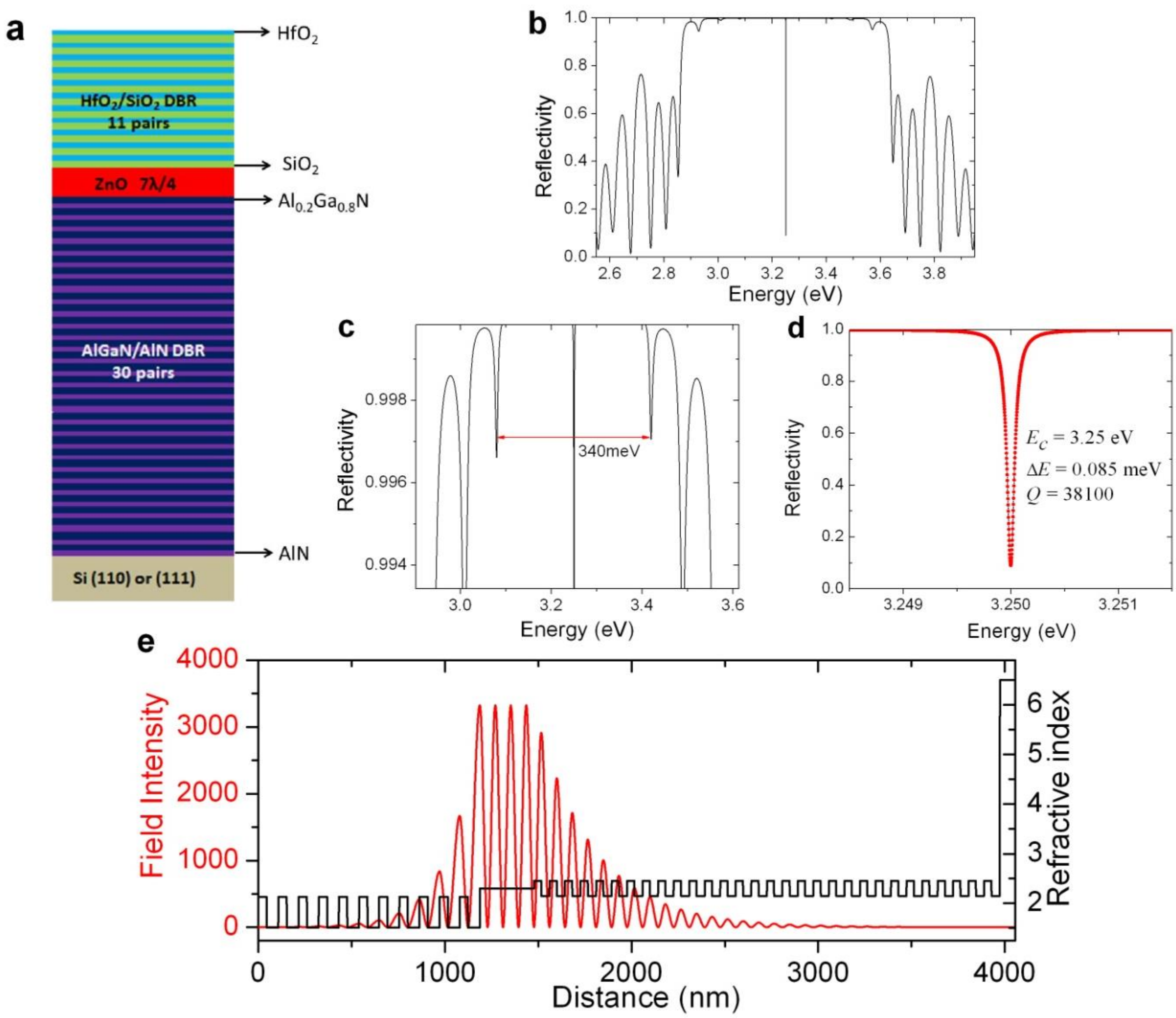

Figure 6.1: The cavity design: **a**. Schematic picture of the semi-hybrid ZnO microcavity structure. **b**. The calculated reflectivity. **c**. An enlarged view of **b** near the cavity mode. **d**. A detailed look of the cavity mode. **e**. The calculated optical field distribution of the cavity mode. The cavity is designed with $E_{cav} = \bar{E}$=3.25eV. For **e**, the incident light is from the left side at zero angle with an intensity of 1.

As described in the state-of-the art section, the Q of semi-hybrid cavities fabricated on Si, as developed by CRHEA, was limited to about 600 (while it was calculated to be slightly less than 1000) because of the limited number of nitride pairs that could be used. Indeed, at that time the cracks appearing due to the thermal expansion mismatch between nitrides and silicon precluded the use of more than thirteen AlN/AlGaN pairs, as the crack density was typically in the order of $1\mu m^{-1}$. Since, as it will be described later, the number of nitride pairs is no longer a constraint the main factors taken into consideration for fixing the number of pairs in the DBRs are: (1) The calculated Q-factor of the cavity structure, which we want to be larger than 10000; (2) The symmetry in the reflectivity values of the two DBR mirrors. A Fabry-Perot microcavity works most efficiently when the two mirrors have identical reflectivity values: If one of the mirrors has a much lower reflectivity than the other, the first essentially limits the cavity Q-factor while further increasing the reflectivity of the “better” mirror does not improve much the cavity properties. With these considerations in mind, transfer matrix simulations were conducted to analyze the influence of the DBRs number of pairs on the cavity *Q*-factor. As shown in Figure 6.2**a**, more than 22 pairs of nitride bilayers can provide, in the ideal case, a cavity *Q*-factor larger than our 10000 target, whereas above 30 pairs (and for 11 pairs in the dielectric DBR) the initial exponential increase of the *Q*-factor saturates at about 40000. Thus, it was decided to fabricate a 30-pair bottom nitride DBR. A similar trend is observed in Figure 6.2**b** for the number of pairs within the dielectric DBR. Moreover, from the experimental point of view it is preferable to have the top DBR slightly less reflective than the bottom DBR, given that light extraction for PL measurements must occur through this last one. Thus, a combination of 30 pairs in the bottom DBR and 11 pairs in the top DBR should be a good tradeoff between reflectivity balance and light extraction, while keeping a sufficiently high *Q*-factor (~40000).

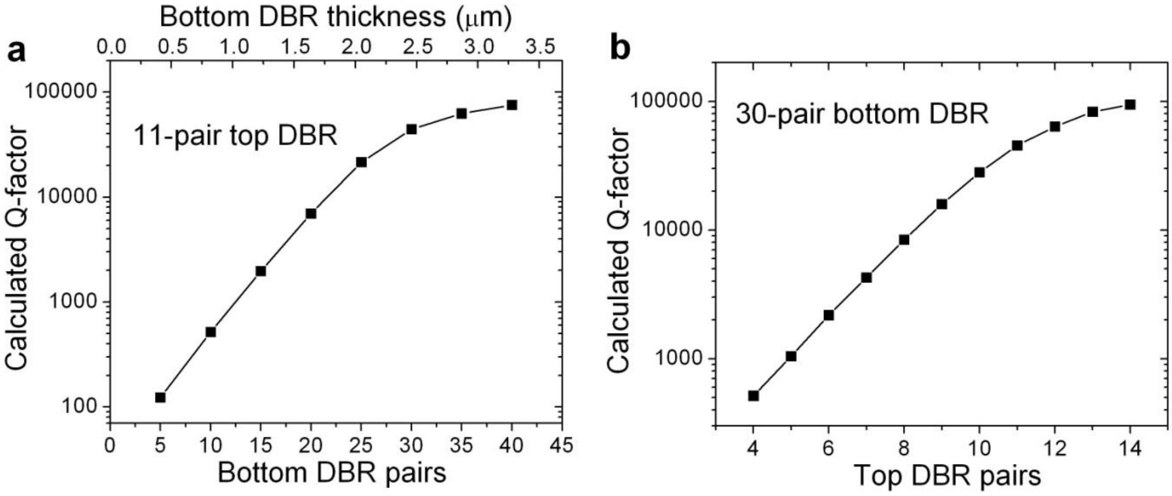

Figure 6.2: Calculated cavity *Q*-factor as a function of **a**. number of bottom $Al_{0.2}Ga_{0.8}N/AlN$ DBR pairs with 11-pair top HfO_2/SiO_2 DBR, **b**. number of top HfO_2/SiO_2 DBR pairs with 30-pair bottom $Al_{0.2}Ga_{0.8}N/AlN$ DBR, supposing a 7λ/4 ZnO bulk cavity.

It is important to notice that during the fabrication process it is very difficult to control the epitaxial growth or dielectric material deposition to have exactly the same parameters as designed by simulation. These deviations can sometimes lead to considerable differences between the expected and the actual performance of the cavity. Figure 6.3 shows the refractive indices of the $Al_xGa_{1-x}N$ alloy measured by Antoine-Vincent *et al* [176], from which on can see that the refractive index of $Al_xGa_{1-x}N$ at ~375nm is very sensitive to the Al composition around x=0.2 (which is our case). During the DBR growth the Al/Ga flux has a gradient across the 2-inch wafer, which results in a variation of the x value over the different regions of the sample, thus leading to a variation of refractive index *n*. Moreover, the thickness of each DBR layer, which is supposed to be $\lambda/4n$, can deviate from this value due to the variation or imprecision on both *n* and on the growth rate. As a result, the actually achieved cavity can be quite different from the ideal one in terms of cavity *Q*-factor, DBR stopband width, DBR penetration depth, etc., even if effects such as interface roughness or residual absorption are neglected.

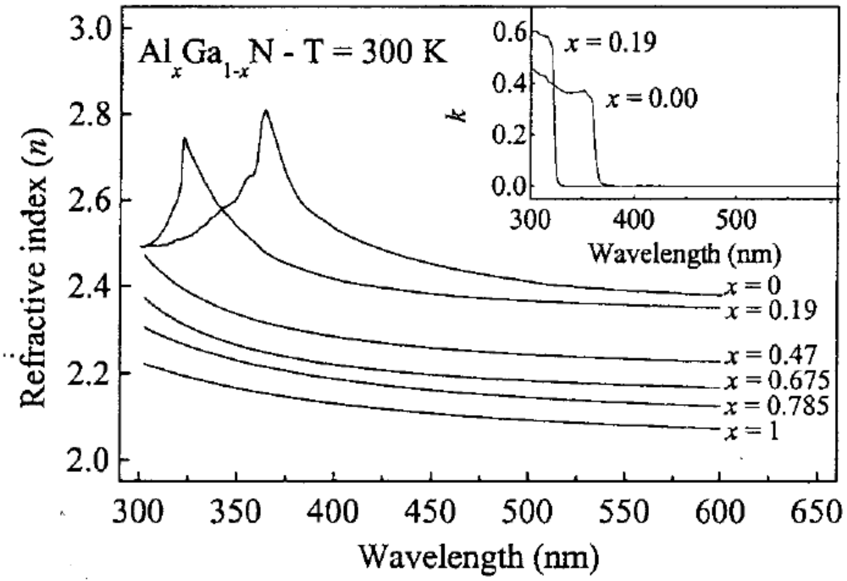

Figure 6.3: Extracted from Reference [176]. Evolution of the refractive index *n* as a function of the wavelength for several Al compositions of $Al_xGa_{1-x}N$ alloy (x=0; 0.19; 0.47; 0.675; 0.785; 1). The inset displays the extinction coefficient *k* for x=50 and x=0.19.

6.1.2 Molecular beam epitaxy

Molecular beam epitaxy (MBE) is widely used in research to grow single crystals, mainly for making semiconductor devices and heterostructures [177]. It was invented in the late 1960s at Bell Telephone Laboratories by J. R. Arthur and Alfred Y. Cho [178]. The operating principle of the MBE is illustrated in Figure 6.4. The chamber where the growth takes place is sketched in Figure 6.4**a** [179]. The stainless steel chamber is continuously pumped to maintain an ultra-high vacuum, typically in the order of ~10^{-10} Torr, which increases to about $10^{-7}/10^{-5}$ Torr during the growth runs, and that results in a very long mean-free-paths for atoms and molecules travelling inside. Most of the source materials (e.g. in this thesis the Zn), are contained in heated cells named Knudsen cells. The vapor of the material produced by heating the cells enters the growth chamber through a small orifice and forms a molecular/atomic beam (in the ultra-high vacuum environment), which can be turned on and off with precise timing using electronically controlled shutters. Molecular/atomic beams from different cells arrive at the substrate where they may react and form epitaxial layers of compound semiconductors. The flux of each molecular/atomic beam is controlled through the temperature of each Knudsen cell, allowing to adjust the ratio of the reactants. For gas elements (e.g. Nitrogen and Oxygen), a plasma generator combined with a mass-flow controller is used instead of the effusion cell; the properties of the generated plasma depend, mainly, on the power of the RF plasma source. Both, the gas and the solid sources employ ultra-high purity raw material that guarantees the quality of the epitaxial layer in terms of residual contamination.

The substrate is mounted on a holder that allows to heat the substrate from the backside by radiation. The substrate can be rotated with a uniform rate during the epitaxial growth, although for the specific case of microcavity structures it is usually stopped in order to induce a thickness and/or composition gradient. During the growth, liquid nitrogen is continuously flowing to cool the chamber walls, so that any material that does not incorporate into the growing crystal will be either pumped or get stuck to the cold surroundings. The growth conditions controlling the quality of the final crystal are mainly the substrate temperature and the fluxes of the different sources (eventually only their ratio). The chamber pressure during the growth is also an important parameter, whose exact value depends on the substrate temperature, source fluxes and pumping rate.

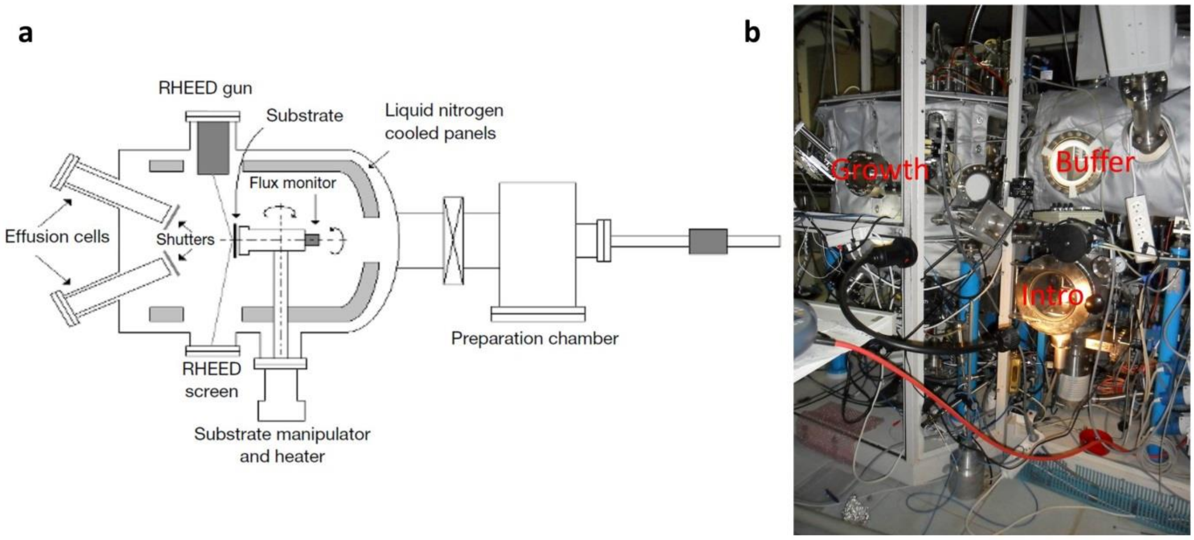

Figure 6.4: Molecular beam epitaxy. **a**. Schematic diagram of an MBE growth chamber (Extracted from Reference [179]). **b**. The ZnO MBE equipment (RIBER Epineat II-VI) at CNRS-CRHEA, with the introduction, buffer and growth chambers identified.

One advantage of MBE compared to other epitaxial reactors is that it allows *in-situ* monitoring techniques to control the growth, among which reflection high-energy electron diffraction (RHEED) is the most commonly used technique, but not the only, for characterizing the epitaxial surface. As sketched in Figure 6.4**a**, RHEED requires an electron gun and a luminescence detector screen. An electron beam generated by the electron gun impinges on the sample with a very small angle relative to the sample surface. As the lattice of the semiconductor is comparable with the De Broglie wavelength of the electrons, the electrons diffracted by the atoms at the sample surface undergo constructive interferences and form regular patterns on the RHEED screen. The resulting pattern provides important information of the sample surface as it is directly related to the arrangement of surface atoms. In the case of two-dimensional (2D) growth, where the sample surface is atomically flat, the electrons are diffracted by a planar atomic array that results in streaky RHEED patterns that remind of crystal truncation rods, as in X-ray diffraction. On the contrary, if the surface is three-dimensional (3D), the electrons are diffracted (even travel through the material) into different angles resulting in spotty RHEED patterns. For polar ZnO, the diffraction patterns can be recorded along two different in-plane directions separated by 30°. Since the lattice spacing along each of these directions is different, the associated RHEED pattern spacings will be accordingly different.

The MBE machine used during this PhD is a RIBER EPINEAT II-VI model, initially dealing with the growth of ZnSe-based materials, and since about 2002 mainly working on ZnO-based materials. It contains four chambers, although only three were used during this thesis: one for introducing the samples into the reactor, one for distributing samples into neighboring chambers, and the growth chamber properly speaking. These are depicted in Figure 6.4**b**. Vacuum valves are used to isolate (valve close) and connect (valve open) different chambers. Each chamber is pumped individually to enable independent operations. The substrate is loaded into the introduction chamber by venting it to ambient pressure (which is pumped again after loading the sample), and transferred with electronically-controlled mechanical arms to the buffer and the growth chamber to start the epitaxy. Sources such as Zn and O cells are located underneath the growth chamber, and the molecular/atomic beams are directed upwards to the substrate surface, which is facing down. The substrate holder is located on a rotation stage and heated from the backside. Two temperature sensors are mounted inside the growth chamber at different locations behind the sample, and give an indication, rather than an absolute measurement, of the substrate temperature. A more accurate measurement of the sample surface temperature is given by a pyrometer, which is placed underneath the growth chamber, but again some approximations must be done to extract the temperature (namely, the emissivity of the surface must be accurately known, which is usually not the case). Thus, again, the obtained temperatures must be considered as reference temperatures enabling to compare between different runs, but they cannot be taken as absolute measurements. A flux gauge can be inserted into the growth chamber to measure the Zn beam flux, whereas an estimation of the actual “active” oxygen flux can be obtained by combining the mass-flow controller information with the residual pressure inside the chamber during the growth run.

6.2 $Al_{0.2}Ga_{0.8}N$/AlN DBRs on Si substrate

The first step to achieve the cavity structure in Figure 6.1**a** is the growth of high quality nitride DBRs. As shown in Figure 6.5 [180], in terms of refractive index contrast the optimum materials for nitride DBRs are AlN/GaN, which exhibit $\Delta n/n$ =20% (where Δn is the refractive index difference between the two materials and n the average refractive index of the two materials). However, due to the large lattice mismatch (2.5%) and large thermal expansion coefficient mismatch (-24.9%) between AlN and GaN, the resulting DBR quality is far below that expected. To overcome these difficulties, the team of N. Grandjean at EPFL has developed AlInN-based DBRs, namely $Al_{0.2}Ga_{0.8}N/Al_{0.85}In_{0.15}N$ [135], which are almost lattice matched while keeping $\Delta n/n$=~10%. Indeed, as already introduced in 3.3.2, by using these materials combination they have been able to achieve Q-factors of several thousands (~2000 in strongly-coupled cavities working in the UV[136], and up to 6400 in weakly-coupled cavities working in the visible [181]). In fact, during this thesis and in the framework of CLERMONT4, we have attempted to fabricate ZnO bulk microcavities on top of $Al_{0.2}Ga_{0.8}N/Al_{0.85}In_{0.15}N$ DBRs provided by EPFL, which exhibited smooth surfaces and high reflectivities. However, due to a reduced number of samples provided for growth optimization and the difficulties in detecting and controlling the substrate temperature, growth of high quality ZnO active layers could not be achieved. Details on this series of experiments can be found in Appendix B.

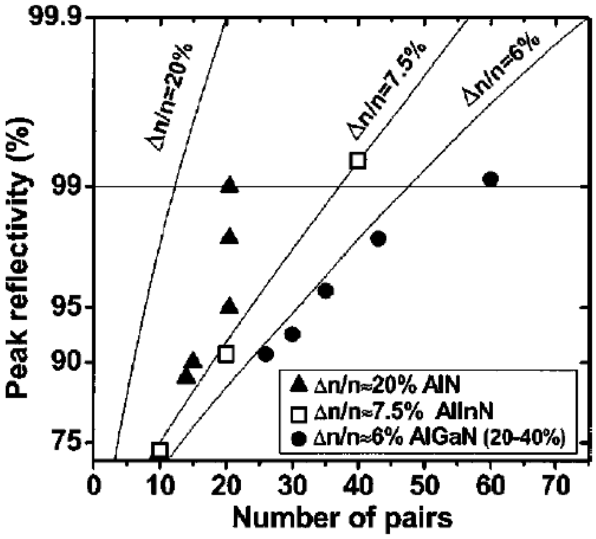

Figure 6.5: Extracted from Reference [180]. Reflectivities of various nitride DBRs as a function of the number of pairs. Symbols correspond to reflectivity measured using AlGaN/GaN or AlInN/GaN DBRs. Full lines are calculated peak reflectivities for various refractive index contrasts ($\Delta n/n$).

Meanwhile, at CNRS-CRHEA the MBE growth of AlN, GaN and $Al_xGa_{1-x}N$ on Si substrates has been intensively studied in the group of F. Semond for fabricating high-quality $Al_xGa_{1-x}N$/AlN DBRs and microcavities [130,132,133]. Indeed, the couple $Al_{0.2}Ga_{0.8}N$/AlN has larger refractive index contrast ($\Delta n/n$ = ~13%) than $Al_{0.2}Ga_{0.8}N/Al_{0.85}In_{0.15}N$, which should lead to larger stopband widths and higher reflectivity, for the same number of pairs.

6.2.1 Growth of thick GaN on patterned Si substrate

As our cavity design contains a 30-pair $Al_{0.2}Ga_{0.8}N$/AlN bottom DBR, a total thickness of ~2.5µm (See top axis of Figure 6.2**b**) nitride layer needs to be grown on the Si substrate. However, growing high-quality (i.e. with low dislocation density and crack-free) thick GaN[1] layers (>1µm) on Si has remained a big challenge for a long time. The major problem lies in the large thermal expansion coefficient mismatch (56%) between GaN and Si, which induces tensile strain during the post-growth cooling that ends up with formation of cracks, as shown in Figure 6.6. Many attempts have been made to increase the critical thickness using multiple layer stacks on planar silicon substrates [125,182-184]. Another option to prevent the appearance of cracks in thick GaN on Si is to pattern the substrate, which is, though, found only in a few previous reports [185-187]. Currently, this strategy has been adopted and intensively studied at CNRS-CRHEA by B. Damilano, Y. Cordier and F. Semond.

---

[1] In our DBR structure we need to grow $Al_{0.2}Ga_{0.8}N$, which exhibits the same difficulties as the GaN growth on Si.

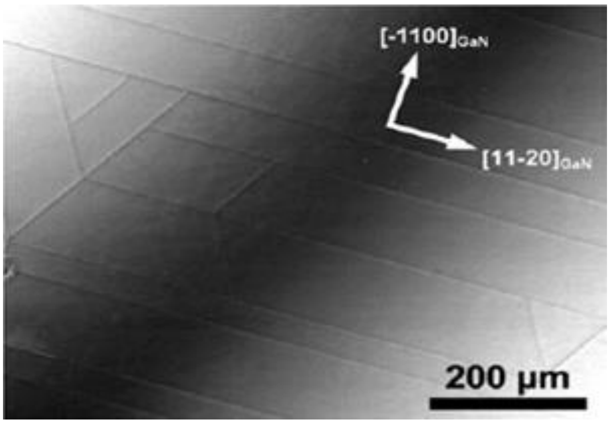

Figure 6.6: Extracted from reference [188]. Optical microscope image showing cracks on an epitaxial GaN layer on Si.

As can be seen in Figure 6.6, where the SEM image of a polar GaN(0001)-on-Si(111) layer is shown, the cracks on GaN propagate along the <1 1 $\bar{2}$ 0> directions, parallel to the *m*-plane. These cracks appear due to an accumulation of tensile strain during the cooling-down and can propagate from the surface of the nitride down to the substrate. Since free surfaces enable efficient strain release [189], the idea behind the recent achievements on growing thick nitride-based DBRs was to create free-surfaces on GaN structures [190,191]: sufficiently large to provide enough space to perform physical studies and even fabricate GaN-based devices (including LEDs), and sufficiently small so that free-surface induced strain relaxation is still effective.

While the most frequently used Si substrate for GaN growth is Si (111), Si (110) has also allowed for obtaining GaN at least as good as that on Si (111) [187,192]. Thus, both kinds of substrates have been patterned. Si (110) is most adapted for using KOH etching technique, as illustrated in Figure 6.7. The Si (110) substrate is patterned with diamond shapes, where the resulting etched side walls are {111} planes. The reason is the anisotropic KOH etching exhibited by Si: the etching rate of the Si (111) plane is two orders of magnitude slower than that of Si (110) planes [193]. As a result, steep sidewalls are formed at the edges of the mesa, which serve as the free walls to release the tensile strain (together with the free walls of the growing GaN). Besides KOH etching, dry SF_6 etching can also be used to make mesas on Si substrates, in which case both Si (111) and Si (110) can be etched with steep sidewalls since the dry etching itself is very directional, normal to the substrate surface. The designed diamond mesa sizes range from 50µm×50µm to 400µm×400µm, with an expectation (confirmed by numerical simulations) that smaller mesas are more likely to result in crack-free GaN layers. Triangle and hexagonal shaped mesas are also designed on some parts of the wafer.

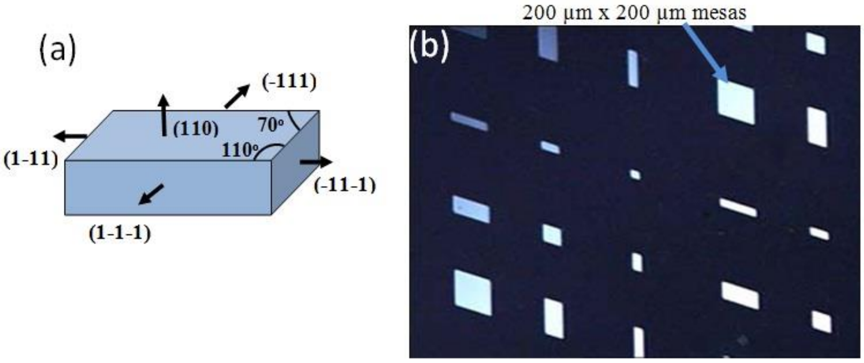

Figure 6.7: Extracted from Reference [190]. **a**. Schematics of a diamond-shaped mesa on Si(110) with four vertical (111) sidewalls. **b**. Optical microscopy image of a patterned Si(110) substrate with different sized and shaped mesas.

The nitride-DBRs epitaxially grown on patterned Si substrates employed in this thesis were fabricated by ammonia-assisted MBE by M. J. Rashid and G. Gommé, in the group of F. Semond at CNRS-CRHEA. Details on the substrate processing and GaN growth can be found in the PhD manuscript of M. J. Rashid [190]. Just to illustrate how powerful strain-relaxation is in such mesas structures, a record thickness of crack-free GaN on Si (8.3µm) was achieved in CRHEA with the help of only one AlN interlayer, as shown in Figure 6.8. This thickness should be compared to ~1µm, which would have been possible on non-patterned Si substrates.

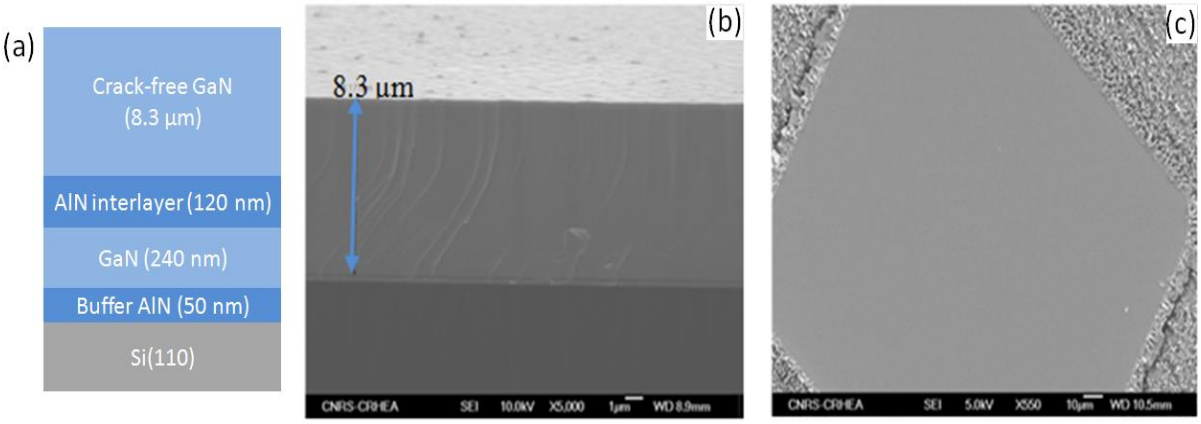

Figure 6.8: Extracted from Reference [190]. **a**. Schematic stacking layers of AlN and GaN on Si(110). **b** and **c**. The cross-section (**b**) and top-view (**c**) scanning electron microscopy (SEM) images of an 8.3 µm thick crack-free GaN layer on a 200 µm × 200 µm diamond-shaped mesa.

6.2.2 $Al_{0.2}Ga_{0.8}N$/AlN DBRs on patterned Si substrate

The technique developed for growing thick GaN on Si is a good starting point for fabricating high quality $Al_{0.2}Ga_{0.8}N$/AlN DBRs with large number of pairs. Indeed, according to our previous experience on non-patterned Si substrates, only 4 pairs of $Al_{0.2}Ga_{0.8}N$/AlN could be stacked without creating cracks. If one continues to grow more pairs regardless of the cracks, finally at 12 to 13 pairs the crack density is so large that the *Q*-factor of the resulting cavity is dramatically affected. This limited the *Q*-factor of our previous cavities to below 600. In this section we will show that by growing on patterned Si substrate, the quality of the DBR and of the resulting cavity can be greatly improved.

30-pair crack-free $Al_{0.2}Ga_{0.8}N$/AlN DBRs on Si(110) and Si(111) substrates have been fabricated and used subsequently for growing ZnO on it. The crack-free DBRs show a total thickness of ~2.5µm. Figure 6.9 shows the typical morphological characterization of the DBR, clearly demonstrating that all the requirements for a high quality DBR are well met: The mesa is completely crack-free (Figure 6.9**a**), the surface RMS roughness is ~1.6nm, with atomic terraces clearly identified (Figure 6.9 **b** and **c**), and the interfaces between layers are sharp and clear (Figure 6.9**d**).

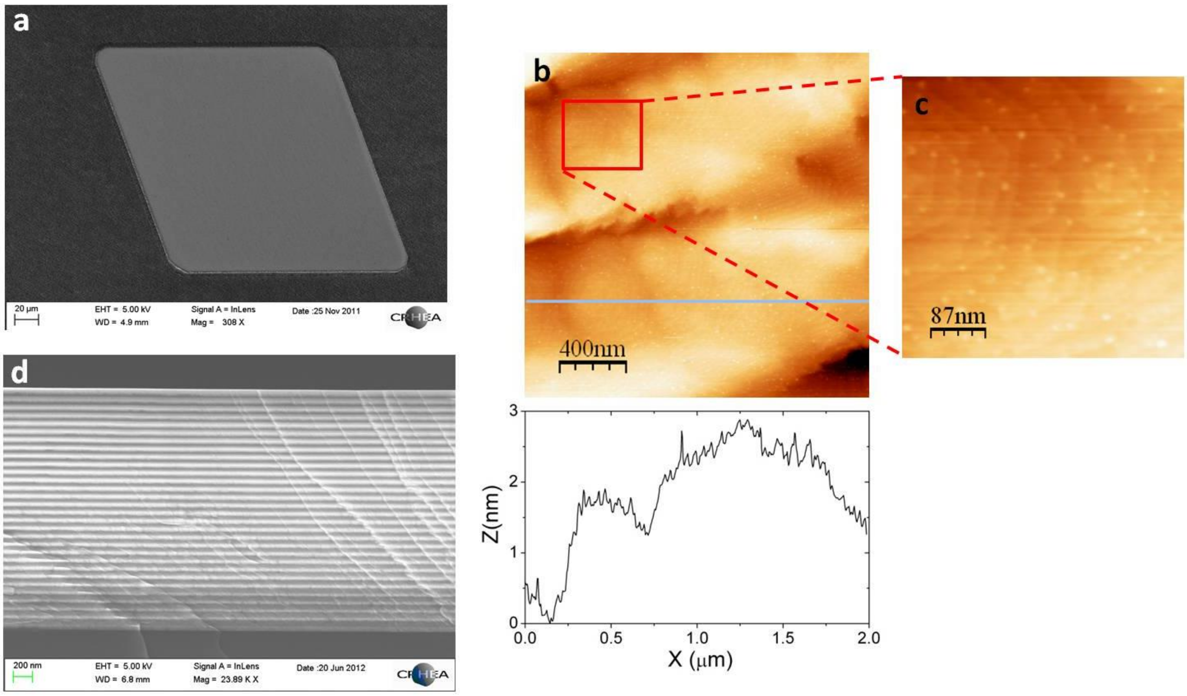

Figure 6.9: Characterization of a 30-pair crack-free $Al_{0.2}Ga_{0.8}N$/AlN DBRs **a**. SEM image of the DBR structure on a 200µm×200µm mesa exhibiting no cracks. **b**. AFM image of the DBR surface demonstrating a RMS roughness of ~1.6nm. The lower panel shows the height profile along the solid line drawn in the upper AFM image **c**. Enlarged view of the red square region in **b**, with atomic terraces clearly seen. **d**. SEM cross-section image of the 30-pair DBR.

The DBRs were optically characterized by reflectivity measurements at Institut Pascal by F. Réveret, from the team of J. Leymarie. Typical spectra measured on the DBR fabricated on a 2-inch Si (110) substrate patterned by KOH etching along the wafer radius are shown in Figure 6.10. While there were some exceptions, for sufficiently small mesas (typically for mesas of lateral size equal or smaller than 200µm) the majority of them are crack-free right after the DBR fabrication. The spectrum in Figure 6.10**a** exhibits a stopband width of ~200meV (FWHM). It is notable that the value of the stop-band width at the measured point does not agree well with our cavity design (~340meV) shown in 6.1.1. Several explanations might be found. These include: a larger Al content in the AlGaN, which would result in a smaller stopband width, as well as the lack of precision in the refractive index of AlGaN in the energy region 3.2-3.6eV, combined with a large variation of the refractive index in this region for small variations of Al content (see Figure 6.3). Indeed, by estimating the $Al_xGa_{1-x}N$ bandgap [194], which corresponds to the end of the oscillation (~4eV) in the reflectivity spectrum, an Al composition of x=0.24 was estimated. To fit the measured reflectivity with transfer matrix simulation (red dashed line of Figure 6.10**a**), refractive index n_{AlGaN}= 2.335 is actually applied. Furthermore, since during the DBR growth the substrate was not rotated, an Al/Ga-flux gradient over the 2-inch sample[1] was obtained; this creates a variation of stop-band position and width, as shown in Figure 6.10**b.** When moving across the sample (along the direction of the arrow), the stop-band width decreases, indicating a reduction of the Ga composition in the AlGaN layers. This, in turn, reduces the refractive index contrast between AlGaN/AlN. Meanwhile, the stop-band position shifts to lower energy, indicating a thickness gradient of the DBR layers along the wafer radius. Although the gradients of Al/Ga flux and layer thicknesses might render some regions of the sample useless for our studies (e.g. several spectra in Figure 6.10**b** are too high in energy for ZnO microcavities), it is important to have them from a practical point of view: (1) They can follow (or not, depending on the sample orientation with respect to the Zn and oxygen cells) the same trend as the cavity mode energy, allowing us to access a certain range of exciton-photon detunings that would be, otherwise, not accessible within the same sample because of stopbands spectrally shifted; (2) they guarantee, if the sample has been correctly grown, that there are always "useful" regions (e.g. in Figure 6.10**a**) on the sample suitable for ZnO cavity fabrication, despite a considerable imprecision of parameters compared to the ideal cavity design.

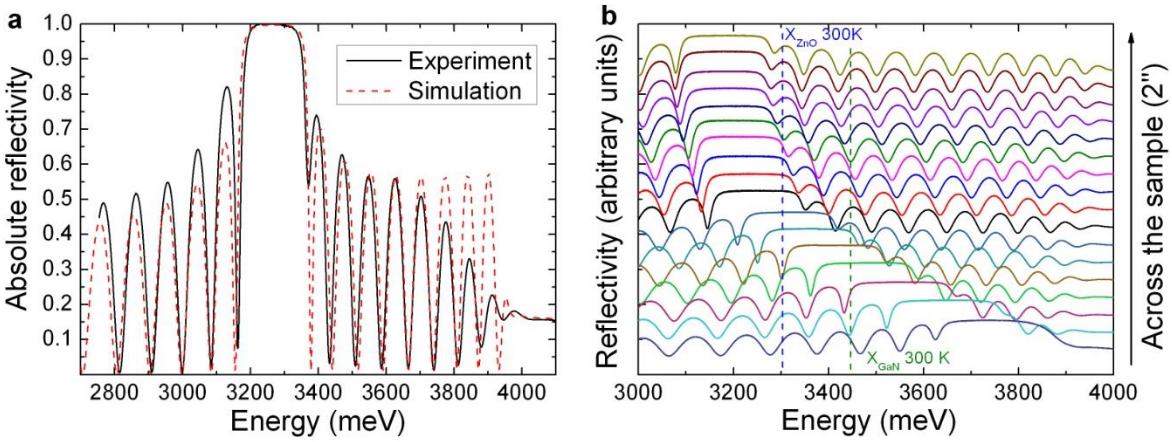

Figure 6.10: The room temperature reflectivity measurements on the 30-pair crack-free $Al_{0.2}Ga_{0.8}N$/AlN DBRs. **a**. Reflectivity spectra measured on one mesa at the wafer center with the corresponding simulated spectrum (red dashed line). **b**. Reflectivity on a series of mesas across the whole sample (2 inch in size). The Al/Ga flux and thickness gradients over the sample change the stop-band position and width.

6.3 Growth of the ZnO active layer: optimizing growth conditions

Once crack-free $Al_{0.2}Ga_{0.8}N$/AlN DBRs on patterned substrates were obtained, the next step was to grow high-quality ZnO layers on them, which constitutes one of the major tasks of this thesis. One of the main difficulties in growing ZnO on nitrides is their relative large lattice mismatch, which amounts to 1.9% for the growth on GaN and to 4.3% for the growth on AlN

---

[1] The Al and Ga beams are not incident normally to the substrate surface but at a certain angle, as sketched in Figure 6.4**a**. Furthermore, this angle depends on the distance of the considered point on the sample with respect to the position of the cell. Thus, even if the sample was rotated, there would be a composition gradient.

[195]. For $Al_{0.2}Ga_{0.8}N$, with an in-plane lattice parameter obtained by assuming Vegard's law, this value amounts to 2.3%.

The ZnO epitaxy is done in the MBE system EPINEAT II-VI introduced in the previous sections. Since it takes much time and effort to fabricate one $Al_{0.2}Ga_{0.8}N$/AlN DBR sample, it was important to ensure that we have the growth conditions perfectly adapted to this epitaxy before actually entering the DBR sample into the growth chamber. Thus, the optimization of the growth conditions had three stages:

Stage 1: growth conditions are initially optimized using commercially-available MOCVD-grown GaN/Sapphire templates. These MOCVD-grown GaN/sapphire templates exhibit Ga polarity, which is the same as the MBE-grown nitride layers on silicon substrates. This point is especially important since the optimum growth conditions for polar ZnO depend mainly on its polarity (i.e. Zn or O polarity), and the ZnO polarity, when grown on nitrides layers, is determined by that of the underlying nitride layer. Thus, since GaN/sapphire and GaN/Si templates exhibit the same polarity, it is possible to use the commercial templates for optimizing the growth conditions.

Stage 2: since for a given heater power the achieved substrate temperature is different depending on the nature of the substrate (sapphire or silicon), we employed samples having only a few layers of nitrides on silicon, and ending by an AlGaN layer, to refine the growth temperature. Besides, given that the surface morphology of the GaN/Sapphire and GaN/Si samples is slightly different (e.g. Figure 6.11), some refinement would have been necessary anyway. Furthermore, we employ these samples to determine precisely the ZnO growth rate on the nitrides/Si templates.

Stage 3: the ZnO growth on the DBR is carried out keeping exactly the same growth parameters that have been previously obtained. In this step the expected ZnO thickness is provided by the cavity design, for which we rely on the growth rate derived in Optimization Stage 2.

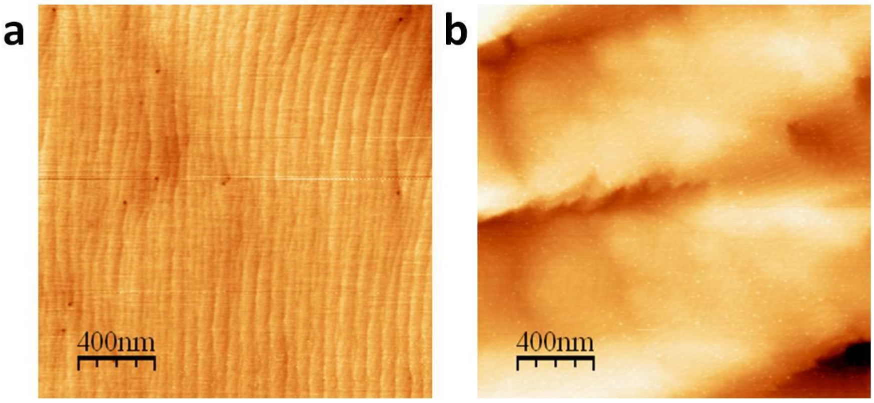

Figure 6.11: **a**. 2×2μm^2 AFM image of GaN/Saphire template displaying RMS roughness of ~0.2nm. **b**. 2×2μm^2 AFM image of 30 pairs of AlGaN/AlN DBR on Si displaying RMS roughness of ~1.6nm.

6.3.1 Influence of growth parameters

In order to illustrate the optimization of certain growth parameters, as carried out for the microcavity series on patterned DBRs, SEM images and RHEED patterns will be employed as a qualitative measure of the samples quality (mainly the surface quality).

For the growth series considered for illustration, 15 growths were carried out, including 8 trial growths on GaN/Sapphire templates, 5 trial growths on AlGaN/AlN/Si templates, and 2 growths on 30-pairs AlGaN/AlN DBRs on Si (full cavities Z1214 and Z1232). During the optimization, three factors were found to be crucial for achieving good ZnO growth:

(1) *The substrate temperature should be sufficiently high.* Typically, on AlGaN/Si templates the temperature should range from 560°C to 630°C. While higher temperatures do not reduce or improve the surface quality, lower temperatures result in a 3D rough surface. Figure 6.12 compares the RHEED and SEM images of two samples grown at different temperatures, while keeping the other parameters identical.

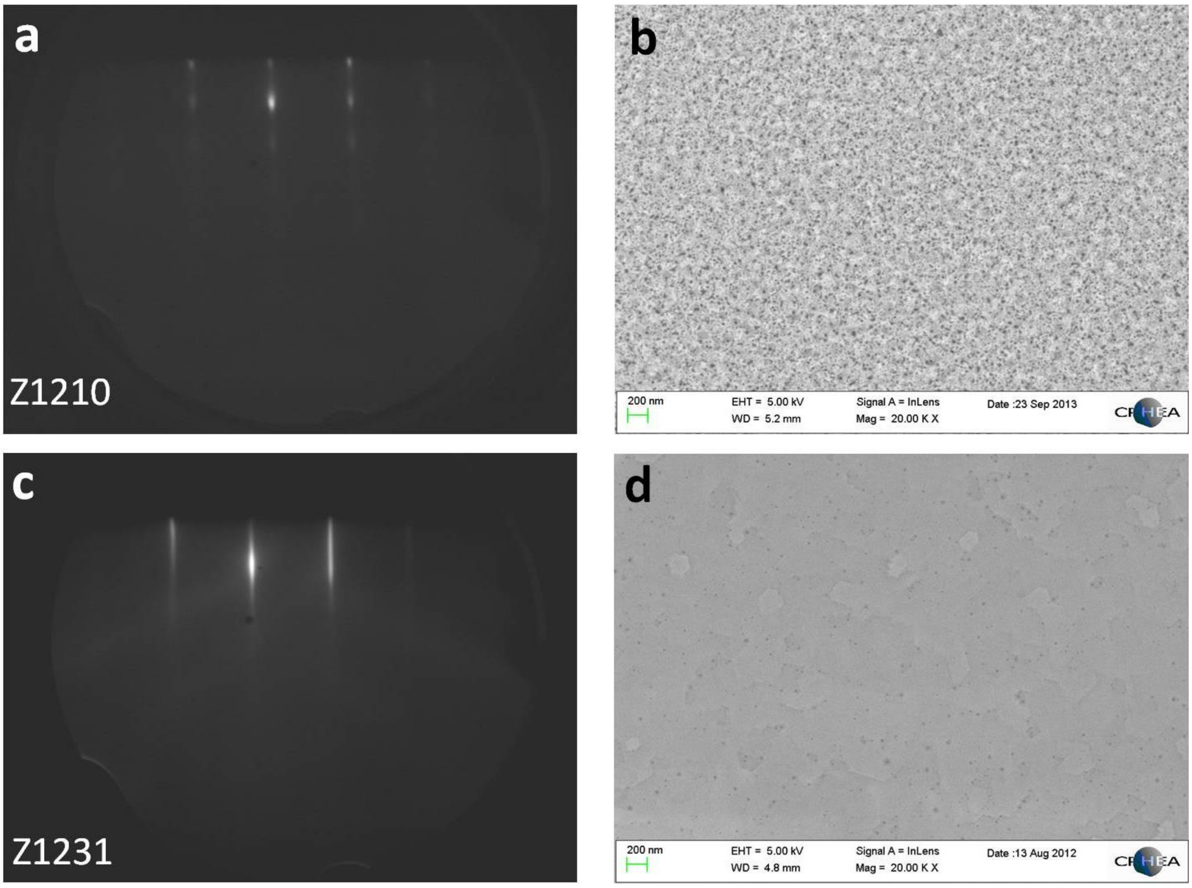

Figure 6.12: Final RHEED (**a** and **c**) and SEM images (**b** and **d**) of two samples grown on AlGaN/Si at different substrate temperatures. **a** and **b** correspond to a growth temperature of T= ~530°C (P=57%), while **c** and **d** correspond to a growth temperature of T=~610°C (P= 69%). All the other growth conditions were kept constant.

It is worth to mention that during the growth, two parameters provide useful information on the temperature of the substrate: the heater power, P, and the substrate surface temperature, T, as measured by a pyrometer. On the one hand, even if we keep P constant, the actual temperature of the employed substrate might be different from sample to sample, since it is influenced by many other factors besides the heating power; in particular, by the thermal conductivity of the substrate and the nature of the sample holder (term in which we include eventual deposits on the holder from previous growths). On the other hand, the temperature measured by the pyrometer depends strongly on the emissivity of the materials, which leads to large differences in the measured T between the optimum growth conditions on GaN/Sapphire (~450-500°C) and on AlGaN/Si (~560-630°C). The situation is even more complicated for the DBRs, which have stacks of more than 60 layers and a patterned surface.

(2) *The Zn-to-O ratio should be sufficiently high* (i.e. the growth should be conducted under Zn-rich conditions, for which the growth rate is limited by the oxygen), which is a consequence of the Zn-polarity adopted by the ZnO layer during growth [196,197]. The Zn-beam flux is mainly givenby the Zn cell temperature, while the O plasma flux is governed by the mass-flow controller located before the entrance of the plasma cell. Figure 6.13 shows the comparison between one sample with the optimal Zn-to-O ratio and a sample with a much smaller Zn-to-O ratio, while keeping other parameters similar.

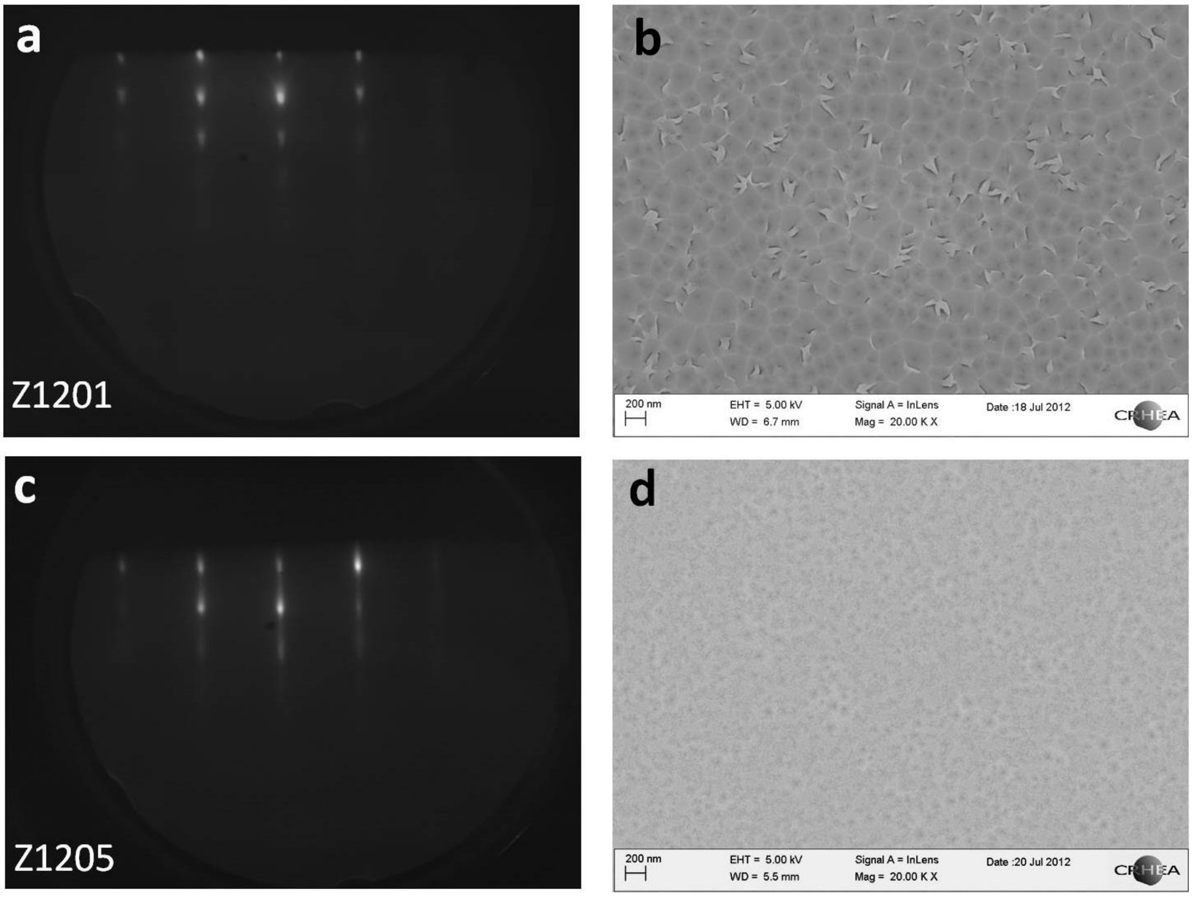

Figure 6.13: Final RHEED (**a** and **c**) and SEM images (**b** and **d**) of two samples grown with different Zn-to-O ratios. **a** and **b** correspond to a Zn cell temperature of 570°C and an O flux of 0.3sccm, while **c** and **d** correspond to a Zn cell temperature of 600°C and an O flux of 0.15sccm.

(3) *A postgrowth annealing improves the final morphology.* Its effect can be inferred from Figure 6.14, which compares the surface properties of one sample before (as shown in Figure 6.13**c** and **d**) and after (as shown in Figure 6.14) the annealing.

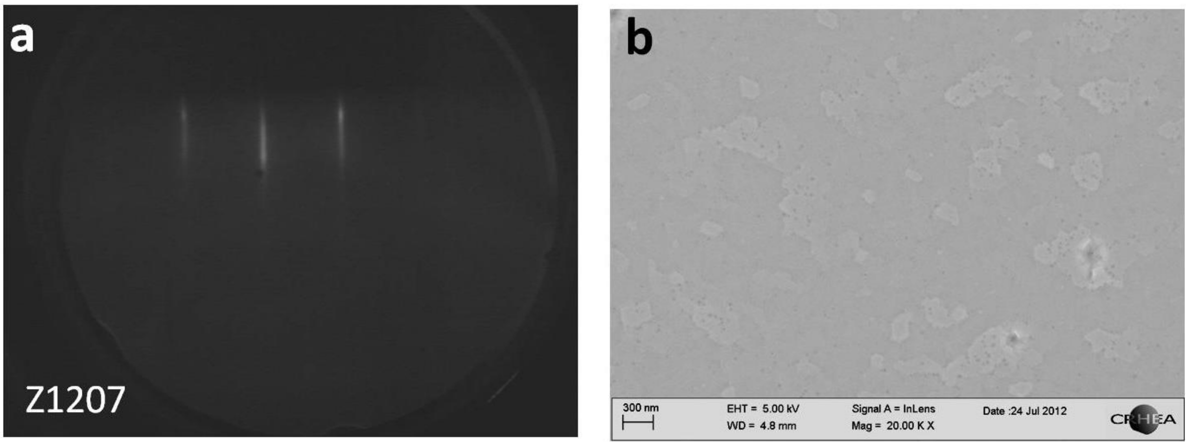

Figure 6.14: Final RHEED (**a**) and SEM image (**b**) of the sample in Figure 6.13**c** and **d** after a postgrowth anealing.

6.3.2 ZnO microcavity: growth sequence

The growth of high-quality ZnO to be used in optical microcavities suffers from a very stringent, and necessary, condition: smooth surfaces and high crystalline quality must be obtained for very thin layers, in the order of hundreds of nanometers. This reduced thickness limits the possibility of improving the crystalline quality by thickening or by applying typical strategies (such as 3D to 2D transitions) that are commonly employed in other material systems. Therefore, even if ZnO/ZnMgO MBE growth has been intensively studied since the early 2000s on Sapphire[198,199], Si [200,201], and more recently on ZnO substrates [202], the growth of microcavities active layers on nitride DBRs has required a dedicated study in its own, which has been carried in CRHEA since 2007.

Indeed, to successfully grow a “thin” ZnO layer on $Al_xGa_{1-x}N$ meeting the previous requirements, three steps are usually employed:

Step (1): Several ZnO monolayers are deposited on the $Al_xGa_{1-x}N$ at low temperature (less than 350°C). The main reason why we need to introduce these monolayers is that at high temperatures, as those used for the growth, the sticking coefficient of Zn atoms on $Al_xGa_{1-x}N$ is relatively low. After the initial deposition, the substrate is heated to high temperature (substrate temperature as used in 6.3.1) under an oxygen plasma so that the thin ZnO layer is “annealed” under oxygen-rich conditions.

Step (2): A ZnO bulk layer, of the designed thickness, is grown at a substrate temperature and at a Zn-to-O ratio as determined in the optimization stages. During this step, the substrate rotation can be stopped either at the beginning, or at any intermediate time, to intentionally introduce a thickness gradient.

Step (3): If necessary, the ZnO layer can be annealed at temperatures (660-700°C) higher than those used during the main growth step in order to improve the crystalline and/or the surface quality.

RHEED patterns will be used in this section to illustrate the surface quality of the ZnO layer at each growth step. The RHEED evolution during the growth of Z1231 (a 7λ/4 ZnO layer on an AlGaN/Si template, grown under the same condition as the ZnO microcavity Z1232 on the real DBR[1]) is shown in Figure 6.15.

First of all it is noteworthy that even if the AlGaN (and also the nitride DBRs) is grown in a different MBE chamber (and sometimes is kept for days, or even weeks, in a conventional plastic box), its RHEED pattern is perfectly streaky when observed in the ZnO-devoted reactor. While it is difficult to be quantitative, the intensity ratio between the AlGaN layer signal and the diffuse background seems to be the same as that obtained after the growth of the nitride DBR (i.e. before exposing it to air). These unaffected RHEED patterns seem to indicate that the AlGaN surface is neither altered, nor reconstructed, nor contaminated by exposing it to air. The main reason is, probably, the strong N-Ga and, especially, the very strong N-Al chemical bond that prevents any surface modification by the ambient atmosphere during the transfer from growth chamber to the other.

After the annealing of the initial several monolayers thick ZnO layer, the RHEED is streaky, as shown in Figure 6.15**b**, and indicates that a suitable surface morphology for continuing the bulk growth is achieved. Nevertheless, it should be noted that some spots can be distinguished along the RHEED rods: this roughnening is simply explained by the lack of a continuous ZnO layer once it has been annealed, given that some mass transport has taken place during the temperature ramp. At high temperature, step (2), and soon after growth starts, the surface becomes roughened and the RHEED pattern reflects a 3D surface (Figure 6.15**c)**. As the growth goes on, the surface gradually smoothens and the RHEED pattern tends to a streaky one, although dots can be still observed along the diffraction rods (Figure 6.15**d** and **e**). A possible growth picture is the following:when the main growth starts on the thin ZnO layer, islands are formed on the surface which roughens it; as growth proceeds, the sizes of these islands increases continuously until, for growth durations sufficiently long enough, they finally coalesce together to form a flat 2D surface. However, the Zn-polar character of the layer, together with the employed Zn-rich conditions, leads to the formation of shallow hexagonal pits, which give rise to the dots in the streaky RHEED pattern. During the post-growth annealing the atoms at the surface rearrange and the 3D features are mostly eliminated, leading to a final 2D surface (Figure 6.15**f** and **g**). Indeed, the post-growth annealing process is essential for most of our ZnO-on-nitride growths.

---

[1] As the DBR is fabricated on a patterned substrate with small-sized mesas (50 to 400μm), it is more clear to show the RHEED evaluation on the non-patterned AlGaN/Si sample. More importantly, in order to protect the ZnO surface from the high energy electron beam for long times, we did not intentionally record high quality RHEED images at every step during the ZnO growths on real DBRs. That is why Z1231 (growth on AlGaN/Si) was chosen for recording high quality RHEED images at each step of the growth, given that it shares the same growth conditions and exhibits the same RHEED evolution as the growths on real DBRs.

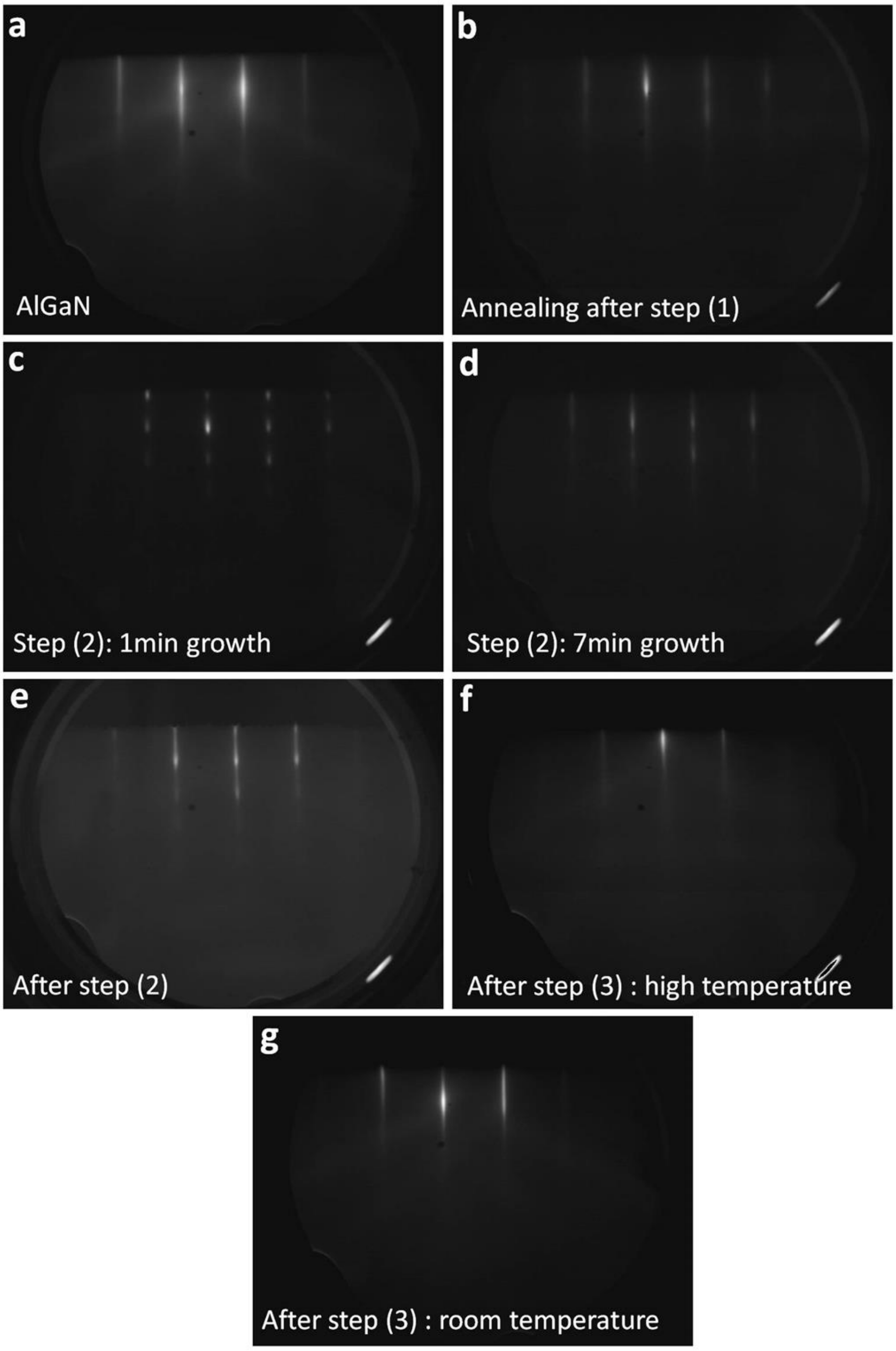

Figure 6.15: RHEED patterns recorded at different steps during the growth of Z1231. **a**. on the AlGaN layer, before ZnO growth. **b**. during the annealing at the end of step (1). **c** and **d**. 1min (**c**) and 7min (**d**) during growth step (2). The total growth time was 1 hour. **e**. right after step (2). **f**. during the postgrowth annealing step (3). **g**. Final RHEED pattern after cooling down the substrate.

Finally, it is worth to mention that even a tiny change in the MBE system may lead to dramatic variations of the optimal growth conditions, requiring for each microcavity series an optimization procedure as that described in 6.3.1.

6.4 The half-cavity

Before deposition of the top HfO_2/SiO_2 DBRs, the half cavities Z1214 and Z1232 were characterized both from a morphological and an optical point of view.

6.4.1 Surface morphology

The surface morphology is characterized with atomic force microscope (AFM), as shown in Figure 6.16. The sample exhibits a surface composed of shallow (~4nm height) terraces. The RMS roughness is ~2.6nm in a 2µm×2µm area, a value comparable with those of the initial $Al_{0.2}Ga_{0.8}N/AlN$ DBRs (~1.6nm see 6.2.2) on which the ZnO was grown. If the size of the investigated area is increased to 5µm×5µm, then the RMS roughness increases further (to about 3.5nm), the main cause being the elongated trenches appearing on the surface of the nitrides DBRs due to the large lattice mismatch between the two constituents materials. Indeed, such trenches can be already observed in Figure 6.9**b**. Indeed, the density of these trenches is not constant across the wafer, and its density depends basically on the local Al composition of the AlGaN layers (see below).

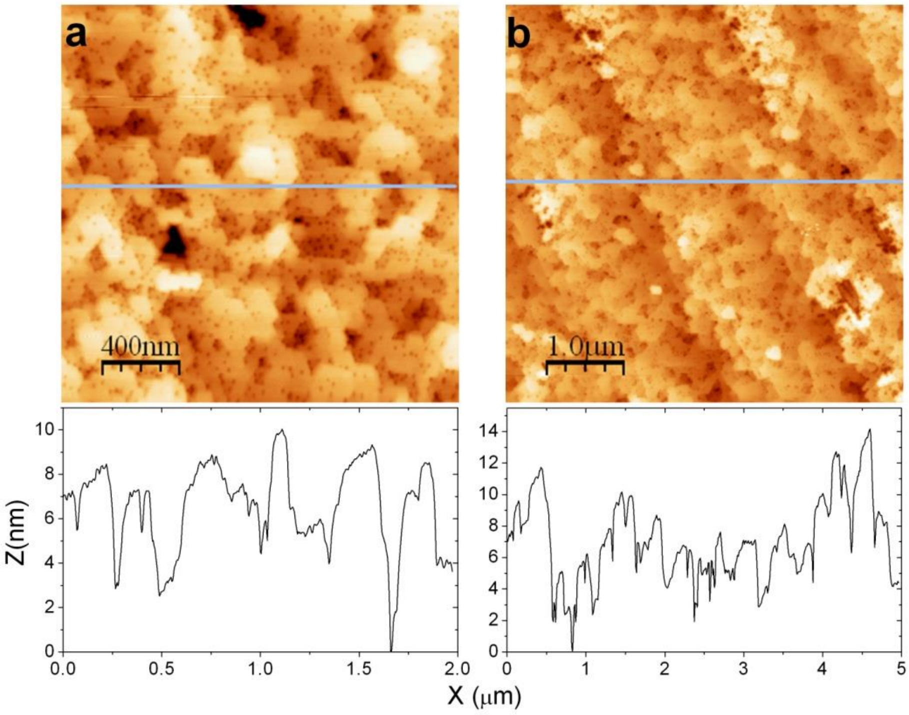

Figure 6.16: AFM images of the half-cavity Z1214 with 2µm×2µm (**a**) and 5µm×5µm (**b**) image sizes. The lower panels show the height (z) profile along the lines (x) drawn in the upper panels. The RMS roughness is 2.60nm for 2µm×2µm area and 3.54nm for 5µm×5µm areas.

For a comprehensive investigation of the whole 2-inch wafer, SEM images are taken at different regions on the cavity Z1214 across the entire wafer, as shown in Figure 6.17. It is clearly seen that the best surfaces are found in regions 3, 4, 5, 7 and 8, while in other regions the surface becomes incompatible with high-Q factor microcavities. In particular, regions 1 and 9 exhibit the roughest surfaces. This trend might be explained by comparing the variation of the surface quality with the orientation of the Al/Ga-fluxes during the AlGaN/AlN DBR fabrication. The general trend of the Al and Ga compositions in the DBR is indicated by an arrow in the upper panel of Figure 6.17. With an increasing Al component in the AlGaN, while the DBR surface improves, the growth of ZnO on top of it becomes more difficult, as the ZnO lattice mismatch increases when going from GaN to AlN. On the other hand, with an increasing Ga composition, the lattice mismatch between the DBR bilayers (AlGaN/AlN) becomes larger, so that the DBR surface becomes traversed by shallow trenches as those observed in Figure 6.9**b**. As a result, good ZnO surfaces are only obtained on the regions where a balance between “too much” Ga and “too much” Al is found, which agrees very well with the picture extracted from Figure 6.17.

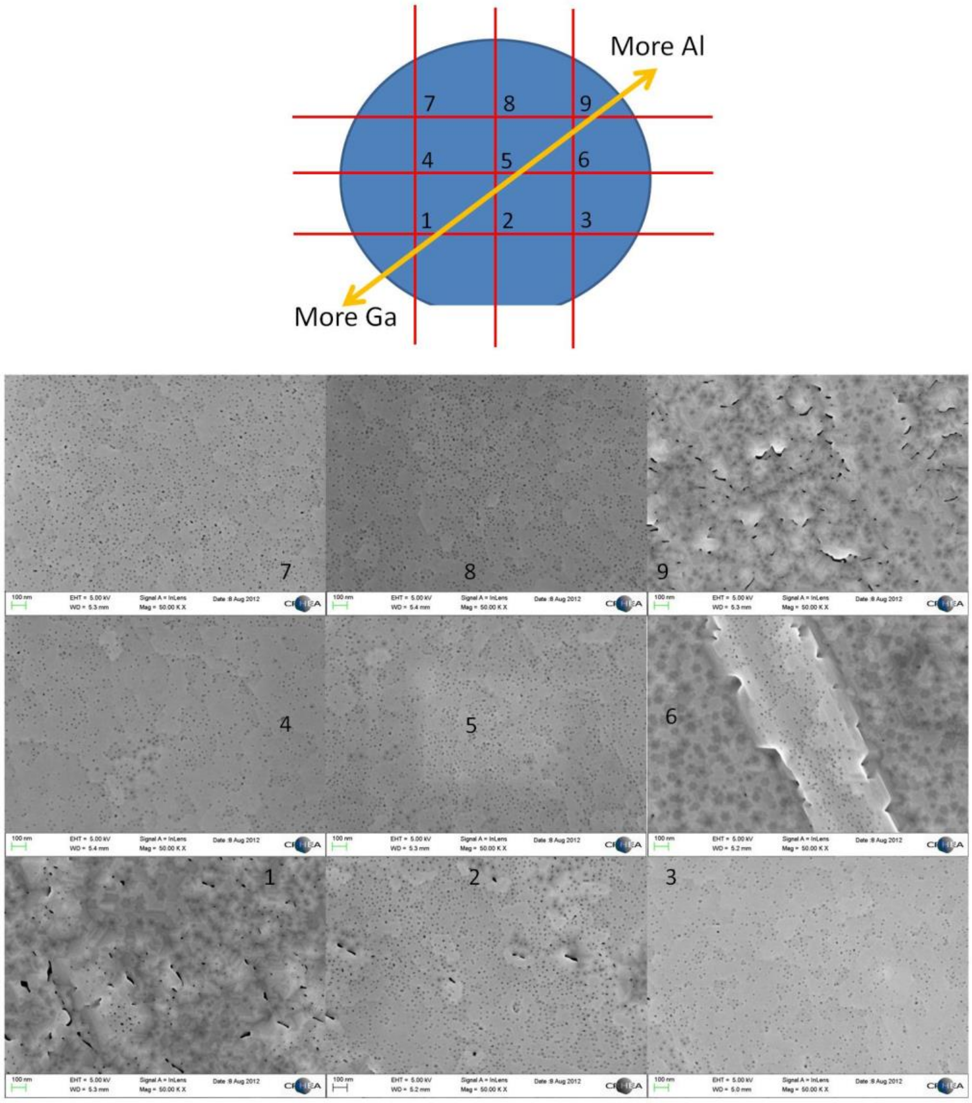

Figure 6.17: SEM images of different regions on the 2-inch size half-cavity Z1214. The upper panel indicates the position of each region where the SEM images in the lower panel were taken. The magnification is 50000 for all images.

While Z1214 and Z1232 exhibit similar morphological properties, differences still exist. As the cavities are fabricated on patterned substrates, it is also interesting to investigate the off-mesa region. The Si (110) substrate employed in the Z1214 microcavity is patterned by KOH etching; this results in extremely rough surfaces on the etched regions, thereby leading to polycrystalline (and even in some cases amorphous) nitrides and ZnO on the off-mesa areas. In stark contrast, the Si (111) substrate used for Z1232 is patterned by reactive ion etching (RIE); this leads to a smooth etched surface. As a consequence, the off-mesa areas are also suitable for DBR and ZnO growths, where the epitaxial surface can be almost as good as on-mesa regions. The only difference with respect to the on-mesa regions is that the off-mesa DBR shows cracks, whereas no cracks are observed on the mesas. The sharp differences on the off-mesa areas are illustrated in Figure 6.18.

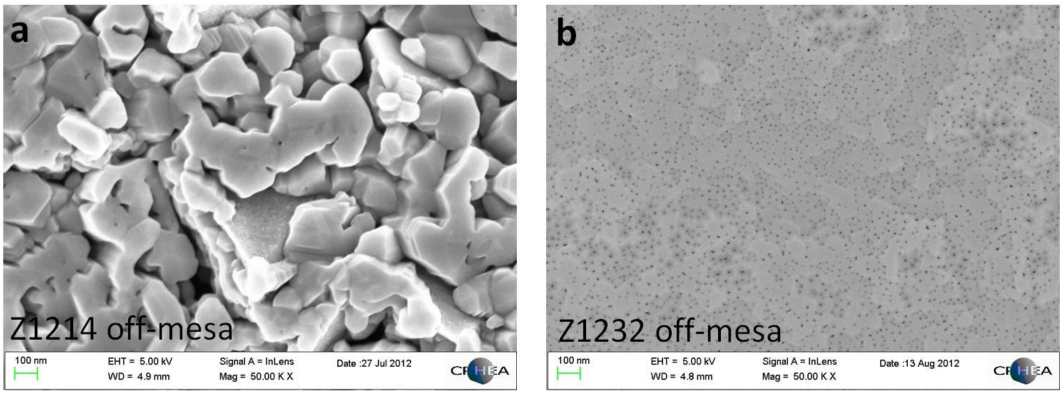

Figure 6.18: SEM images of the off-mesa regions on the half-cavities Z1214 (**a**) etched by KOH and Z1232 (**b**) etched by RIE.

Nevertheless, it seems that the KOH etching patterning displays an advantage compared to the RIE etching one. Indeed, we did observe that cracks start to appear on some of the previously crack-free mesas, several months after the ZnO growth. According to our experience, this effect seems much more likely to occur on Z1232 than on Z1214, probably demonstrating an advantage of using Si (110) substrate and KOH etching. However, to quantitatively confirm this, a thorough investigation on the crack densities over the whole 2-inch wafer within a period of at least several months immediately after the growth needs to be conducted, which was beyond the main scope of this thesis.

6.4.2 Optical properties

The optical properties of the half-cavities are characterized with angle-integrated μ-PL measurements at room temperature at CNRS-CRHEA. Although the top DBR is not yet deposited, the ZnO-air interface can serve as the top mirror, given that a reflectivity of around 15.5% is expected and, thus, cavity modes should be sustained. A typical spectrum at room-temperature is shown in Figure 6.19**a**, where the exciton (X) and cavity (C) modes are clearly identified. Here, we do not use the term polariton to describe the system since it is not certain from our data that strong coupling was achieved on the half-cavity. However, previous experience on low-*Q* cavities would tend to suggest so [17]. At room temperature the exciton exhibits a linewidth of 53.6meV, a typical value for single crystalline bulk ZnO (see Figure 4.7), while the cavity mode displays a linewidth of 50.5meV, i.e. a *Q* of 64 (if we assume that we are in the weak coupling-regime). Figure 6.19**b** shows spectra measured on a series of mesas across the sample, along which a ZnO thickness gradient is present. The optical mode goes from 3.19eV up to the the exciton emission (at 3.30meV) before fainting down. This indicates accessibility to a large range of detunings. Unfortunately, the first Bragg mode goes from 3.12eV to an energy close to the exciton emission. This might pose a problem and limit the use of only one half of the sample, given that polaritons might eventually relax to Bragg-associated polaritons whose lifetime is much smaller [36,157]. It should be noticed that the variation of the cavity mode energy was measured across 1-inch range, which indicates a high homogeneity of the ZnO thickness, compared to the fully-hybrid cavity described in chapters 4 and 5.

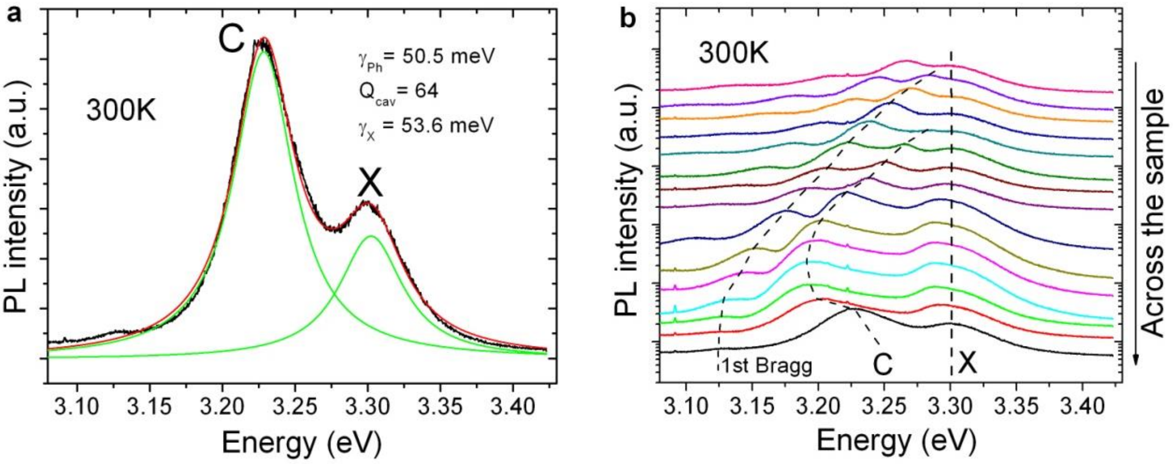

Figure 6.19: Room temperature angle-integrated μ-PL measurements on the half cavity Z1214. **a**. Spectra taken on one spot with fitted curves (green) for the cavity and exciton modes. **b**. A series of spectra taken across the sample (within ~1 inch area).

6.5 The complete cavity

The last step of the cavity fabrication is the deposition of an 11-pair HfO_2/SiO_2 DBR, which was carried out by S. Bouchoule at CNRS-LPN. The morphological properties of the complete cavities were first characterized at CNRS-CRHEA, while the optical properties were analyzed at Institut Pascal and Laboratoire Charles Coulomb.

6.5.1 Morphological properties

The main morphological properties of the complete semi-hybrid ZnO microcavities are shown in Figure 6.20. The complete cavity displays an RMS roughness of 2.6nm in a 2μm×2μm region, reproducing that of the epitaxial ZnO surface. This evidences again the high quality of the HfO_2/SiO_2 dielectric DBRs developed at CNRS-LPN, which reproduce the surface quality of the underlying layers irrespective of their original roughness value. The optical microscope images show that most of the mesas are crack-free (all in this image, but not 100% over the wafer), and this even after an 83-layers growth/deposition (60-layers in the bottom DBR, 1 layer ZnO, and 22-layers in the top DBR), after growth/deposition of 5 different materials in 3 different reactors. Furthermore, sharp and straight interfaces between different layers can be clearly identified from the cross-section SEM image.

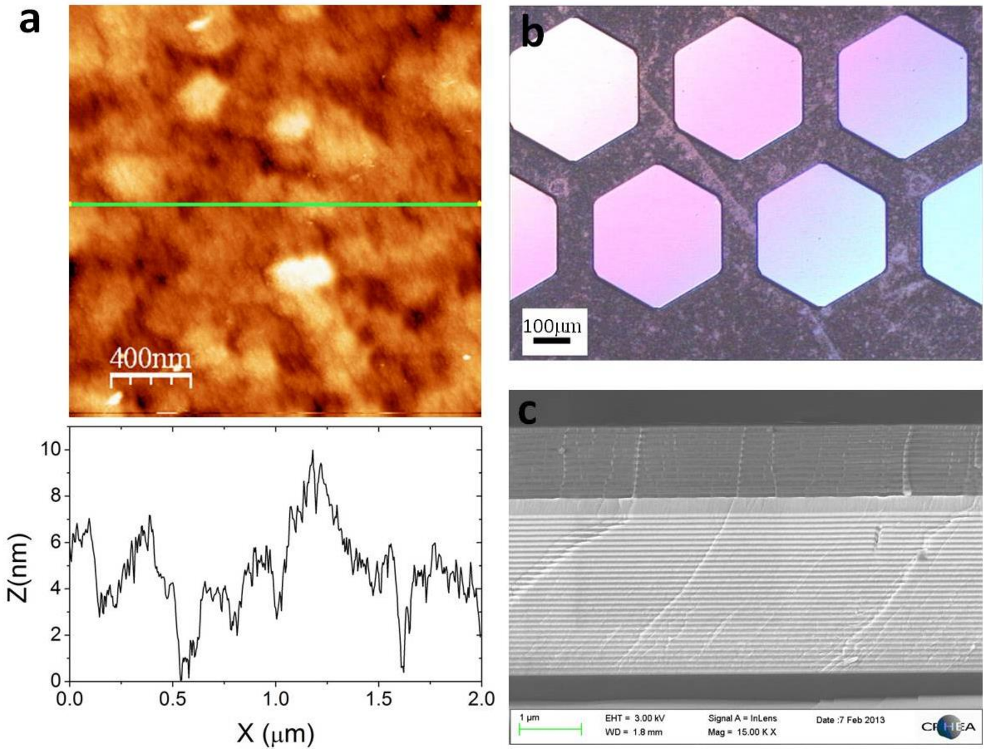

Figure 6.20: Morphological characterization of the complete semi-hybrid ZnO microcavities, including AFM image (**a**), optical microscope image (**b**) and cross-section SEM image (**c**). The lower panel of **a** shows the height profile along the line drawn in the upper AFM image, with RMS roughness of~2.6nm. **a** and **b** are taken on Z1214 while **c** is taken on Z1232.

6.5.2 Optical properties: Linear regime

The linear optical properties of the complete cavities have been characterized while only preliminary results on the nonlinear behavior of these cavities could be achieved before writing this PhD manuscript.

***Q*-factor and spatial homogeneity**

As we have mentioned at the beginning of this chapter, the main reason why we have addressed the fabrication of semi-hybrid ZnO microcavities is the need of spatially-homogenous active layer thickness and, thereby, of the polariton potential landscape. This is the first, and necessary, step to predefine arbitrary polariton potentials at will. The homogeneity of the active layer thickness is revealed in Figure 6.21**a**, where the LPB energy is constant along a distance of 80μm (at ~3.164eV, with a root-mean-square deviation of less than 1meV).

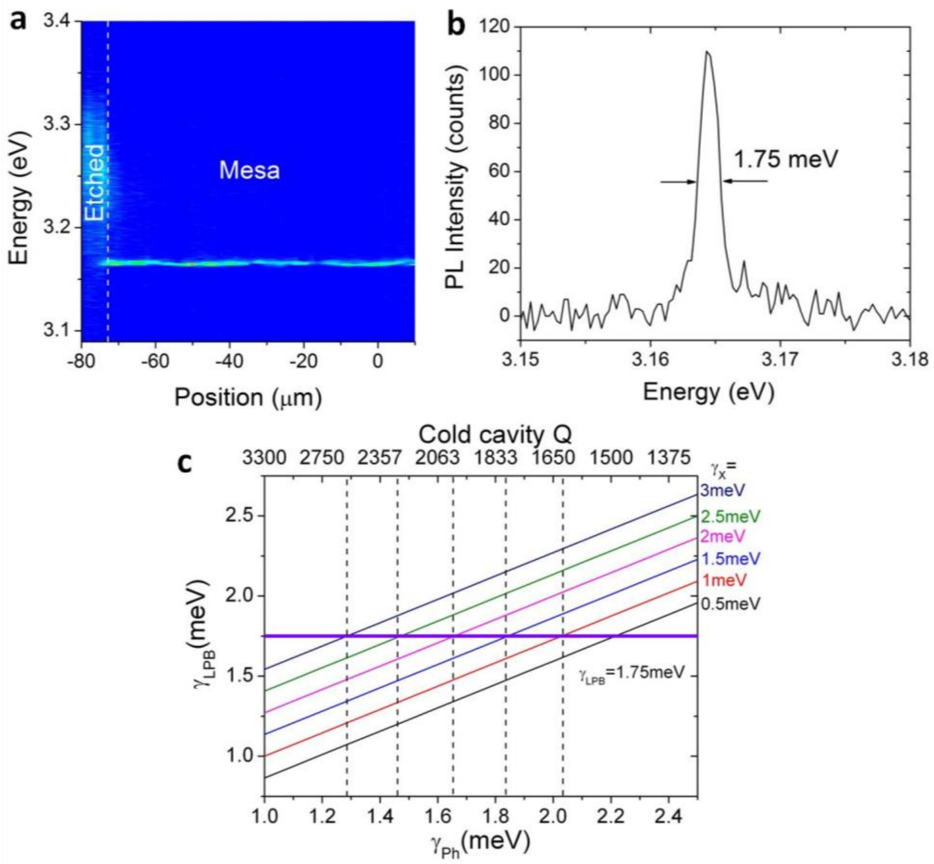

Figure 6.21: **a**. μ-PL spectra measured at zero angle as a function of the position on the cavity (Z1214). The series of spectra, taken with 1μm intervals, cover both the etched area (off the mesa) and the mesa. **b**. A typical spectrum taken on the mesa. At this point the detuning is ~-85meV and the polariton photon fraction ~73% **c**. Calculated LPB linewidth γ_{LPB} (photon fraction 73%) as a function of the cold cavity Q (cavity photon linewidth γ_{Ph}) with different exciton-induced broadenings γ_X ranging from 0.5 to 3meV. The thick horizontal line represents γ_{LPB}=1.75meV as measured in **b**.

Besides a spatial homogeneity much larger than that on the fully-hybrid microcavity described in chapters 4 and 5, the value of the Q-factor needs to be larger than that obtained on semi-hybrid cavities without substrate patterning (see 3.3.3 for the state-of-the-art), otherwise polariton condensation would be hardly achievable at high temperatures. Indeed, from the spectrum measured at zero angle in Figure 6.21**b**, one can identify a FWHM of 1.75meV, and thereby a “Q-factor” of ~1800. If we assume that the cavity operates in the strong-coupling regime, as will be demonstrated hereafter, the measured point exhibits a detuning ~-85meV and a photonic fraction of ~73%, which were both calculated taking into account the measured Rabi splitting (as presented below). Similarly to the discussion in 4.3.3, and despite the larger photonic fraction, the measured Q-factor is still impacted by the excitonic broadening. Again, a more realistic estimation of the Q-factor has been done by considering this excitonic contribution (at room-temperature), as shown in Figure 6.21**c.** While the value of the estimated Q-factor depends on the exact broadening we assume for excitons [151] (which are again separated in energy more than one LO-phonon energy), it possibly ranges from 1500 to 2700 (See 4.3.3 for more discussion). While smaller than on the fully-hybrid cavity, these values should be compared with those of other semi-hybrid cavities: ~200-600 for the previously reported ZnO semi-hybrid microcavities grown on non-patterned

DBRs [39,43], ~2800 for the semi-hybrid GaN microcavities [31,136], and ~ 450 for the monolithic ZnO microcavities which exhibits a narrower stopband width (~180meV) [162].

Strong-coupling regime: Rabi splitting

Angle-resolved photoluminescence was performed with a setup employing a goniometer and a coupled fiber, to enable access to angles as large as 80° (similar as in Appendix A of Reference [59]). Instead of using a small pumping spot as in the fully-hybrid cavity, the excitation spot size is ~50µm, whose use is enabled by the negligible thickness gradient within one single mesa. A polarizer was added to allow detecting either s- or p-polarized emission; in the following, only p-polarization images will be shown, as in Figure 6.22, under continuous wave excitation (which implies, in this case, below threshold). A fitting of the polariton dispersions (white lines) using a coupled-oscillator model reveals a detuning of -94meV and a Rabi splitting of ~165meV at the measured point. As seen in Figure 6.22**a**, at small angles (< 30°) the energy position of the DBRs Bragg modes is far from the excitonic and cavity-mode energies. However, at higher angles (from 40° to 80°) the first and second Bragg modes from the bottom DBR, and the first Bragg mode from the top DBR, get closer to the excitonic reservoir and modify the dispersion of the LPB associated to the cavity mode. This situation is very similar to that observed in CdTe cavities [157] as well as in the first semi-hybrid ZnO cavities [36], based on nitride DBRs too, in which strong-coupling with cavity and Bragg modes was observed. The effective coupling between all the modes at large angles is highlighted in Figure 6.22.

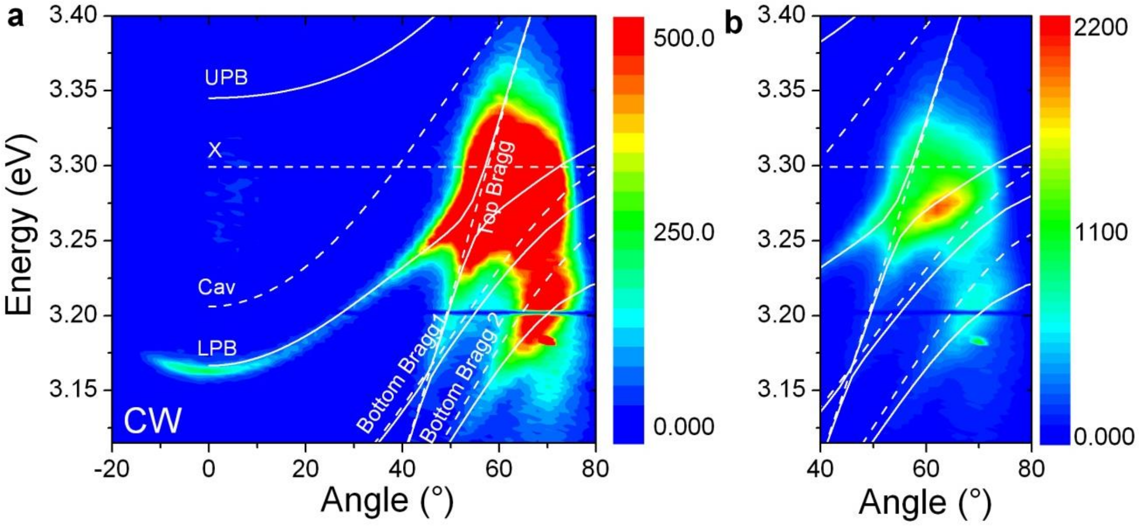

Figure 6.22: **a**. Angle-resolved spectra measurement below threshold using continuous wave (CW) excitaion. **b**. Unsaturated image (which saturates the false-color scale in **a**) between 40° and 80°. The excitation spot is ~50µm and the detection is for p-polarized light. Solid lines (resp. dashed lines) show the dispersions of the polariton modes (resp. bare exciton, cavity and Bragg modes) obtained through the simulation with the coupled-oscillator model. The measured point exhibits a Rabi splitting of ~165meV and a detuning of -94meV.

6.5.3 Optical properties: Nonlinear regime.

The presence of LPB^{Braggs} close to the LPB^{Cav} at high k vectors might compromise the achievement of polariton lasing; indeed, previous observations had shown the relaxation of polaritons from LPB^{Cav} towards LPB^{Braggs} that, unfortunately, exhibit a much smaller lifetime. If the excitation power is increased (it should be recalled that quasi-CW excitation is used), at a certain threshold power, the apparent bottleneck at about 50° seems to be overcome and polariton condensation occurs at the bottom of the LPB, as shown in Figure 6.23. The moderate blueshift, of ~9meV (i.e. $<6\%\times\Omega_{Rabi}$), is better seen in Figure 6.24. It is noted that condensates with nonvanishing wavevectors, which correspond to those of the LPB^{Braggs} at the energy of the k=0 condensate, appear concomitantly (see the enlarged view around the lasing energy on the top inset of Figure 6.23). While the exact origin of these condensates it not yet clear, they might be related to accelerated condensates guided in-plane (similar to waveguide polaritons [203]), and coupled outwards through the DBR polariton modes, or to parametrically scattered polaritons [44]).

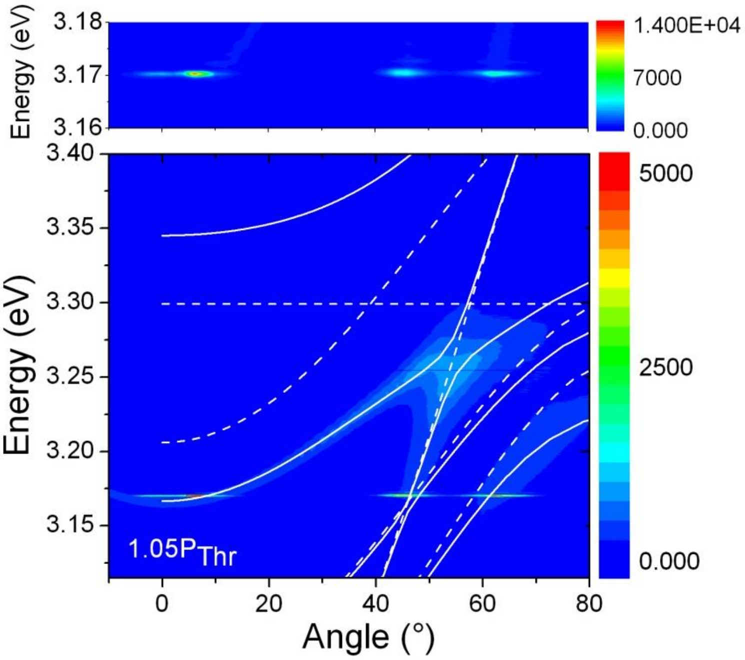

Figure 6.23: Angle-resolved spectra measurement above threshold ($1.05P_{Thr}$) under quasi-continous excitation (pulse duration 400ps and repetition rate 4kHz). An enlarged view around the lasing mode, with a proper full scale, is shown in the inset. The excitation spot is ~50µm and the detection is for p-polarized light. The white lines show the simulated strongly-coupled modes, as in Figure 6.22**a**.

A series of spectra with increasing incident power, acquired under “large” spot conditions, are plotted in Figure 6.24**a**. The spectra were taken at the same spot used in Figure 6.23 at zero angle and without the polarizer. While at threshold single mode lasing occurs, the multimode character of the laser is clearly observed even at excitation powers just slightly above threshold, as shown in Figure 6.24**a**. The origin of the multi-mode lasing might be found in condensate localization within the large pumping area (~50µm), as suggested by the mapping of the LPB energy below threshold, which indicates the possibility of discrete cavity mode jumps in the order of some meV. The lasing features are characterized by a non-linear increase of the integrated emission intensity by two orders of magnitude with an increase of less than 20% of the pumping power, and a linewidth sharpening by a factor larger than 10. The linewidth is getting continuously broadened before reaching the lasing threshold, similar to some zero-angle power-dependent series that we have measured from the fully-hybrid microcavities (e.g. Figure 5.10**e**). This behavior resembles some previous reports in ZnO [41] and GaAs [204] systems. The blue shift is ~9meV, i.e. ~20% of the energy difference between the exciton and the LPB minimum, which robustly evidences that the lasing occurs in the strong coupling regime. The ratio is larger than that of the fully-hybrid microcavity discussed in Chapter 5, but comparable to the values observed in other ZnO [41,42] or GaN [30] publications. The lasing threshold, 50.8μJ/pulse, seems extremely large compared to the fully-hybrid microcavity (~1nJ/pulse at room temperature). However, if we consider the much larger pumping spot size used in the current experiment (50-60μm vs. 2μm), the actual excitation intensity should be only ~50-80 times larger. Currently, experiments are undergoing to study the condensate threshold but with smaller pumping spots, which will enable direct comparison with the threshold results shown in chapter 5.

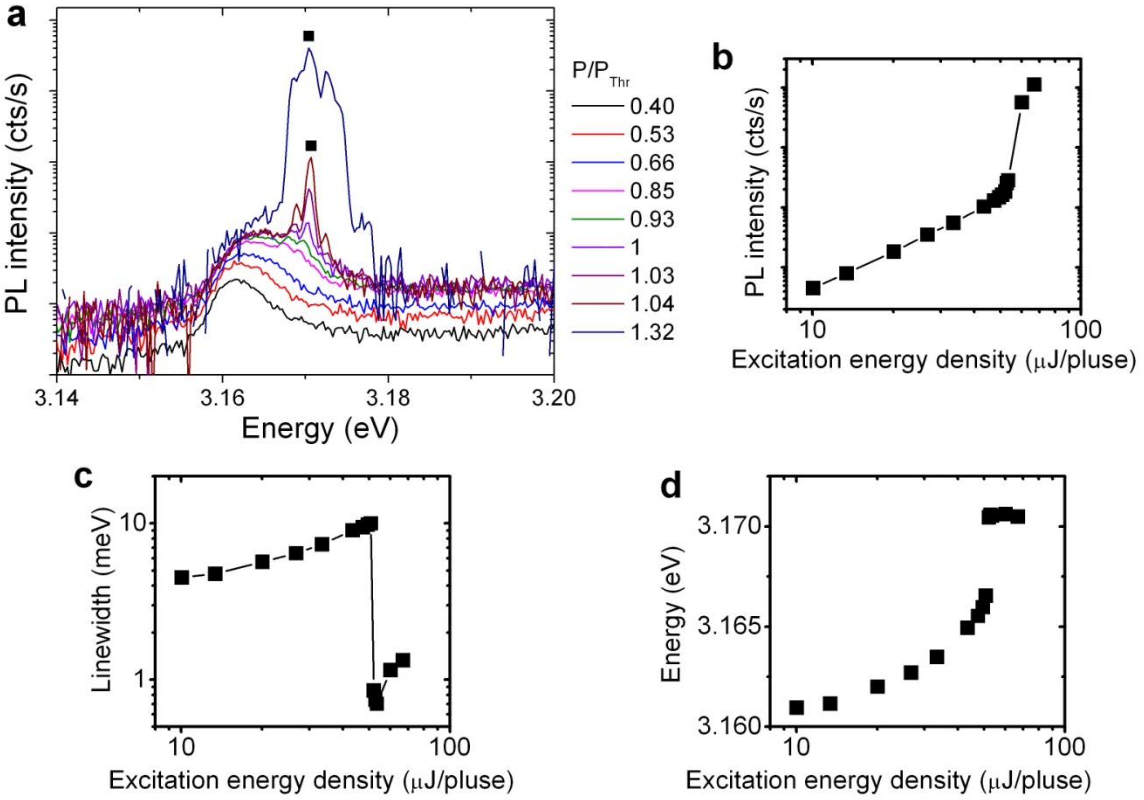

Figure 6.24: **a**. Spectra as a function of excitation energy measured on the same spot as in Figure 6.23. The threshold P_{Thr} corresponds to an excitation energy of 50.8μJ/pulse. The spectra are taken at k=0 with a pumping spot of ~50μm. **b**, **c** and **d**, Integrated PL intensity (**b**), spectral linewidth (**c**) and LPB/lasing mode energy (**d**) as a function of excitation energy. In the cases of multi-mode lasing, the linewidths and mode energies correspond to the main peaks labeled by the square symbols in **a**.

6.6 Conclusion

In this chapter the fabrication and characterization of a series of semi-hybrid ZnO-bulk microcavities were discussed. In terms of fabrication, the achievement of high quality $Al_{0.2}Ga_{0.8}N$/AlN DBRs on patterned silicon substrate is highlighted, followed by the detailed description of the MBE growth that finally leads to the successful fabrication of a ZnO active layer. Morphological and optical characterizations performed first on the half-cavities, i.e. before the top DBR deposition, show a high optical quality active region together with a smooth surface. These features allowed to obtain a *Q*-factor ~1800 and room temperature polariton lasing. Further spectroscopic investigations on these cavities are currently being performed.

Conclusion

Context

This PhD thesis was conducted within the framework of a European Marie-Curie Initial Training Network (ITN) “CLERMONT4” (September 1st, 2009, to August 31st, 2013), which was devoted to the physics and applications of exciton-polaritons. The initial objective of this PhD thesis work was to fabricate and demonstrate a ZnO-based exciton-polariton laser working at room temperature, and it has been successfully fulfilled by means of two different fabrication approaches that have resulted in: fully-hybrid (qualitatively different to previous works) and semi-hybrid (quantitatively different to previous attempts) ZnO microcavities. In addition, a large panel of spectroscopic studies was performed to investigate the physics of ZnO exciton-polaritons. Globally, this work, including the cavity design, the material growth, the device fabrication and the optical spectroscopy, has been carried out through a fruitful collaboration between four CNRS laboratories, all of them participating in CLERMONT4: CRHEA (Centre de Recherche sur l’Hétéro-Epitaxie et ses Application), Institut Pascal, L2C (Laboratoire Charles Coulomb) and LPN (Laboratoire de Photonique et de Nanostructures).

Summary of the experimental results

The fully-hybrid ZnO microcavity developed in this thesis involves a completely new fabrication strategy that was originated in CNRS-CRHEA: the basic idea is quite simple, since it consists in thinning a ZnO substrate, down to a few hundreds of nanometers, and surrounding the remaining ZnO by two HfO_2/SiO_2 DBRs. Indeed, the idea is not essentially new as it was investigated previously by CNRS-CRHEA [159,164,205]; however, our original approach to the problem overcomes the difficulties associated to either the etch-stop layer [159,164] or the selectively-etched substrate [205] , which limited in previous attempts the crystalline quality and the interface smoothness of the active material. The merit of the new fabrication strategy lies in the fact that it requires neither an etch-stop layer nor an epitaxial growth of ZnO, thereby keeping the best possible crystalline quality of the active region. The successful fabrication has led to a record *Q*-factor (~2500-4000) among all ZnO-based planar microcavities and a large Rabi splitting (~250meV), comparable to those obtained in ZnO microwires, where the exciton-cavity field overlap is maximized. The fabrication-related thickness gradient has allowed a continuous tuning of the polariton mode energy for various cavity lengths (going from λ to 6λ), enabling to access any possible cavity-exciton detuning. Room temperature exciton-polariton lasing has been unambiguously demonstrated, with lasing features typically 5 to 10 times better than other contemporary reports [42,43].

The characteristics of the fully-hybrid ZnO microcavity have enabled to investigate further the physics related to exciton-polaritons. First of all, the polariton condensation phase diagram has been derived for the first time on a ZnO-based microcavity, within an unprecedented range of exciton-photon detunings (-214meV to +450meV) and from low to room temperature. The exciton fraction of the achieved polariton condensates ranges from 17% to 96%, corresponding to a tuning of exciton-polariton effective mass, lifetime and interaction constant by more than 1 order of magnitude [206]. LO-phonon assisted polariton relaxation has been shown to be extremely efficient in ZnO, which should not be a surprise given the polar character of ZnO; this efficient mechanism seems to be at the origin of the optimum condensation detuning at high (above 200K) and intermediate (from 100k to 200K) temperatures. Moreover, on the thick regions of the microcavity, where multiple LPBs are present, mode-competition has been observed and employed to test our understanding of the phase diagram (i.e. of the tradeoff between Kinetics and Thermodynamics). Furthermore, under certain conditions it has been possible to switch polariton condensation between two different LPB branches, created at the same spot: in this way, without changing neither the thickness of the cavity nor the polariton potential landscape, it has been possible to investigate the effects of the excitonic reservoir and of the photonic mode gradient on polariton condensates with different matter-light fractions.

The fabrication of an improved semi-hybrid ZnO microcavity follows a more established fabrication strategy, involving ZnO epitaxial growth on nitride DBRs and final deposition of a dielectric DBR on top: in this sense, the results obtained in this thesis can be considered as a quantitative improvement, sufficiently important to allow for polariton lasing at room-temperature. This approach requires overcoming a series of technological challenges, among which the growth of nitride DBRs with a large (>15) number of pairs is the most difficult to achieve, mainly due to the high-density cracks induced by the thermal expansion coefficient mismatch between the nitrides and the Si substrate. At CNRS-CRHEA the problem was solved, in one recent PhD work, by creating mesas on a Si substrate before the nitride growth. 30 pairs of crack-free $Al_{0.2}Ga_{0.8}N$/AlN DBRs have been achieved on such patterned Si (110) and Si (111) substrates, exhibiting smooth surface morphology (roughness ~1.6nm), high reflectivity and stopband width of ~200meV. Another significant challenge is to growth high quality ZnO active layer on these DBRs. The optimized ZnO active layer presents good morphological (surface roughness ~2.6nm) and optical (room temperature exciton linewidth ~53.6meV) properties. The full microcavity, completed by depositing 11 pairs of HfO_2/SiO_2 DBRs, exhibits an extremely low (compared to the Rabi splitting and to the homogeneous exciton linewidth) photonic inhomogeneous broadening and a *Q*-factor of ~2000. Finally, room temperature polariton lasing has been demonstrated.

In addition to the major experimental results stated above, other attempts have been also made to seek for further improvements either in terms of *Q*-factor (ZnO epitaxial growth on the AlGaN/AlInN DBRs provided by EPFL), or in terms of *Q*-factor and stopband width (ZnO deposition on dielectric DBRs).

Perspectives

The current cavities open the door to a number of spectroscopic experiments and pave the way for the fabrication of ZnO-based microcavities with even better figures of merit.

(1) In terms of exciton-polariton physics

From our results, together with those obtained in GaN cavities at EPFL [46,47], it seems that there is no univocal relationship between Material and Phase diagram, but that for a given material the exact phase diagram depends too in the Rabi splitting and the *Q*-factor, for instance. In this sense, it will be very interesting to compare the phase diagram on the semi-hybrid cavity, where both the Rabi splitting and the *Q*-factor are smaller. The results will allow us, in turn, to verify the accuracy of our polariton relaxation model and, eventually, improve it.

Second, in this thesis we did not focus on the demonstration of thermal equilibrium of the polariton system[1], as the small excitation spot (~2µm) used to investigate the fully-hybrid cavity results in a strong polariton repulsive potential, as induced by the exciton reservoir, that ejects polaritons out of the excitation spot. In order to carry out a systematic study and to demonstrate room temperature quasi-BEC, a large excitation spot is needed, which in turn requires a high-*Q* microcavity with negligible photonic disorder. Despite the possibility that these requirements could be met with the currently studied micocavities, the demonstration of quasi-BEC at room temperature might demand higher quality microcavities, either fully-hybrid ones with reduced thickness gradient or semi-hybrid ones with increased bottom DBR reflectivity and larger stop-band widths[2]. Besides, such improved microcavities will enable to study the spatial coherence of the polariton system, below and above threshold, and characterize more in detail how does its expansion occurs; in particular, the study of spatial coherence will provide information on the character of the condensates: droplet (like in CdTe microcavities) Vs extended (like in GaAs cavities).

Finally, many research topics of polaritonic physics, such as superfluidity and solitons, involve investigating the propagation of polariton condensates, currently performed at low temperatures. High quality ZnO microcavities provide the opportunity to carry out polariton propagation studies at room temperature and, especially, with polaritons of very different excitonic content. Thus, it will be possible to study the influence of the polariton effective mass on the condensates propagation and on their interaction with defects. It should be noted that preliminary experiments at low temperature, both at Institut Pascal and L2C, have shown ZnO polariton condensates propagating along the thickness gradient of the fully-hybrid cavity more than 10µm away from the excitation spot. In the future, instead of using the naturally formed potential "landscapes" (See Figure 4.9 for example) inherited from the fabrication process, it should be possible to "imprint" engineered potentials and to manipulate polariton condensates at will.

---

[1] Although some of our measurements seem to indicate quasi-thermal equilibrium, systematic studies were not yet performed.

[2] As discussed in Chapter 6, it seems that the Ga content of the AlGaN/AlN DBRs in the semi-hybrid microcavities (Z1214 and Z1232) is lower than the cavity design, resulting in a *Q*-factor and a stop-band width smaller than in the ideal case.

(2) In terms of fabrication technologies

Since a number of studies will require longer polariton lifetimes and, therefore, larger *Qs*, further improvement of the current fabrication techniques is necessary: For the fully-hybrid microcavities, a more reliable process to control the ZnO thickness gradient and surface roughness needs to be developed. For the semi-hybrid microcavities, a quantitative improvement requires using AlGaN alloys with almost no Al, so that larger stop band widths should be achieved. This will also increase the *Q* factor, for the same number of pairs, but since currently the number of pairs is not a limit it might be further increased if necessary (see Figure 6.2).

In addition, new cavity structures are to be exploited, among which the most promising one involves embedding homoepitaxial ZnO/ZnMgO quantum wells (QWs), especially those grown along nonpolar axes, in the fully-hybrid ZnO microcavities. Indeed, homoepitaxy of ZnO/ZnMgO QWs on ZnO substrate has been intensively studied in CNRS-CRHEA during the past years, and high quality nonpolar QWs have been achieved, exhibiting enhanced emission intensity and suppressed thermal quenching of photoluminescence, compared to bulk ZnO or heteroepitaixal QWs [202,207]. The advantage of using QWs as the active media lies in several aspects. First, it further increases the exciton binding energy and oscillator strength, as well as the ratio between radiative and non-radiative recombination at room temperature, with respect to bulk ZnO. Furthermore, since nonpolar QWs can be grown, the detrimental effects of the quantum confined Stark effect [208] in the recombination rates of QWs can be neglected. Second, as the QWs are thin compared to bulk materials, the overall absorption by the active media is greatly reduced. This could probably enable the observation of the upper polariton branch in reflectivity. Third, the use of QWs might contribute to further decrease the polariton condensation threshold, as theoretically predicted [141]. Our preliminary studies aiming at fabricating such QW microcavities are presented in Appendix C. The main technical difficulty is to etch completely the ZnO substrate on which the ZnO/ZnMgO QWs are grown, without seriously affecting the QW structure. This will require intensive investigations on both the ZnMgO growth and the etching technology.

Whatever novelties the future will bring, the sky above ZnO polaritonics seems completely clear for the next years.

Conclusion

Contexte

Cette thèse a été réalisée dans le cadre d'un réseau européen Marie-Curie Initial Training Network (ITN), «CLERMONT4» (du 1er Septembre 2009 au 31 Août 2013), qui était dédié à l'étude de la physique des polaritons de cavité et ses possibles applications. L'objectif initial de ce travail de thèse était de fabriquer et de démontrer un laser à polaritons à base de ZnO et travaillant à température ambiante. Cet objectif a été atteint avec succès utilisant deux méthodes de fabrication différentes qui ont abouti à des microcavités entièrement hybrides (qualitativement différentes des travaux précédents) et semi-hybrides (quantitativement différentes des tentatives précédentes) à base de ZnO. En outre, un large éventail de mesures optiques ont été utilisées pour appréhender la physique des polaritons de cavité et ont permis de mettre en évidence certaines des particularités dues à l'utilisation de ZnO comme zone active. De façon générale, ces travaux, y compris la conception de la structure de la cavité, la croissance des matériaux, la fabrication des dispositifs et la spectroscopie optique, ont été réalisés grâce à une collaboration fructueuse entre quatre laboratoires du CNRS, chacun d'entre eux partenaires dans CLERMONT4: CRHEA (Centre de Recherche sur l'Hétéro-Epitaxie et ses Application), Institut Pascal, L2C (Laboratoire Charles Coulomb) et LPN (Laboratoire de Photonique et de Nanostructures).

Résumé des résultats expérimentaux

La microcavité entièrement hybride à base de ZnO fabriquée dans cette thèse implique une stratégie de fabrication complètement nouvelle qui a été développée au CNRS-CRHEA: l'idée principale est assez simple puisqu'elle consiste à amincir un substrat de ZnO, qui fait 500 micromètres d'épaisseur initialement, jusqu'à quelques centaines de nanomètres et entourer ce ZnO par deux DBRs à base de HfO_2/SiO_2. Strictement parlant, cette idée n'est pas nouvelle puisqu'elle elle a été considérée auparavant par le CNRS-CRHEA [159,164,205] comme moyen de fabrication de cavités; pourtant, notre approche originale surmonte les difficultés liées soit à la couche d'arrêt [159,164] soit à la gravure sélective du substrat [205], qui ont limité, lors des tentatives précédentes, la qualité cristalline et/ou la rugosité de l'interface entre la zone active et un des deux DBRs. Le mérite de la nouvelle stratégie de fabrication réside dans le fait qu'elle ne nécessite ni couche d'arrêt, ni croissance hétéro-épitaxiale de ZnO, ce qui permet de garder une qualité cristalline optimale de la région active. Cette fabrication a conduit à une valeur record pour le facteur Q (~2500-4000) parmi toutes les microcavités planaires à base de ZnO et un grand éclatement de Rabi (~250meV), comparable à ceux obtenus dans les microfils de ZnO, où le recouvrement entre les excitons et le mode optique atteint presque les 100%. Par ailleurs, le gradient d'épaisseur lié à la méthode de fabrication a permis un réglage continu de l'énergie du mode de polariton pour des longueurs de cavité différentes, allant de $\lambda/2$ à 6λ (ou au-delà) ; ceci a permis d'accéder à tous les désaccords cavité-exciton possibles. Enfin, un laser à polaritons fonctionnant à température ambiante a été démontré sans ambiguïté, avec des figures de mérite en général 5 à 10 fois meilleures que celles des autres rapports contemporains [42,43].

Cette microcavité entièrement hybride a permis d'approfondir l'étude des polaritons de cavité et apermis, en particulier, d’avoir accès à des condensats de polaritons très différents (par exemple très excitoniques) de ceux obtenus dans d’autres systèmes. Tout d'abord, le diagramme de phases de condensation des polaritons a été établi pour la première fois dans une microcavité à base de ZnO, et ce, dans une gamme de désaccord exciton-photon sans précédent (-214meV à +450meV) et depuis les basses températures jusqu’à la température ambiante. Le poids excitonique des condensats de polaritons varie ainsi de 17% à 96%, ce qui correspond à une modification de la masse effective des polaritons, de leur temps de vie et de leur constante d’interaction de plus d’un ordre de grandeur [206]. Le diagramme de phases a mis en évidence que la relaxation de polaritons assistée par phonons LO est très efficace dans ZnO, ce qui ne devrait pas être une surprise étant donné le caractère polaire de ZnO; ce mécanisme efficace semble être à l'origine du désaccord optimal entre la cavité et les excitons pour la condensation aux hautes températures (supérieures à 200 K) et aux températures intermédiaires (de 100 K à 200 K). En outre, sur les régions épaisses de la microcavité, où plusieurs LPBs sont présentes, une compétition de modes, similaire à celle observée dans des lasers en couplage faible, a été observée et utilisée pour tester notre compréhension du diagramme de phases, qui traduit le compromis entre cinétique et thermodynamique. En outre, dans certaines conditions il a été possible de contrôler la condensation de polaritons de façon à l’obtenir dans deux branches LPB différentes mais créées au même endroit: de cette façon, sans changer ni l'épaisseur de la cavité ni le potentiel excitonique, il a été possible d'étudier l’effet du réservoir excitonique et du gradient du mode photonique sur les condensats de polaritons en fonction de leur poids lumière Vs matière.

Pour la fabrication des microcavités semi-hybrides à base de ZnO une stratégie de fabrication plus sophistiquée a été employée : elle implique la croissance épitaxiale de ZnO sur des DBRs nitrures et le dépôt d'un DBR diélectrique au-dessus: en ce sens, les résultats obtenus dans cette thèse peuvent être considérés comme une amélioration quantitative, plus que qualitative, et suffisamment importante pour permettre l’obtention d’un laser à polaritons à température ambiante, ce qui n’avait pas été possible auparavant.. Cette approche nécessite surmonter une série de difficultés technologiques, parmi lesquelles la croissance de DBR nitrures avec un grand nombre (>15) de paires est la plus sérieuse. En effet, la différence de coefficients de dilatation thermiques entre les nitrures et le substrat Si entraîne inéluctablement l’apparition de fissures dans des couches AlGaN épaisses et riches en Al. Au CNRS- CRHEA le problème a été résolu, dans un travail de doctorat récent, en réalisant l’épitaxie des nitrures sur des mesas de Si et non plus sur un substrat Si planaire. Des DBRs $Al_{0.2}Ga_{0.8}N/AlN$ avec 30 paires et sans fissures ont été réalisés sur des substrats Si (110) et Si (111) patternés, présentant une morphologie de surface lisse (rugosité ~1.6nm), une forte réflectivité et une largeur de bande d’arrêt d'environ 200meV. Une autre difficulté importante est la croissance de la couche active de ZnO, qui doit maintenir une grande qualité cristalline sur les DBRs. La couche active de ZnO optimisée présente de bonnes propriétés morphologiques (rugosité de surface ~2.6nm) et optiques. La microcavité complète, achevée par le dépôt du DBRs supérieur, fait de 11 paires de HfO_2/SiO_2, présente un élargissement inhomogène photonique extrêmement faible (par rapport à l'éclatement de Rabi et à la largeur homogène de l'exciton) et un facteur *Q* ~2000. Enfin, un laser à polaritons à température ambiant a été démontré aussi avec cette approche.

En plus des résultats expérimentaux mentionnés ci-dessus, d'autres tentatives ont été également testées pour obtenir des améliorations, soit en termes de facteur *Q* (la croissance épitaxiale de ZnO sur des DBRs AlGaN/AlInN fournis par EPFL), ou en termes de facteur *Q* et de largeur de bande d'arrêt (dépôt de ZnO sur des DBRs diélectriques).

Perspectives

Les cavités actuelles ouvrent la porte à un certain nombre de mesures optiques impossibles auparavant et ouvrent la voie à la fabrication de microcavités à base de ZnO avec des figures de mérite améliorées.

(1) En termes de physique de polaritons de cavité

A partir de nos résultats, et tenant compte aussi de ceux obtenus dans des cavités GaN à l'EPFL [46,47], il semble qu'il n'y ait pas de relation univoque entre le matériau employé comme zone active et le diagramme de phases, mais que pour un matériau donné le diagramme de phases exacte dépende aussi de l'éclatement de Rabi et du facteur *Q*. Dans ce sens, il sera très intéressant de comparer le diagramme de phases de la cavité semi-hybride, où l'éclatement de Rabi et le facteur *Q* sont plus petits, avec celui déjà obtenu dans la cavité entièrement hybride. Ces résultats vont nous permettre de vérifier l'exactitude de notre modèle de relaxation des polaritons et, éventuellement, de l'améliorer.

Deuxièmement, dans cette thèse nous ne nous sommes pas focalisés sur la démonstration de l'équilibre thermique du système de polaritons[1], tout au contraire, puisque l'utilisation d'une tâche d'excitation petite (~2µm) aboutit à un potentiel polaritonique répulsif, induit par la présence du réservoir excitonique, qui confère une certaine énergie cinétique additionnelle aux polaritons. Afin d'effectuer une étude systématique et de démontrer une quasi-BEC à température ambiante, une tâche d'excitation large est fondamentale, ce qui nécessite du coup une microcavité de fort Q et un désordre photonique négligeable. En dépit de la possibilité que ces exigences soient remplies dans les micocavités actuellement étudiées, la démonstration d'une quasi-BEC à température ambiante pourrait exiger des microcavités de meilleure qualité : pour cela nous avons deux possibilités, des cavités entièrement hybrides à faible gradient d'épaisseur, ou des semi-hybrides avec la réflectivité du DBR inférieur plus élevée et une largeur de bande d'arrêt plus grande[2]. Par ailleurs, ces microcavités améliorées

---

[1] Bien que certaines de nos mesures semblent indiquer un quasi-équilibre thermique, des études systématiques n'ont pas encore été réalisées.

[2] Comme indiqué dans le Chapitre 6, il semble que le contenu en Ga dans les DBRS AlGaN/AIN utilisés dans les microcavités semi-hybrides (Z1214 et Z1232) est inférieur à celui prévu lors de la conception de la cavité, ce qui conduit à un facteur *Q* et une largeur de bande d'arrêt inférieurs au cas idéal.

permettront d'étudier la cohérence spatiale du système de polaritons, en-dessous et au-dessus du seuil, et de caractériser plus en détail comment son expansion se produit; en particulier, l'étude de la cohérence spatiale fournira des informations sur le caractère des condensats de polaritons dans les cavités ZnO: gouttelettes (comme dans les microcavités CdTe) Vs étendu (comme dans les cavités GaAs).

Enfin, beaucoup de sujets de recherche de la physique de polaritons, tels que la superfluidité et les solitons, impliquent l'étude de la propagation de condensats de polaritons, ce qui est actuellement réalisé à basse température. Les microcavités ZnO offrent la possibilité de réaliser des études de propagation de polaritons à température ambiante et, surtout, avec des polaritons de poids excitonique très différent. Ainsi, il sera possible d'étudier l'influence de la masse effective des polaritons sur la propagation des condensats et sur leur interaction avec des défauts. Il convient de noter que des expériences préliminaires à basse température, à l'Institut Pascal et au L2C, ont montré des condensats de polaritons se propageant sur 10-15 micromètres le long du gradient d'épaisseur de la cavité entièrement hybride, loin du point d'excitation. À l'avenir, au lieu d'utiliser le potentiel polaritonique formé naturellement (Voir Figure 4.9 par exemple) et involontairement hérité du processus de fabrication, il devrait être possible de réaliser volontairement des potentiels arbitraires et de manipuler les condensats de polaritons à volonté.

(2) En termes des technologies de fabrication

Puisqu’un certain nombre d'études nécessiteront des temps de vie de polaritons plus longs et, par conséquence, des *Q*s plus élevés, il faudra poursuivre l'amélioration des techniques de fabrication actuelles. Pour les microcavités entièrement hybrides, un processus plus fiable pour contrôler le gradient d'épaisseur de ZnO et la rugosité de surface doit être développé. Pour les microcavités semi-hybrides, une amélioration quantitative nécessite l'utilisation d’alliages AlGaN avec très peu d’Al, afin que le contraste d’indice entre les deux matériaux (AlGaN et AlN) du DBR soit plus grand. Cela permettra d'augmenter de façon simultanée la largeur de la bande d’arrêt du miroir ainsi que le facteur *Q* (voir Figure 6.2).

En outre, de nouvelles structures de cavité doivent être exploitées, dont la plus prometteuse consiste à intégrer des puits quantiques homoépitaxiés de ZnO/ZnMgO dans la zone active de la cavité. En effet, l’homoépitaxie des puits quantiques de ZnO/ZnMgO sur des substrats de ZnO a été étudiée de façon intense au CNRS-CRHEA pendant ces dernières années, et des puits quantiques non-polaires de grande qualité ont été réalisés, comme en témoigne une réduction de l’intensité de luminescence entre basse température et température ambiante beaucoup plus faible que dans du ZnO massif ou dans des puits quantiques heteroepitaxiés [202,207]. Les avantages d'utiliser des puits quantiques comme zone active résident dans plusieurs domaines. D'abord, ceci augmente encore l'énergie de liaison de l’exciton et sa force d’oscillateur, ainsi que le rapport entre le taux de recombinaison radiative et non radiative à température ambiante, par rapport au ZnO massif. En outre, puisque des puits quantiques non-polaires peuvent être épitaxiés, l'effet Stark quantique confiné [208] néfaste peut être supprimé. Deuxièmement, comme les puits quantiques sont minces par rapport au matériau massif, l’absorption totale de la zone active est considérablement réduite. Cela pourrait probablement permettre l'observation de la branche haute de polaritons haute dans des mesures de réflectivité. Troisièmement, l'utilisation de puits quantiques pourrait contribuer à diminuer encore le seuil de condensation de polaritons, comme prévu théoriquement [141]. Nos études préliminaires visant à fabriquer ces microcavités avec des puits quantiques sont présentées à l'annexe C. La difficulté technique principale est de graver complètement le substrat de ZnO sur lequel les puits quantiques de ZnO/ZnMgO sont épitaxiés, sans affecter sérieusement la qualité optique des puits quantiques. Cela nécessitera encore des recherches sur la croissance de ZnMgO et la technologie de gravure.

Quelles que soient les nouveautés que l'avenir apportera, le ciel au-dessus de la polaritonique à base de ZnO semble complètement dégagé pour les prochaines années.

Résumé en Français

Titre de thèse en Français :
Fabrication et Caractérisation des Microcavités à Base de ZnO en Régime de Couplage Fort : Laser à Polariton

Résumé :

L’interaction entre lumière et matière est un domaine de recherche en pleine expansion depuis quelques années. Dans une cavité optique où l’on a introduit des émetteurs, si le confinement optique est suffisamment fort les photons peuvent être réabsorbés par les émetteurs avant qu'ils n'échappent de la cavité, réémis à nouveau dans la cavité, réabsorbés et ainsi de suite, menant à un échange d'énergie réversible entre l'émetteur et la cavité. Dans cette situation le couplage lumière et matière donne naissance à de nouveaux états propres, construits à partir des modes nus de l'émetteur et la cavité, et le système est dit dans le **régime de couplage fort**. Dans un semiconducteur, le premier état excité reçoit le nom d’exciton, une quasi-particule formée par un paire électron-trou liée par l'interaction de Coulomb. Hopfield a démontré qu’un photon dans un semiconducteur se couple efficacement aux excitons de même vecteur d'onde, donnant lieu à de nouveaux états propres appelés polaritons excitoniques [10]. Dans cette situation, l'énergie est conservée car elle passe de façon réversible des excitons aux photons, et vice versa. Les polaritons excitoniques sont des quasi-particules, partiellement matière, partiellement lumière. Les photons sont des bosons. Les excitons sont, quant à eux, des bosons composites qui peuvent perdre leur caractère bosonique aux fortes densités (dites de Mott) quand les interactions entre électrons ou entre trous deviennent comparables à l’interaction au sein de la paire électron-trou. Par conséquent, les polaritons pourront eux aussi perdre leur caractère bosonique aux fortes densités. Dans le but d'améliorer le couplage entre lumière et matière dans ces systèmes semiconducteurs, des cavités avec de grands facteurs de qualité et de petits volumes modaux ont été intensément étudiées, surtout depuis le début des années 1990 [9]. Le régime de couplage fort a été mis en évidence dans une microcavité à base de puits quantiques de GaAs par Weisbuch *et al* en 1992 [12] : l'anti-croisement de la branche basse de polaritons (LPB) et la branche haute de polaritons (UPB) a été observé. Cet article fondateur a ouvert la voie au développement *de la polaritonique* en tant qu’un domaine en soi. Pendant les années suivantes, le régime de couplage fort a été observé également dans d'autres systèmes semiconducteurs, y compris dans du ZnCd(Mg)Se(S) [13], dans du CdTe [14], dans des organiques [15], dans du GaN [16] et, finalement, dans du ZnO [17].

L'idée de condensation de Bose-Einstein (BEC) a été proposée par Einstein en 1925, en développant un travail de jeunesse de Bose : elle implique l’accumulation d’un nombre illimité de bosons dans l'état de plus basse énergie d'un système donné [18]. La condensation de Bose-Einstein a été démontré pour la première fois avec des atomes ultra-froids en 1995 par Cornell, Wieman et Ketterle [19,20]. Parallèlement, des efforts ont été investis pour démontrer la BEC des excitons dans des systèmes semiconducteurs [21-23]. La température

critique à laquelle la transition de phase BEC est obtenue était de l'ordre du nanokelvin, pour les atomes, et en-dessous 1K pour les excitons. Comme la température critique pour la BEC est inversement proportionnelle à la masse effective des particules qui condensent, des températures critiques beaucoup plus élevées (en effet, de cryogénique à température ambiante) pourraient être espérées dans un système constitué à base de polaritons de cavité, étant donné que comme leurs masses effectives peuvent être inférieures quelques ordres de grandeur à celle des excitons. Un autre intérêt des cavités est d'introduire un minimum d'énergie dans la courbe de dispersion des polaritons excitoniques et rendre possible la thermalisation des polaritons. Par contraste, les structures libres homogènes à 3D ne présentent pas de minimum d'énergie, les polaritons excitoniques ont tendance à s'accumuler dans la région dite de "bottleneck" [11], ce qui rend l’obtention de l'équilibre thermique très difficile. En 1996, Imamoglu *et al* ont proposé que l'émission de lumière cohérente devrait être possible à partir d’une cavité en couplage fort dans laquelle les polaritons occupent tous le même état (dans l’occurrence, l'état fondamental de la cavité). Dans cet article, il était suggéré que l’occupation massive de l’état de base pourrait être facilitée par diffusion bosonique stimulée [24]. Si un tel dispositif était fabriqué, il recevrait le nom de «**laser à polaritons**», étant donné qu’il émettrait de la lumière cohérente et que le mécanisme de gain serait dû aux polaritons. Le premier rapport expérimental d’un laser à polaritons sans ambiguïté a été publié par Le Si Dang *et al* en 1998 [25], suivi par la première démonstration de la **BEC des polaritons de cavité** par Kasprzak *et al*, en 2006 [26]. Tous les deux ont été réalisés dans des microcavités à base de CdTe et à ~5K. Ces réalisations, ainsi que beaucoup d'autres, ont fortement encouragé les études sur les condensats de polaritons pendant les 10 années suivantes [27,28].

Les énergies de liaison des excitons dans GaAs et CdTe massifs sont 4 et 10 meV, respectivement, et pourraient augmenter jusqu'à 25meV dans les puits quantiques à base de CdTe [11]. Ces valeurs rendent les excitons dans ces matériaux seulement appropriés pour l'observation des non-linéarités à basse température [29]. Pour cette raison, depuis le début des années 2000 beaucoup d'attention a été accordée aux matériaux semiconducteurs à large bande interdite tels que les organiques, le GaN et le ZnO, qui devaient rendre possible la fabrication des dispositifs polaritoniques fonctionnant à température ambiante. En effet, les premiers lasers à polaritons à température ambiante ont été démontrés dans des microcavités à base de GaN massif d’abord et à base de puits quantiques ensuite, en 2007 et 2008 respectivement [30,31]. Deux ans plus tard, en 2010, le laser à polaritons à température ambiante a également été observé dans une microcavité à base d’un semiconducteur organique [32].

Le ZnO est un semiconducteur II-VI émettant dans la gamme UV (bande interdite ~3.36eV à température ambiante), et est considéré comme l'un des matériaux les plus adaptés pour les lasers à polaritons à température ambiante [33]. Son énergie de liaison d'exciton atteint 60meV dans du matériau massif c'est à dire beaucoup plus grande que $k_B T$ à température ambiante. Ses grandes forces d'oscillateur, généralement quatre à dix fois plus grandes que dans du GaN, peuvent conduire à un éclatement de Rabi important, tandis que sa forte densité de Mott devrait permettre de garder le comportement bosonique des excitons même à des densités de particules élevées. Cependant, le manque d'études technologiques préalables autour de matériau, si nous le comparons au GaN par exemple, conduit à un certain nombre de difficultés techniques qui ont entravé la fabrication de microcavités à base de ZnO jusqu'à très récemment. En effet, avant que cette thèse ne commence il n'y avait pas eu de rapport de laser à polaritons à base de ZnO, même si le couplage fort avait été déjà démontré à basse température [17] et même à température ambiante [34-38]. Néanmoins, de grands progrès dans le domaine de la polaritonique à base de ZnO ont été réalisés au cours des trois dernières années. Un laser à polaritons en ZnO a été démontrée pour la première fois à 120K par un consortium CNRS [39] en 2011, en collaboration avec l'EPFL, suivi par une étude sur la relaxation de polaritons assistée par émission de phonons optiques [40] en 2012. L'année 2012 a vu une explosion de publications sur les lasers à polaritons à base de ZnO, y compris le rapport de Franke *et al* [41] autour de 200K, et la publication controversée du laser à polaritons à température ambiante par Lu et Lai *et al* [42,43]. En outre, les études par Xie *et al* [44], en 2012, et Trichet *et al* [45], en 2013, ont indiqué que la condensation de polaritons pourrait être atteint dans des microfils de ZnO .

Dans ce manuscrit de thèse, nous décrivons la fabrication et caractérisation de microcavités à base de ZnO qui fonctionnent en régime de couplage fort, et qui ont permis l'observation de la condensation de polaritons dans une grande gamme de désaccord exciton-photon et de basse température à température ambiante.

La première partie de ce manuscrit présente les propriétés du semiconducteur ZnO, ainsi que les principes de travail des microcavités optiques la microcavité, et les fondamentaux du couplage fort et de la condensation de polaritons. D'abord, les propriétés physiques de ZnO et de ses excitons sont présentées (le chapitre 1). Les concepts fondamentaux à propos d'excitons, y compris l'énergie de liaison, les règles de sélection des transitions optiques, la force de l'oscillateur et la densité de Mott, sont présentés, soulignant les spécificités de ZnO. Ensuit les principes fondamentaux des microcavités planaires sont présentés (le chapitre 2). La méthode de matrice de transfert pour simuler la propagation de la lumière dans des systèmes multi-couches est décrite en détail. Les principes de fonctionnement des DBRs ainsi que des résonateurs Fabry-Perot, constitués d'une couche diélectrique placée entre deux DBRs, sont présentés. Finalement, une description détaillée des polaritons de cavité et une revue historique de ce domaine de recherche sont données (chapitre 3), y compris les concepts de polariton de cavité et couplage fort, les principes fondamentaux de condensation de polaritons, et un aperçu des principaux résultats dans les microcavités à semiconducteurs à large bande interdite, en particulier dans des microcavités à base de ZnO.

Les deuxième et troisième parties de ce manuscrit présentent les résultats expérimentaux obtenus dans les microcavités entièrement hybrides (les chapitres 4 et 5) et semi-hybrides (le chapitre 6) à base de ZnO.

La microcavité entièrement hybride à base de ZnO fabriquée dans cette thèse implique une stratégie de fabrication complètement nouvelle qui a été développée au CNRS-CRHEA: l'idée principale est assez simple puisqu'elle consiste à amincir un substrat de ZnO, qui fait 500 micromètres d'épaisseur initialement, jusqu'à quelques centaines de nanomètres et entourer ce ZnO par deux DBRs à base de HfO_2/SiO_2. Strictement parlant, cette idée n'est pas nouvelle puisqu'elle elle a été considérée auparavant par le CNRS-CRHEA [159,164,205] comme moyen de fabrication de cavités; pourtant, notre approche originale surmonte les difficultés liées soit à la couche d'arrêt [159,164] soit à la gravure sélective du substrat [205], qui ont limité, lors des tentatives précédentes, la qualité cristalline et/ou la rugosité de l'interface entre la zone active et un des deux DBRs. Le mérite de la nouvelle stratégie de fabrication réside dans le fait qu'elle ne nécessite ni couche d'arrêt, ni croissance hétéro-épitaxiale de ZnO, ce qui permet de garder une qualité cristalline optimale de la région active. Cette fabrication a conduit à une valeur record pour le facteur Q (~2500-4000) parmi toutes les microcavités planaires à base de ZnO et un grand éclatement de Rabi (~250meV), comparable à ceux obtenus dans les microfils de ZnO, où le recouvrement entre les excitons et le mode optique atteint presque les 100%. Par ailleurs, le gradient d'épaisseur lié à la méthode de fabrication a permis un réglage continu de l'énergie du mode de polariton pour des longueurs de cavité différentes, allant de $\lambda/2$ à 6λ (ou au-delà) ; ceci a permis d'accéder à tous les désaccords cavité-exciton possibles. Enfin, un laser à polaritons fonctionnant à température ambiante a été démontré sans ambiguïté, avec des figures de mérite en général 5 à 10 fois meilleures que celles des autres rapports contemporains [42,43].

Cette microcavité entièrement hybride a permis d'approfondir l'étude des polaritons de cavité et apermis, en particulier, d'avoir accès à des condensats de polaritons très différents (par exemple très excitoniques) de ceux obtenus dans d'autres systèmes. Tout d'abord, le diagramme de phases de condensation des polaritons a été établi pour la première fois dans une microcavité à base de ZnO, et ce, dans une gamme de désaccord exciton-photon sans précédent (-214meV à +450meV) et depuis les basses températures jusqu'à la température ambiante. Le poids excitonique des condensats de polaritons varie ainsi de 17% à 96%, ce qui correspond à une modification de la masse effective des polaritons, de leur temps de vie et de leur constante d'interaction de plus d'un ordre de grandeur [206]. Le diagramme de phases a mis en évidence que la relaxation de polaritons assistée par phonons LO est très efficace dans ZnO, ce qui ne devrait pas être une surprise étant donné le caractère polaire de ZnO; ce mécanisme efficace semble être à l'origine du désaccord optimal entre la cavité et les excitons pour la condensation aux hautes températures (supérieures à 200 K) et aux températures intermédiaires (de 100 K à 200 K). En outre, sur les régions épaisses de la microcavité, où plusieurs LPBs sont présentes, une compétition de modes, similaire à celle observée dans des lasers en couplage faible, a été observée et utilisée pour tester notre compréhension du diagramme de phases, qui traduit le compromis entre cinétique et thermodynamique. En outre, dans certaines conditions il a été possible de contrôler la condensation de polaritons de façon à l'obtenir dans deux branches LPB différentes mais créées au même endroit: de cette façon, sans changer ni l'épaisseur de la cavité ni le potentiel excitonique, il a été possible d'étudier l'effet du réservoir excitonique et du gradient du mode photonique sur les condensats de polaritons en fonction de leur poids lumière Vs matière.

Pour la fabrication des microcavités semi-hybrides à base de ZnO une stratégie de fabrication plus sophistiquée a été employée : elle implique la croissance épitaxiale de ZnO sur des DBRs nitrures et le dépôt d'un DBR diélectrique au-dessus: en ce sens, les résultats obtenus dans cette thèse peuvent être considérés comme une amélioration quantitative, plus que qualitative, et suffisamment importante pour permettre l'obtention d'un laser à polaritons à température ambiante, ce qui n'avait pas été possible auparavant.. Cette approche nécessite surmonter une série de difficultés technologiques, parmi lesquelles la croissance de DBR nitrures avec un grand nombre (>15) de paires est la plus sérieuse. En effet, la différence de coefficients de dilatation thermiques entre les nitrures et le substrat Si entraîne inéluctablement l'apparition de fissures dans des couches AlGaN épaisses et riches en Al. Au CNRS- CRHEA le problème a été résolu, dans un travail de doctorat récent, en réalisant l'épitaxie des nitrures sur des mesas de Si et non plus sur un substrat Si planaire. Des DBRs $Al_{0.2}Ga_{0.8}N$/AlN avec 30 paires et sans fissures ont été réalisés sur des substrats Si (110) et Si (111) patternés, présentant une morphologie de surface lisse (rugosité ~1.6nm), une forte réflectivité et une largeur de bande d'arrêt d'environ 200meV. Une autre difficulté importante est la croissance de la couche active de ZnO, qui doit maintenir une grande qualité cristalline sur les DBRs. La couche active de ZnO optimisée présente de bonnes propriétés morphologiques (rugosité de surface ~2.6nm) et optiques. La microcavité complète, achevée par le dépôt du DBRs supérieur, fait de 11 paires de HfO_2/SiO_2, présente un élargissement inhomogène photonique extrêmement faible (par rapport à l'éclatement de Rabi et à la largeur homogène de l'exciton) et un facteur Q ~2000. Enfin, un laser à polaritons à température ambiant a été démontré aussi avec cette approche.

En plus des résultats expérimentaux mentionnés ci-dessus, d'autres tentatives ont été également testées pour obtenir des améliorations, soit en termes de facteur Q (la croissance épitaxiale de ZnO sur des DBRs AlGaN/AlInN fournis par EPFL), ou en termes de facteur Q et de largeur de bande d'arrêt (dépôt de ZnO sur des DBRs diélectriques).

List of Acronyms

2D ------ 2 dimensional
3D ------ 3 dimensional
AFM ------ atomic force microscopy
CNRS ------ Centre National de la Recherche Scientifique
CRHEA ------ Centre de Recherche sur l'Hétéro-Epitaxie et ses Application
DAP ------ donor-acceptor-pair
DBR ------ distributed Bragg reflector
D^0X ------ donor-bound exciton
EPFL ------ Ecole Polytechnique Fédérale de Lausanne
FWHM ------ full width half maximum
HWHM ------ half width half maximum
L2C ------ Laboratoire Charles Coulomb
LASMEA ------ Laboratoire des Sciences et Matériaux pour l'Electronique et d'Automatique
LO- ------ longitudinal optical-
LPB ------ lower polariton branch
LPN ------ Laboratoire de Photonique et de Nanostructures
μPL ------ micro-photoluminescence
MBE ------ molecular beam epitaxy
MOCVD ------ metal organic chemical vapor deposition
MQW ------ multiple quantum well
PL ------ photoluminescence
PLD ------ pulsed laser deposition
QW ------ quantum well
RHEED ------ reflection high-energy electron diffraction
RIE ------ reactive ion etching
RMS ------ root-mean-square
SEM ------ scanning electron microscopy
TEM ------ transmission electron microscopy
TES ------ two-electron-satellite
UPB ------ upper polariton branch
XRD ------ X-ray diffraction

Appendix

A. Deposition of polycrystalline ZnO/ZnMgO heterostructures on dielectric DBRs

In the next pages several alternative fabrication approaches, which have been tested and have been up to now unsuccessful, will be described.

The most widely adopted strategy for fabricating a fully-hybrid ZnO microcavity, as stated in 3.3.3, is to directly deposit ZnO bulk or ZnO/ZnMgO quantum wells (QWs) on dielectric DBRs. Even if the resulting active region is polycrystalline, it is possible to obtain good enough crystalline quality to achieve strong coupling regime and polariton lasing, as successfully demonstrated by the team of Prof. Dr. M. Grundmann and Dr. R. Schmidt-Grund in Universität Leipzig [35,41], where the ZnO/ZnMgO thin films were deposited using pulsed laser deposition (PLD). At CRHEA-CNRS we have employed molecular beam epitaxy (MBE) to deposit both, ZnO and ZnO/ZnMgO QWs, on top of HfO_2/SiO_2 and Si_xN_y/SiO_2 DBRs, fabricated by the team of S. Bouchoule (LPN-CNRS), and YSZ[1]/Al_2O_3 DBRs fabricated by PLD at Universität Leipzig.

The general strategy to optimize the properties of the deposited material was to vary the Zn and O fluxes, while keeping a low substrate temperature (~100°C). As revealed by RHEED, the layers were polycrystalline. To illustrate the quality of the resulting samples, a ZnO/ZnMgO sample will be used. The aim was to fabricate a $3\lambda/2$ cavity with two ZnO insertions, ~20nm thick each, placed at the antinodes of the cavity mode. The active region was deposited on a 9.5-pair HfO_2/SiO_2 DBR on Si. The cross-section SEM image, displayed in Figure A.1, shows clear interfaces between the layers of the HfO_2/SiO_2 DBR and the ZnMgO layer deposited on top. Furthermore, the two ZnO insertions can be clearly identified. However, the AFM image indicates a RMS surface roughness of ~10nm, which is too large for obtaining *Q* factors as high as expected.

---

[1] YSZ means Yttrium stabilized Zirconia

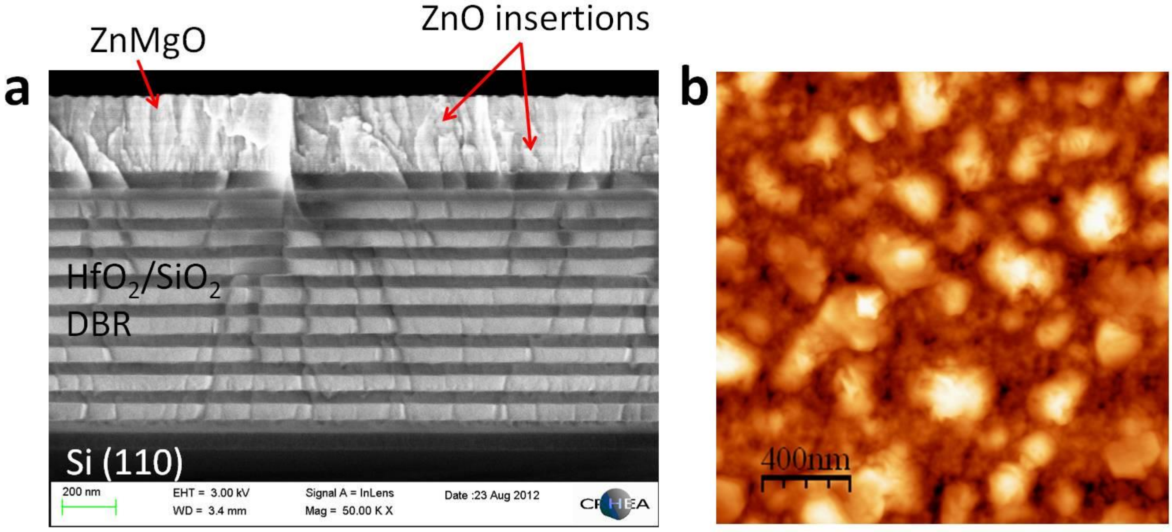

Figure A.1: **a**. Cross-section scanning electron microscopy (SEM) image of the ZnO QW half-cavity. **b**. Atomic force microscopy (AFM) image of the half-cavity surface, exhibiting a root-mean-square (RMS) roughness of 10.8nm.

The room temperature photoluminescence (PL) measured at CNRS-CRHEA[1] is shown in Figure A.2. The ZnO insertion exciton emission is located at ~3.33meV, i.e. above the free-exciton emission in bulk ZnO, while the ZnMgO barrier appears at 3.67eV, indicating a Mg content of approximately ~18% [209]. The fact that the energy emission of the ZnO insertions appears at energies larger than those of bulk ZnO material might indicate: either the annealing carried out after the growth gives rise to some Mg diffusion from the “barriers” into the insertions, or the strong-coupling pushes the UPB far above the ZnO bandgap (the UPB being visible because of a reduced ZnO absorption: indeed, the ZnO thickness is of the order of $\lambda/4$). A wide and pronounced emission from deep-levels is observed in the visible range, emission that is modulated by a series of Bragg modes (Figure A.2**a**). A detailed view near the ZnO insertion energy is presented in Figure A.2**b**, where two peaks can be identified (green curves). The peak at higher energy (~3.326meV) corresponds to the ZnO insertions and exhibits a linewidth of 192meV, while the other at lower energy (~3.223meV) corresponds to the cavity mode displaying a linewidth of 84.7meV, i.e. a *Q*-factor of ~38. While the cavity mode varies continuously with the cavity thickness, as shown in Figure A.2**c**, the “ZnO insertion” energy does not vary at all. These observations point towards a Mg diffusion from the barriers into the ZnO insertion, rather than to a strong-coupling effect, in order to explain the high energy emission of the ZnO insertions.

---

[1] Continuous wave excitation with a frequency-doubled Ar-ion laser (λ=244nm) for all the PL measurements shown in the Appendix.

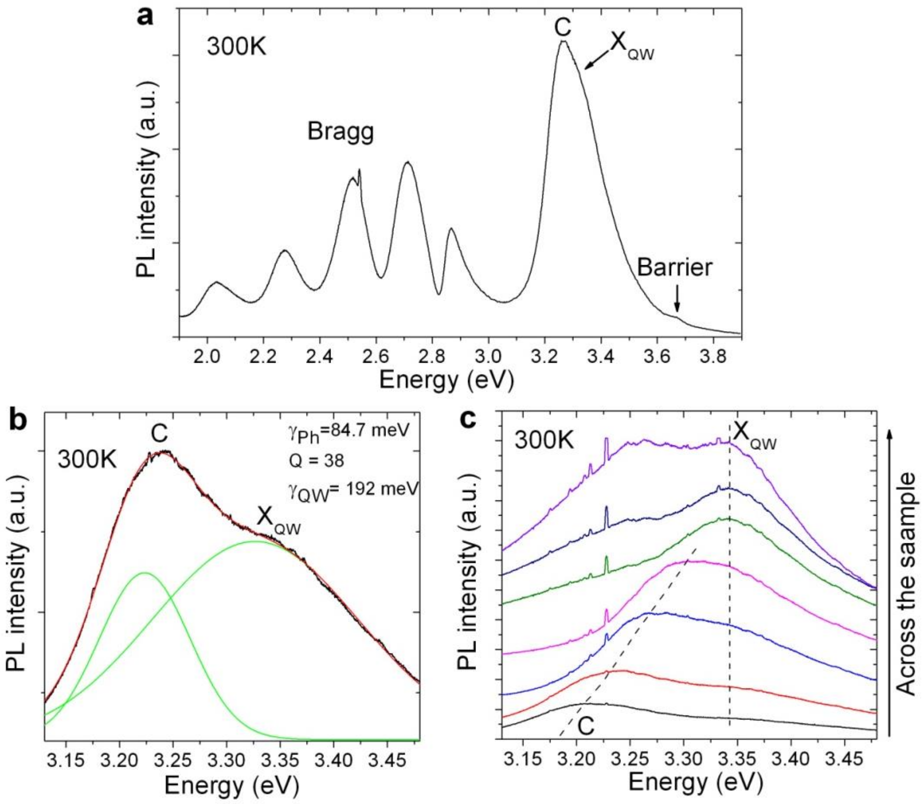

Figure A.2: Photoluminescence (PL) from a ZnO/ZnMgO-based half-cavity. **a**. Large range spectrum. **b**. Detailed spectrum near the ZnO insertion exciton energy, fitted with the excitonic mode (X_{QW}) and the cavity (C) mode (The green curves present the two fitted peaks and the red curve presents the overall fitted data). **c**. Spectra measured by moving the excitation spot across the sample. The measurements were carried out under continuous wave excitation with a frequency-doubled Ar-ion laser (λ=244nm). The sharp peaks in **a** and **c** correspond to the harmonics of the excitation laser.

The previous results illustrate the difficulty in obtaining simultaneously a smooth surface and an active region of “sufficient” optical quality. Indeed, the fact that the MBE growth proceeds immediately by forming a 3D polycrystalline layer precludes achieving smooth surfaces (the best results so far that have been achieved at CNRS-CRHEA give a RMS roughness of 3nm), even if low-temperature ZnMgO layers are used as buffer layers. On the contrary, PLD can enable amorphous ZnO layers to be grown, thereby maintaining a smooth surface; subsequently, and with the aim of recovering some exciton emission, the layers can be annealed at high temperatures, leading to the results presented in references [41]. Thus, in terms of fabrication strategy it seems that this approach requires PLD, or growth methods other than MBE.

B. Growth of ZnO on MOCVD-grown AlInN/AlGaN DBRs on GaN templates

The AlGaN/AlInN DBRs fabricated in the group of Prof. Dr. N. Grandjean at Ecole Polytechnique Fédérale de Lausanne (EPFL, Switzerland) have led to fruitful investigations of exciton-polaritons in wide bandgap materials, including the first demonstration of room temperature polariton lasers in 2007 [31] and 2008 [30]. The $Al_{0.85}In_{0.15}N/Al_{0.2}Ga_{0.8}N$ DBRs, fabricated by metal-organic chemical vapor deposition (MOCVD), exhibit extremely smooth surfaces (RMS <5Å), high reflectivity values 99.5% and stopband widths ~100meV [135], as shown in Figure B.1.

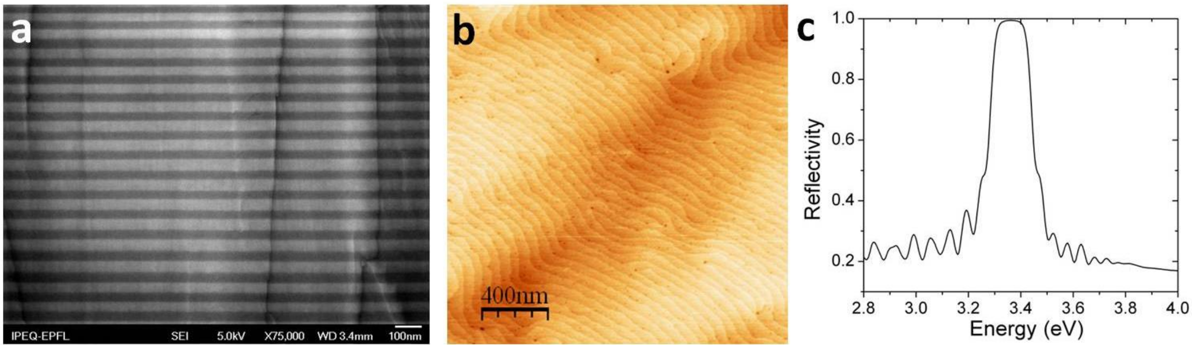

Figure B.1: Characterization of the 40 pair AlInN/AlGaN DBR grown by MOCVD at EPFL. **a**. Cross-section SEM image. **b**. AFM image of the surface displaying a RMS roughness of 0.29nm. **c**. Reflectivity spectrum. **a** and **c** were provided by EPFL.

In order to achieve high quality ZnO thin films on the DBRs, we made a complete optimization of the growth conditions on GaN/Al_2O_3 templates, as illustrated in Chapter 6. However, even if we could achieve very high quality ZnO growth on the trial GaN/Al_2O_3 templates, both in terms of surface roughness and optical quality, the optimized growth conditions could not be transposed onto the DBR. The main problem was caused by the difficulty in identifying the “real” surface temperature on the DBR, compared to that of the GaN templates on sapphire: on the one hand the periodic structure of the 40-pair DBR, containing totally 80 layers with periodically varying permittivity, modified the pyrometer reading and, on the other hand, it is not clear whether for the same heating power the surface temperature on the DBR is the same as on the GaN templates, giving the low thermal conductivity of AlInN layers. As a result, the exact substrate temperature during the growth on the DBR may have deviated from that employed during the optimization series. This can be understood by comparing the results on the “test” GaN templates and on the DBR, as shown in Figure B.2: whereas the growth on the bare GaN templates led to a smooth surface (streaky RHEED and RMS roughness of ~1.1nm on $2\times2\mu m^2$ areas), the ZnO surface on the real DBR, grown under the same conditions, turns to be extremely rough (spotty RHEED and roughness scale sufficiently large to manifest itself on the SEM images).

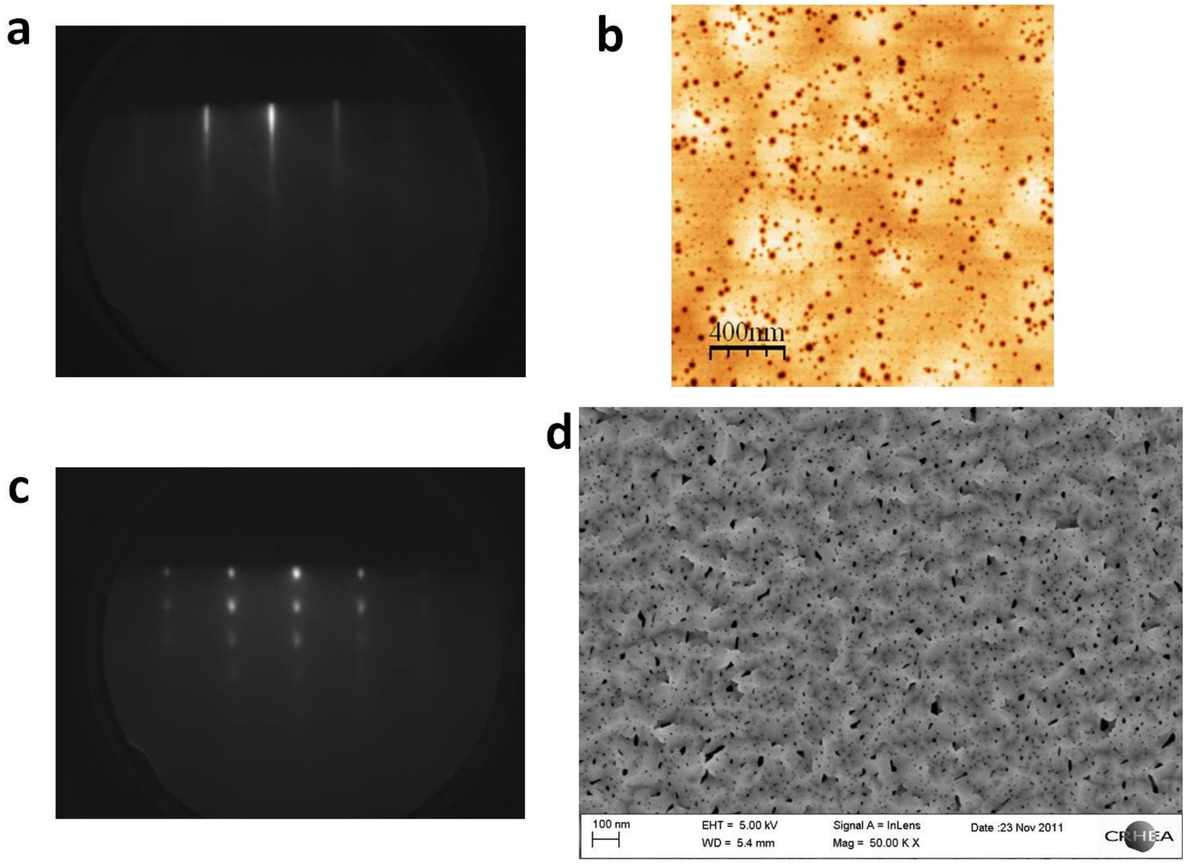

Figure B.2: RHEED pattern (**a**) and AFM image (**b**) ($2\times2\mu m^2$) of the ZnO layer grown on GaN/Al_2O_3 templates under optimal growth conditions, displaying a RMS roughness of 1.1nm. RHEED pattern (**c**) and SEM image (**d**) of the ZnO layer grown on the AlInN/AlGaN DBR with similar growth condition as **a**.

Since ZnO, compared to nitrides, can be very easily etched away, removal of the rough ZnO layer was attempted with the aim of reusing the AlInN/AlGaN DBR. Thus, the ZnO/Nitride-DBR was annealed under a mixture of hydrogen and ammonia atmosphere to remove the topmost ZnO. The SEM image of the sample surface after ZnO removal is displayed in Figure B.3**a**, where some surface damage on the nitride DBR can be inferred. Nevertheless, the 2D RHEED (Figure B.3**b)** indicates that a good re-growth might still be possible to achieve. Photoluminescence measurements were also performed indicating that all the ZnO had been removed.

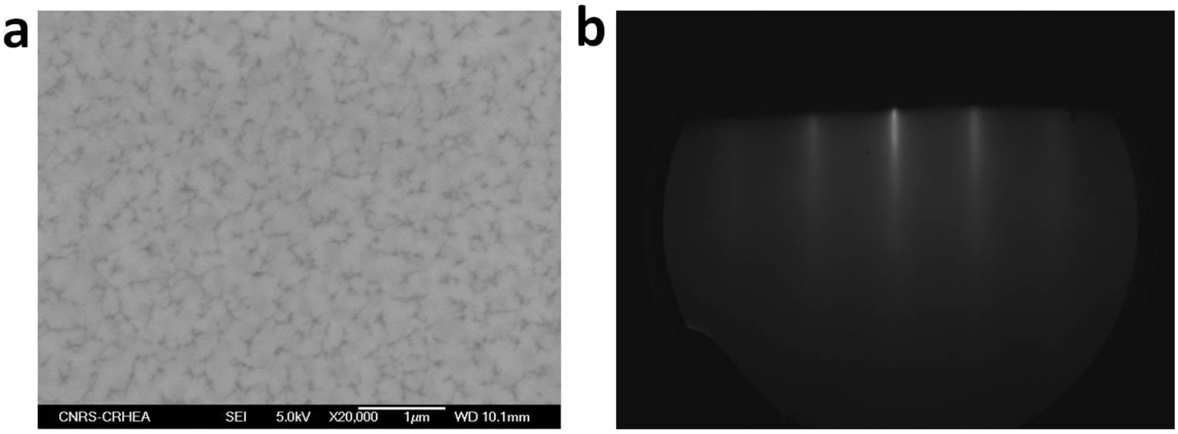

Figure B.3: SEM image (**a**) and RHEED (**b**) of the sample surface after the hydrogen/ammonia etching.

Despite a non-ideal initial surface (Figure B.3**a**), we did end up with a better ZnO surface than the previous attempt, most probably because this time we had a better estimation of the DBR temperature. The relevant results are shown in Figure B.4. The final RHEED pattern shows streaky features superimposed with some faint spots, which results from smooth surfaces, with typical lateral dimensions of tens of nanometers, on top of a rough surface whose length scale is of hundreds of nanometers. This morphology can be better observed in the SEM (Figure B.4**b**) and AFM (Figure B.4**c**) images. Unfortunately, the surface roughness measured by AFM (~10nm) is still too large for a high *Q*-factor microcavity. Finally, in the room temperature PL measurement Bragg modes, from the AlInN/AlGaN DBR, as well as the ZnO-related excitonic emission could be identified.

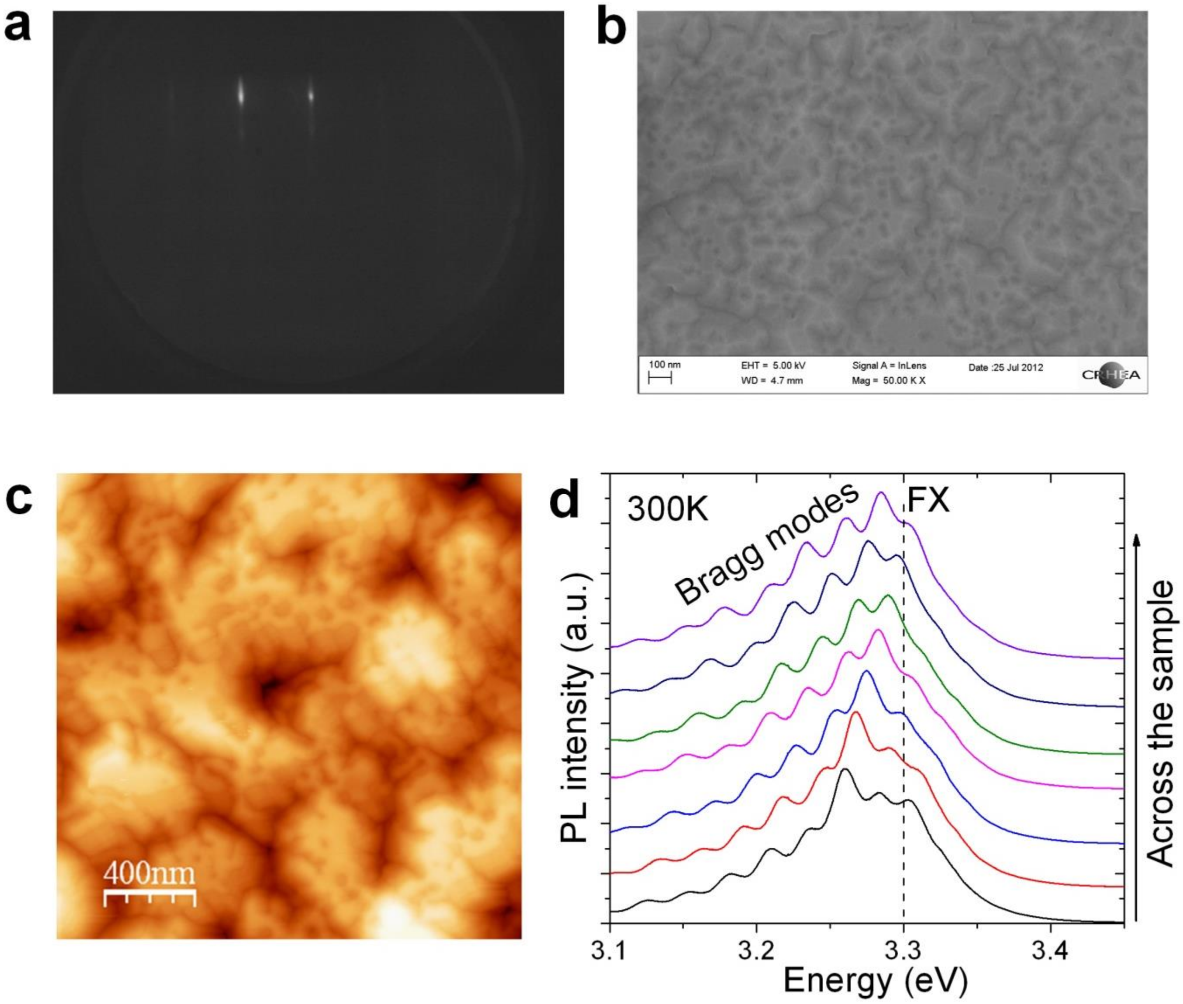

Figure B.4: RHEED pattern (**a**), SEM (**b**) and AFM (**c**) (2×2μm^2) images of the ZnO layer re-grown on the AlInN/AlGaN DBR (as explained in the main text), displaying a RMS surface roughness of 9.9nm. **d**. Room temperature PL spectra of the half-cavity when moving the excitation spot across the sample, with the ZnO free exciton emission (FX) and Bragg modes identified. The thickness of the half-cavity was designed to be 7λ/4.

In summary, contrary to the deposition on dielectric DBRs, the unsuccessful growth on the AlInN-based DBRS was mainly due to technical problems rather than to intrinsic ones. In this sense, future work based on this approach seems still promising. However, in any case there will be an intrinsic difficulty that should be considered: the stopband is too narrow, compared to the Rabi splitting expected in ZnO microcavities, which will probably lead to considerable coupling between excitons and Bragg modes.

C. Towards fully-hybrid ZnO microcavities with nonpolar homoepitaxial ZnO/ZnMgO quantum wells

Homoepitaxial growth of nonpolar ZnO/ZnMgO QWs has been intensively studied at CNRS-CRHEA by Dr. J. M. Chauveau, Dr. C. Deparis and Dr. C. Morhain [202,207,210,211]. The quasi-ideal properties of those homoepitaxial QWs have prompted the idea to use them as the active regions of ZnO-based microcavities. As already discussed in the section "Conclusion and Perspectives" of this thesis, the advantages of using nonpolar QWs include the enhancement of room temperature performance, the suppression of quantum confirmed stark effect, and the "theoretically-predicted" decrease of condensation threshold. While the homoeptaxial ZnO/ZnMgO quantum wells grown at CNRS-CRHEA exhibit excellent crystalline and optical quality, the question is how to embed them into a microcavity.

Thus, we will first describe the growth and characterization of the active region containing ZnO/ZnMgO QWs, and then we will present some preliminary studies attempting to incorporate such an active region into a fully-hybrid microcavity.

The design of the homoepitaxial active region is shown in Figure C.1**a**. The whole active region is grown on an *m*-nonpolar ZnO substrate so that every epitaxial layer is also *m*-nonpolar. The total length of the active region is designed to be 2λ, with the exact dimensions detailed in Figure C.1**a**. The structure contains 3 sets of QWs located at the antinodes of the cavity mode, with each set consisting of 3 $ZnO/Zn_{0.85}Mg_{0.15}O$ QWs. This structure was grown by Dr. C. Deparis at CNRS-CRHEA and exhibited a very smooth surface (<5Å), as evidenced in Figure C.1**b**.

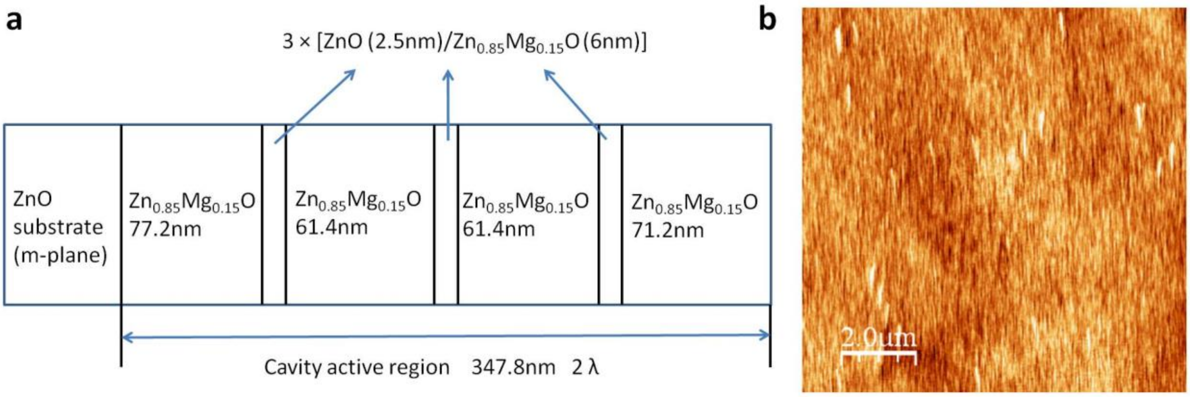

Figure C.1: **a**. Structural design of the homoepitaxial active region. **b**. AFM image ($10\times10\mu m^2$) of the epitaxial surface, displaying a RMS roughness ~0.39nm.

The optical properties of the m-nonpolar ZnO/ZnMgO QW structure of Figure C.1 were studied by temperature-dependent PL at CNRS-CRHEA: the results are shown in Figure C.2. As the c-axis is parallel to the sample surface, we are able to easily collect the light polarized both perpendicularly ($E \perp c$) and parallel ($E \parallel c$) to the c-axis[1], which mainly correspond to the A/B excitons[2] ($E \perp c$) and C exciton ($E \parallel c$), respectively (see 1.3.3). The temperature dependent spectra of the two polarizations are shown in Figure C.2**a** and **b**. In both cases, the free QW exciton (FX_{QW}) and its phonon replicas (FX_{QW}-LO and FX_{QW}-2LO) are clearly identified, exhibiting a continuous redshift with increasing temperature. For the $E \perp c$ polarization, the localized QW excitons (LX_{QW}) [212] dominate the PL emission at low temperature, which disappear with increasing temperature as most of them become thermally delocalized into free QW excitons. The emission from the ZnO substrate is also present at low temperature (labeled as Xs in Figure C.2**a**); its features have already been discussed in 4.3.2[3]. However, it is overwhelmed by the QW emission at higher temperatures due to its stronger thermal quenching (Figure C.2**f**), as will be discussed below. For the $E \parallel c$ polarization, and at low temperature, the emission is much weaker than for $E \perp c$, as the C exciton is much less populated than A/B excitons. Indeed, at low temperature (<70K) the dominating features in Figure C.2**b** (circled by the blue dashed line and labeled by "$E \perp c$" in blue) are actually from $E \perp c$ polarized emission, due to the imperfect polarizer selectivity (the factor is roughly 1 to 300). As temperature is raised, the C exciton becomes increasingly populated and its emission intensity rapidly dominates the $E \parallel c$ polarization spectra.

The emission energies of the QW excitons are plotted in Figure C.2**c**, showing a difference of ~40meV between the A/B and C excitons. The weak emission of the ZnMgO barrier, centered at ~3.605eV at 10K (not shown), indicates an actual Mg content of ~12% [209] and high crystalline quality, with most created excitons diffusing into the ZnO QWs. The excitonic linewidths (Figure C.2**d**) for $E \perp c$ and $E \parallel c$ display a similar trend, being 3~5meV at low temperature and broadened up to ~36meV at room temperature. One of the most interesting properties of m-nonpolar QWs is the evolution of their emission intensity with increasing temperature, as illustrated in Figure C.2**e** and **f**. In order to compare the thermal quenching of the A/B QW exciton emission with that of bulk ZnO, the emission intensity evolution of the ZnO substrate, which was studied in 4.3.2, is plotted together with the intensity corresponding to $E \perp c$ in Figure C.2**f**; in both cases, the integrated intensity at 10K was normalized to be 1. It is clearly seen that the thermal quenching of the QW emission is at least one order of magnitude less than that of the bulk ZnO, which could probably lead to an enhanced performance of the resulting photonic devices at room temperature.

---

[1] As the light collection is normal to the sample surface.

[2] As B and A excitons are close in energy (~5meV), at "high" temperatures they cannot be individually resolved in the PL experiments.

[3] Even if the ZnO substrate studied in 4.3.2 was Zn polar, the emitting features are the same as for the $E \perp c$ polarization of a nonpolar substrate, which is what is measured here.

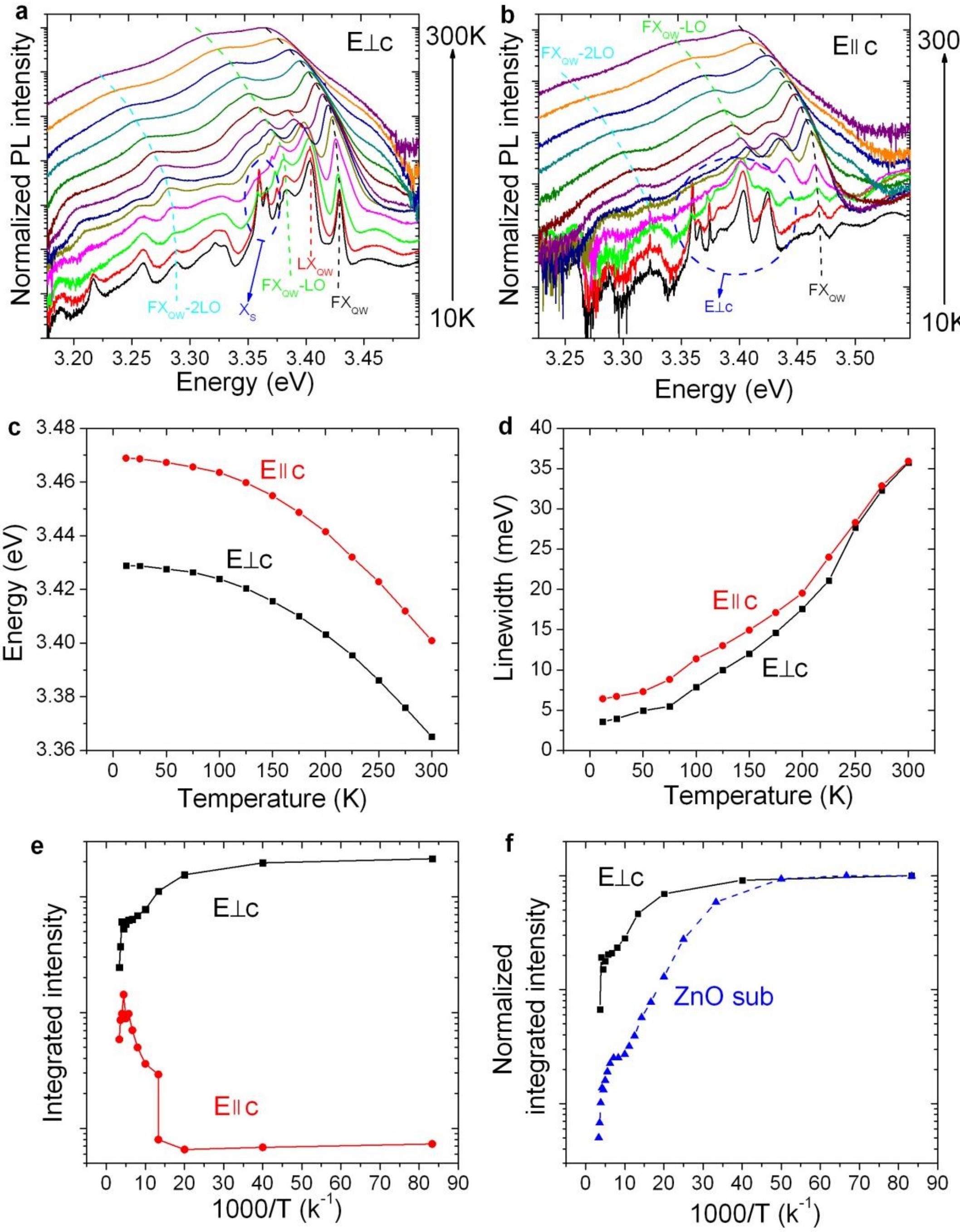

Figure C.2: Optical properties of the grown *m*-nonpolar ZnO/ZnMgO QW structure. Temperature dependent spectra for $E \perp c$ (**a**) and $E \parallel c$ (**b**) polarizations: at 10K and from 25K to 300K by 25K intervals. Typical emission features are connected by dashed lines with different colors. See the main text for their identification **c**. Energy vs. temperature of the free QW excitons (FX$_{\mathrm{QW}}$) for $E \perp c$ (black square) and $E \parallel c$ (red circle) polarizations. **d**. Spectral linewidth (FWHM) of the free QW exciton emissions as a function of temperature, for $E \perp c$ (black square) and $E \parallel c$ (red circle) polarizations. **e**. Integrated emission intensity as a function of 1000/temperature for $E \perp c$ (black square) and $E \parallel c$ (red circle) polarizations. **f**. Normalized integrated emission intensity as a function of 1000/temperature for $E \perp c$ polarization (black square), compared with the same properties for a Zn-polar ZnO substrate (blue triangles).

To fabricate a fully-hybrid microcavity with such a QW structure as the active region is, however, difficult. A similar approach as illustrated in Figure 4.1 has been proposed, while replacing the ZnO substrate in Figure 4.1**a** by the structure shown in Figure C.1**a** (with the epitaxial layer facing up). Moreover, in Step (c) we need to remove all the ZnO substrate while keeping the epitaxial layer barely affected, instead of just thinning the structure to a certain thickness. This kind of process has been used in Reference [159], where the authors etched completely the Si substrate with the help of an AlN etch-stop layer. For the structure discussed in this section, a successful process would require finding a wet or dry etching recipe that can selective etch ZnO with respect to ZnMgO. Unfortunately, we did not find such an etchant or recipe for Mg content of ~12%. We did find that reactive ion etching might exhibit a notable selectivity between ZnO and ZnMgO for “high” Mg contents of ~40%. With such a high Mg content, high quality epitaxial QWs are difficult to achieve because of the larger lattice mismatch and, moreover, the elastic strain stored in the layers is sufficiently large to promote layers cracking once the substrate is etched away.

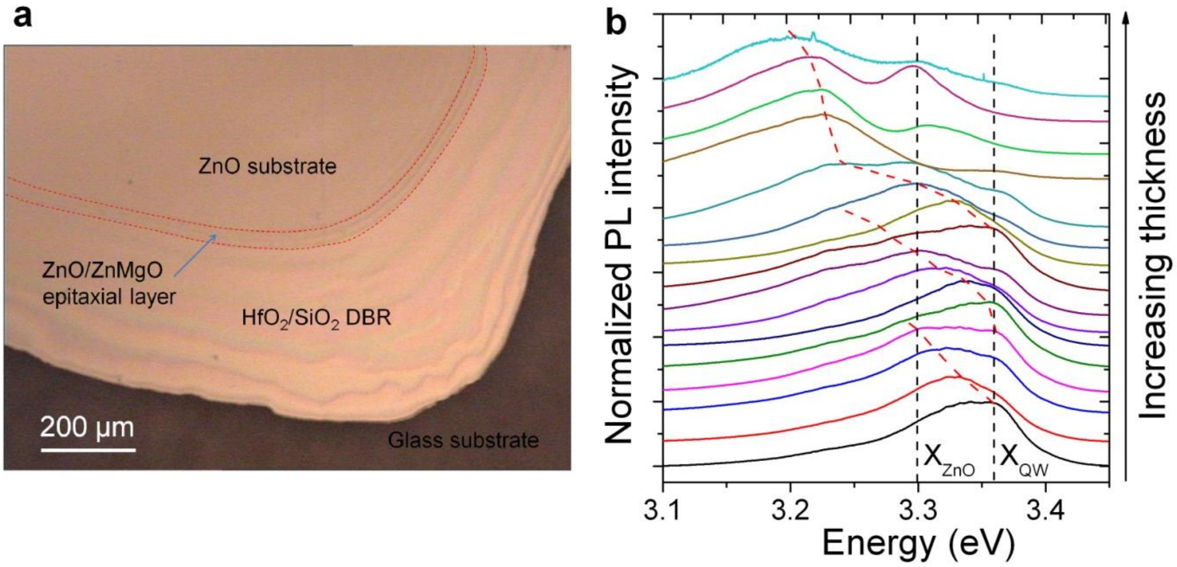

Figure C.3: **a**. Optical microscope image of the half-cavity fabricated with the method mentioned in the main text. The dashed red lines depict the border of the region where the ZnO/ZnMgO epitaxial layer is exposed. **b**. Room temperature μ-PL spectra of the half-cavity around the exposed ZnO/ZnMgO region in **a**, obtained by moving the excitation spot along the thickness gradient. The dashed black lines indicate the A exciton energy of ZnO substrate (X_{ZnO}) and the epitaxial QWs (X_{QW}), and the dashed red lines give a trend of how the optical modes move with increasing thickness.

Finally, with the aim of achieving a ZnO QW cavity, we applied exactly the same etching/polishing method employed in 4.1.2 (illustrated in Figure 4.1**c**); this results in a large thickness gradient, as shown by the interference fringes on the optical microscope image in Figure C.3**a**. In this case the epitaxial layers, whose total thickness is 2λ, are only exposed within a narrow area (in between the two dashed red lines), while most of the surface is still covered by several hundreds of nanometers of ZnO substrate. Similar to the sample discussed in Chapter 4, the photonic inhomogeneous broadening can be significant on the region where the QW epitaxial structure is exposed. Room temperature μPL measurements (excitation spot ~2μm) were performed at CRHEA to investigate the optical properties of the half-cavity, as shown in Figure C.3. The QW exciton emission (X_{WQ}) dominates the spectra for the smallest thicknesses, and gradually vanishes when going to larger cavity thicknesses, where bulk ZnO exciton emission (X_{ZnO}) becomes dominant. In the thicker parts of the sample optical modes of different orders, connected with dashed red lines in Figure C.3 b, can be resolved and their redshift with increasing thickness can be followed. However, in the thinnest region, where the QW emission dominates, the photonic inhomogeneous broadening is so large that the optical mode cannot be individually resolved and it overlaps with the QW emission.

In summary, the established cavity fabrication process is not good enough to achieve a QW-based microcavity. Further work needs to be conducted in order to find a recipe for selectively etch ZnO with respect to ZnMgO.

Bibliography

[1] E. M. Purcell, "Spontaneous emission probabilities at radio frequencies " Phys. Rev. **69** (11-12), 681 (1946).

[2] P. Goy, J. M. Raimond, M. Gross, and S. Haroche, "Observation of Cavity-Enhanced Single-Atom Spontaneous Emission," Physical Review Letters **50** (24), 1903-1906 (1983).

[3] R. G. Hulet, E. S. Hilfer, and D. Kleppner, "Inhibited Spontaneous Emission by a Rydberg Atom," Physical Review Letters **55** (20), 2137-2140 (1985).

[4] Y. Kaluzny, P. Goy, M. Gross, J. M. Raimond, and S. Haroche, "Observation of Self-Induced Rabi Oscillations in Two-Level Atoms Excited Inside a Resonant Cavity: The Ringing Regime of Superradiance," Physical Review Letters **51** (13), 1175-1178 (1983).

[5] R. J. Thompson, G. Rempe, and H. J. Kimble, "Observation of normal-mode splitting for an atom in an optical cavity," Physical Review Letters **68** (8), 1132-1135 (1992).

[6] M. Brune, F. Schmidt-Kaler, A. Maali, J. Dreyer, E. Hagley, J. M. Raimond, and S. Haroche, "Quantum Rabi Oscillation: A Direct Test of Field Quantization in a Cavity," Physical Review Letters **76** (11), 1800-1803 (1996).

[7] R. N. Hall, G. E. Fenner, J. D. Kingsley, T. J. Soltys, and R. O. Carlson, "Coherent Light Emission From GaAs Junctions," Physical Review Letters **9** (9), 366-368 (1962).

[8] H. Soda, K. Iga, C. Kitahara, and Y. Suematsu, "GaInAsP/InP surface emitting injection lasers," Japanese Journal of Applied Physics **18** (12), 2329-2330 (1979).

[9] K. J. Vahala, "Optical microcavities," Nature **424** (6950), 839-846 (2003).

[10] J. J. Hopfield, "Theory of the Contribution of Excitons to the Complex Dielectric Constant of Crystals," Physical Review **112** (5), 1555-1567 (1958).

[11] P. Y. Yu and M. Cardona, *Fundamentals of Semiconductors: Physics and Material Properties*. (Springer-Verlag, 1996).

[12] C. Weisbuch, M. Nishioka, A. Ishikawa, and Y. Arakawa, "Observation of the coupled exciton-photon mode splitting in a semiconductor quantum microcavity," Physical Review Letters **69** (23), 3314-3317 (1992).

[13] P. Kelkar, V. Kozlov, H. Jeon, A. V. Nurmikko, C. C. Chu, D. C. Grillo, J. Han, C. G. Hua, and R. L. Gunshor, "Excitons in a II-VI semiconductor microcavity in the strong-coupling regime," Physical Review B **52** (8), R5491-R5494 (1995).

[14] R. André, D. Heger, Le Si Dang, and Y. Merle d'Aubigné, "Spectroscopy of polaritons in CdTe-based microcavities," Journal of Crystal Growth **184–185** (0), 758-762 (1998).

[15] D. G. Lidzey, D. D. C. Bradley, M. S. Skolnick, T. Virgili, S. Walker, and D. M. Whittaker, "Strong exciton-photon coupling in an organic semiconductor microcavity," Nature **395** (6697), 53-55 (1998).

[16] N. Antoine-Vincent, F. Natali, D. Byrne, A. Vasson, P. Disseix, J. Leymarie, M. Leroux, F. Semond, and J. Massies, "Observation of Rabi splitting in a bulk GaN microcavity grown on silicon," Physical Review B **68** (15), 153313 (2003).

[17] F. Médard, J. Zuniga-Perez, P. Disseix, M. Mihailovic, J. Leymarie, A. Vasson, F. Semond, E. Frayssinet, J. C. Moreno, M. Leroux, S. Faure, and T. Guillet, "Experimental observation of strong light-matter coupling in ZnO microcavities: Influence of large excitonic absorption," Physical Review B **79** (12), 125302 (2009).

[18] A Einstein, "Quantentheorie des einatomigen idealen Gases," Sitzungsberichte der Preussischen Akademie der Wissenschaften **1**, 3 (1925).

[19] M. H. Anderson, J. R. Ensher, M. R. Matthews, C. E. Wieman, and E. A. Cornell, "Observation of Bose-Einstein Condensation in a Dilute Atomic Vapor," Science **269** (5221), 198-201 (1995).

[20] K. B. Davis, M. O. Mewes, M. R. Andrews, N. J. van Druten, D. S. Durfee, D. M. Kurn, and W. Ketterle, "Bose-Einstein Condensation in a Gas of Sodium Atoms," Physical Review Letters **75** (22), 3969-3973 (1995).

[21] L. V. Butov, A. L. Ivanov, A. Imamoglu, P. B. Littlewood, A. A. Shashkin, V. T. Dolgopolov, K. L. Campman, and A. C. Gossard, "Stimulated Scattering of Indirect Excitons in Coupled Quantum Wells: Signature of a Degenerate Bose-Gas of Excitons," Physical Review Letters **86** (24), 5608-5611 (2001).

[22] L. V. Butov, C. W. Lai, A. L. Ivanov, A. C. Gossard, and D. S. Chemla, "Towards Bose-Einstein condensation of excitons in potential traps," Nature **417** (6884), 47-52 (2002).

[23] D. Snoke, S. Denev, Y. Liu, L. Pfeiffer, and K. West, "Long-range transport in excitonic dark states in coupled quantum wells," Nature **418** (6899), 754-757 (2002).

[24] A. Imamoglu, R. J. Ram, S. Pau, and Y. Yamamoto, "Nonequilibrium condensates and lasers without inversion: Exciton-polariton lasers," Physical Review A **53** (6), 4250-4253 (1996).

[25] Le Si Dang, D. Heger, R. André, F. Bœuf, and R. Romestain, "Stimulation of Polariton Photoluminescence in Semiconductor Microcavity," Physical Review Letters **81** (18), 3920-3923 (1998).

[26] J. Kasprzak, M. Richard, S. Kundermann, A. Baas, P. Jeambrun, J. M. J. Keeling, F. M. Marchetti, M. H. Szymanska, R. Andre, J. L. Staehli, V. Savona, P. B. Littlewood, B. Deveaud, and Le Si Dang, "Bose-Einstein condensation of exciton polaritons," Nature **443** (7110), 409-414 (2006).

[27] H. Deng, H. Haug, and Y. Yamamoto, "Exciton-polariton Bose-Einstein condensation," Reviews of Modern Physics **82** (2), 1489-1537 (2010).

[28] A. Kavokin, J. J. Baumberg, G. Malpuech, and F. P. Laussy, *Microcavities*. (Oxford University Press, Oxford, 2007).

[29] M. Saba, C. Ciuti, J. Bloch, V. Thierry-Mieg, R. Andre, Le Si Dang, S. Kundermann, A. Mura, G. Bongiovanni, J. L. Staehli, and B. Deveaud, "High-temperature ultrafast polariton parametric amplification in semiconductor microcavities," Nature **414** (6865), 731-735 (2001).

[30] G. Christmann, R. Butte, E. Feltin, J.-F. Carlin, and N. Grandjean, "Room temperature polariton lasing in a GaN/AlGaN multiple quantum well microcavity," Applied Physics Letters **93** (5), 051102-051103 (2008).

[31] S. Christopoulos, G. Baldassarri Höger von Högersthal, A. J. D. Grundy, P. G. Lagoudakis, A. V. Kavokin, J. J. Baumberg, G. Christmann, R. Butté, E. Feltin, J. F. Carlin, and N. Grandjean, "Room-Temperature Polariton Lasing in Semiconductor Microcavities," Physical Review Letters **98** (12), 126405 (2007).

[32] S. Kena Cohen and S. R. Forrest, "Room-temperature polariton lasing in an organic single-crystal microcavity," Nat Photon **4** (6), 371-375 (2010).

[33] M. Zamfirescu, A. Kavokin, B. Gil, G. Malpuech, and M. Kaliteevski, "ZnO as a material mostly adapted for the realization of room-temperature polariton lasers," Physical Review B **65** (16), 161205 (2002).

[34] J.-R. Chen, T.-C. Lu, Y.-C. Wu, S.-C. Lin, W.-R. Liu, W.-F. Hsieh, C.-C. Kuo, and C.-C. Lee, "Large vacuum Rabi splitting in ZnO-based hybrid microcavities observed at room temperature," Applied Physics Letters **94** (6), 061103-061103 (2009).

[35] C. Sturm, H. Hilmer, R. Schmidt-Grund, and M. Grundmann, "Observation of strong exciton–photon coupling at temperatures up to 410K," New Journal of Physics **11** (7), 073044 (2009).

[36] S. Faure, C. Brimont, T. Guillet, T. Bretagnon, B. Gil, F. Medard, D. Lagarde, P. Disseix, J. Leymarie, J. Zuniga-Perez, M. Leroux, E. Frayssinet, J. C. Moreno, F. Semond, and S. Bouchoule, "Relaxation and emission of Bragg-mode and cavity-mode polaritons in a ZnO microcavity at room temperature," Applied Physics Letters **95** (12), 121102-121103 (2009).

[37] R. Shimada, J. Xie, V. Avrutin, U. Ozgur, and H. MorkoC, "Cavity polaritons in ZnO-based hybrid microcavities," Applied Physics Letters **92** (1), 011127-011123 (2008).

[38] L. Sun, Z. Chen, Q. Ren, K. Yu, L. Bai, W. Zhou, H. Xiong, Z. Q. Zhu, and X. Shen, "Direct Observation of Whispering Gallery Mode Polaritons and their Dispersion in a ZnO Tapered Microcavity," Physical Review Letters **100** (15), 156403 (2008).

[39] T. Guillet, M. Mexis, J. Levrat, G. Rossbach, C. Brimont, T. Bretagnon, B. Gil, R. Butte, N. Grandjean, L. Orosz, F. Reveret, J. Leymarie, J. Zuniga-Perez, M. Leroux, F. Semond, and S. Bouchoule, "Polariton lasing in a hybrid bulk ZnO microcavity," Applied Physics Letters **99** (16), 161104-161103 (2011).

[40] L. Orosz, F. Réveret, F. Médard, P. Disseix, J. Leymarie, M. Mihailovic, D. Solnyshkov, G. Malpuech, J. Zuniga-Pérez, F. Semond, M. Leroux, S. Bouchoule, X.

Lafosse, M. Mexis, C. Brimont, and T. Guillet, "LO-phonon-assisted polariton lasing in a ZnO-based microcavity," Physical Review B **85** (12), 121201 (2012).

[41] H. Franke, C. Sturm, R. Schmidt-Grund, G. Wagner, and M. Grundmann, "Ballistic propagation of exciton–polariton condensates in a ZnO-based microcavity," New Journal of Physics **14** (1), 013037 (2012).

[42] Y.-Y. Lai, Y.-P. Lan, and T.-C. Lu, "High-temperature polariton lasing in a strongly coupled ZnO microcavity," Applied Physics Express **5** (8), 082801 (2012).

[43] T.-C. Lu, Y.-Y. Lai, Y.-P. Lan, S.-W. Huang, J.-R. Chen, Y.-C. Wu, W.-F. Hsieh, and H. Deng, "Room temperature polariton lasing vs. photon lasing in a ZnO-based hybrid microcavity," Opt. Express **20** (5), 5530-5537 (2012).

[44] W. Xie, H. Dong, S. Zhang, L. Sun, W. Zhou, Y. Ling, J. Lu, X. Shen, and Z. Chen, "Room-Temperature Polariton Parametric Scattering Driven by a One-Dimensional Polariton Condensate," Physical Review Letters **108** (16), 166401 (2012).

[45] A. Trichet, E. Durupt, F. Médard, S. Datta, A. Minguzzi, and M. Richard, "Long-range correlations in a 97% excitonic one-dimensional polariton condensate," Physical Review B **88** (12), 121407 (2013).

[46] R. Butté, J. Levrat, G. Christmann, E. Feltin, J. F. Carlin, and N. Grandjean, "Phase diagram of a polariton laser from cryogenic to room temperature," Physical Review B **80** (23), 233301 (2009).

[47] J. Levrat, R. Butté, E. Feltin, J.-F. Carlin, N. Grandjean, D. Solnyshkov, and G. Malpuech, "Condensation phase diagram of cavity polaritons in GaN-based microcavities: Experiment and theory," Physical Review B **81** (12), 125305 (2010).

[48] R. Johne, D. D. Solnyshkov, and G. Malpuech, "Theory of exciton-polariton lasing at room temperature in ZnO microcavities," Applied Physics Letters **93** (21), 211105-211103 (2008).

[49] C.F. Klingshirn, B. K. Meyer, A. Waag, A. Hoffmann, and J.M.M. Geurts, *Zinc oxide: from fundamental properites towards novel applications*. (Springer, 2010).

[50] U. Ozgur, Ya I. Alivov, C. Liu, A. Teke, M. A. Reshchikov, S. Dogan, V. Avrutin, S. J. Cho, and H. Morkoc, "A comprehensive review of ZnO materials and devices," Journal of Applied Physics **98** (4), 041301-041103 (2005).

[51] F. Médard, "Conception et spectroscopie de microcavités à base de ZnO en régime de couplage fort pour l’obtention d’un laser à polaritons", PhD dissertation, UNIVERSITÉ BLAISE PASCAL – CLERMONT-FERRAND II, 2010.

[52] A. Dal Corso, M. Posternak, R. Resta, and A. Baldereschi, "Ab initio study of piezoelectricity and spontaneous polarization in ZnO," Physical Review B **50** (15), 10715-10721 (1994).

[53] M.R. Wagner, U. Haboeck, P. Zimmer, A. Hoffmann, S. Lautenschlager, C. Neumann, J. Sann, and B. K. Meyer,"Photonic properties of ZnO epilayers", Proc. of SPIE, Vol. 6174, pp. 64740X, 2007.

[54] M. R. Wagner, J.-H. Schulze, R. Kirste, M. Cobet, A. Hoffmann, C. Rauch, A. V. Rodina, B. K. Meyer, U. Röder, and K. Thonke, "Γ_7 valence band symmetry related hole fine splitting of bound excitons in ZnO observed in magneto-optical studies," Physical Review B **80** (20), 205203 (2009).

[55] B. K. Meyer, H. Alves, D. M. Hofmann, W. Kriegseis, D. Forster, F. Bertram, J. Christen, A. Hoffmann, M. Straßburg, M. Dworzak, U. Haboeck, and A. V. Rodina, "Bound exciton and donor–acceptor pair recombinations in ZnO," physica status solidi (b) **241** (2), 231-260 (2004).

[56] R. J. Elliott, "Intensity of Optical Absorption by Excitons," Physical Review **108** (6), 1384-1389 (1957).

[57] W. Y. Liang and A. D. Yoffe, "Transmission Spectra of ZnO Single Crystals," Physical Review Letters **20** (2), 59-62 (1968).

[58] A. Trichet, "One-dimensional polaritons in ZnO microwires: Towards one-dimensional quantum degenerated gas of bosons", PhD dissertation, L'université de Grenoble, 2012.

[59] G. Christmamn, "III-Nitride based microcavities: towards polariton condensation at room temperature", PhD dissertation, Ecole Polytechnique Fédérale de Lausanne, 2009.

[60] E. Rosencher and B. Vinter, *Optoelectronics*. (Cambridge University Press, Cambridge, 2002).

[61] S. F. Chichibu, T. Sota, G. Cantwell, D. B. Eason, and C. W. Litton, "Polarized photoreflectance spectra of excitonic polaritons in a ZnO single crystal," Journal of Applied Physics **93** (1), 756-758 (2003).

[62] W. J. Rappel, L. F. Feiner, and M. F. H. Schuurmans, "Exciton-polariton picture of the free-exciton lifetime in GaAs," Physical Review B **38** (11), 7874-7876 (1988).

[63] O. Aoudé, P. Disseix, J. Leymarie, A. Vasson, E. Aujol, and B. Beaumont, "Femtosecond time-resolved interferences of resonantly excited excitons in bulk GaN," Superlattices and Microstructures **36** (4–6), 607-614 (2004).

[64] E. Mallet, P. Disseix, D. Lagarde, M. Mihailovic, F. Réveret, T. V. Shubina, and J. Leymarie, "Accurate determination of homogeneous and inhomogeneous excitonic broadening in ZnO by linear and nonlinear spectroscopies," Physical Review B **87** (16), 161202 (2013).

[65] C. F. Klingshirn, R. Hauschild, J. Fallert, and H. Kalt, "Room-temperature stimulated emission of ZnO: Alternatives to excitonic lasing," Physical Review B **75** (11), 115203 (2007).

[66] A. V. Rodina, M. Strassburg, M. Dworzak, U. Haboeck, A. Hoffmann, A. Zeuner, H. R. Alves, D. M. Hofmann, and B. K. Meyer, "Magneto-optical properties of bound excitons in ZnO," Physical Review B **69** (12), 125206 (2004).

[67] J. Serrano, F. J. Manjón, A. H. Romero, A. Ivanov, M. Cardona, R. Lauck, A. Bosak, and M. Krisch, "Phonon dispersion relations of zinc oxide: Inelastic neutron scattering and ab initio calculations," Physical Review B **81** (17), 174304 (2010).

[68] D. I. Babic and S. W. Corzine, "Analytic expressions for the reflection delay, penetration depth, and absorptance of quarter-wave dielectric mirrors," Quantum Electronics, IEEE Journal of **28** (2), 514-524 (1992).

[69] G. Panzarini, L. C. Andreani, A. Armitage, D. Baxter, M. S. Skolnick, V. N. Astratov, J. S. Roberts, A. V. Kavokin, M. R. Vladimirova, and M. A. Kaliteevski, "Cavity-polariton dispersion and polarization splitting in single and coupled semiconductor microcavities," Phys. Solid State **41** (8), 1223-1238 (1999).

[70] F. Medard, D. Lagarde, J. Zuniga-Perez, P. Disseix, M. Mihailovic, J. Leymarie, E. Frayssinet, J. C. Moreno, F. Semond, M. Leroux, and S. Bouchoule, "Influence of the excitonic broadening on the strong light-matter coupling in bulk zinc oxide microcavities," Journal of Applied Physics **108** (4), 043508-043505 (2010).

[71] R. Houdre, R. P. Stanley, U. Oesterle, M. Ilegems, and C. Weisbuch, "Room temperature exciton-photon Rabi splittig in a semiconductor microcavity," Le Journal de Physique IV **3**, C5-51-C55-58 (1993).

[72] R. P. Stanley, R. Houdré, C. Weisbuch, U. Oesterle, and M. Ilegems, "Cavity-polariton photoluminescence in semiconductor microcavities: Experimental evidence," Physical Review B **53** (16), 10995-11007 (1996).

[73] S. Faure, T. Guillet, P. Lefebvre, T. Bretagnon, and B. Gil, "Comparison of strong coupling regimes in bulk GaAs, GaN, and ZnO semiconductor microcavities," Physical Review B **78** (23), 235323 (2008).

[74] B. Gayral, "Controlling spontaneous emission dynamics in semiconductor micro cavities," Ann. Phys. Fr. **26** (2), 1-135 (2001).

[75] M. O. Scully and M. S. Zubairy, *Quantum optics*. (Cambridge University Press, 2002).

[76] S. Pau, G. Björk, J. Jacobson, H. Cao, and Y. Yamamoto, "Microcavity exciton-polariton splitting in the linear regime," Physical Review B **51** (20), 14437-14447 (1995).

[77] J. Klaers, J. Schmitt, F. Vewinger, and M. Weitz, "Bose-Einstein condensation of photons in an optical microcavity," Nature **468** (7323), 545-548 (2010).

[78] V. Savona, L. C. Andreani, P. Schwendimann, and A. Quattropani, "Quantum well excitons in semiconductor microcavities: Unified treatment of weak and strong coupling regimes," Solid State Communications **93** (9), 733-739 (1995).

[79] R. Houdré, "Early stages of continuous wave experiments on cavity-polaritons," physica status solidi (b) **242** (11), 2167-2196 (2005).

[80] G. Dasbach, C. Diederichs, J. Tignon, C. Ciuti, Ph Roussignol, C. Delalande, M. Bayer, and A. Forchel, "Polarization inversion via parametric scattering in quasi-one-dimensional microcavities," Physical Review B **71** (16), 161308 (2005).

[81] J. M. Blatt, K. W. Böer, and W. Brandt, "Bose-Einstein Condensation of Excitons," Physical Review **126** (5), 1691-1692 (1962).

[82] C. Comte and P. Nozières, "Exciton Bose condensation : the ground state of an electron-hole gas - I. Mean field description of a simplified model," J. Phys. France **43** (7), 1069-1081 (1982).

[83] J. M. Kosterlitz and D. J. Thouless, "Ordering, metastability and phase transitions in two-dimensional systems," Journal of Physics C: Solid State Physics **6** (7), 1181 (1973).

[84] Z. Hadzibabic, P. Kruger, M. Cheneau, B. Battelier, and J. Dalibard, "Berezinskii-Kosterlitz-Thouless crossover in a trapped atomic gas," Nature **441** (7097), 1118-1121 (2006).

[85] F. Tassone and Y. Yamamoto, "Exciton-exciton scattering dynamics in a semiconductor microcavity and stimulated scattering into polaritons," Physical Review B **59** (16), 10830-10842 (1999).

[86] P. G. Savvidis, J. J. Baumberg, R. M. Stevenson, M. S. Skolnick, D. M. Whittaker, and J. S. Roberts, "Angle-Resonant Stimulated Polariton Amplifier," Physical Review Letters **84** (7), 1547-1550 (2000).

[87] R. Balili, V. Hartwell, D. Snoke, L. Pfeiffer, and K. West, "Bose-Einstein Condensation of Microcavity Polaritons in a Trap," Science **316** (5827), 1007-1010 (2007).

[88] E. Wertz, L. Ferrier, D. D. Solnyshkov, R. Johne, D. Sanvitto, A. Lemaitre, I. Sagnes, R. Grousson, A. V. Kavokin, P. Senellart, G. Malpuech, and J. Bloch, "Spontaneous formation and optical manipulation of extended polariton condensates," Nat Phys **6** (11), 860-864 (2010).

[89] D. Bajoni, P. Senellart, E. Wertz, I. Sagnes, A. Miard, A. Lemaître, and J. Bloch, "Polariton Laser Using Single Micropillar GaAs-GaAlAs Semiconductor Cavities," Physical Review Letters **100** (4), 047401 (2008).

[90] A. Amo, J. Lefrere, S. Pigeon, C. Adrados, C. Ciuti, L. Carusotto, R. Houdre, E. Giacobino, and A. Bramati, "Superfluidity of polaritons in semiconductor microcavities," Nat Phys **5** (11), 805-810 (2009).

[91] A. Amo, D. Sanvitto, F. P. Laussy, D. Ballarini, E. del Valle, M. D. Martin, A. Lemaitre, J. Bloch, D. N. Krizhanovskii, M. S. Skolnick, C. Tejedor, and L. Vina, "Collective fluid dynamics of a polariton condensate in a semiconductor microcavity," Nature **457** (7227), 291-295 (2009).

[92] K. G. Lagoudakis, M. Wouters, M. Richard, A. Baas, I. Carusotto, R. Andre, Le Si Dang, and B. Deveaud-Pledran, "Quantized vortices in an exciton-polariton condensate," Nat Phys **4** (9), 706-710 (2008).

[93] G. Roumpos, M. D. Fraser, A. Loffler, S. Hofling, A. Forchel, and Y. Yamamoto, "Single vortex-antivortex pair in an exciton-polariton condensate," Nat Phys **7** (2), 129-133 (2011).

[94] M. Sich, D. N. Krizhanovskii, M. S. Skolnick, A. V. Gorbach, HartleyR, D. V. Skryabin, E. A. Cerda-Mendez, BiermannK, R Hey, and P. V. Santos, "Observation of bright polariton solitons in a semiconductor microcavity," Nat Photon **6** (1), 50-55 (2012).

[95] A. Amo, S. Pigeon, D. Sanvitto, V. G. Sala, R. Hivet, I. Carusotto, F. Pisanello, G. Leménager, R. Houdré, E Giacobino, C. Ciuti, and A. Bramati, "Polariton Superfluids Reveal Quantum Hydrodynamic Solitons," Science **332** (6034), 1167-1170 (2011).

[96] R. Hivet, H. Flayac, D. D. Solnyshkov, D. Tanese, T. Boulier, D. Andreoli, E. Giacobino, J. Bloch, A. Bramati, G. Malpuech, and A. Amo, "Half-solitons in a polariton quantum fluid behave like magnetic monopoles," Nat Phys **8** (10), 724-728 (2012).

[97] T. K. Paraïso, M. Wouters, Y. Léger, F. Morier-Genoud, and B. Deveaud-Plédran, "Multistability of a coherent spin ensemble in a semiconductor microcavity," Nat Mater **9** (8), 655-660 (2010).

[98] A. Baas, J. Ph Karr, M. Romanelli, A. Bramati, and E. Giacobino, "Optical bistability in semiconductor microcavities in the nondegenerate parametric oscillation regime: Analogy with the optical parametric oscillator," Physical Review B **70** (16), 161307 (2004).

[99] L. Ferrier, E. Wertz, R. Johne, D. Solnyshkov, P. Senellart, I. Sagnes, A. Lemaître, G. Malpuech, and J. Bloch, "Interactions in Confined Polariton Condensates," Physical Review Letters **106** (12), 126401 (2011).

[100] T. K. Paraïso, D. Sarchi, G. Nardin, R. Cerna, Y. Leger, B. Pietka, M. Richard, O. El Daïf, F. Morier-Genoud, V. Savona, and B. Deveaud-Plédran, "Enhancement of microcavity polariton relaxation under confinement," Physical Review B **79** (4), 045319 (2009).

[101] G. Tosi, G. Christmann, N. G. Berloff, P. Tsotsis, T. Gao, Z. Hatzopoulos, P. G. Savvidis, and J. J. Baumberg, "Sculpting oscillators with light within a nonlinear quantum fluid," Nat Phys **8** (3), 190-194 (2012).

[102] D. Bajoni, E. Semenova, A. Lemaître, S. Bouchoule, E. Wertz, P. Senellart, and J. Bloch, "Polariton light-emitting diode in a GaAs-based microcavity," Physical Review B **77** (11), 113303 (2008).

[103] S. I. Tsintzos, N. T. Pelekanos, G. Konstantinidis, Z. Hatzopoulos, and P. G. Savvidis, "A GaAs polariton light-emitting diode operating near room temperature," Nature **453** (7193), 372-375 (2008).

[104] A. A. Khalifa, A. P. D. Love, D. N. Krizhanovskii, M. S. Skolnick, and J. S. Roberts, "Electroluminescence emission from polariton states in GaAs-based semiconductor microcavities," Applied Physics Letters **92** (6), 061107-061103 (2008).

[105] T. C. H. Liew, A. V. Kavokin, T. Ostatnický, M. Kaliteevski, I. A. Shelykh, and R. A. Abram, "Exciton-polariton integrated circuits," Physical Review B **82** (3), 033302 (2010).

[106] T. Gao, P. S. Eldridge, T. C. H. Liew, S. I. Tsintzos, G. Stavrinidis, G. Deligeorgis, Z. Hatzopoulos, and P. G. Savvidis, "Polariton condensate transistor switch," Physical Review B **85** (23), 235102 (2012).

[107] A. V. Kavokin, I. A. Shelykh, T. Taylor, and M. M. Glazov, "Vertical Cavity Surface Emitting Terahertz Laser," Physical Review Letters **108** (19), 197401 (2012).

[108] C. Schneider, A. Rahimi-Iman, N. Y. Kim, J. Fischer, I. G. Savenko, M. Amthor, M. Lermer, A. Wolf, L. Worschech, V. D. Kulakovskii, I. A. Shelykh, M. Kamp, S. Reitzenstein, A. Forchel, Y. Yamamoto, and S. Hofling, "An electrically pumped polariton laser," Nature **497** (7449), 348-352 (2013).

[109] P. Bhattacharya, B. Xiao, A. Das, S. Bhowmick, and J. Heo, "Solid State Electrically Injected Exciton-Polariton Laser," Physical Review Letters **110** (20), 206403 (2013).

[110] F. Tassone, C. Piermarocchi, V. Savona, A. Quattropani, and P. Schwendimann, "Bottleneck effects in the relaxation and photoluminescence of microcavity polaritons," Physical Review B **56** (12), 7554-7563 (1997).

[111] A. I. Tartakovskii, D. N. Krizhanovskii, G. Malpuech, M. Emam-Ismail, A. V. Chernenko, A. V. Kavokin, V. D. Kulakovskii, M. S. Skolnick, and J. S. Roberts, "Giant enhancement of polariton relaxation in semiconductor microcavities by polariton-free carrier interaction: Experimental evidence and theory," Physical Review B **67** (16), 165302 (2003).

[112] J. Kasprzak, D. D. Solnyshkov, R. André, Le Si Dang, and G. Malpuech, "Formation of an Exciton Polariton Condensate: Thermodynamic versus Kinetic Regimes," Physical Review Letters **101** (14), 146404 (2008).

[113] L. Pitaevskii and S. Stringari, *Bose-Einstein Condensation*. (Oxford Science Publications, Oxford, UK., 2003).

[114] M. Wouters and L. Carusotto, "Excitations in a Nonequilibrium Bose-Einstein Condensate of Exciton Polaritons," Physical Review Letters **99** (14), 140402 (2007).

[115] M. Wouters, L. Carusotto, and C. Ciuti, "Spatial and spectral shape of inhomogeneous nonequilibrium exciton-polariton condensates," Physical Review B **77** (11), 115340 (2008).

[116] D. Tanese, D. D. Solnyshkov, A. Amo, L. Ferrier, E. Bernet-Rollande, E. Wertz, I. Sagnes, A. Lemaître, P. Senellart, G. Malpuech, and J. Bloch, "Backscattering Suppression in Supersonic 1D Polariton Condensates," Physical Review Letters **108** (3), 036405 (2012).

[117] D. Bajoni, P. Senellart, A. Lemaître, and J. Bloch, "Photon lasing in GaAs microcavity: Similarities with a polariton condensate," Physical Review B **76** (20), 201305 (2007).

[118] P. Tsotsis, P. S. Eldridge, T. Gao, S. I. Tsintzos, Z. Hatzopoulos, and P. G. Savvidis, "Lasing threshold doubling at the crossover from strong to weak coupling regime in GaAs microcavity," New Journal of Physics **14** (2), 023060 (2012).

[119] H. Deng, G. Weihs, D. Snoke, J. Bloch, and Y. Yamamoto, "Polariton lasing vs. photon lasing in a semiconductor microcavity," Proceedings of the National Academy of Sciences **100** (26), 15318-15323 (2003).

[120] J. Frenkel, "On the Transformation of light into Heat in Solids. I," Physical Review **37** (1), 17-44 (1931).

[121] D. Pile, "Organic polariton laser," Nat Photon **4** (6), 402-402 (2010).

[122] Y. Wei, J. S. Lauret, L. Galmiche, P. Audebert, and E. Deleporte, "Strong exciton-photon coupling in microcavities containing new fluorophenethylamine based perovskite compounds," Opt. Express **20** (9), 10399-10405 (2012).

[123] Z. Han, H.-S. Nguyen, F. Boitier, Y. Wei, K. Abdel-Baki, J.-S. Lauret, J. Bloch, S. Bouchoule, and E. Deleporte, "High-Q planar organic-inorganic Perovskite-based microcavity," Opt. Lett. **37** (24), 5061-5063 (2012).

[124] G. Lanty, S. Zhang, J. S. Lauret, E. Deleporte, P. Audebert, S. Bouchoule, X. Lafosse, J. Zuñiga-Pérez, F. Semond, D. Lagarde, F. Médard, and J. Leymarie, "Hybrid cavity polaritons in a ZnO-perovskite microcavity," Physical Review B **84** (19), 195449 (2011).

[125] A. Dadgar, M. Poschenrieder, J. Blasing, K. Fehse, A. Diez, and A. Krost, "Thick, crack-free blue light-emitting diodes on Si(111) using low-temperature AlN interlayers and in situ Si_xN_y masking," Applied Physics Letters **80** (20), 3670-3672 (2002).

[126] S. Nakamura, T. Mukai, and M. Senoh, "Candela-class high-brightness InGaN/AlGaN double-heterostructure blue-light-emitting diodes," Applied Physics Letters **64** (13), 1687-1689 (1994).

[127] A. Avramescu, T. Lermer, J. Muller, S. Tautz, D. Queren, S. Lutgen, and U. Strauss, "InGaN laser diodes with 50 mW output power emitting at 515 nm," Applied Physics Letters **95** (7), 071103-071103 (2009).

[128] G. Cosendey, A. Castiglia, G. Rossbach, J.-F. Carlin, and N. Grandjean, "Blue monolithic AlInN-based vertical cavity surface emitting laser diode on free-standing GaN substrate," Applied Physics Letters **101** (15), 151113-151114 (2012).

[129] D. Kasahara, D. Morita, T. Kosugi, K. Nakagawa, J. Kawamata, Y. Higuchi, H. Matsumura, and T. Mukai, "Demonstration of Blue and Green GaN-Based Vertical-Cavity Surface-Emitting Lasers by Current Injection at Room Temperature," Appl. Phys. Express **4** (7), 072103 (2011).

[130] F. Semond, I. R. Sellers, F. Natali, D. Byrne, M. Leroux, J. Massies, N. Ollier, J. Leymarie, P. Disseix, and A. Vasson, "Strong light-matter coupling at room temperature in simple geometry GaN microcavities grown on silicon," Applied Physics Letters **87** (2), 021102-021103 (2005).

[131] I. R. Sellers, F. Semond, M. Leroux, J. Massies, P. Disseix, A. L. Henneghien, J. Leymarie, and A. Vasson, "Strong coupling of light with A and B excitons in GaN microcavities grown on silicon," Physical Review B **73** (3), 033304 (2006).

[132] F. Réveret, P. Disseix, J. Leymarie, A. Vasson, F. Semond, M. Leroux, and J. Massies, "Influence of the mirrors on the strong coupling regime in planar GaN microcavities," Physical Review B **77** (19), 195303 (2008).

[133] F. Stokker-Cheregi, A. Vinattieri, F. Semond, M. Leroux, I. R. Sellers, J. Massies, D. Solnyshkov, G. Malpuech, M. Colocci, and M. Gurioli, "Polariton relaxation bottleneck and its thermal suppression in bulk GaN microcavities," Applied Physics Letters **92** (4), 042119-042113 (2008).

[134] A. Alyamani, D. Sanvitto, A. A. Khalifa, M. S. Skolnick, T. Wang, F. Ranalli, P. J. Parbrook, A. Tahraoui, and R. Airey, "GaN hybrid microcavities in the strong coupling regime grown by metal-organic chemical vapor deposition on sapphire substrates," Journal of Applied Physics **101** (9), 093110-093113 (2007).

[135] E. Feltin, J. F. Carlin, J. Dorsaz, G. Christmann, R. Butte, M. Laugt, M. Ilegems, and N. Grandjean, "Crack-free highly reflective AlInN/AlGaN Bragg mirrors for UV applications," Applied Physics Letters **88** (5), 051108-051103 (2006).

[136] G. Christmann, D. Simeonov, R. Butte, E. Feltin, J. F. Carlin, and N. Grandjean, "Impact of disorder on high quality factor III-V nitride microcavities," Applied Physics Letters **89** (26), 261101-261103 (2006).

[137] E. Feltin, G. Christmann, R. Butte, J. F. Carlin, M. Mosca, and N. Grandjean, "Room temperature polariton luminescence from a GaN/AlGaN quantum well microcavity," Applied Physics Letters **89** (7), 071107-071103 (2006).

[138] R. Butté, G. Christmann, E. Feltin, J. F. Carlin, M. Mosca, M. Ilegems, and N. Grandjean, "Room-temperature polariton luminescence from a bulk GaN microcavity," Physical Review B **73** (3), 033315 (2006).

[139] G. Christmann, R. Butté, E. Feltin, J. F. Carlin, and N. Grandjean, "Impact of inhomogeneous excitonic broadening on the strong exciton-photon coupling in quantum well nitride microcavities," Physical Review B **73** (15), 153305 (2006).

[140] J. J. Baumberg, A. V. Kavokin, S. Christopoulos, A. J. D. Grundy, R. Butté, G. Christmann, D. D. Solnyshkov, G. Malpuech, G. Baldassarri Höger von Högersthal, E. Feltin, J. F. Carlin, and N. Grandjean, "Spontaneous Polarization Buildup in a Room-Temperature Polariton Laser," Physical Review Letters **101** (13), 136409 (2008).

[141] D. Solnyshkov, H. Ouerdane, and G. Malpuech, "Kinetic phase diagrams of GaN-based polariton lasers," Journal of Applied Physics **103** (1), 016101-016103 (2008).

[142] G. Malpuech, Y. G. Rubo, F. P. Laussy, P. Bigenwald, and A. V. Kavokin, "Polariton laser: thermodynamics and quantum kinetic theory," Semiconductor Science and Technology **18** (10), S395 (2003).

[143] G. Rossbach, J. Levrat, A. Dussaigne, G. Cosendey, M. Glauser, M. Cobet, R. Butté, N. Grandjean, H. Teisseyre, M. Bockowski, I. Grzegory, and T. Suski, "Tailoring the light-matter coupling in anisotropic microcavities: Redistribution of oscillator strength in strained m-plane GaN/AlGaN quantum wells," Physical Review B **84** (11), 115315 (2011).

[144] J. Levrat, G. Rossbach, A. Dussaigne, G. Cosendey, M. Glauser, M. Cobet, R. Butté, N. Grandjean, H. Teisseyre, M. Boćkowski, I. Grzegory, and T. Suski, "Nonlinear emission properties of an optically anisotropic GaN-based microcavity," Physical Review B **86** (16), 165321 (2012).

[145] R. Atanasov, F. Bassani, A. D'Andrea, and N. Tomassini, "Exciton properties and optical response in $In_xGa_{1-x}As$/GaAs strained quantum wells," Physical Review B **50** (19), 14381-14388 (1994).

[146] A. Amo, M. D. Martin, L. Vina, A. I. Toropov, and K. S. Zhuravlev, "Photoluminescence dynamics in GaAs along an optically induced Mott transition," Journal of Applied Physics **101** (8), 081717-081715 (2007).

[147] N. Cain, M. O'Neill, J. E. Nicholls, T. Stirner, W. E. Hagston, and D. E. Ashenford, "Photoluminescence of CdTe/CdMnTe multiple quantum wells excited near the Mott transition," Journal of Luminescence **75** (4), 269-275 (1997).

[148] G. Christmann, R. Butté, E. Feltin, A. Mouti, P. A. Stadelmann, A. Castiglia, J.-F. Carlin, and N. Grandjean, "Large vacuum Rabi splitting in a multiple quantum well GaN-based microcavity in the strong-coupling regime," Physical Review B **77** (8), 085310 (2008).

[149] K. Kornitzer, T. Ebner, K. Thonke, R. Sauer, C. Kirchner, V. Schwegler, M. Kamp, M. Leszczynski, I. Grzegory, and S. Porowski, "Photoluminescence and reflectance spectroscopy of excitonic transitions in high-quality homoepitaxial GaN films," Physical Review B **60** (3), 1471-1473 (1999).

[150] C. P. Dietrich, M. Lange, C. Sturm, R. Schmidt-Grund, and M. Grundmann, "One- and two-dimensional cavity modes in ZnO microwires," New Journal of Physics **13** (10), 103021 (2011).

[151] A. Trichet, L. Sun, G. Pavlovic, N. A. Gippius, G. Malpuech, W. Xie, Z. Chen, M. Richard, and Le Si Dang, "One-dimensional ZnO exciton polaritons with negligible thermal broadening at room temperature," Physical Review B **83** (4), 041302 (2011).

[152] Q. Xu, D. Fattal, and R. G. Beausoleil, "Silicon microring resonators with 1.5-?m radius," Opt. Express **16** (6), 4309-4315 (2008).

[153] Z. Chen, "Zone-Edge Lasing in Micro-Assembled Polariton Crystals", in *conference of PLMCN* (Crete, Creece, 2013).

[154] R. Schmidt-Grund, B. Rheinländer, C. Czekalla, G. Benndorf, H. Hochmuth, M. Lorenz, and M. Grundmann, "Exciton–polariton formation at room temperature in a planar ZnO resonator structure," Appl. Phys. B **93** (2-3), 331-337 (2008).

[155] R. Schmidt-Grund, H. Hilmer, A. Hinkel, C. Sturm, B. Rheinländer, V. Gottschalch, M. Lange, J. Zúñiga-Pérez, and M. Grundmann, "Two-dimensional confined photonic wire resonators – strong light–matter coupling," physica status solidi (b) **247** (6), 1351-1364 (2010).

[156] C. Sturm, H. Hilmer, R. Schmidt-Grund, and M. Grundmann, "Exciton–polaritons in a ZnO-based microcavity: polarization dependence and nonlinear occupation," New Journal of Physics **13** (3), 033014 (2011).

[157] M. Richard, R. Romestain, R. Andre, and Le Si Dang, "Consequences of strong coupling between excitons and microcavity leaky modes," Applied Physics Letters **86** (7), 071916-071913 (2005).

[158] T. Guillet, C. Brimont, P. Valvin, B. Gil, T. Bretagnon, F. Medard, M. Mihailovic, J. Zuniga-Perez, M. Leroux, F. Semond, and S. Bouchoule, "Laser emission with excitonic gain in a ZnO planar microcavity," Applied Physics Letters **98** (21), 211105-211103 (2011).

[159] L. Orosz, F Rveret, S. Bouchoule, J Zuniga-Perez;rez, F Medard, J. Leymarie, P. Disseix, M. Mihailovic, E. Frayssinet, F. Semond, M. Leroux, M. Mexis, C. Brimont, and T. Guillet, "Fabrication and optical properties of a fully-hybrid epitaxial ZnO-based microcavity in the strong-coupling regime," Applied Physics Express **4** (7), 072001 (2011).

[160] J.-R. Chen, T.-C. Lu, Y.-C. Wu, S.-C. Lin, W.-F. Hsieh, S.-C. Wang, and Hui Deng, "Characteristics of exciton-polaritons in ZnO-based hybrid microcavities," Opt. Express **19** (5), 4101-4112 (2011).

[161] Y.-Y. Lai, Y.-P. Lan, and T.-C. Lu, "Strong light-matter interaction in ZnO microcavities," Light: Science & Applications **2**, e76 (2013).

[162] S. Kalusniak, S. Sadofev, S. Halm, and F. Henneberger, "Vertical cavity surface emitting laser action of an all monolithic ZnO-based microcavity," Applied Physics Letters **98** (1), 011101-011103 (2011).

[163] S. Halm, S. Kalusniak, S. Sadofev, H. J. Wunsche, and F. Henneberger, "Strong exciton-photon coupling in a monolithic ZnO/(Zn,Mg)O multiple quantum well microcavity," Applied Physics Letters **99** (18), 181121-181123 (2011).

[164] K. Bejtka, F. Reveret, R. W. Martin, P. R. Edwards, A. Vasson, J. Leymarie, I. R. Sellers, J. Y. Duboz, M. Leroux, and F. Semond, "Strong light-matter coupling in ultrathin double dielectric mirror GaN microcavities," Applied Physics Letters **92** (24), 241105-241103 (2008).

[165] M. Richard, "Quansi-condensation de polaritons sous excitation incohérente dans les microcavités II-VI à base de CdTe", PhD dissertation, Université Joseph Fourrier - Grenoble 1, 2004.

[166] "http://www.crystec.de/zno-e.html".

[167] M. Richard, J. Kasprzak, R. Romestain, R. André, and Le Si Dang, "Spontaneous Coherent Phase Transition of Polaritons in CdTe Microcavities," Physical Review Letters **94** (18), 187401 (2005).

[168] J. Levrat, "Physics of polariton condensates in GaN-based planar microcavities", PhD dissertation, Ecole Polytechnique Fédérale de Lausanne, 2012.

[169] P. Corfdir, J. Levrat, G. Rossbach, R. Butté, E. Feltin, J. F. Carlin, G. Christmann, P. Lefebvre, J. D. Ganière, N. Grandjean, and B. Deveaud-Plédran, "Impact of biexcitons on the relaxation mechanisms of polaritons in III-nitride based multiple quantum well microcavities," Physical Review B **85** (24), 245308 (2012).

[170] M. Aßmann, J. Tempel, F. Veit, M. Bayer, A. Rahimi-Iman, A. Löffler, S. Höfling, S. Reitzenstein, L. Worschech, and A. Forchel, "From polariton condensates to highly photonic quantum degenerate states of bosonic matter," Proceedings of the National Academy of Sciences **108** (5), 1804-1809 (2011).

[171] E. Wertz, L. Ferrier, D. D. Solnyshkov, P. Senellart, D. Bajoni, A. Miard, A. Lemaitre, G. Malpuech, and J. Bloch, "Spontaneous formation of a polariton condensate in a planar GaAs microcavity," Applied Physics Letters **95** (5), 051108-051103 (2009).

[172] E. Wertz, A. Amo, D. D. Solnyshkov, L. Ferrier, T. C. H. Liew, D. Sanvitto, P. Senellart, I. Sagnes, A. Lemaître, A. V. Kavokin, G. Malpuech, and J. Bloch, "Propagation and Amplification Dynamics of 1D Polariton Condensates," Physical Review Letters **109** (21), 216404 (2012).

[173] H. Haug and S. Koch, "On the Theory of Laser Action in Dense Exeiton Systems," physica status solidi (b) **82** (2), 531-543 (1977).

[174] B. Sermage, G. Malpuech, A. V. Kavokin, and V. Thierry-Mieg, "Polariton acceleration in a microcavity wedge," Physical Review B **64** (8), 081303 (2001).

[175] M. Aßmann, F. Veit, M. Bayer, A. Löffler, S. Höfling, M. Kamp, and A. Forchel, "All-optical control of quantized momenta on a polariton staircase," Physical Review B **85** (15), 155320 (2012).

[176] N. Antoine-Vincent, F. Natali, M. Mihailovic, A. Vasson, J. Leymarie, P. Disseix, D. Byrne, F. Semond, and J. Massies, "Determination of the refractive indices of AlN, GaN, and $Al_xGa_{1-x}N$ grown on (111)Si substrates," Journal of Applied Physics **93** (9), 5222-5226 (2003).

[177] W. P. McCray, "MBE deserves a place in the history books," Nat Nano **2** (5), 259-261 (2007).

[178] A. Y. Cho and J. R. Arthur, "Molecular beam epitaxy," Progress in Solid State Chemistry **10, Part 3** (0), 157-191 (1975).

[179] P. N. Prasad, *Nanophotonics*. (John Wiley & Sons, Hoboken, New Jersey, 2004).

[180] J. F. Carlin, J. Dorsaz, E. Feltin, R. Butte, N. Grandjean, M. Ilegems, and M. Laugt, "Crack-free fully epitaxial nitride microcavity using highly reflective AlInN/GaN Bragg mirrors," Applied Physics Letters **86** (3), 031107-031103 (2005).

[181] R. Butté, G. Christmann, E. Feltin, A. Castiglia, J. Levrat, G. Cosendey, A. Altoukhov, J.-F. Carlin, and N. Grandjean,"Room temperature polariton lasing in III-nitride microcavities: a comparison with blue GaN-based vertical cavity surface emitting lasers", Proc. SPIE, Vol. 7216, pp. 721619-721619-721616, 2009.

[182] E. Feltin, B. Beaumont, M. Laügt, P. de Mierry, P. Vennéguès, M. Leroux, and P. Gibart, "Crack-Free Thick GaN Layers on Silicon (111) by Metalorganic Vapor Phase Epitaxy," physica status solidi (a) **188** (2), 531-535 (2001).

[183] A. Dadgar, J. Christen, T. Riemann, S. Richter, J. Blasing, A. Diez, A. Krost, A. Alam, and M. Heuken, "Bright blue electroluminescence from an InGaN/GaN multiquantum-well diode on Si(111): Impact of an AlGaN/GaN multilayer," Applied Physics Letters **78** (15), 2211-2213 (2001).

[184] E. Frayssinet, Y. Cordier, H. P. D. Schenk, and A. Bavard, "Growth of thick GaN layers on 4-in. and 6-in. silicon (111) by metal-organic vapor phase epitaxy," physica status solidi (c) **8** (5), 1479-1482 (2011).

[185] Y. Honda, Y. Kuroiwa, M. Yamaguchi, and N. Sawaki, "Growth of GaN free from cracks on a (111)Si substrate by selective metalorganic vapor-phase epitaxy," Applied Physics Letters **80** (2), 222-224 (2002).

[186] S. Zamir, B. Meyler, and J. Salzman, "Thermal microcrack distribution control in GaN layers on Si substrates by lateral confined epitaxy," Applied Physics Letters **78** (3), 288-290 (2001).

[187] B. Zhang, H. Liang, Y. Wang, Z. Feng, K. W. Ng, and K. M. Lau, "High-performance III-nitride blue LEDs grown and fabricated on patterned Si substrates," Journal of Crystal Growth **298** (0), 725-730 (2007).

[188] E. Feltin, "Hétéro-épitaxie de nitrure de gallium sur substrat de silicium (111) et applications", PhD dissertation, Universié de Nice Sophia-Antipolis, 2003.

[189] M. Hugues, P. A. Shields, F. Sacconi, M. Mexis, M. Auf der Maur, M. Cooke, M. Dineen, A. Di Carlo, D. W. E. Allsopp, and J. Zuniga-Perez, "Strain evolution in GaN nanowires: From free-surface objects to coalesced templates," Journal of Applied Physics **114** (8), 084307-084309 (2013).

[190] M. J. Rashid, "Fabrication and study of AlN optical resonators containing GaN quantum dots for UV emitters and new concepts for the growth of GaN on silicon substrates.", PhD dissertation, Universié de Nice Sophia-Antipolis, 2012.

[191] T. Hossain, "GaN based structures on patterned silicon substrate: stress and strain analysis", PhD dissertation, Universié de Nice Sophia-Antipolis, 2012.

[192] Y. Cordier, J. C. Moreno, N. Baron, E. Frayssinet, S. Chenot, B. Damilano, and F. Semond, "AlGaN/GaN high electron mobility transistor grown by molecular beam epitaxy on Si(110): comparisons with Si(111) and Si(001)," physica status solidi (c) **6** (S2), S1020-S1023 (2009).

[193] B. Wu, A. Kumar, and S. Pamarthy, "High aspect ratio silicon etch: A review," Journal of Applied Physics **108** (5), 051101-051120 (2010).

[194] M. Leroux, F. Semond, F. Natali, D. Byrne, F. Cadoret, B. Damilano, A. Dussaigne, N. Grandjean, A. Le Louarn, S. Vézian, and J. Massies, "About some optical properties of AlxGa1−xN /GaN quantum wells grown by molecular beam epitaxy," Superlattices and Microstructures **36** (4–6), 659-674 (2004).

[195] H. Morkoc, S. Strite, G. B. Gao, M. E. Lin, B. Sverdlov, and M. Burns, "Large-band-gap SiC, III-V nitride, and II-VI ZnSe-based semiconductor device technologies," Journal of Applied Physics **76** (3), 1363-1398 (1994).

[196] K. Sakurai, M. Kanehiro, K. Nakahara, T. Tetsuhiro, S. Fujita, and S. Fujita, "Effects of oxygen plasma condition on MBE growth of ZnO," Journal of Crystal Growth **209** (2–3), 522-525 (2000).

[197] T. E. Murphy, S. Walavalkar, and J. D. Phillips, "Epitaxial growth and surface modeling of ZnO on c-plane Al_2O_3," Applied Physics Letters **85** (26), 6338-6340 (2004).

[198] S. Sadofev, S. Blumstengel, J. Cui, J. Puls, S. Rogaschewski, P. Schafer, Yu G. Sadofyev, and F. Henneberger, "Growth of high-quality ZnMgO epilayers and ZnO/ZnMgO quantum well structures by radical-source molecular-beam epitaxy on sapphire," Applied Physics Letters **87** (9), 091903-091903 (2005).

[199] S. Blumstengel, S. Sadofev, H. Kirmse, and F. Henneberger, "Extreme low-temperature molecular beam epitaxy of ZnO-based quantum structures," Applied Physics Letters **98** (3), 031907-031903 (2011).

[200] A. Nahhas, H. K. Kim, and J. Blachere, "Epitaxial growth of ZnO films on Si substrates using an epitaxial GaN buffer," Applied Physics Letters **78** (11), 1511-1513 (2001).

[201] W. Guo, M. B. Katz, C. T. Nelson, T. Heeg, D. G. Schlom, B. Liu, Y. Che, and X. Q. Pan, "Epitaxial ZnO films on (111) Si substrates with Sc[sub 2]O[sub 3] buffer layers," Applied Physics Letters **94** (12), 122107-122103 (2009).

[202] J. M. Chauveau, M. Teisseire, H. Kim-Chauveau, C. Deparis, C. Morhain, and B. Vinter, "Benefits of homoepitaxy on the properties of nonpolar (Zn,Mg)O/ZnO quantum wells on a-plane ZnO substrates," Applied Physics Letters **97** (8), 081903-081903 (2010).

[203] P. M. Walker, L. Tinkler, M. Durska, D. M. Whittaker, I. J. Luxmoore, B. Royall, D. N. Krizhanovskii, M. S. Skolnick, I. Farrer, and D. A. Ritchie, "Exciton polaritons in semiconductor waveguides," Applied Physics Letters **102** (1), 012109-012104 (2013).

[204] E. Kammann, H. Ohadi, M. Maragkou, A. V. Kavokin, and P. G. Lagoudakis, "Crossover from photon to exciton-polariton lasing," New Journal of Physics **14** (10), 105003 (2012).

[205] F. Reveret, K. Bejtka, P. R. Edwards, S. Chenot, I. R. Sellers, P. Disseix, A. Vasson, J. Leymarie, J. Y. Duboz, M. Leroux, F. Semond, and R. W. Martin, "Strong light-matter coupling in bulk GaN-microcavities with double dielectric mirrors fabricated by two different methods," Journal of Applied Physics **108** (4), 043524-043526 (2010).

[206] F. Li, L. Orosz, O. Kamoun, S. Bouchoule, C. Brimont, P. Disseix, T. Guillet, X. Lafosse, M. Leroux, J. Leymarie, M. Mexis, M. Mihailovic, G. Patriarche, F. Réveret, D. Solnyshkov, J. Zuniga-Perez, and G. Malpuech, "From Excitonic to Photonic Polariton Condensate in a ZnO-Based Microcavity," Physical Review Letters **110** (19), 196406 (2013).

[207] J. M. Chauveau, M. Teisseire, H. Kim-Chauveau, C. Morhain, C. Deparis, and B. Vinter, "Anisotropic strain effects on the photoluminescence emission from heteroepitaxial and homoepitaxial nonpolar (Zn,Mg)O/ZnO quantum wells," Journal of Applied Physics **109** (10), 102420-102426 (2011).

[208] D. A. B. Miller, D. S. Chemla, T. C. Damen, A. C. Gossard, W. Wiegmann, T. H. Wood, and C. A. Burrus, "Band-Edge Electroabsorption in Quantum Well Structures: The Quantum-Confined Stark Effect," Physical Review Letters **53** (22), 2173-2176 (1984).

[209] A. Ohtomo, M. Kawasaki, T. Koida, K. Masubuchi, H. Koinuma, Y. Sakurai, Y. Yoshida, T. Yasuda, and Y. Segawa, "$Mg_xZn_{1-x}O$ as a II--VI widegap semiconductor alloy," Applied Physics Letters **72** (19), 2466-2468 (1998).

[210] D. Tainoff, M. Al-Khalfioui, C. Deparis, B. Vinter, M. Teisseire, C. Morhain, and J. M. Chauveau, "Residual and nitrogen doping of homoepitaxial nonpolar m-plane ZnO films grown by molecular beam epitaxy," Applied Physics Letters **98** (13), 131915-131913 (2011).

[211] P. Muret, D. Tainoff, C. Morhain, and J.-M. Chauveau, "Donor and acceptor levels in ZnO homoepitaxial thin films grown by molecular beam epitaxy and doped with plasma-activated nitrogen," Applied Physics Letters **101** (12), 122104-122104 (2012).

[212] A. Ashrafi, "Exciton localization in inhomogeneously broadened ZnO/$Mg_xZn_{1-x}O$ quantum wells," Journal of Applied Physics **107** (12), 123527-123525 (2010).

Acknowledgements

This thesis results from three years' continuous hard work that I would not have completed without the help of many others. Herein I would like to give my most faithful acknowledgements to those who have been guiding me, helping me, and sharing the pain and happiness with me during the last three years.

First of all, I feel myself very lucky to have the best PhD supervisor that I can ever imagine: Dr. Jesus Zuniga-Perez. As a researcher, he is knowledgeable, skillful, modest, honest, enthusiastic and prudent. As a supervisor, he cares about the students' careers like his own. He was always willing to help me with academic questions, being able to discuss with me frequently and follow very well my research progress. He also provided me with useful information and suggestions for my future career. In addition to research, Jesus also cares about my daily life and has given me a lot of help on that. Though strict with academics, he is very easygoing in daily life as a good friend.

I would like to thank Dr. Jean-Yves Duboz, the director of CRHEA and my PhD supervisor. He is very knowledgeable and has always tried to create good lab environment for the PhD students. He has been very interested in the polariton research field and has provided helpful insights and critical ideas onto my thesis work.

I would like to thank Prof. Alberto Bramati, Prof. Maurice Skolnick, Dr. Aristide Lemaître and Dr. Maxime Richard who have accepted to be the jury of this thesis and provided valuable comments and discussions on my work.

This PhD work has been carried out in the framework of the European Marie-Curie Initial Training Network (ITN) "CLERMONT4", for which I would like first to express my gratitude to the network coordinator, Prof. Dr. Alexey Kavokin. The "CLERMONT4" project has provided me with numerous opportunities, including a good salary and travelling allowance, participation in international conferences, workshops and project meetings, as well as doing research work in other laboratories. In this network, and therefore in my PhD work, the achievements regarding ZnO microcavities come from a joint effort of four CNRS labs, many thanks must be devoted to all our partners:

At LPN, Dr. Sophie Bouchoule and Xavier Lafosse have developed high quality dielectric DBRs. Without their excellent work the ZnO microcavities would not have been fabricated. Especially important was the enthusiasm and energy displayed by Dr. Sophie Bouchoule, who has always pushed us forward and brought about numerous valuable suggestions on the processing/growth of the cavities.

At Institut Pascal, spectroscopic studies on the ZnO microcavities have been performed in the group of Prof. Dr. Joel Leymarie, with experiments being conducted with (and by) Dr. François Réveret and Laurent Orosz, who have made great contributions to the main work of

this thesis. Besides, I would also like to thank Prof. Dr. Pierre Disseix and Dr. Martine Mihailovic for their fruitful discussions. The theoretical analysis of the ZnO polariton lasers has been performed by Dr. Guillaume Malpuech and Dr. Dmitry Solnyshkov. Their elegant work has enabled deep and comprehensive understanding of our experimental results, from which all the members in this collaboration benefited. Special acknowledgements should be given again to Dr. Malpuech for his efforts in organizing the production of our article published, after a long journey through many hands, in Physical Review Letters.

At L2C, acknowledgements must be given to the group of Dr. Thierry Guillet who has conducted excellent spectroscopic studies leading to the demonstration of the ZnO polariton lasers at room temperature. People having been working on the project and with whom I performed measurements at L2C include: Dr. Thierry Guillet, Dr. Christelle Brimont, Dr. Meletis Mexis, Olfa Kamoun and Rereao Hahe. Thanks should also be given to Dr. Bernard Gil for his continuous support to the research at LC2.

I would like to thank Prof. Dr. Nicolas Grandjean and Dr. Raphael Butté at EPFL for providing us with high quality AlInN/AlGaN DBRs.

Finally, I must thank my colleagues at CRHEA, especially those with whom I have spent more time and who have contributed most to my PhD project. Dr. Fabrice Semond, together with his students Dr. Mohammad Junaebur Rashid and Guillaume Gommé, has developed the fabrication technique of the high-quality AlGaN/AlN DBRs on patterned Si substrate, which was the key step for achieving the semi-hybrid microcavities in this thesis. I would like to thank Dr. Mathieu Leroux for helping me understanding many physical concepts and teaching strict experimental methodology, Dr. Jean-Michel Chauveau and Dr. Christiane Deparis for their pioneering works on the ZnO/ZnMgO homoeptiaxial growth, and Sébastien Chenot for his invaluable help in the sample fabrication. I would like to thank Michèle Pefferkorn for her helps in the visa issues, Ann-Marie Galiana for her helps in all my trips and courses. Moreover, I would like to thank all my colleagues who have shared the happy time with me in CRHEA and who have helped me with my daily work and life, especially Stéphanie Rennesson, Dr. Mohammad Junaebur Rashid, Philippe Vennéguès and Dr. Benjamin Damilano.

The Côte d’Azur in France is among the most enjoyable places in the world and it has been my happiest time to live and work there for three years. Especially the participation in the Symphony Orchestra of Sophia-Antipolis has enabled me to explore more music that I haven’t learned about in China and has brought me great fun. Besides south France, Paris is also one of my favorite places where I stayed five months for spectroscopy experiments in the group of Prof. Alberto Bramati at Laboratoire Kastler Brossel. During working in Paris I have got lots of help from Dr. Godefroy Leménager, Dr. Kenneth Maussang, Dr. Jonathan Roslund, Mathieu Manceau, Yin Cai and other colleagues. The city of Paris, filled by an art-and-culture atmosphere, has deeply attracted me, not to mention the happy time that I have spent there with my new friends. The three years and four months’ experience in France will be a precious memory throughout my life.

Last but not least, I would like to give my greatest thanks to my parents. They are very open-minded and have been always supporting me whatever my decisions were. As the only child of the family, I have been back home only twice during my five years’ work in Canada and France. However, they didn’t show any unhappiness on that. Without their support I would not have been able to finish my education and research work. I wish I will be able to spend more time with them in the future.